National Technical University of Athens
School of Mechanical Engineering
Fluids Section
Parallel CFD & Optimization Unit

The Continuous Adjoint Method for Automotive Aeroacoustic Shape Optimization

PhD Thesis

Christos S. Kapellos

Supervisor: Kyriakos C. Giannakoglou
Professor, NTUA

Athens, 2019

National Technical University of Athens
School of Mechanical Engineering
Fluids Section
Parallel CFD & Optimization Unit

The Continuous Adjoint Method for Automotive Aeroacoustic Shape Optimization

PhD Thesis

Christos S. Kapellos

Examination Committee:

1. Kyriakos Giannakoglou (Supervisor)*
   Professor, NTUA, School of Mechanical Engineering
2. Spyridon Voutsinas*
   Professor, NTUA, School of Mechanical Engineering
3. Vasileios Riziotis*
   Assistant Professor, NTUA, School of Mechanical Engineering
4. Konstantinos Mathioudakis
   Professor, NTUA, School of Mechanical Engineering
5. Konstantinos Belibassakis
   Professor, NTUA, School of Naval Architecture & Marine Engineering
6. Thomas Rung
   Professor Dr.-Ing, Hamburg University of Technology, Institute for Fluid Dynamics and Ship Theory
7. Volker Schulz
   Professor Dr, University of Trier, Department of Mathematics

* Member of the advisory committee.

Athens, 2019

Disclaimer

The results, opinions and conclusions of this dissertation are not necessarily those of the Volkswagen AG.

Die Ergebnisse, Meinungen und Schlüße dieser Dissertation sind nicht notwendigerweise die der Volkswagen AG.

Abstract

The present doctoral thesis deals with the mathematical formulation, programming and verification of the continuous adjoint method to the constituent parts of an existing noise prediction chain for automotive aeroacoustics. The proposed method is applied to optimize a generic vehicle, the SAE body, in order to reduce wind noise in its interior.

When a car travels at high speeds, flow-induced noise is generated in the region near the side mirror and is radiated towards all directions, reaching also the side window. Its vibrational response to this acoustic load generates in turn sound waves that propagate into the cabin and are perceived by the passengers as noise. An existing aeroacoustic framework simulating these physical mechanisms consists of an Improved Delayed Detached Eddy Simulation (IDDES) of the Navier-Stokes equations to obtain the unsteady pressure distribution on the mirror, the Kirchhoff Integral method to compute the radiated acoustic pressure on the side window, the bending wave equation on the side window to compute its deflection and, finally, the wave equation in the interior to obtain the interior sound field.

The continuous adjoint method in this thesis is based on the aforementioned framework which is split in two domains; the exterior domain that includes the flow-induced noise generation and radiation to the window and the interior domain that includes the vibroacoustic model for window vibration and interior wave propagation. These systems are firstly examined separately and, then, coupled and the contintuous adjoint chain for vehicle aeroacoustic optimization is proposed.

Regarding the vibroacoustic model, the bending wave equation is solved on the car's side window, using as a source term the pressure load obtained by the exterior domain. The resulting window acceleration is then used as a boundary condition for the wave equation that is solved in the cabin to compute the interior sound field. The Sound Pressure Level at a point near the driver's ear is then defined as the objective function and the adjoint wave and bending wave equations are derived. These must be solved backwards in time and in the following order: the adjoint wave equation is solved first by considering a monopole source term at the location where the objective function is defined. The propagation of the adjoint interior pressure in the cabin is computed and used thereupon as a source term for the adjoint bending wave equation, solved at the window. The resulting adjoint deflection is then used in the expression of the sensitivity derivative term on the window. This term is used later to couple the interior and exterior domains and additional emphasis is laid upon its discretization. A hand-differentiated expression is proposed to ensure its accuracy. The developed method is verified against Finite Differences and, then, is applied to the cabin of the SAE body to minimize interior noise using synthetic pressure waves as a load on the window.

The continuous adjoint method for the flow-induced sound radiation with the

Kirchhoff Integral is proposed where the differentiated Kirchhoff Integral is used to compute the boundary condition of the adjoint velocity on the noise radiating (Kirchhoff) surface and, then, the unsteady adjoint Navier-Stokes equations are solved backwards in time. It should be noted that the time window where the simulation is performed and the one over which the objective function is evaluated do not coincide. This is reflected on the adjoint boundary conditions along the body and the time integration of the sensitivity derivatives. Furthermore, to ensure the consistency of the continuous adjoint-based gradients, grid sensitivities are taken into account which gives rise to the adjoint grid displacement equations along with an additional term in the sensitivity derivatives expression. The proposed method is verified against Finite Differences on a 3D turbulent flow around a cylinder and, then, applied to the SAE body. Firstly, a sensitivity map analysis is conducted to investigate the influence the sensitivity derivative integration time window has on its computation but, also, to prove the importance of including the adjoint grid displacement equations. Finally, an optimization of the side mirror is performed, targeting at minimizing the radiated flow-induced sound at the vehicle's side window.

After the formulation and verification of the continuous adjoint method for the systems of equations in the interior and exterior domains, their coupling is presented. Through the solution of the adjoint aeroacoustic chain, the sensitivity of the interior acoustic pressure with respect to a normal displacement of the mirror is computed to indicate the way the mirror shape should change, in order to improve the aeroacoustic performance of the vehicle. The method is applied to compute the adjoint aeroacoustic sensitivity map on the side mirror of the generic SAE vehicle and successfully perform several optimization cycles. In addition, the impact that optimizing for each individual step of the noise prediction chain has on interior noise is investigated.

Finally, two approaches are proposed, in order to perform the aforementioned adjoint analysis, focusing however on a specific frequency range; the first approach uses an objective function which includes the Fourier Transform and is integrated over frequencies whereas the second one uses a signal processing filter that preserves only the necessary frequency components. The adjoint formulation, advantages and drawbacks of each approach are discussed. The adjoint aeroacoustic chain including the filtering process is finally used to compute sensitivity maps on the mirror for the frequency range 800Hz-4000Hz and also for each 1/3 Octave Band in this range.

Keywords: Computation Fluid Dynamics, Continuous Adjoint Methods, Shape Optimization, Computational Aeroacoustics, Vehicle Aeroacoustics

Contents

Chapter 1

Introduction

1.1 Motivation

AEROACOUSTIC performance is an important comfort and safety factor for modern cars. High levels of interior cabin noise can negatively impact the perception of the vehicle's quality and, more importantly, lead to fatigue and reduced concentration of the driver. At high speeds, generally above 100 km/h, flow-induced noise transmitting in the interior tends to contribute more to overall noise, to other sources, such as the engine, powertrain and wheels.

Wind noise is mainly related to the exterior flow around the side mirror and the A-pillar. The pressure fluctuations on these regions create noise which is radiated to all directions. A part of it meets the side window and acts as an acoustic load. This, together with the strong hydrodynamic pressure, excite the front side window to vibration, which in turn generates sound waves, that propagate into the cabin and are perceived as noise by the passengers, fig. 1.1.

Reducing interior noise can be achieved by isolating the cabin with high quality sealing and acoustic glazing, however this results to increased car weight and costs. Therefore, another approach is to focus on mitigating aeroacoustic noise generated by the vehicle's form, particularly by car components such as the side mirror and the A-pillar rain gutter. This is why car manufacturers have invested considerable effort over the last years firstly to gain insight into aerodynamic noise creation and propagation to the interior and, secondly, to develop high-fidelity numerical methods that can predict interior noise level, without the need of a wind tunnel experiment.

Although recently developed numerical methods have been proved to accurately predict vehicle interior Sound Pressure Level (SPL), the correlation between geometry changes of noise generating components (side mirror) and interior noise is still not clear for broadband (wide range of frequencies) noise. Therefore, a numerical tool that can provide insight into geometry modifications that improve

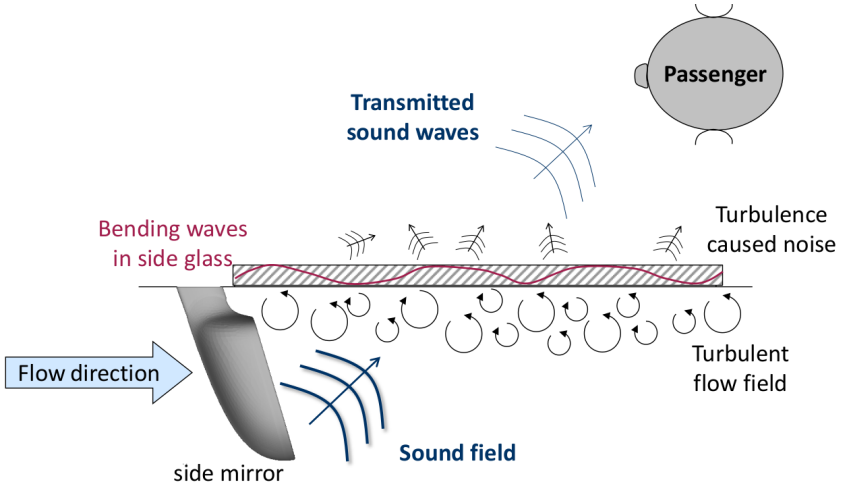

Figure 1.1: Physical mechanisms of flow-induced noise creation and transmission into vehicle interior.

aeroacoustic performance would not only significantly support aeroacoustic engineers in design decision making but also enable the shape optimization of car components and contribute so to the automation of the virtual vehicle development.

This doctoral thesis aims at developing the continuous adjoint method to an existing noise prediction chain, in order to efficiently compute the sensitivity of noise-related objective functions with respect to geometry modifications of noise-radiating car components.

1.2 Literature Survey

1.2.1 Computational Methods for Vehicle Aeroacoustics

The numerical simulation of the aforementioned physical mechanisms of noise generation and propagation into the vehicle interior can be split into parts. The first one includes the flow simulation and sound radiation to the side window, by thus coping with the external domain. The second part deals with the structural vibration of the window and the propagation of the generated sound waves to the cabin interior.

An aerodynamic simulation, as might be the standard process for vehicle aerodynamic development, would not be sufficient for an aeroacoustic simulation, since there is additional information about the near- and far-field acoustics needed for an accurate aeroacoustic prediction. Computational AeroAcoustics (CAA) is the research field that deals with the challenge of examining the different properties of the hydrodynamic flow field and the acoustic sound field [79, 80, 30].

In fact, the wavelengths that must be resolved for the acoustic field are 10 times bigger, since the convection velocity of the turbulence and vortex structures follow the flow velocity which is smaller than the speed of sound. In addition, the energy content in acoustics for low Mach numbers is much smaller, compared to the hydrodynamic one.

To tackle these challenges, two approaches can be followed [26]. In Direct Noise Computation (DNC), the unsteady compressible Navier-Stokes equations are solved to resolve simultaneously both the hydrodynamic and acoustic scales [11]. In this case however, because the acoustic energy content is quite smaller than the hydrodynamic, the accuracy of the acoustic solution is prone to numerical errors and artefacts, such as numerical dissipation and dispersion. This is not always easy to identify and, therefore, fine grid resolution, high-order methods and numerical schemes and sophisticated boundary conditions must be used [50, 25].

The second approach, namely the hybrid-CAA methods, examines the flow and acoustic problems separately [137]. In the first step, the hybrid methods utilize a high-fidelity flow simulation tool to resolve the necessary turbulence and flow structures, but not the radiated sound field. After identifying the acoustic sources in the flow, they switch to the computation of noise radiation, either by solving additionally simpler field equations, such as the Linearized Euler Equations (LEE) [51, 37, 96], or by using acoustic analogies [88]. An acoustic analogy is derived based on an aeroacoustic theory, by rearranging the equations of conservation of mass and momentum, by making them represent the sound propagation in the hypothetical medium (with a partial differential operator) of sound sources. The unsteady flow field is used to compute the sound sources and, then, the operator is inverted to compute the radiated sound field. Several approaches have been proposed through the years, starting with the most general formulation of Ffowks Williams and Hawkings (FW-H) [141], to many more which are tailored to specific applications [29, 18, 19, 75].

The development of CAA methods for vehicle aeroacoustics has focused mainly on the flow-induced noise radiation from car components such as the side mirror and the A-pillar. These type of geometries have been firstly numerically simulated on isolated enviroments. For instance, in [126, 9, 83], the flow and sound radiation around a mirror-like shape on a flat plate was simulated whereas in [32], several A-pillar rain gutter profiles on a flat plate were investigated.

For the purpose of investigating the flow-induced noise creation mechanisms in real car geometries, the German Aeroacoustic Working Group [1] built a full-scale test body of the SAE fullback type 4. Through the years, several numerical methods were developed and compared to experimental results. In [59, 60] sunroof buffeting was examined. In [53], the SAE model was rebuilt so that noise in

[1] Members of the German Aeroacoustic Working Group were Volkswagen AG, Audi AG, Dr. Ing. h.c. Porsche AG and Daimler AG

the interior can be transmitted through the only side window of the vehicle. A numerical and experimental study was performed investigating the fundamental aspects of external flow generated sound and its propagation into the interior. The dynamic loading on the side window, computed with several Computational Fluid Dynamics (CFD) codes and measured in the experiments was compared. The importance of including the acoustic part of the flow for wind noise prediction in production car applications was indicated firstly in [57] and demonstrated in [23].

In [128] and [68], two different process chains to simulate of wind noise generation and propagation into the vehicle interior were proposed. Schell [128] compared several methods to compute the pressure load on the side window, including a DNC and a hybrid-CAA utilizing a compressible DES with different acoustic analogies (Lighthill [46], Moehring [94], Acoustic Perturbation Equations (APE) [37]). Regarding the acoustic field, it was shown that the numerical artefacts caused mostly by the grid refinement transition have an impact in the case of a DNC. The APE proved to be the most efficient approach, since it blends out this numerical noise and predicts accurately the acoustic pressure on the side window. The vibrational response of the latter as well as the sound field in the interior compartment were simulated using a combined Finite Element (FE)/Statistic Energy Analysis (SEA) method [17].

On the other hand, Kabat vel Job used a hybrid-CAA method [68], where an incompressible IDDES is combined with the Kirchhoff Integral method [38] to compute the radiated acoustic pressure on the window. Its vibrational response is then simulated by solving the bending wave equation, using a Finite Area method, and the interior propagation is computed by solving the wave equation in a second computational mesh, in the interior of the vehicle. The validation of the method with experimental results on the SAE body and on a production car demonstrated that this method can accurately predict the interior SPL.

Once a numerical method that can accurately predict noise interior has been implemented and validated, it is possible to develop a numerical optimization method in order to drive the shape optimization of noise radiating car components, such as the car's side mirror.

1.2.2 Optimization Methods for CFD/CAA problems

In shape optimization for CFD/CAA problems, the geometry to be optimized is controlled via a number of design variables b_n, $n \in [1, N]$. To assess the performance of a given set of b_n and, thus, of a given geometry, the Partial Differential Equations (PDEs) that govern the corresponding physical phenomena, namely the state equations, are numerically solved at first. Afterwards, the objective function J to be minimized is computed. Its value depends on the values of the design variables as well as any fields computed through the solution of the state equa-

tions. The optimization methods seeks for the optimal set of b_n that minimizes J.

In engineering problems and particularly in those in the CFD/CAA fields, two classes of optimization methods are mostly used in the literature, the stochastic (gradient-free) and the derministic (gradient-based) and they differentiate based on the approach followed to search the design space for the optimal set of b_n.

Stochastic methods [31, 93, 118, 10] update the design variables in a randomized or heuristic-based manner. A notable representative of these are the Evolutionary Algorithms (EA) which rely on a population-based optimization that mimics natural evolution operations to explore the entire design space. Main advantages of EAs [58, 34, 4, 42, 81] include the ability to find global optima, the ability to solve multi-objective optimization so as to compute the Pareto fronts of non-dominated solutions and non-intrusiveness, since the evaluation solver can be used as a black-box. However, a large amount of evaluations is required to achieve convergence which makes them computationally expensive, especially for problems with many design variables, such as the ones usually found in CFD/-CAA problems.

Deterministic methods [45, 13, 14, 103, 86, 95, 131], also called gradient-based methods (GBM), start from an initial set of parameters and update the values of the design variables in each optimization iteration using the information of the derivative of the objective function. This is achieved with the line search method which first finds a descent direction $\vec{p}$ along which J will be reduced and then solves a one-dimensional optimization problem to compute a step size α as follows, [103]

$$\min_{a>0} J(b_n + ap_n) \;\; for \;\; n = 1, N \tag{1.1}$$

The descent direction can be computed with various methods:

1. The gradient (steepest) descent selects the opposite of the derivative of J w.r.t. b_n as the descent direction, $p_n = -\delta J/\delta b_n b_n$, and is simple to implement but can become very slow.
2. The Newton method additionaly uses the second-derivative (Hessian) of J, $p_n = -(\delta^2 J/(\delta b_n \delta b_m))^{-1} \delta J/\delta b_n b_m$, and exhibits a faster convergence but requires additional effort for the computation of the Hessian.
3. The quasi-Newton methods, an alternative to the Newton method, such as the BFGS [41] and the SR1 [21], which use an approximation of the Hessian and, thus, are also very fast.
4. The conjugate gradient [40] uses $p_n = -\delta J/\delta b_n b_n + \beta p_n^{prev}$ where p_n^{prev} is the descent direction of the previous iteration and β a scalar that ensures that p_n and p_n^{prev} are conjugate. Although this method does not attain the fast convergence rates of the Newton and quasi-Newton methods, it is more efficient in terms of memory requirements.

The step size a may be exactly determined by the algorithm that computes $\vec{p}$ (for instance in the case of the conjugate gradient), otherwise it is loosely approximated in a number of ways, such as using the backtracking algorithm [8] or the Wolfe conditions [142, 143].

A major factor for the efficiency of a GBM is the way the derivatives of the corresponding objective function w.r.t. the design variables, also called sensitivity derivatives (SD), are computed. The most straightforward way is to use Finite Differences (FD). Each design variable is perturbed by an infinitesimally small quantity, ϵ, and the objective function is re-evaluated. The gradient of the objective function can be then assessed with a Central Differences (CD) scheme as

$$\frac{\delta J}{\delta b_n} = \frac{J(b_1, b_2, ..., b_n + \epsilon, ..., b_N) - J(b_1, b_2, ..., b_n - \epsilon, ..., b_N)}{2\epsilon} \tag{1.2}$$

The value of ϵ is usually determined with trial-and-error so that the FD values are ϵ-independent. However, for small values of ϵ the accuracy of the derivative is prone to round-off errors. In addition, as seen in eq. 1.2 , the number of evaluations of J scales linearly with N and, thus, the derivative computation becomes computationally expensive for problems with a large number of design variables.

A variant of FD is the complex variable method, which reads

$$\frac{\delta J}{\delta b_n} = \frac{Im\left[J(b_1, b_2, ..., b_n + i\epsilon, ..., b_N)\right]}{\epsilon} \tag{1.3}$$

where $i = \sqrt{-1}$ and Im is the imaginary part of the complex function J. Using eq. 1.3 overcomes the limitation of ϵ-dependence [101] but still scales linearly with the number of design variables.

On the other hand, adjoint methods [121, 62] have already been proved to be an efficient way to compute the derivative of J with respect to a set of design variables, as required by the GBMs. To do so, the system of adjoint equations is firstly solved at a cost comparable to that of the state (primal) equations and, then, the computed adjoint and primal fields are used to compute the SDs. Hence, the computational cost is independent of the number of design variables and comparable to that of the numerical solution of the primal equations.

Two main approaches appear in the literature to derive the adjoint equations and the expression of the SDs. In the discrete adjoint approach [35, 5, 7, 44], the objective function is augmented using the discretized residuals of the primal equations. After differentiating the augmented objective function and rearranging, the adjoint variables are computed by numerically solving the resulting system of adjoint equations, being already in discrete form. In this case, one way to compute the desired derivatives is to "hand differentiate" any variable of the source code of the computer program. Another approach, the Algorithmic Differentiation

(AD) [47, 27, 54] performs this automatically, either by enriching the code with automatically generated code [117] or by overloading the source code's operators in order to track all operations performed and then reproduce their derivative [15, 48, 135].

In continuous adjoint, the augmented objective function is firstly differentiated and, following a mathematical development, the adjoint equations, boundary conditions and sensitivity derivatives are derived in a continuous form [62, 63, 6]. The continuous adjoint equations are then discretized and numerically solved to compute the adjoint fields and, through them, the sensitivity derivatives.

The advantages of each formulation has been thoroughly discussed in the literature [43, 97, 120]. The discrete approach delivers the exact gradient of the discrete objective function which ensures that the optimization algorithm can fully converge. In addition, its implementation is conceptually straightforward. The continuous approach on the other hand, offers a much clearer view of the physical meaning of the adjoint variables. Moreover, the implementation is simpler and allows for different discretization of the adjoint equations, as long as they are consistent. Finally, the memory requirements are much less compared to the discrete approach.

1.2.3 Adjoint Methods for Design Optimization in Flow & Wave Problems

The adjoint method has been established in engineering optimization workflows related to problems governed by PDEs, as in fluid mechanics, as it offers an efficient way to compute the gradient of objective functions. From the very first steps made by Lions [82], Pironneau [121] and Jameson [62] until today, both continuous and discrete adjoint formulations are in use in a wide range of applications, among others in the aerospace/aeronautical industry [124, 91, 76], in the automotive industry [106], in ship technology [67], in wind turbine design [133], in seismic tomography [39, 119] and in sensitivity analysis for shallow-water wave control [127].

From a theoretical point of view, several formulations have been presented in the literature to develop the continuous adjoint method, with two main representatives. The first formulation [123, 66, 64], results in a SD expression which comprises both surface (defined along the surface to be optimized) and field (defined over the whole computational domain) integrals. The latter include the so-called grid sensitivities which are essentially the influence that the displacement of the interior grid nodes have on the objective function but the extra computational cost might not be negligible. The second formulation [6, 65, 110], results in a SD expression which comprises only surface integrals and, thus, the information from the interior grid is neglected. Although this approach has been considered

advantageous due to the decreased cost of the SD computation, Kavvadias [71] demonstrated that such an assumption may introduce high numerical errors in the SD accuracy. To alleviate this problem and to also maintain the efficiency of this formulation, a grid displacement equation was incorporated in [71]. It should be noted that in the discrete adjoint approach the grid sensitivities are inherently present in the SD expression and the adjoint to grid displacement is used to avoid their costly computation [102, 92, 61].

Specifically in the automotive industry, the adjoint can be found in a wide range of applications from internal ducts and exhaust systems optimization to external aerodynamic design [106, 70, 112]. The first attempt to tackle a noise reduction problem in cars with the adjoint method was made by Papoutsis [113]. An approximate surrogate model for aeroacoustics was used as an objective function, expressed by the integral of the squared turbulent viscosity over a volume residing next to the driver's window. To do so, the turbulence Spalart-Allmaras turbulence model was differentiated [114]. As explained later on, such an objective function focuses mostly on low frequencies dominated by turbulence length scales. The aforementioned applications were all based on the continuous adjoint formulation. The memory requirements and the complexity of the primal flow solver pose difficulties to discrete formulations, although a recent work [56] proposed a discrete approach which was also applied to car external aerodynamics.

In the majority of the aforementioned applications, the problems are governed or assumed to be governed by steady state equations. Continuous and discrete formulations for unsteady problems have been presented targeting at improving mean aerodynamic coefficients in airfoils [98, 89], wings [99, 144] and cylinders [138, 24]. It will be shown in the following chapters that a distinct feature of the unsteady adjoint equations is that they are solved backwards in time. In addition, at least some of the primal flow fields are required to solve the unsteady adjoint equations which means that they must be stored during the primal computation. Since a full storage becomes prohibitive for large test cases, the checkpointing technique [49] is commonly used to store only a set of the primal fields (checkpoints) and the rest are recomputed starting from those. The binomial distribution as well as dynamic reallocation [139] can be used in order to minimize recomputations for a given number of checkpoints and time steps.

The fact that the unsteady adjoint method for real-world applications is extremely demanding in computational cost and storage requirements has delayed its application to complex cases. With the advancements in computer technology, it has become possible to overcome these limitations and adjoint optimization for unsteady flows has started being used. This is imperative in scientific areas such as aeroacoustics where all problems are inherently unsteady. Economon [33] formulated the continuous approach for the inhomogeneous wave equation of Ffowcs Williams-Hawkins, while Zhou [145] applied the discrete method for the permeable Ffowcs Williams-Hawkins surface approach. In [12], the discrete approach

was applied to a coupled CFD/CAA solver using LES and the Acoustic Perturbation Equations (APE), in order to minimize trailing-edge noise radiation using a porous material. Oezkaya [147] and Hay [55] presented the discrete adjoint method for the optimization of acoustic liners, where the Linearized Euler Equations were used as the acoustic analogy. The described research focuses however on flows governed by periodicity which are usually dominated by a specific frequency. Kim [74] used an adjoint-based optimization to reduce noise induced by a Mach 1.3 jet by adding thermal sources to the compressible Navier-Stokes equations. Although the objective function considered only the squared pressure fluctuations over a control volume without any acoustic radiation, the radiated broadband noise propagated to the far-field computed afterwards with a FW-H formulation was also reduced.

1.3 Goal & Outline of Thesis

As seen in the described literature, recent years have seen the emergence of the adjoint method in the field of aeroacoustics. Nevertheless, most of these are still limited to RANS simulations of periodic problems, whereas the ones using LES are applied to mid-size test cases and for short simulation times.

Motivated from vehicle aeroacoustics, this thesis focuses on the unsteady continuous adjoint method for real-world aeroacoustic problems governed by highly turbulent flows and propagation of waves. Based on the hybrid CFD/CAA approach presented in [68], the continuous adjoint equations are derived to minimize the interior wind noise level in a vehicle, by taking into account the external flow, the sound radiation from the side mirror to the window, the window's vibration and, finally, the interior wave propagation. The outcome of this method are the surface sensitivity derivatives on the mirror that indicate the directions in which its shape should be modified to reduce noise transmitting into the vehicle interior.

The followed approach to tackle this problem divides the described noise transmission chain into two domains, the exterior and the interior one. The former focuses on the flow-induced noise creation and its radiation from the vehicle's side mirror to the window; the latter domain concerns with the window vibration due to the acoustic load and the interior propagation of the generated sound waves.a In this PhD thesis, the adjoint method is developed and verified firstly for each domain separately and, in the last chapters, the two domains are coupled to derive the adjoint aeroacoustic chain. All adjoint methods and the Kirchhoff Integral solver presented in this thesis are programmed and implemented in the open source CFD toolbox OpenFOAM©, [3]. A short summary of each chapter follows below.

In **Chapter 2**, the hybrid CFD/CAA approach proposed in [68] that predicts the wind noise transmitting into a traveling vehicle is described. The governing

equations of the noise creation and transmission mechanisms, based on which the following chapters of this thesis will formulate the continuous adjoint method, are presented. In addition, the simulation process as well as validation results [68] are summarized, with kind permission of Volkswagen Group Research. This aims to demonstrate the accuracy of the primal analysis and to also give an overview of the challenges faced at aeroacoustic design.

In **Chapter 3**, the continuous adjoint method to the bending wave and wave equation which govern the window vibration and interior propagation, respectively, is formulated. The SD w.r.t. synthetic waves imposed on the window as an acoustic load are computed and compared to FD to verify the adjoint gradients.

Chapter 4 formulates the continuous adjoint method to the incompressible Navier-Stokes equations, solved around the vehicle to obtain the velocity and pressure fields and, also, to the Kirchhoff Integral (KI) acoustic analogy, used to propagate the unsteady pressure distribution on the side mirror's surface to the side window. During the mathematical formulation, grid displacement models are taken into consideration, to ensure the consistency and, consequently, accuracy, of the computed SD. In addition, emphasis is laid upon the distinction in the mathematical formulation between the time window of the unsteady simulation and the time window over which the objective function is integrated.

In **Chapter 5**, the implementation of the KI solver, developed in this thesis in order to facilitate functionalities needed by the adjoint method, is described. Afterwards, the method for adjoint-based minimization of flow-induced radiation, presented in chapter 4, is verified. To minimize the extensive computational cost of the unsteady adjoint method and to ensure that the FD have converged, a smaller test case is selected for the verification, investigating the turbulent flow around a cylinder. Finally, the proposed method is applied to optimize the side mirror of the SAE body in order to reduce noise on the vehicle's side window.

Chapter 6 couples the adjoint equations presented in chapters 3 and 4 and presents the adjoint aeroacoustic chain, consisting of the adjoint wave equation, the adjoint bending wave equation, the adjoint Kirchhoff Integral and the adjoint Navier-Stokes equations. These are solved to compute the sensitivity map on the side mirror of the SAE body which indicate gemetry modifications that reduce interior SPL. In addition, the impact that optimizing for each individual step of the noise prediction chain has on interior noise is investigated.

In order to assess the SPL in the frequency domain, **Chapter 7** proposes two approaches; a frequency-defined objective function which includes the Fourier Transform of the time-series to be minimized and a signal processing filter that filters out any unwanted frequencies at an early part of the noise prediction chain. The adjoint formulation as well as the advantages and drawbacks of each approach are discussed and the filter is eventually implemented to compute sensitivity maps for specific frequency ranges, using the method presented in chapter 6.

In **Appendix A**, the test case used for the adjoint verification in chapter 5 is discussed and a grid independence study is also presented.

Chapter 2

Prediction of Flow-Induced Noise Propagation to Vehicle Interior

Aeroacoustic performance of cars is determined by flow-induced noise that transmits into the vehicle interior and is perceived by the passengers. It is an important factor for vehicle design not only for comfort but also for safety, as it is associated with fatigue, and must be taken into consideration early on during the vehicle development process. This is why car manufacturers have invested considerable effort over the last years firstly to gain insight into aerodynamic noise creation and propagation into the interior and, secondly, to develop high-fidelity numerical methods that can predict the interior noise level.

Wind noise is related mainly to the exterior flow around the side mirror and the A-pillar and dominates the cabin noise level for mid to high driving speeds. The vibrational response of the front window structure to the external pressure loads generates sound waves that propagate in the vehicle's cabin and are perceived as noise. For today's car configurations, the sound field is generated mainly by pressure fluctuations on the car's side mirror and A-pillar rain gutter, as shown in [53], although the side mirror can also be considered as the main contributor to wind noise.

A process that simulates the aforementioned physical mechanisms and can accurately assess the aeroacoustic performance of vehicles has been developed at Volkswagen Group Research by Kabat vel Job [68]. This method computes the incompressible flow field with an Improved Delayed Detached Eddy Simulation (IDDES) [129] of the Navier-Stokes equations and the Spalart-Allmaras turbulence model. For low speed turbulent flows, it is safe to assume that the hydrodynamic pressure on the surface of the sound radiating object dominates its acoustic counterpart [9] and, thus, a flow solution provided by a high-fidelity unsteady incompressible flow solver is sufficient to resolve the physics of noise creation [68]. The generated noise on the car's mirror is then transmitted to the near- and far-field with an acoustic analogy, the Kirchhoff Integral method [75],

which offers simplicity in implementation and accuracy for non-rotating configurations [19]. In order to obtain the sound pressure at a set of receivers on the vehicle's side window, the pressure and its time and space derivatives, weighted by directivity coefficients, are integrated over a control surface surrounding the noise sources on the side mirror. The Ffowcs Williams-Hawkings (FW-H) equation [141] could also be used; however, since, for low Mach number flows, the quadrupole sources associated with viscosity effects are negligible compared to the surface sources, these can be neglected and this formulation leads essentially to the same sound sources on the body with the Kirchhoff Integral method, for control surfaces on non-moving bodies. The vibrational response of the window to the acoustic and hydrodynamic load is then simulated by solving the bending wave equation. The last part of the process chain is the acoustic propagation in the interior, which is computed by solving the wave equation in the interior domain of the vehicle.

This PhD thesis aims at developing the continuous adjoint method based on the existing primal noise prediction simulation process described above. Therefore, this chapter presents the primal equations that govern the aforementioned physical mechanisms of wind noise creation and transmission to the vehicle interior and explains the process and the coupling between the steps of the aeroacoustic framework:

1. Wind noise creation controlled by the numerical solution of the **unsteady incompressible Navier-Stokes equations**.
2. Acoustic radiation from the vehicle mirror to the side window using the **Kirchhoff Integral method**.
3. Window's structural vibration by solving the **Bending Wave equation**.
4. Propagation to interior by solving the **Wave equation**.

Afterwards, an overview of the noise prediction chain in OpenFOAM© is given [68] and the test case which is used in this thesis, the SAE body, is presented. Since the convergence and accuracy of the adjoint method depends among other on the corresponding primal procedure, the results of the experimental validation of the primal aeroacoustic analysis applied to the SAE body from [68] are repeated in this chapter with kind permission of Volkswagen Group Research.

2.1 Unsteady Flow Simulation

The governing equations of the flow problem for automotive applications are the unsteady Navier-Stokes equations for incompressible fluid flows. These are writ-

ten as, [77],

$$R^p = \frac{\partial v_j}{\partial x_j} = 0 \tag{2.1}$$

$$R_i^v = \frac{\partial v_i}{\partial t} + v_j \frac{\partial v_i}{\partial x_j} - \frac{\partial \tau_{ij}}{\partial x_j} + \frac{\partial p}{\partial x_i} = 0\ ,\ i = 1, 2, 3 \tag{2.2}$$

where v_i are the velocity components, p the static pressure divided by the density, $\tau_{ij} = (\nu + \nu_t)\left(\frac{\partial v_i}{\partial x_j} + \frac{\partial v_j}{\partial x_i}\right)$ the stress tensor and ν and ν_t are the bulk and turbulent viscosities, respectively. Throughout this thesis, repeated indices imply that the Einstein summation rule is applied.

The one-equation Spalart-Allmaras (S-A) turbulence model [130], enhanced by the Improved Delayed Detached Eddy Simulation (IDDES) technique [129], is added to the primal equations. This approach blends a Wall Modelled LES (WMLES) with a DDES, depending on the inflow turbulent content. The sub-grid length-scale of this strategy depends on both grid spacings and wall distances. Furthermore, by modifying the definition of the DDES length scale, the DDES behavior of the model gives improved solutions for attached (compared to RANS) and separated (compared to DES) flows.

The turbulence model equation reads

$$R^{\widetilde{\nu}} = \frac{\partial \widetilde{\nu}}{\partial t} + v_j \frac{\partial \widetilde{\nu}}{\partial x_j} - \frac{\partial}{\partial x_j}\left[\left(\nu + \frac{\widetilde{\nu}}{\sigma}\right)\frac{\partial \widetilde{\nu}}{\partial x_j}\right] - \frac{\sigma_b^2}{\sigma}\left(\frac{\partial \widetilde{\nu}}{\partial x_j}\right)^2 - \widetilde{\nu} P(\widetilde{\nu}) + \widetilde{\nu} D(\widetilde{\nu}) = 0 \tag{2.3}$$

where $\widetilde{\nu}$ is the turbulence state variable. The eddy viscosity coefficient ν_t is, then, expressed in terms of $\widetilde{\nu}$ as

$$\nu_t = \widetilde{\nu} f_{v1} \tag{2.4}$$

The production and dissipation terms in eq. 2.3 are given by

$$P(\widetilde{\nu}) = c_{b1}\widetilde{S}\ \ ,\quad D(\widetilde{\nu}) = c_{w1} f_w(\widetilde{S})\left(\frac{\widetilde{\nu}}{\tilde{d}}\right)^2 \tag{2.5}$$

where

$$\widetilde{S} = S f_{v3} + \frac{\widetilde{\nu}}{d_w^2 k^2} f_{v2}\ \ ,\quad S = \left| e_{ijk}\frac{\partial v_k}{\partial x_j}\right| \tag{2.6}$$

with S standing for the vorticity magnitude.

What distinguishes the IDDES technique is the definition of the length scale $\tilde{d}$

in the destruction term as

$$\tilde{d} = \tilde{f}_d(1 + f_e)l_{RANS} + (1 - \tilde{f}_d)l_{LES} \tag{2.7}$$

where l_{RANS} and l_{LES} are the RANS and LES turbulence length scales respectively. For the Spalart-Allmaras turbulence model, $l_{RANS} = d_w$, where d_w is the wall distance and $l_{LES} = C_{DES}\,\Psi\,\Delta$, where $C_{DES} = 0.65$ is the fundamental empirical constant of DES, Ψ is a low-Reynolds number correction and Δ is the subgrid length-scale [129].

The blending function $\tilde{f}_d$ is defined by

$$\tilde{f}_d = max\{(1 - f_{dt}), f_B\} \tag{2.8}$$

where $f_{dt} = 1 - tanh[(8r_{dt})^3]$ and r_{dt} is a marker of the wall region equal to 1 in a log layer and to 0 in a free shear flow. Function f_B varies from 0 (LES mode) to 1 (RANS mode) and is given by $f_B = min\{2exp(-9a^2), 1.0\}$ with $a = 0.25 - d_w/h_{max}$, where h_{max} is the maximum local cell size.

The empirical blending function f_e is designed to be close to zero when the grid used in the simulation is sufficient for a wall-resolved LES or when the IDDES model, eq. 2.7 , performs solely as a RANS model. This is to prevent the excessive reduction in the RANS Reynolds stresses which has been observed in the interaction of the RANS and LES regions in the vicinity of their interface.

Functions $\tilde{f}_d$ and f_e blend the two branches of the IDDES model, depending on the inflow conditions:

- DDES branch: responsible for the DDES-like functionality of IDDES, becoming active only when the inflow conditions do not have any turbulent content. In this case $f_e = 0$ and $\tilde{f}_d = f_B = 1$, so eq. 2.7 reduces to $\tilde{d} = l_{RANS}$.
- Wall Modelled LES (WMLES) branch: intended to be active only when the inflow conditions used in the simulation are unsteady and impose some turbulent content and the grid is fine enough to resolve boundary layer dominant eddies. In this case $r_{dt} \ll 1$ and, consequently, $\tilde{f}_d = f_B = 0$, so eq. 2.7 reduces to $\tilde{d} = l_{LES}$.

The remaining model functions are given by

$$f_{v1} = \frac{\chi^3}{\chi^3 + x_{v1}^3} \;\;,\;\; f_{v2} = \frac{1}{\left(1 + \frac{\chi}{c_{v2}}\right)^3}$$

$$f_{v3} = \frac{(1+\chi f_{v1})}{c_{v2}}\left[3\left(1 + \frac{\chi}{c_{v2}}\right) + \left(\frac{\chi}{c_{v2}}\right)^2\right]\left(1 + \frac{\chi}{c_{v2}}\right)^{-3}$$

$$\chi = \frac{\widetilde{\nu}}{\nu} \;\;,\;\; f_w = g\left(\frac{1 + c_{w3}^6}{g^6 + c_{w3}^6}\right)^{1/6}$$

$$g = r + c_{w2}(r^6 - r), r = \frac{\widetilde{\nu}}{\widetilde{S}k^2 d_w^2} \tag{2.9}$$

The values used for the constants of the model [130] are $c_{b1} = 0.1355$, $c_{b2} = 0.622$, $k = 0.41$, $\sigma = 2/3$, $c_{w1} = c_{b1}/k^2 + (1 + c_{b2})/\sigma$, $c_{w2} = 0.3$, $c_w 3 = 2$, $c_{v1} = 7.1$ and $c_{v2} = 5$.

The boundary conditions that close the mathematical problem are summarized below. At the inlet, velocity takes its farfield value, the vehicle's speed, a zero Neumann condition is imposed on the pressure and the turbulence variable $\widetilde{\nu}$ is computed through eq. 2.4 based on the eddy viscosity ratio. On the vehicle and the wind tunnel floor, a zero Dirichlet condition is imposed on the velocity and $\widetilde{\nu}$ and a zero Neumann condition on pressure. The side walls of the wind tunnel are considered as symmetry planes and a symmetry boundary condition is imposed on all variables. At the outlet, a zero Neumann condition in imposed on the velocity, which is clipped to zero in case of backflow, a zero Neumann condition is imposed on the $\widetilde{\nu}$ and a zero Dirichlet on the pressure.

2.2 Flow-Induced Noise Radiation

After solving the unsteady Navier-Stokes and Spalart-Allmaras equations in the external domain, as presented in the previous section, the unsteady pressure distribution on the mirror is obtained and a surface integral method for sound extrapolation to the far-field, the Kirchhoff Integral method, is used.

The Kirchhoff Integral method is derived based on the wave equation and encloses the source sound sources with a control surface that is mathematically represented by a function, $f(x,t) = 0$, defined such that $\frac{\partial f}{\partial x_i} = \hat{n}_i$, where $\hat{n}_i$ is the unit normal vector pointing into the fluid. The Kirchhoff equation reads, [38],

$$\begin{aligned} \Box^2 p'(x,t) &= -\left(\frac{\partial p'}{\partial t}\frac{v_n^s}{a_0^2} + \frac{\partial p'}{\partial n}\right)\delta(f) \\ &\quad -\frac{\partial}{\partial t}\left(p'\frac{v_n^s}{a_0^2}\delta(f)\right) - \frac{\partial}{\partial x_i}(p'\hat{n}_i\delta(f)) \\ &\equiv Q_{kir} \end{aligned} \tag{2.10}$$

where $\Box = \frac{1}{a_0^2}\frac{\partial^2}{\partial t^2} - \frac{\partial^2}{\partial {x_i}^2}$ is the D'Alembert operator, $\delta(f)$ is the Dirac delta function and v_n^s is the surface normal velocity, in case this is moving.

Due to the fact that the Kirchhoff acoustic analogy is valid only in the region of the flow governed by the linear wave equation, the assumption that nonlinear effects are negligible is overall made. This can be shown by examining a more general acoustic analogy, namely the Fwocks-Williams Hawkings (FW-H), [141],

that is derived based on the conservation laws in fluid mechanics and reads

$$\begin{aligned}\Box^2 p'(x,t) &= \frac{\overline{\partial}^2}{\partial x_i \partial x_j}[T_{ij}H(f)] \\ &- \frac{\partial}{\partial x_i}[(p'\delta_{ij}\hat{n}_j + \rho v_i(v_n - v_n^s))\delta(f)] \\ &+ \frac{\partial}{\partial t}[(\rho_0 v_n^s + \rho(v_n - v_n^s))\delta(f)] \end{aligned} \tag{2.11}$$

where $T_{ij} = \rho v_i v_j$ is the Lighthill stress tensor, $H(f)$ is the Heaviside function and v_n is the fluid velocity in the direction normal to the surface $f = 0$.

In [18], eqs. 2.10 and eq. 2.11 are compared and it is shown that the first can be rewritten as

$$\Box^2 p'(x,t) = Q_{kir} + \frac{\overline{\partial}^2 T_{ij}}{\partial x_i \partial x_j} H(f) \tag{2.12}$$

It is seen that the additional term in FW-H is a tensorial volume source term that is associated with viscosity effects. For low-Mach flows, surface noise sources dominate the volume sources [18], so the latter can be neglected and is, thus, accurate to use the Kirchhoff Integral. This assumption is valid for the applications presented in this paper, as explained in section 2.5.

In [68] and also in this thesis, the Kirchhoff integration surface is selected to coincide with the surface of the side mirror, S_{W_P} and is, thus, non-moving and impermeable. An applicable form can then be derived for the calculation of the radiated acoustic pressure at the receiver $x_{rec,i}$ which reads

$$p_{ac}(t, \vec{x}_{rec}) = \frac{\rho}{4\pi} \int_{S_{W_P}} \left[-\frac{1}{R}\frac{\partial p}{\partial n} + \left(\frac{1}{R^2} p + \frac{1}{a_0 R}\frac{\partial p}{\partial t} \right) \hat{r}_i \hat{n}_i \right]_{ret} dS = 0 \tag{2.13}$$

Here, a_0 is the ambient speed of sound, $r_i = x_{rec,i} - x_i$ the vector connecting the source and the receiver positions and R its magnitude whereas $\hat{r}_i = \frac{r_i}{R}$. In addition, density appears anew in eq. 2.13, because p is derived by the CFD pressure field which is already divided by ρ.

The terms on the r.h.s. of eq. 2.13 have a clear physical meaning; the first is known as thickness noise whereas the second and third as loading noise. The r.h.s. of eq. 2.13 is expressed at the retarted time which is the time instant that a sound wave leaves the source to reach the receiver at t

$$\tau = t - \frac{R}{a_0} \tag{2.14}$$

In addition, since a zero Neumann condition is imposed on the pressure along S_W

in the preceding CFD solution, the first term vanishes and the Kirchhoff integral reduces to

$$R^{p_{ac}} = p_{ac}(t, \vec{x}_{rec}) - \frac{1}{4\pi} \int_{S_W} \underbrace{\left[\frac{1}{R^2} p + \frac{1}{a_0 R} \frac{\partial p}{\partial t} \right]_{ret}}_{g_{ret,i}} \hat{r}_i \, \hat{n}_i \, dS = 0 \tag{2.15}$$

For each receiver placed on the side window, eq. 2.15 is solved and the sound sources are integrated over the noise radiating side mirror to compute the acoustic pressure.

2.3 Window Vibration

The main contribution to sound radiation into the vehicle interior compartment comes from the lateral vibrational response of the side window. Although frequency domain-based methods, such as Statistical Energy Analysis (SEA) methods are frequently used for this case [16, 128], a time-domain method was developed in [68], which can utilize the complete transient and spatial information obtained from the CFD solution and the Kirchhoff Integral propagation.

The window can be approximated as a thin plate with thickness h and density ρ_w and its lateral deformation is described by the Kirchhoff plate theory [84, 122], which is sufficient for bending wavelengths that remain smaller than the thickness of the window. The governing equation of the window deflection is thus governed by the 2D bending wave equation that reads

$$R^w = \frac{\partial^2 w}{\partial t^2} + \frac{D}{m'} \frac{\partial^4 w}{\partial x_i^2 \partial x_j^2} + \frac{\partial}{\partial t} \left[\eta_1 \frac{D}{m'} \frac{\partial^4 w}{\partial x_i^2 \partial x_j^2} + \eta_2 w - \eta_3 \sqrt{\frac{D}{m'}} \frac{\partial^2 w}{\partial {x_j}^2} \right] - \frac{p_{load}}{m'} = 0 \tag{2.16}$$

where $p_{load} = p_{ac} + p$, p_{ac} is the radiated acoustic pressure and p_{hyd} the hydrodynamic (incompressible CFD) pressure computed on the side window, $m' = \rho_w h$ is the normalised window mass and $D = EI$ the window bending stiffness that depends on the Young modulus E and the moment of inertia for the thin plate cross-section.

Eq. 2.16 consists of the biharmonic wave operator of the window deflection w as well as three damping terms that ensure a frequency dependent damping behavior. In order to calibrate the values of the damping coefficients η_i, $i = 1, 2, 3$ a hammershock experiment can be conducted, where the damping characteristics of the window are measured after a hit with a hammer, as explained in [68].

Since the PDE of eq. 2.16 is of fourth order, two boundary conditions must

be imposed on w at each window edge, which depend on the window's mounting type. A clamped window imposes a zero Dirichlet and zero Neumann condition

$$w = 0 \quad \text{and} \quad \frac{\partial w}{\partial x_i} n_{e,i} = 0 \tag{2.17}$$

where $n_{e,i}$ is a unit vector tangent to the window surface and also normal to its edge. For a simply supported window, a zero Dirichlet and zero Laplacian condition

$$w = 0 \quad \text{and} \quad \frac{\partial^2 w}{\partial {x_j}^2} = 0 \tag{2.18}$$

is imposed.

In addition, two initial conditions are imposed for the starting time t_{start} of the simulation

$$w = 0 \quad \text{and} \quad \frac{\partial w}{\partial t} = 0 \text{ for } t = t_{start} \tag{2.19}$$

The bending wave equation differentiates substantially from other wave equations, due to its dispersive behaviour, as bending waves propagate with different speeds for different frequencies. The dispersion relation derived from the homogeneous bending wave equation reads

$$k_B = \sqrt{\omega} \sqrt[4]{\frac{m'}{D}} \text{ and } c_B = \sqrt{\omega} \sqrt[4]{\frac{D}{m'}} \tag{2.20}$$

where ω, k_B and c_B are the frequency, wavelength and speed of the bending waves, respectively.

Furthermore, the coincidence frequency is defined as

$$f_c = \frac{\sqrt{3} a_0^2}{\pi h} \sqrt{\frac{\rho(1-\nu^2)}{E}} \tag{2.21}$$

This is the frequency where the acoustic wavelengths match the bending wavelengths and energy is efficiently transferred from the side window into the cabin by radiation. Bending waves that have a much smaller propagation speed are radiated, but decay exponentially on the distance from the window. Bending waves travelling faster than the ambient speed of sound will radiate in an angle that depends on their speed [28].

2.4 Interior Propagation

The previous section described the propagation of bending waves and how energy is transferred through the side window. A combination of SEA and Boundary Element Methods (BEM) is often used in literature to compute the reverberant and direct sound field in the vehicle cabin [16, 128], due to their low computational time and lack of need for an interior acoustic computational domain. In the method developed in [68] and used in this thesis however, the complete spatially resolved sound field is computed by solving the acoustic wave equation in the interior domain, Ω_{int},

$$R^{p_{int}} = \frac{1}{a_0^2}\frac{\partial^2 p_{int}}{\partial t^2} - \frac{\partial^2 p_{int}}{\partial x_i^{2^2}} = 0 \tag{2.22}$$

The resulting field is composed of the direct radiated field of the side window and the reverberant field resulting from reflections on the boundary interior walls.

The boundary condition on the interior side of the window is associated with the window deflection. The induced acoustic field at the surface of a vibrating panel S_{wi} is expressed by its lateral acceleration as

$$\frac{\partial p_{int}}{\partial x_i} n_i = \rho_0 \frac{\partial^2 w}{\partial t^2} \tag{2.23}$$

where n_i refers to the components of the unit vectors which are normal to the wall, pointing outwards from the computational domain.

An impedance boundary condition is imposed for the acoustic pressure at the remaining wall boundaries of the vehicle interior, given by [22],

$$\frac{\partial p_{int}}{\partial x_i} n_i = -\frac{1}{v_c}\frac{\partial p_{int}}{\partial t} \tag{2.24}$$

Here, a part of the acoustic waves is reflected and another part is absorbed, depending on the convective velocity v_c. The latter is defined as [22]

$$v_c = 2v_0 \frac{1+\sqrt{\overline{R}}}{1-\sqrt{\overline{R}}} \tag{2.25}$$

where $\overline{R}$ is the average reflection coefficient $\overline{R}$, given by

$$\overline{R} = 1 - \frac{24ln(10)V_{int}}{a_0 T_{60} A_{int}} \tag{2.26}$$

The constants of eq. 2.26 depend on the geometry of the interior compartment, specifically its volume V_{int} and overall surface area A_{int}. T_{60} is the reverberation time measured for the cabin, that is the time required for sound to decay by 60dB.

This formulation ensures the correct long term energy loss of a diffusive acoustic field in V_{int} and reproduces the correct T_{60} time. When the convective velocity tends to infinity, the boundary condition turns to a zero Neumann, representing an acoustically hard wall. When the convective velocity is equal to the ambient sound velocity there is no reflection and the boundary condition allows a full transmission through acting as an open window.

In addition, two initial conditions are imposed at the starting time t_{start} of the simulation

$$p_{int} = 0 \quad \text{and} \quad \frac{\partial p_{int}}{\partial t} = 0 \text{ for } t = t_{start} \tag{2.27}$$

2.5 Noise Prediction Chain in OpenFOAM© and the SAE Body Test Case

The described steps for an aeroacoustic simulation in cars have been implemented in the open source toolbox OpenFOAM© by Kabat vel Job [68]. The noise prediction chain is also used in this thesis for the primal analysis and an overview follows.

The flow equations are solved using the standard transient incompressible solver *pisoFoam* using the Spalart-Allmaras turbulence model and the built-in IDDES technique. The Kirchhoff Integral solver is significantly enhanced in this PhD thesis in order to accommodate functionalities, such the backward in time integration needed for its adjoint, and, therefore, its implementation is discussed in detail in section 5.1.2. The bending wave equation is solved on the car's side window using the Finite Area functionality of OpenFOAM [134] whereas a Finite Volume approach is used to solve the wave equation in the car's interior. The numerical setup for the IDDES and the simulation of the vibroacoustic model are thoroughly discussed in sections 5.1 and 3.4 respectively.

In this PhD thesis, a generic vehicle geometry, the SAE Body, is used as a test case to verify and apply the continuous adjoint method to the aeroacoustic optimization framework based on the described equations. The SAE Body test case is based on the SAE Type 4 car body and was firstly presented in [59, 60],

where sunroof buffeting was investigated and, afterwards, in [53], where the same set-up shown in this PhD thesis was used. More information about the design and construction of the model can be found in the same publication. This model, shown in fig. 2.1, is built in such a way that only the noise transmission through the front side window is relevant, except for very low frequencies. In fact, the front side window at the driver's side is the only window of the model, while the rest of the structure is nearly rigid and highly damped.

The CAE (Computer-Aided Engineering) model consists similarly of two shells, as presented in fig. 2.2. The outter shell is used to mesh the geometry and the external domain, Ω_{ext}, where the equations governing the external aerodynamics, eqs. 2.1 , 2.2 and 2.3, are solved. The inner shell is used to mesh the interior domain Ω_{int}, that is the vehicle cabin including the vibrating window, where eqs. 2.16 and 2.22 are solved. The sound radiation from the mirror to the side window, eq. 2.13 , uses the surface elements on the side mirror as sources and the surface elements of the internal domain on the side window as receivers. The mirror geometry used in this PhD thesis is shown in fig. 2.3.

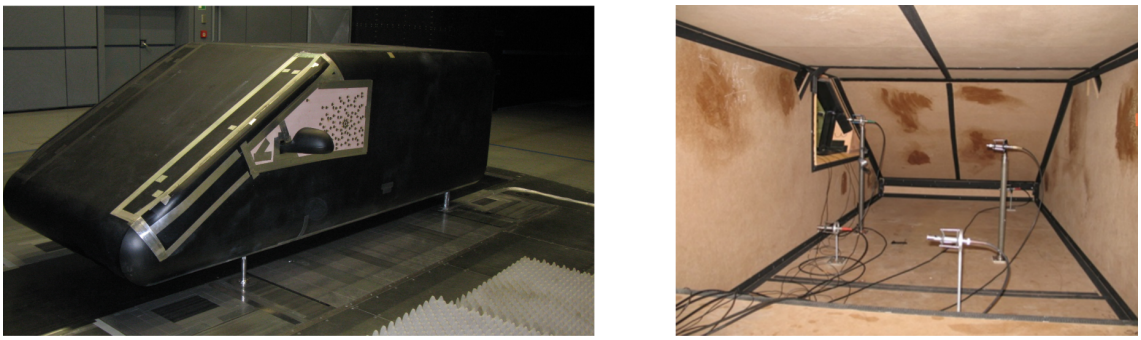

Figure 2.1: SAE Type 4 Model in wind tunnel at AUDI AG from [68]: Exterior (left) and interior (right) vehicle geometry. Sound can be transmitted to the interior through the only window of the vehicle, on its left side. The accelerator sensors on the side window (left) and the microphones in the interior (right) were used to measure the window acceleration and interior sound pressure level respectively, in order to compare the measured data with the numerical results.

In order to demonstrate the accuracy of the existing noise prediction chain, based on which the continuous adjoint method is developed in this PhD thesis, the results of the experimental validation of the aforementioned method performed by Kabat vel Job [68] are summarized in this chapter, with kind permission of Volkswagen Group Research. In fig. 2.4, the data computed by the numerical method and those measured during the experiments conducted in the AUDI wind tunnel, are compared. Specifically, the Sound Velocity Level, averaged over all sensors on the vibrating side window (fig. 2.1, left), and the Sound Pressure Level (SPL), averaged over all the vehicle's cabin microphones (fig. 2.1, right), are presented. Two main conclusions are drawn, by analysing the figures. Firstly, the numerical

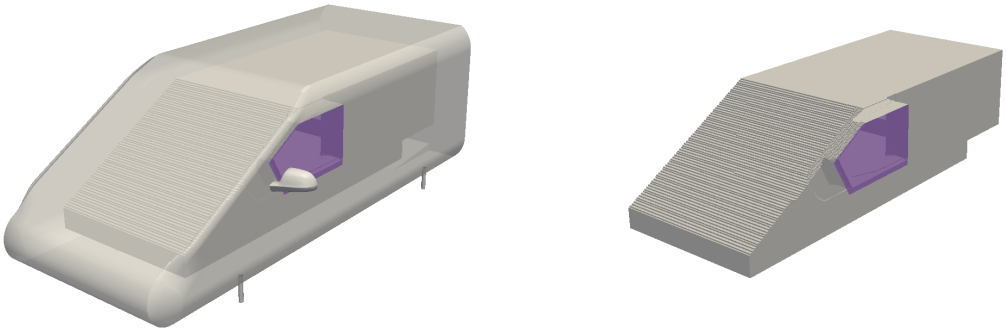

Figure 2.2: SAE Type 4 CAE Model: Exterior (left) and interior (right) vehicle walls. The only window of the vehicle, through which sound is transmitted to the interior, is coloured in magenta.

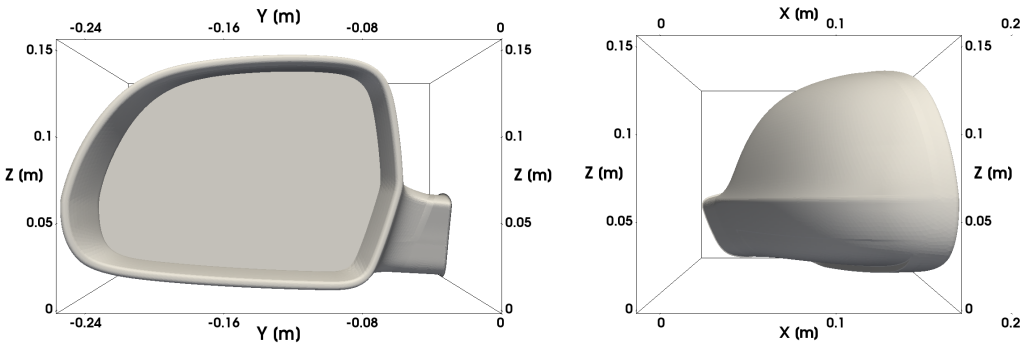

Figure 2.3: Side mirror of the SAE Type 4 CAE Model.

method proposed in [68] and also used in this PhD thesis for the primal analysis shows good agreement with the experimental data, in a frequency window between 800Hz and 4000Hz, which is of interest for passenger comfort. The discrepancies seen for frequencies above 5KHz can be due to the grid resolution, while the ones seen for frequencies below 300Hz are practically irrelevant for consideration in vehicle aeroacoustics. Secondly, both the hydrodynamic and acoustic part of the pressure on the window contribute to the windows vibration and interior SPL. The former is responsible for low frequency noise, up to 1kHz and the latter for higher frequencies, above 1kHz. The hydrodynamic pressure excitation is derived by the instantaneous pressure field on the window, while the acoustic pressure is the radiated acoustic field mainly from the side mirror to the window.

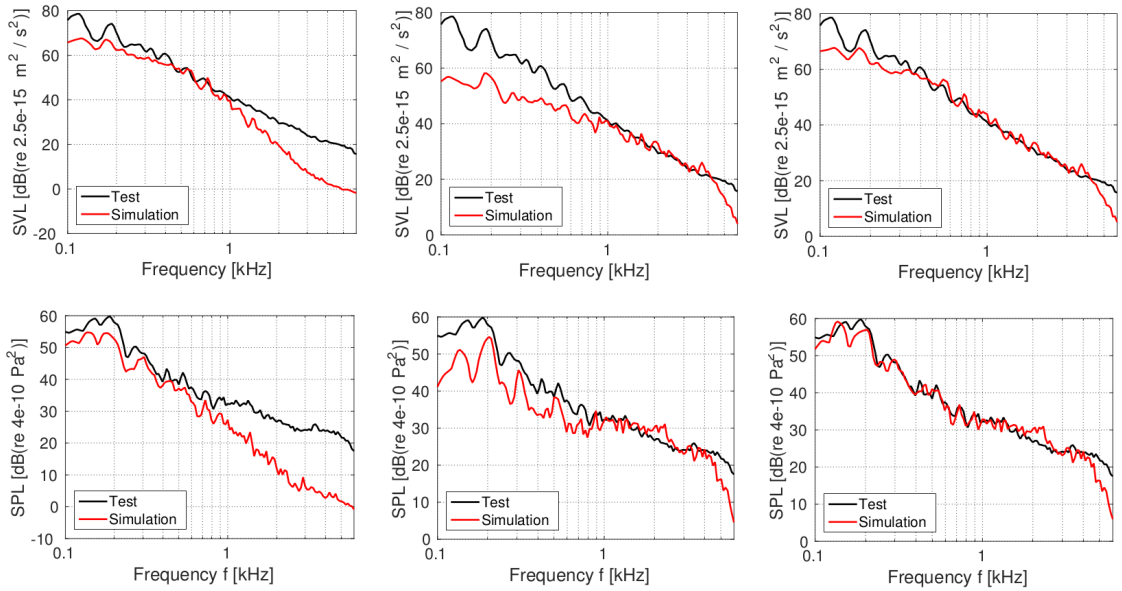

(a) pure hydrodynamic pressure (b) pure acoustic pressure (c) total pressure (hydrodynamic + acoustic)

Figure 2.4: Comparison of results derived by the described method and experiment reproduced from [68]: Resulting Sound Velocity Level on side window (top row) and Sound Pressure Level in cabin (bottom row) due to different types of excitation; average of all sensors shown in 1/24 th octave bands.

2.6 Conclusions

This chapter presented the constituent steps and the corresponding governing PDEs of an OpenFOAM-based aeroacoustic framework that can be used in the automotive industry to assess the aeroacoustic performance of cars, as proposed in [68]. There are the unsteady incompressible Navier-Stokes equations, the Kirchhoff Integral acoustic analogy, the bending wave equation and the wave equation solved on the corresponding exterior and interior domains of the car geometry.

Equations governing the physical mechanisms of flow-induced noise generation and transmission to the vehicle's interior are the starting point of the continuous adjoint method formulation in the following chapters.

Chapter 3

Continuous Adjoint Formulation to the Vibroacoustic Model of the Vehicle Interior

This chapter presents the development of the continuous adjoint method for the physical mechanisms that govern the noise propagation into the vehicle interior through the vibrating window. In the primal process presented in chapter 2, the lateral response of the window to the pressure load is governed by the bending wave equation and the acoustic propagation in the vehicle interior by the wave equation. By simulating the window vibration and the radiation of the generated sound waves in the interior compartment, the sound field in the interior becomes known and an objective function related to the sound pressure level can be assessed for specific points or regions of interest, such as the area near the driver's ear.

In the past, the adjoint method has been used for problems governed by equations that include wave operators but is mostly found in the research fields of seismic tomography for wave field inversion [39, 119] or of sensitivity analysis for shallow-water wave control [127]. In the context of aeroacoustics, the continuous adjoint formulation was used in [33] for the FW-H equation, however it was restricted to a 2D isolated airfoil. Moreover, no continuous or discrete adjoint formulation has been proposed before for acoustics in vehicle applications.

In this chapter, the mathematical formulation of the continuous adjoint method for the computation of derivatives of objective functions used in sound propagation in the interior of vehicles, governed by the coupled system of the 2D bending wave equation for the 3D surface of the window and the 3D wave equation in the interior is presented for the first time in the literature.

Later on it is shown that the adjoint equations are solved backwards in time but also in reverse order. In the primal process, information travels from the vibrating side window to the vehicle interior whereas in the adjoint process, adjoint information travels from the internal domain to the external one. Therefore, the mathematical derivation of the adjoint equations considers first the wave equation

in the interior, afterwards the bending wave equation at the window and, finally, the coupled vibroacoustic model.

The accuracy of the developed method is verified against Finite Differences (FD). The method computes the sensitivity derivatives expression of an objective function, defined in the vehicle interior, with respect to design variables that affect the acoustic load on the window. This is the first step to couple the interior adjoint process with the exterior one, presented in the next chapter.

Throughout this thesis, several objective functions of the same form are defined which target at minimizing the fluctuations of a quantity Φ. Such an objective function can be defined as

$$J = \frac{1}{T_{of}} \int_{T_{of}} (\Phi - \overline{\Phi})^2 dt = \frac{1}{T_{of}} \int_{T_{of}} \Phi'^2 dt \tag{3.1}$$

where T_{of} is the time-window over which the objective function is integrated, Φ' is the fluctuation of Φ and the overbar symbols indicates a mean value over T_{of}.

The differentiation of eq. 3.1 w.r.t. b_n yields

$$\begin{aligned} \frac{\delta J}{\delta b_n} &= \frac{2}{T_{of}} \int_{T_{of}} \Phi' \left(\frac{\delta \Phi}{\delta b_n} - \frac{\delta \overline{\Phi}}{\delta b_n} \right) dt \\ &= \frac{2}{T_{of}} \left(\int_{T_{of}} \Phi' \frac{\delta \Phi}{\delta b_n} dt - \frac{\delta \overline{\Phi}}{\delta b_n} \underbrace{\int_{T_{of}} \Phi' dt}_{=0} \right) \\ &= \frac{2}{T_{of}} \int_{T_{of}} \Phi' \frac{\delta \Phi}{\delta b_n} dt \end{aligned} \tag{3.2}$$

In the development that follows in this and the next chapters, all objective functions used are cast in the form of eq. 3.1 and their derivatives in the form of eq. 3.2 .

3.1 Adjoint to the Wave Equation

This section focuses only on the wave equation solved in the vehicle compartment, Ω_{int}, to compute the interior propagation of waves generated by a given side window deflection. It is assumed that the design variables b_n affect w, thus

$$w = w(\vec{b}, \vec{x}, t) \tag{3.3}$$

For example, b_n could be the thickness or density of the side window which influence its vibrational response.

3.1.1 Objective Function Expression for Vehicle Interior and its Differentiation

When considering the aeroacoustic performance of a vehicle, the main point of interest is the region near the driver's ear (receiver). The perceived noise is related to the interior pressure fluctuations and, thus, an appropriate objective function can be defined as

$$J_{int} = \frac{1}{T_{of}} \int_{T_{of}} p'^2_{int}\, dt \Big|_P \tag{3.4}$$

where P is the point of interest, i.e. the receiver. In this thesis, this point coincides with a microphone placed near the driver's ear. Eq. 3.4 is differentiated and yields

$$\frac{\delta J_{int}}{\delta b_n} = \frac{2}{T_{of}} \int_{T_{of}} p'_{int} \frac{\delta p_{int}}{\delta b_n} dt \Big|_P \tag{3.5}$$

3.1.2 Formulation of the Field Adjoint Equation and its Initial Condition

Starting point of the continuous adjoint formulation is the definition of the augmented objective function which includes the time and space integral of the inner product of the equation residual with its adjoint quantity, here

$$L_{WE} = J_{int} + \int_{T_s} \int_{\Omega_{int}} q_{int} R^{p_{int}} d\Omega dt \tag{3.6}$$

where WE stands for *Wave Equation*, $R^{p_{int}}$ is the residual of the wave equation, eq. 2.22 , q_{int} is the adjoint interior pressure and T_s is the time window over which the simulation is performed, starting at t_{start} and ending at t_{end}. This time window does not necessarily coincide with T_{of}, over which the objective function is integrated, as depicted in the example of fig. 3.1. The impact of these time windows on the adjoint solution is discussed in chapter 4.

The derivative of L_{WE} w.r.t. b_n yields

$$\frac{\delta L_{WE}}{\delta b_n} = \frac{\delta J_{int}}{\delta b_n} + \int_{T_s} \int_{\Omega_{int}} q_{int} \frac{\delta R^{p_{int}}}{\delta b_n} d\Omega dt \tag{3.7}$$

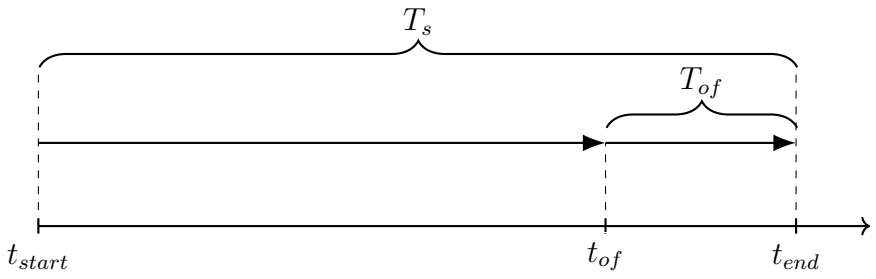

Figure 3.1: Example of the time windows used in the primal analysis: the simulation is performed over T_s, starting at t_{start} and ending at t_{end}, whereas the objective function is integrated only over T_{of}, starting at t_{of}.

Notice that, since the interior geometry remains fixed during the optimization and domain Ω_{int} does not vary by changing the design variables b_n, the total variation of the volume integral is equal to the integral of the total variation of its integrand.

The second r.h.s. term of eq. 3.7 is developed as

$$\begin{aligned}\int_{T_s}\int_{\Omega_{int}} q_{int}\frac{\delta R^{p_{int}}}{\delta b_n}d\Omega dt &= \int_{T_s}\int_{\Omega_{int}} q_{int}\left(\frac{1}{a_0^2}\frac{\delta}{\delta b_n}\left(\frac{\partial^2 p_{int}}{\partial t^2}\right)-\frac{\delta}{\delta b_n}\left(\frac{\partial^2 p_{int}}{\partial {x_i}^2}\right)\right)d\Omega dt \\ &= \int_{T_s}\int_{\Omega_{int}} q_{int}\left(\frac{1}{a_0^2}\frac{\partial^2}{\partial t^2}\left(\frac{\delta p_{int}}{\delta b_n}\right)-\frac{\partial^2}{\partial {x_i}^2}\left(\frac{\delta p_{int}}{\delta b_n}\right)\right)d\Omega dt\end{aligned} \tag{3.8}$$

The first term on the r.h.s. of eq. 3.8 is further developed by using the Green-Gauss theorem in time

$$\begin{aligned}\int_{T_s}\int_{\Omega_{int}} q_{int}\frac{1}{a_0^2}\frac{\partial^2}{\partial t^2}\left(\frac{\delta p_{int}}{\delta b_n}\right)d\Omega dt &= -\int_{T_s}\int_{\Omega_{int}}\frac{1}{a_0^2}\frac{\partial q_{int}}{\partial t}\frac{\partial}{\partial t}\left(\frac{\delta p_{int}}{\delta b_n}\right)d\Omega dt \\ &+ \int_{\Omega_{int}}\frac{1}{a_0^2}\,q_{int}\,\frac{\partial}{\partial t}\left(\frac{\delta p_{int}}{\delta b_n}\right)\,d\Omega\Big|_{t_{start}}^{t_{end}} \\ &= \int_{T_s}\int_{\Omega_{int}}\frac{1}{a_0^2}\frac{\partial^2 q_{int}}{\partial t^2}\frac{\delta p_{int}}{\delta b_n}d\Omega dt \\ &- \int_{\Omega_{int}}\frac{1}{a_0^2}\frac{\partial q_{int}}{\partial t}\frac{\delta p_{int}}{\delta b_n}\,d\Omega\Big|_{t_{start}}^{t_{end}} \\ &+ \int_{\Omega_{int}}\frac{1}{a_0^2}\,q_{int}\,\frac{\partial}{\partial t}\left(\frac{\delta p_{int}}{\delta b_n}\right)\,d\Omega\Big|_{t_{start}}^{t_{end}}\end{aligned} \tag{3.9}$$

where t_{start} and t_{end} are the starting and ending times of the simulation respectively.

The second term on the r.h.s. of eq. 3.8 is developed by using the Green-Gauss theorem in space

$$
\begin{aligned}
-\int_{T_s}\int_{\Omega_{int}} q_{int}\frac{\partial^2}{\partial {x_i}^2}\left(\frac{\delta p_{int}}{\delta b_n}\right) d\Omega dt &= \int_{T_s}\int_{\Omega_{int}} \frac{\partial q_{int}}{\partial x_i}\frac{\partial}{\partial x_i}\left(\frac{\delta p_{int}}{\delta b_n}\right) d\Omega dt \\
&- \int_{T_s}\int_{S_{int}} q_{int}\frac{\partial}{\partial x_i}\left(\frac{\delta p_{int}}{\delta b_n}\right) n_i d\Omega dt \\
&= -\int_{T_s}\int_{\Omega_{int}} \frac{\partial^2 q_{int}}{\partial {x_i}^2}\frac{\delta p_{int}}{\delta b_n} d\Omega dt \\
&+ \int_{T_s}\int_{S_{int}} \frac{\partial q_{int}}{\partial x_i} n_i \frac{\delta p_{int}}{\delta b_n} d\Omega dt \\
&- \int_{T_s}\int_{S_{int}} q_{int}\frac{\partial}{\partial x_i}\left(\frac{\delta p_{int}}{\delta b_n}\right) n_i \, d\Omega dt \quad (3.10)
\end{aligned}
$$

where S_{int} is the boundary of the interior domain, comprising the interior side of the side window S_{wi} and the other interior walls S_{wa}.

For surface integrals on S_{wa}, eq. 2.24 is used and these terms yield

$$
\begin{aligned}
&-\int_{T_s}\int_{S_{wa}} q_{int}\frac{\partial}{\partial x_i}\left(\frac{\delta p_{int}}{\delta b_n}\right) n_i dS dt + \int_{T_s}\int_{S_{wa}} \frac{\partial q_{int}}{\partial x_i} n_i \frac{\delta p_{int}}{\delta b_n} dS dt \\
= &-\int_{T_s}\int_{S_{wa}} q_{int}\frac{\delta}{\delta b_n}\left(\frac{\partial p_{int}}{\partial x_i} n_i\right) dS dt + \int_{T_s}\int_{S_{wa}} \frac{\partial q_{int}}{\partial x_i} n_i \frac{\delta p_{int}}{\delta b_n} dS dt \\
= &\int_{T_s}\int_{S_{wa}} q_{int}\frac{\delta}{\delta b_n}\left(\frac{1}{v_c}\frac{\partial p_{int}}{\partial t}\right) dS dt + \int_{T_s}\int_{S_{wa}} \frac{\partial q_{int}}{\partial x_i} n_i \frac{\delta p_{int}}{\delta b_n} dS dt \\
= &\int_{T_s}\int_{S_{wa}} \frac{1}{v_c} q_{int}\frac{\partial}{\partial t}\left(\frac{\delta p_{int}}{\delta b_n}\right) dS dt + \int_{T_s}\int_{S_{wa}} \frac{\partial q_{int}}{\partial x_i} n_i \frac{\delta p_{int}}{\delta b_n} dS dt \\
= &-\int_{T_s}\int_{S_{wa}} \frac{1}{v_c}\frac{\partial q_{int}}{\partial t}\frac{\delta p_{int}}{\delta b_n} dS dt + \int_{S_{wa}} \frac{1}{v_c} q_{int}\frac{\delta p_{int}}{\delta b_n} dS\Big|_{t_{start}}^{t_{end}} + \int_{T_s}\int_{S_{wa}} \frac{\partial q_{int}}{\partial x_i} n_i \frac{\delta p_{int}}{\delta b_n} dS dt \\
= &\int_{T_s}\int_{S_{wa}} \left(-\frac{1}{v_c}\frac{\partial q_{int}}{\partial t} + \frac{\partial q_{int}}{\partial x_i} n_i\right)\frac{\delta p_{int}}{\delta b_n} dS dt + \int_{S_{wa}} \frac{1}{v_c} q_{int}\frac{\delta p_{int}}{\delta b_n} dS\Big|_{t_{start}}^{t_{end}} \quad (3.11)
\end{aligned}
$$

The surface integrals on S_{wi} are further developed, with the use of the boundary condition imposed on the interior side of the window, eq. 2.23 , and yields

$$
\begin{aligned}
&-\int_{T_s}\int_{S_{wi}} q_{int}\frac{\partial}{\partial x_i}\left(\frac{\delta p_{int}}{\delta b_n}\right) n_i dS dt + \int_{T_s}\int_{S_{wi}} \frac{\partial q_{int}}{\partial x_i} n_i \frac{\delta p_{int}}{\delta b_n} dS dt \\
= &-\int_{T_s}\int_{S_{wi}} q_{int}\frac{\delta}{\delta b_n}\left(\frac{\partial p_{int}}{\partial x_i} n_i\right) dS dt + \int_{T_s}\int_{S_{wi}} \frac{\partial q_{int}}{\partial x_i} n_i \frac{\delta p_{int}}{\delta b_n} dS dt
\end{aligned}
$$

$$
\begin{aligned}
&= \int_{T_s}\int_{S_{wi}} q_{int}\frac{\delta}{\delta b_n}\left(\rho_0\frac{\partial^2 w}{\partial t^2}\right)dSdt + \int_{T_s}\int_{S_{wi}}\frac{\partial q_{int}}{\partial x_i}n_i\frac{\delta p_{int}}{\delta b_n}dSdt \\
&= \int_{S_{wi}}\left(-q_{int}\rho_0\frac{\delta}{\delta b_n}\left(\frac{\partial w}{\partial t}\right)dSdt + \frac{\partial q_{int}}{\partial t}\rho_0\frac{\delta w}{\delta b_n}\right)dS\Bigg|_{t_{start}}^{t_{end}} \\
&+ \int_{T_s}\int_{S_{wi}}\rho_0\frac{\partial^2 q_{int}}{\partial t^2}\frac{\delta w}{\delta b_n}dSdt + \int_{T_s}\int_{S_{wi}}\frac{\partial q_{int}}{\partial x_i}n_i\frac{\delta p_{int}}{\delta b_n}dSdt
\end{aligned}
\tag{3.12}
$$

By replacing eqs. 3.5 , 3.9, 3.10, 3.11 and 3.12 into eq. 3.7 , the expression for the derivative of L_{WE} w.r.t. b_n yields

$$
\begin{aligned}
\frac{\delta L_{WE}}{\delta b_n} &= \int_{T_s}\int_{\Omega_{int}}\left(\frac{1}{a_0^2}\frac{\partial^2 q_{int}}{\partial t^2} - \frac{\partial^2 q_{int}}{\partial {x_i}^2}\right)\frac{\delta p_{int}}{\delta b_n}d\Omega dt + \int_{T_{of}}\int_{\Omega_{int}}\frac{2}{T_{of}}p'_{int}\frac{\delta p_{int}}{\delta b_n}d\Omega dt \\
&+ \int_{\Omega_{int}}\frac{1}{a_0^2}\,q_{int}\,\frac{\partial}{\partial t}\left(\frac{\delta p_{int}}{\delta b_n}\right)d\Omega\Bigg|_{t_{start}}^{t_{end}} - \int_{\Omega_{int}}\frac{1}{a_0^2}\,\frac{\partial q_{int}}{\partial t}\frac{\delta p_{int}}{\delta b_n}\,d\Omega\Bigg|_{t_{start}}^{t_{end}} \\
&+ \int_{S_{wa}}\frac{1}{v_c}q_{int}\frac{\delta p_{int}}{\delta b_n}dS\Bigg|_{t_{start}}^{t_{end}} + \int_{S_{wi}}\left(-q_{int}\rho_0\frac{\delta}{\delta b_n}\left(\frac{\partial w}{\partial t}\right) + \frac{\partial q_{int}}{\partial t}\rho_0\frac{\delta w}{\delta b_n}\right)dS\Bigg|_{t_{start}}^{t_{end}} \\
&+ \int_{T_s}\int_{S_{wa}}\left(-\frac{1}{v_c}\frac{\partial q_{int}}{\partial t} + \frac{\partial q_{int}}{\partial x_i}n_i\right)\frac{\delta p_{int}}{\delta b_n}dSdt + \int_{T_s}\int_{S_{wi}}\frac{\partial q_{int}}{\partial x_i}n_i\frac{\delta p_{int}}{\delta b_n}dSdt \\
&+ \int_{T_s}\int_{S_{wi}}\rho_0\frac{\partial^2 q_{int}}{\partial t^2}\frac{\delta w}{\delta b_n}dSdt
\end{aligned}
\tag{3.13}
$$

The second term on the r.h.s. of eq. 3.13 can be expressed as a time integral over T_s by using the Heaviside function H as

$$
\int_{T_{of}}\int_{\Omega_{int}}\frac{2}{T_{of}}p'_{int}\frac{\delta p_{int}}{\delta b_n}d\Omega dt = \int_{T_s}\int_{\Omega_{int}}\frac{2}{T_{of}}p'_{int}H(t-t_{of})\frac{\delta p_{int}}{\delta b_n}d\Omega dt \tag{3.14}
$$

where t_{of} is the starting time of the objective function integration.

By zeroing the multipliers of $\delta p_{int}/\delta b_n$ in the first two volume integral of eq. 3.13 the adjoint wave equation is derived

$$
R^{q_{int}} = \frac{1}{a_0^2}\frac{\partial^2 q_{int}}{\partial t^2} - \frac{\partial^2 q_{int}}{\partial {x_i}^2} + \frac{2}{T_{of}}p'_{int}H(t-t_{of})\Big|_P = 0 \tag{3.15}
$$

The wave equation is self-adjoint, meaning that the derived adjoint equation has the same differential operators as the primal. The difference is the additional source term, $\frac{2}{T_{of}}p'_{int}H(t-t_{of})$ expressed at point P, which arises from the differentiation of the J_{int}, eq. 3.4 , and takes non-zero values only during T_{of}, therefore

acting only during the time over which the objective function is integrated.

The remaining volume integrals are expressed at $t = t_{start}$ and $t = t_{end}$ and contribute to the initial conditions of eq. 3.15. At $t = t_{start}$, the interior pressure p_{int} and its time derivative are fixed and equal to zero, eq. 2.27, thus their derivatives w.r.t. the design variables b_n is zero. At $t = t_{end}$, q_{int} and its time derivative are set to zero, in order to eliminate the term that contains $\delta p_{int}/\delta b_n$. So, the initial conditions for the adjoint problem are defined at the end of the simulation time as

$$q_{int} = 0 \text{ and } \frac{\partial q_{int}}{\partial t} = 0\,, \text{ for } t = t_{end} \tag{3.16}$$

Eq. 3.16 imposes that the adjoint wave equation must be solved backwards in time. The surface integral on the wall S_{wa}, which is expressed at $t = t_{start}$ and $t = t_{end}$ vanishes after imposing the initial conditions, eqs. 3.16, whereas the one defined on the window vanishes as well, because of the primal initial conditions for the window deflection problem, eq. 2.19.

3.1.3 Adjoint Boundary Conditions

After satisfying the adjoint wave equation in the interior, the remaining terms of eq. 3.13 yield

$$\begin{aligned}\frac{\delta L_{WE}}{\delta b_n} &= \int_{T_s}\int_{S_{wa}} \left(-\frac{1}{v_c}\frac{\partial q_{int}}{\partial t} + \frac{\partial q_{int}}{\partial x_i}n_i\right)\frac{\delta p_{int}}{\delta b_n} dS dt \\ &+ \int_{T_s}\int_{S_{wi}} \frac{\partial q_{int}}{\partial x_i} n_i \frac{\delta p_{int}}{\delta b_n} dS dt \\ &+ \int_{T_s}\int_{S_{wi}} \rho_0 \frac{\partial^2 q_{int}}{\partial t^2}\frac{\delta w}{\delta b_n} dS dt\end{aligned} \tag{3.17}$$

Interior Walls, S_{wa}

Similarly to the field integrals, the multiplier of $\delta p_{int}/\delta b_n$ in the first term on the r.h.s. of eq. 3.17 is set to zero and the boundary condition for the adjoint interior pressure q_{int} on the interior walls is derived as follows

$$\frac{\partial q_{int}}{\partial x_i} n_i = \frac{1}{v_c}\frac{\partial q_{int}}{\partial t} \tag{3.18}$$

Comparing eq. 3.18 with the primal boundary condition on S_{wa}, eq. 2.24, it is clear that it is the same reflective boundary condition, having the opposite sign in the time derivative. This can be explained by taking into consideration that the

adjoint wave equation is solved backwards in time.

Window, S_{wi}

The multiplier of $\delta p_{int}/\delta b_n$ in the second term on the r.h.s. of eq. 3.17 is set to zero and a zero Neumann boundary condition for the adjoint interior pressure q_{int} on the interior side of the window is derived

$$\frac{\partial q_{int}}{\partial x_i} n_i = 0 \tag{3.19}$$

3.1.4 Final Expression of the Sensitivity Derivatives for Vehicle Interior

After satisfying the adjoint wave equation for the interior and its initial and boundary conditions, the remaining term of eq. 3.17 is the final expression for the sensitivity derivatives and reads

$$\frac{\delta L_{WE}}{\delta b_n} = \int_{T_s} \int_{S_{wi}} \rho_0 \frac{\partial^2 q_{int}}{\partial t^2} \frac{\delta w}{\delta b_n} dS dt \tag{3.20}$$

It is the derivative of the objective function, eq. 3.4 , with respect to any design variables b_n that affect the window deflection w, which is the excitation of the wave propagation into the interior compartment. In case there is a closed-form expression for w, term $\delta w/\delta b_n$ can be analytically computed and eq. 3.20 is used to compute gradients w.r.t. the parameters that directly affect w; otherwise, eq. 3.20 is used as a coupling condition with the adjoint bending wave equation solved on the window as seen in section 3.3.

3.2 Adjoint to Bending Wave Equation

This section focuses on the adjoint to the bending wave equation that predicts the vibrational response of a window to a given pressure load. The design variables of the optimization problems considered here affect this load, it is thus

$$p_{load} = p_{load}(\vec{b}, \vec{x}, t) \tag{3.21}$$

In practice, b_n could be the parameters of a surrogate model for computing the pressure load on the window or the variables of a simulation of the external flow

and sound radiation.

3.2.1 Objective Function Expression for Vehicle's Window and its Differentiation

A suitable objective function to investigate the window vibration can be defined as the time average of the squared window deflection fluctuations which reads

$$J_{vib} = \frac{1}{T_{of}} \int_{T_{of}} \int_{S_{wi}} {w'}^2 dt dS \tag{3.22}$$

The derivative of eq. 3.22 w.r.t. b_n yields

$$\frac{\delta J_{vib}}{\delta b_n} = \frac{2}{T_{of}} \int_{T_{of}} \int_{S_{wi}} w \frac{\delta w}{\delta b_n} dt dS \tag{3.23}$$

3.2.2 Formulation of the Surface Adjoint Equation and its Initial Conditions

The augmented objective function for the bending wave problem is written as

$$L_{vib} = J_{vib} + \int_{T_s} \int_{S_{wi}} z R^w dS dt \tag{3.24}$$

where R^w is the residual of the bending wave equation, eq. 2.16, and z is the adjoint deflection.

Its differentiation w.r.t. the design variable b_n yields

$$\frac{\delta L_{vib}}{\delta b_n} = \frac{\delta J_{vib}}{\delta b_n} + \int_{T_s} \int_{S_{wi}} z \frac{\delta R^w}{\delta b_n} dS dt \tag{3.25}$$

The second term on the r.h.s. of eq. 3.25 is further expanded as

$$\begin{aligned} \int_{T_s} \int_{S_{wi}} z \frac{\delta R^w}{\delta b_n} dS dt &= \int_{T_s} \int_{S_{wi}} z \left\{ \frac{\delta}{\delta b_n} \left(\frac{\partial^2 w}{\partial t^2} \right) + \frac{D}{m'} \frac{\delta}{\delta b_n} \left(\frac{\partial^4 w}{\partial x_i^2 \partial x_j^2} \right) \right. \\ &+ \left. \frac{\delta}{\delta b_n} \left(\frac{\partial}{\partial t} \left[\eta_1 \frac{D}{m'} \frac{\partial^4 w}{\partial x_i^2 \partial x_j^2} + \eta_2 w - \eta_3 \sqrt{\frac{D}{m'}} \frac{\partial^2 w}{\partial {x_j}^2} \right] \right) \right. \end{aligned}$$

$$
\begin{aligned}
&- \frac{\delta}{\delta b_n}\left(\frac{p_{load}}{m'}\right)\Bigg\} dSdt \\
&= \int_{T_s}\int_{S_{wi}} z\left\{\frac{\partial^2}{\partial t^2}\left(\frac{\delta w}{\delta b_n}\right) + \frac{D}{m'}\frac{\partial^4}{\partial x_i^2 \partial x_j^2}\left(\frac{\delta w}{\delta b_n}\right)\right. \\
&+ \frac{\partial}{\partial t}\left[\eta_1 \frac{D}{m'}\frac{\partial^4}{\partial x_i^2 \partial x_j^2}\left(\frac{\delta w}{\delta b_n}\right) + \eta_2 \frac{\delta w}{\delta b_n} - \eta_3 \sqrt{\frac{D}{m'}}\frac{\partial^2}{\partial {x_j}^2}\left(\frac{\delta w}{\delta b_n}\right)\right] \\
&- \left.\frac{1}{m'}\frac{\delta p_{load}}{\delta b_n}\right\} dSdt
\end{aligned}
\tag{3.26}
$$

Each term on the r.h.s. of eq. 3.26 is further expanded by using the Green-Gauss theorem in space or time as follows, with L being the boundary edge of S_{wi} and with $n_{e,i}$ being the components of the normal vector on the window edges that is also tangent to its surface.

$$
\int_{T_s}\int_{S_{wi}} z\frac{\partial^2}{\partial t^2}\left(\frac{\delta w}{\delta b_n}\right) dSdt = \int_{T_s}\int_{S_{wi}} \frac{\partial^2 z}{\partial t^2}\frac{\delta w}{\delta b_n} dSdt + \int_{S_{wi}}\left[z\frac{\partial}{\partial t}\left(\frac{\delta w}{\delta b_n}\right) - \frac{\partial z}{\partial t}\frac{\delta w}{\delta b_n}\right]_{start}^{end} dS
\tag{3.27}
$$

$$
\begin{aligned}
\int_{T_s}\int_{S_{wi}} z\,\frac{D}{m'}\frac{\partial^4}{\partial x_i^2 \partial x_j^2}\left(\frac{\delta w}{\delta b_n}\right) dSdt &= -\int_T\int_{S_{wi}} \frac{D}{m'}\frac{\partial z}{\partial x_j}\frac{\partial^3}{\partial {x_i}^2 \partial x_j}\left(\frac{\delta w}{\delta b_n}\right) dSdt \\
&+ \int_T\int_L \frac{D}{m'} z n_{e,j}\frac{\partial^3}{\partial {x_i}^2 \partial x_j}\left(\frac{\delta w}{\delta b_n}\right) dldt \\
&= \int_T\int_{S_{wi}} \frac{D}{m'}\frac{\partial^2 z}{\partial {x_i}^2}\frac{\partial^2}{\partial {x_i}^2}\left(\frac{\delta w}{\delta b_n}\right) dSdt \\
&- \int_T\int_L \frac{D}{m'}\frac{\partial z}{\partial x_i} n_{e,i}\frac{\partial^2}{\partial {x_j}^2}\left(\frac{\delta w}{\delta b_n}\right) dldt \\
&+ \int_T\int_L \frac{D}{m'} z n_{e,j}\frac{\partial^3}{\partial {x_i}^2 \partial x_j}\left(\frac{\delta w}{\delta b_n}\right) dldt \\
&= -\int_T\int_{S_{wi}} \frac{D}{m'}\frac{\partial^3 z}{\partial {x_i}^2 \partial x_j}\frac{\partial}{\partial x_j}\left(\frac{\delta w}{\delta b_n}\right) dSdt \\
&+ \int_T\int_L \frac{D}{m'}\frac{\partial^2 z}{\partial {x_i}^2} n_{e,j}\frac{\partial}{\partial x_j}\left(\frac{\delta w}{\delta b_n}\right) dldt \\
&- \int_T\int_L \frac{D}{m'}\frac{\partial z}{\partial x_i} n_{e,i}\frac{\partial^2}{\partial {x_j}^2}\left(\frac{\delta w}{\delta b_n}\right) dldt \\
&+ \int_T\int_L \frac{D}{m'} z n_{e,j}\frac{\partial^3}{\partial {x_i}^2 \partial x_j}\left(\frac{\delta w}{\delta b_n}\right) dldt
\end{aligned}
$$

$$
\begin{aligned}
&= \int_T \int_{S_{wi}} \frac{D}{m'} \frac{\partial^4 z}{\partial x_i^2 \partial x_j^2} \frac{\delta w}{\delta b_n} dS dt \\
&- \int_T \int_L \frac{D}{m'} \frac{\partial^3 z}{\partial {x_i}^2 \partial x_j} n_{e,j} \frac{\delta w}{\delta b_n} dl dt \\
&+ \int_T \int_L \frac{D}{m'} \frac{\partial^2 z}{\partial {x_i}^2} n_{e,j} \frac{\partial}{\partial x_j} \left(\frac{\delta w}{\delta b_n} \right) dl dt \\
&- \int_T \int_L \frac{D}{m'} \frac{\partial z}{\partial x_i} n_{e,i} \frac{\partial^2}{\partial {x_j}^2} \left(\frac{\delta w}{\delta b_n} \right) dl dt \\
&+ \int_T \int_L \frac{D}{m'} z n_{e,j} \frac{\partial^3}{\partial {x_i}^2 \partial x_j} \left(\frac{\delta w}{\delta b_n} \right) dl dt \qquad (3.28)
\end{aligned}
$$

$$
\begin{aligned}
\int_T \int_{S_{wi}} \eta_1 \frac{D}{m'} z \frac{\partial}{\partial t} \left(\frac{\partial^4}{\partial x_i^2 \partial x_j^2} \left(\frac{\delta w}{\delta b_n} \right) \right) dS dt &= - \int_T \int_{S_{wi}} \eta_1 \frac{D}{m'} \frac{\partial z}{\partial t} \frac{\partial^4}{\partial x_i^2 \partial x_j^2} \left(\frac{\delta w}{\delta b_n} \right) dS dt \\
&+ \int_{S_{wi}} \eta_1 \frac{D}{m'} z \frac{\partial^4}{\partial x_i^2 \partial x_j^2} \left(\frac{\delta w}{\delta b_n} \right) dS \Big|_{start}^{end} \\
&= \int_{T_s} \int_{S_{wi}} \eta_1 \frac{D}{m'} \frac{\partial}{\partial t} \left(\frac{\partial^4 z}{\partial x_i^2 \partial x_j^2} \right) \frac{\delta w}{\delta b_n} dS dt \\
&+ \int_T \int_L \eta_1 \frac{D}{m'} \frac{\partial^3}{\partial {x_i}^2 \partial x_j} \left(\frac{\partial z}{\partial t} \right) n_{e,j} \frac{\delta w}{\delta b_n} dl dt \\
&- \int_T \int_L \eta_1 \frac{D}{m'} \frac{\partial^2}{\partial {x_i}^2} \left(\frac{\partial z}{\partial t} \right) n_{e,j} \frac{\partial}{\partial x_j} \left(\frac{\delta w}{\delta b_n} \right) dl dt \\
&+ \int_T \int_L \eta_1 \frac{D}{m'} \frac{\partial}{\partial x_i} \left(\frac{\partial z}{\partial t} \right) n_{e,i} \frac{\partial^2 \frac{\delta w}{\delta b_n}}{\partial {x_j}^2} dl dt \\
&- \int_T \int_L \eta_1 \frac{D}{m'} \frac{\partial z}{\partial t} \frac{\partial^3}{\partial {x_i}^2 \partial x_j} \left(\frac{\delta w}{\delta b_n} \right) n_{e,j} dl dt \\
&+ \int_{S_{wi}} \eta_1 \frac{D}{m'} z \frac{\partial^4}{\partial x_i^2 \partial x_j^2} \left(\frac{\delta w}{\delta b_n} \right) dS \Big|_{start}^{end} \qquad (3.29)
\end{aligned}
$$

$$
\begin{aligned}
\int_T \int_{S_{wi}} \eta_2 z \frac{\partial}{\partial t} \left(\frac{\delta w}{\delta b_n} \right) dS dt &= - \int_T \int_{S_{wi}} \eta_2 \frac{\partial z}{\partial t} \frac{\delta w}{\delta b_n} dS dt \\
&+ \int_{S_{wi}} \eta_2 z \frac{\delta w}{\delta b_n} dS \Big|_{start}^{end} \qquad (3.30)
\end{aligned}
$$

$$\begin{aligned}\int_T\int_{S_{wi}} \eta_3\sqrt{\frac{D}{m'}}z\frac{\partial}{\partial t}\left(\frac{\partial^2}{\partial {x_i}^2}\left(\frac{\delta w}{\delta b_n}\right)\right)dSdt &= -\int_T\int_{S_{wi}} \eta_3\sqrt{\frac{D}{m'}}\frac{\partial}{\partial t}\left(\frac{\partial^2 z}{\partial {x_i}^2}\right)\frac{\delta w}{\delta b_n}dSdt \\ &+ \int_T\int_L \eta_3\sqrt{\frac{D}{m'}}\frac{\partial}{\partial x_i}\left(\frac{\partial z}{\partial t}\right)n_{e,i}\frac{\delta w}{\delta b_n}dldt \\ &- \int_T\int_L \eta_3\sqrt{\frac{D}{m'}}\frac{\partial z}{\partial t}n_{e,i}\frac{\partial}{\partial x_i}\left(\frac{\delta w}{\delta b_n}\right)dldt \\ &+ \int_{S_{wi}} \eta_3\sqrt{\frac{D}{m'}}z\frac{\partial^2}{\partial {x_i}^2}\left(\frac{\delta w}{\delta b_n}\right)dS\Bigg|_{start}^{end}\end{aligned} \tag{3.31}$$

By replacing eqs. 3.27, 3.28, 3.29, 3.30 and 3.31 into eq. 3.26 and then eqs. 3.23 and 3.26 into 3.25 the expression of the derivative of L_{vib} w.r.t. b_n yields

$$\begin{aligned}\frac{\delta L_{vib}}{\delta b_n} &= \int_T\int_{S_{wi}}\left\{\frac{\partial^2 z}{\partial t^2}+\frac{D}{m'}\frac{\partial^4 z}{\partial x_i^2\partial x_j^2}-\frac{\partial}{\partial t}\left[\eta_1\frac{D}{m'}\frac{\partial^4 z}{\partial x_i^2\partial x_j^2}+\eta_2 z-\eta_3\sqrt{\frac{D}{m'}}\frac{\partial^2 z}{\partial {x_i}^2}\right]\right\}\frac{\delta w}{\delta b_n}dSdt \\ &+ \int_{T_{of}}\int_{\Omega_{int}}\frac{2}{T_{of}}w\frac{\delta w}{\delta b_n}dSdt \\ &+ \int_{S_{wi}}\left[z\frac{\delta}{\delta b_n}\left(\frac{\partial w}{\partial t}\right)-\frac{\partial z}{\partial t}\frac{\delta w}{\delta b_n}\right]_{start}^{end}dS \\ &+ \int_{S_{wi}}\left[\eta_1\frac{D}{m'}z\frac{\partial^4}{\partial x_i^2\partial x_j^2}\left(\frac{\delta w}{\delta b_n}\right)dS+\eta_2 z\frac{\delta w}{\delta b_n}-\eta_3\sqrt{\frac{D}{m'}}z\frac{\partial^2}{\partial {x_i}^2}\left(\frac{\delta w}{\delta b_n}\right)\right]_{start}^{end} \\ &+ \int_T\int_L\left\{-\frac{D}{m'}\frac{\partial^3 z}{\partial {x_i}^2\partial x_j}n_{e,j}+\eta_1\frac{D}{m'}\frac{\partial}{\partial t}\left(\frac{\partial^3 z}{\partial {x_i}^2\partial x_j}\right)n_{e,j}-\eta_3\sqrt{\frac{D}{m'}}\frac{\partial}{\partial t}\left(\frac{\partial z}{\partial x_i}\right)n_{e,i}\right\}\frac{\delta w}{\delta b_n}dldt \\ &+ \int_T\int_L\left\{\frac{D}{m'}\frac{\partial^2 z}{\partial {x_i}^2}n_{e,j}-\eta_1\frac{D}{m'}\frac{\partial}{\partial t}\left(\frac{\partial^2 z}{\partial {x_i}^2}\right)n_{e,j}+\eta_3\sqrt{\frac{D}{m'}}\frac{\partial z}{\partial t}n_{e,i}\right\}\frac{\partial}{\partial x_i}\left(\frac{\delta w}{\delta b_n}\right)n_{e,i}dldt \\ &+ \int_T\int_L\left\{-\frac{D}{m'}\frac{\partial z}{\partial x_i}n_{e,i}+\eta_1\frac{D}{m'}\frac{\partial}{\partial t}\left(\frac{\partial z}{\partial x_i}\right)n_{e,i}\right\}\frac{\partial^2}{\partial {x_i}^2}\left(\frac{\delta w}{\delta b_n}\right)dldt \\ &+ \int_T\int_L\left\{\frac{D}{m'}zn_{e,j}-\eta_1\frac{D}{m'}\frac{\partial z}{\partial t}\right\}\frac{\partial^3}{\partial {x_i}^2\partial x_j}\left(\frac{\delta w}{\delta b_n}\right)n_{e,j}dldt \\ &- \int_T\int_{S_{wi}}\frac{1}{m'}z\frac{\delta p_{load}}{\delta b_n}dSdt\end{aligned} \tag{3.32}$$

By zeroing the multipliers of $\delta w/\delta b_n$ in the first time and surface integral of

eq. 3.32 , the adjoint bending wave equation is derived

$$R^z = \frac{\partial^2 z}{\partial t^2} + \frac{D}{m'}\frac{\partial^4 z}{\partial x_i^2 \partial x_j^2} - \frac{\partial}{\partial t}\left[\eta_1 \frac{D}{m'}\frac{\partial^4 z}{\partial x_i^2 \partial x_j^2} + \eta_2 z - \eta_3 \sqrt{\frac{D}{m'}}\frac{\partial^2 z}{\partial {x_i}^2}\right] + \frac{2}{T_{of}} w H(t - t_{of}) = 0 \tag{3.33}$$

The biharmonic operator is also self-adjoint, so the adjoint bending wave equation has the same form as the primal one. The only difference is the opposite sign of the time derivative of the damping terms. This is attributed to the fact that the adjoint equations are solved backwards in time, imposed by the initial conditions derived from the third term on the r.h.s. of eq. 3.32 .

At $t = t_{start}$, $\delta w / \delta b_n$ is zero, as deflection and its time derivative are independent of the design variables, eq. 2.19 . At $t = t_{end}$, the multipliers of $\delta w / \delta b_n$ and $\delta \left(\partial z / \partial t\right) / \delta b_n$ are set to zero and, thus, the two initial conditions are

$$z = 0 \text{ and } \frac{\partial z}{\partial t} = 0 \text{ for } t = t_{end} \tag{3.34}$$

3.2.3 Adjoint Boundary Conditions

By satisfying the adjoint bending wave equation, eq. 3.33 and its initial conditions, eq. 3.34 , eq. 3.32 reduces to the following expression

$$\begin{aligned}
\frac{\delta L_{vib}}{\delta b_n} &= \int_T \int_L \left\{ -\frac{D}{m'}\frac{\partial^3 z}{\partial {x_i}^2 \partial x_j} n_{e,j} + \eta_1 \frac{D}{m'}\frac{\partial}{\partial t}\left(\frac{\partial^3 z}{\partial {x_i}^2 \partial x_j}\right) n_{e,j} - \eta_3 \sqrt{\frac{D}{m'}}\frac{\partial}{\partial t}\left(\frac{\partial z}{\partial x_i}\right) n_{e,i} \right\} \frac{\delta w}{\delta b_n} dl dt \\
&+ \int_T \int_L \left\{ \frac{D}{m'}\frac{\partial^2 z}{\partial {x_i}^2} n_{e,j} - \eta_1 \frac{D}{m'}\frac{\partial}{\partial t}\left(\frac{\partial^2 z}{\partial {x_i}^2}\right) n_{e,j} + \eta_3 \sqrt{\frac{D}{m'}}\frac{\partial z}{\partial t} n_{e,i} \right\} \frac{\partial}{\partial x_i}\left(\frac{\delta w}{\delta b_n}\right) n_{e,i} dl dt \\
&+ \int_T \int_L \left\{ -\frac{D}{m'}\frac{\partial z}{\partial x_i} n_{e,i} + \eta_1 \frac{D}{m'}\frac{\partial}{\partial t}\left(\frac{\partial z}{\partial x_i}\right) n_{e,i} \right\} \frac{\partial^2}{\partial {x_i}^2}\left(\frac{\delta w}{\delta b_n}\right) dl dt \\
&+ \int_T \int_L \left\{ \frac{D}{m'} z n_{e,j} - \eta_1 \frac{D}{m'}\frac{\partial z}{\partial t} \right\} \frac{\partial^3}{\partial {x_i}^2 \partial x_j}\left(\frac{\delta w}{\delta b_n}\right) n_{e,j} dl dt \\
&- \int_T \int_{S_{wi}} \frac{1}{m'} z \frac{\delta p_{load}}{\delta b_n} dS dt
\end{aligned} \tag{3.35}$$

A zero Dirichlet condition is imposed on the window deflection along all window edges and for both types of mounting, eqs. 2.17 and 2.18. Therefore, $\delta w / \delta b_n$ along the edges is zero and the first term on the r.h.s. of eq. 3.35 vanishes. To eliminate the third and fourth term on the r.h.s. of eq. 3.35 , a zero Dirichlet condition is

imposed on z.

Clamped Window Edges, L_{cla}

In case of a clamping mounting type, eq. 2.18, an addition zero Neumann condition is imposed on the deflection along the edges, thus, the second term in eq. 3.35 vanishes. A zero Neumann condition is imposed on the adjoint deflection z to set the multiplier of $\partial^2 \left(\delta w / \delta b_n\right) / \partial x_i^2$ to zero and eliminate the second term on the r.h.s. of eq. 3.35. For a clamped window, the adjoint boundary conditions for z are summarized as follows

$$z = 0 \quad \text{and} \quad \frac{\partial z}{\partial x_i} n_{e,i} = 0 \tag{3.36}$$

Supported Window Edges, L_{sup}

If the window is simply supported, a zero Laplacian condition is imposed on w in addition to the zero Dirichlet one. In this case, the third term vanishes, since $\frac{\partial^2}{\partial {x_i}^2}\left(\frac{\delta w}{\delta b_n}\right) = 0$ and a zero Laplacian condition must be imposed for the adjoint deflection to eliminate the second term on the r.h.s. of eq. 3.35. Consequently, for a simply supported window, the adjoint boundary conditions are

$$z = 0 \quad \text{and} \quad \frac{\partial^2 z}{\partial {x_j}^2} = 0 \tag{3.37}$$

3.2.4 Final Expression of the Sensitivity Derivatives for Vehicle's Window

After satisfying the adjoint bending wave equation on the side window and its initial and boundary conditions, the remaining term in eq. 3.35 is the final expression for the sensitivity derivatives that reads

$$\frac{\delta L_{vib}}{\delta b_n} = -\int_T \int_{S_{wi}} \frac{1}{m'} z \frac{\delta p_{load}}{\delta b_n} dS dt \tag{3.38}$$

Eq. 3.38 indicates the sensitivity of the window vibration, governed by the bending wave equation, w.r.t. design variables that control the pressure load on the window, p_{load}.

3.3 Adjoint to the Coupled Vibroacoustic Model

Sections 3.1 and 3.2 have examined the wave and bending wave equations separately, as two systems that are solved independently. Here, the complete vibroacoustic model will be considered, where the window vibration is simulated and, then, used to predict the interior sound propagation. The adjoint method computes the gradient of the objective function defined in the vehicle interior, eq. 3.4 , w.r.t. to design variables b_n that indirectly affect the input pressure load on the window. In the case of a two-objective optimization that targets both at minimizing the interior pressure and window deflection, eq. 3.22 would also be taken into account.

The augmented objective function here takes into account both equations, eqs. 2.16 and 2.22, in order to derive the adjoint coupling of the two systems.

$$L_{int} = J_{int} + \int_{T_s}\int_{\Omega_{int}} q_{int} R^{p_{int}} d\Omega dt + \int_{T}\int_{S_{wi}} z R^{w} dS dt \tag{3.39}$$

The augmented objective function is differentiated w.r.t. b_n which leads to

$$\frac{\delta L_{int}}{\delta b_n} = \frac{\delta J_{int}}{\delta b_n} + \int_{T_s}\int_{\Omega_{int}} q_{int} \frac{\delta R^{p_{int}}}{\delta b_n} d\Omega dt + \int_{T}\int_{S_{wi}} z \frac{\delta R^{w}}{\delta b_n} dS dt \tag{3.40}$$

The development of the three terms on the r.h.s. of eq. 3.40 has already been presented in sections 3.1 and 3.2. The wave equation is derived, eq. 3.15 with the initial conditions, eq. 3.16 and boundary conditions eqs. 3.18 and 3.19. However, the term on the r.h.s. of eq. 3.20 includes the derivative of the window deflection $\delta w/\delta b_n$ and is now grouped with the first term of eq. 3.32 . After setting the multiplier of $\delta w/\delta b_n$ to zero, this term ends up in the adjoint bending wave equation, as follows

$$R^z = \frac{\partial^2 z}{\partial t^2} + \frac{D}{m'}\frac{\partial^4 z}{\partial x_i^2 \partial x_j^2} - \frac{\partial}{\partial t}\left[\eta_1 \frac{D}{m'}\frac{\partial^4 z}{\partial x_i^2 \partial x_j^2} + \eta_2 \frac{1}{m'} z - \eta_3 \sqrt{\frac{D}{m'}}\frac{\partial^2 z}{\partial {x_i}^2}\right] + \rho_0 \frac{\partial^2 q_{int}}{\partial t^2} = 0 \tag{3.41}$$

As mentioned, the source term on the r.h.s. of eq. 3.41 for the coupled interior system is now the second time derivative of the interior adjoint pressure q_{int}. It should be noted that the adjoint equations are not only solved backwards in time but also in reverse order: during the primal process, energy is transmitted through the vibrating window from the exterior to the interior, so information travels from the external to the internal domain; in the adjoint process, the adjoint wave

equation in the interior is solved first and the adjoint information travels from the the internal domain to the external one, through the adjoint vibration, excited by the adjoint interior pressure computed on the window.

If J_{vib} was also taken into account during the optimization, eq. 3.41 would have two source terms, one derived from the objective function, as seen in eq. 3.33, and one from the coupling with the interior. The initial and boundary conditions for both systems are the same as the ones presented in eqs. 3.34, 3.36 and 3.37.

The final sensitivity derivatives expression yields

$$\frac{\delta L_{int}}{\delta b_n} = -\int_T \int_{S_{wi}} \frac{1}{m'} z \frac{\delta p_{load}}{\delta b_n} dS dt \tag{3.42}$$

It is essentially the same expression as eq. 3.38. It indicates, however, the sensitivity of the objective function defined in the vehicle interior, J_{int}, w.r.t. design variables that control the input pressure load on the window vibration. In case there is a closed-form expression for p_{load}, as in the test case shown in sections 3.5 and 3.6, the gradient of the pressure load can analytically be calculated. Otherwise, when p_{load} is derived from the solution of another set of equations, the right hand side term in eq. 3.42 is coupled with the corresponding adjoint equations, similarly to the way the adjoint wave equation was coupled to the adjoint bending wave equation. Chapter 6 presents such an example, where p_{load} is derived by the solution of the unsteady incompressible Navier-Stokes equations and the Kirchhoff Integral acoustic analogy.

3.4 Implementation of the Method

The presented vibroacoustic model and its adjoint are implemented in the open source toolbox OpenFOAM©, in version 17.12.

The bending wave equation, eq. 2.16, is solved on a curved surface in the three-dimensional space, the car's side window. The Finite Area functionality of OpenFOAM was used, where effects of surface curvature are built into the differential and discretization operators, ensuring this way high accuracy [134]. The spatial gradients are discretized with a Least Squares scheme. The fourth-order biharmonic operator cannot be implemented implicitly in the current finite area infrastructure and is, thus, added explicitly as a source term. The time derivatives are discretized with a first order scheme and an explicit time marching scheme is used. For this reason and in order to also take the difference of propagation speeds of waves in the window and in the air into account, eq. 2.20, the bending wave equation is solved with a small timestep, usually smaller than the one used for the wave equation or the CFD solution. For the discretization of the wave equation, a second order scheme was used to compute the spatial gradients and

a first order scheme for the time derivative.

When the coupled vibroacoustic model is considered, the bending wave and wave equations are solved in sequence at each iteration. The flow of information between the equations and their different time steps is shown in fig. 3.2. The source term of eq. 2.16, that is the pressure load on the window, is usually derived by a CFD solution and is expressed at the CFD time steps. The vibration problem, as described before, utilizes a much smaller timestep and the source term values at the vibration time steps are derived with linear interpolation between the adjacent CFD time steps. At $t_{vib}^{i,j}$, which is any vibration time step between the CFD time steps t_{CFD}^{j} and t_{CFD}^{j+1}, the pressure load is given by

$$p_{load}\big|_{t_{vib}^{i,j}} = a_{vib}^{i}\, p_{load}\big|_{t_{CFD}^{j}} + (a_{vib}^{i} - 1) p_{load}\big|_{t_{CFD}^{j+1}} \tag{3.43}$$

where $0 \leq i < N_{vib}$, $0 \leq a_{vib}^{i} = i/N_{vib} < 1$ and N_{vib} is the number of additional time steps in the vibration loop, compared to the CFD. To solve eq. 2.22 for p_{int}, the window acceleration is required at each interior propagation time step, eq. 2.23. This is derived directly from the coinciding vibration time step, as seen in fig. 3.2.

In the mathematical development of section 3.3, it was shown that information travels backwards in time and in reverse order during the adjoint integration. Firstly, the adjoint wave equation is solved, excited by a volume source term which requires p_{int} at the point where J_{int} is defined. The interior pressure time-series for this point is fully stored during the primal solution, since the memory requirements are negligible. At each interior propagation time step, the second time derivative of q_{int} is computed on the side window to be used as a source term for the adjoint bending wave equation, eq. 3.33. Similarly to the primal procedure, this term is linearly interpolated at the adjoint vibration time steps, which coincide with the ones of the primal vibration. Afterwards, the sensitivity derivatives, eq. 3.20, is computed at the corresponding CFD time steps and is either integrated over time, or used as a coupling condition (chapter 6). Two approaches can be used to formulate the discretization and computation of this term.

The first approach discretizes the unsteady terms in the integrand of eq. 3.20 at the CFD time steps and the adjoint deflection z is given by the corresponding solution of the adjoint bending wave equation for the corresponding time steps. The numerical integration is then performed for all CFD time steps using Δt_{CFD} and reads

$$-\int_T \int_{S_{wi}} \frac{1}{m'} z \frac{\delta p_{load}}{\delta b_n} dS dt \simeq \; - \sum_{j=1}^{N_{CFD}-1} \int_{S_{wi}} \frac{1}{m'} \left[z \frac{\delta p_{load}}{\delta b_n} \right]_{t_{CFD}^{j}} dS \Delta t_{CFD}$$

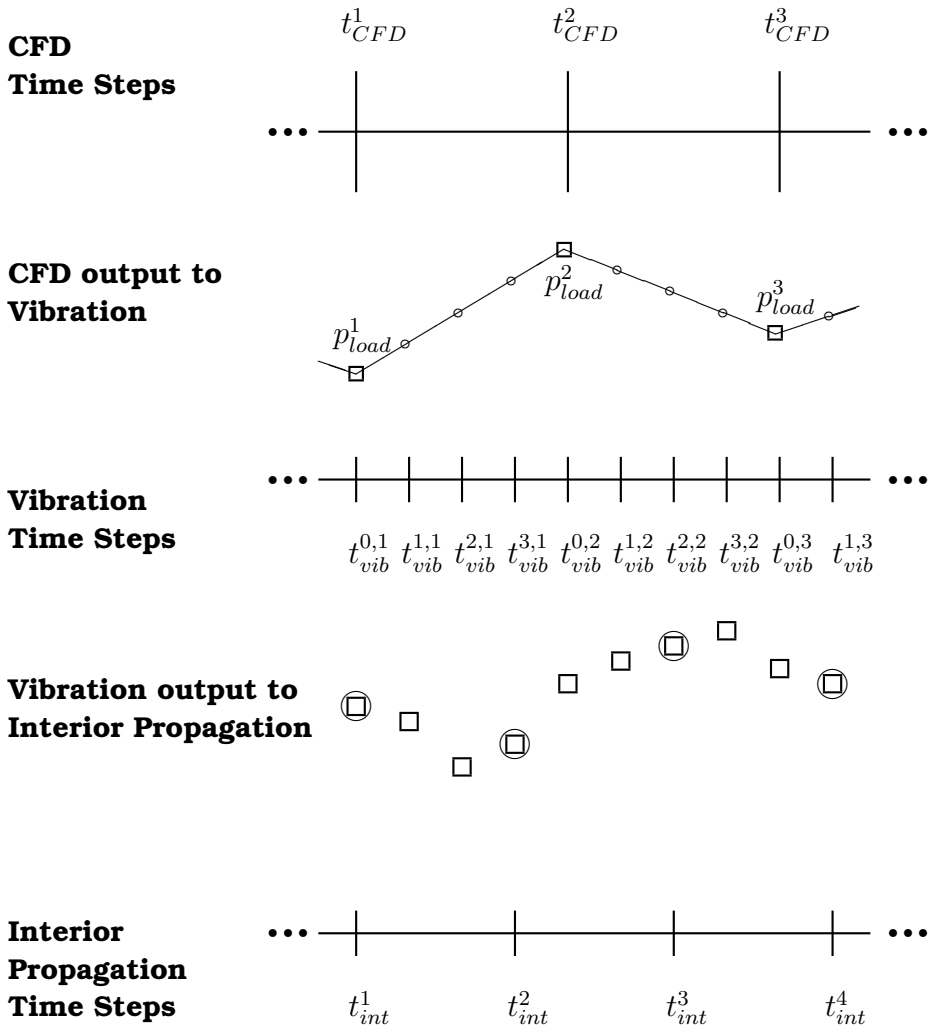

Figure 3.2: Time discretization for the solution of the external flow, window vibration and interior propagation. equation solution. The output (squares, second row) of the CFD solution is linearly interpolated to the bending wave time steps (circles, second row). The output of the bending wave equation (squares, fourth row) expressed at the interior propagation timesteps (circles, fourth row) is used. Here, the ratio between the timesteps was selected for the figure visualization and does not relate to the actual one.

$$
\begin{aligned}
&+ \int_{S_{wi}} \frac{1}{m'} \left(\left[z \frac{\delta p_{load}}{\delta b_n} \right]_{t^0_{CFD}} + \left[z \frac{\delta p_{load}}{\delta b_n} \right]_{t^{N_{CFD}}_{CFD}} \right) dS \frac{\Delta t_{CFD}}{2} \\
&= - \sum_{j=1}^{N_{CFD}-1} \int_{S_{wi}} \frac{1}{m'} z \Big|_{t^{0,j}_{vib}} \frac{\delta p_{load}}{\delta b_n} \Big|_{t^j_{CFD}} dS \Delta t_{CFD}
\end{aligned}
$$

$$
\begin{aligned}
&+ \int_{S_{wi}} \frac{1}{m'} z \Big|_{t_{vib}^{0,0}} \frac{\delta p_{load}}{\delta b_n}\Big|_{t_{CFD}^{0}} dS \, \frac{\Delta t_{CFD}}{2} \\
&+ \int_{S_{wi}} \frac{1}{m'} z \Big|_{t_{vib}^{0,N_{CFD}}} \frac{\delta p_{load}}{\delta b_n}\Big|_{t_{CFD}^{N_{CFD}}} dS \, \frac{\Delta t_{CFD}}{2}
\end{aligned} \tag{3.44}
$$

where N_{CFD} is the number of CFD time steps.

The second approach discretizes the term at the vibration time steps, following the hand-differentiation of eq. 3.43 that yields

$$
\begin{aligned}
& - \int_T \int_{S_{wi}} \frac{1}{m'} z \frac{\delta p_{load}}{\delta b_n} dS dt \\
\simeq & - \sum_{j=0}^{N_{CFD}-1} \sum_{i=0}^{N_{vib}} \int_{S_{wi}} \frac{1}{m'} \left[z \frac{\delta p_{load}}{\delta b_n} \right]_{t_{vib}^{i,j}} dS \Delta t_{vib} \\
& + \int_{S_{wi}} \frac{1}{m'} \left(\left[z \frac{\delta p_{load}}{\delta b_n} \right]_{t_{CFD}^{0}} + \left[z \frac{\delta p_{load}}{\delta b_n} \right]_{t_{CFD}^{N_{CFD}}} \right) dS \frac{\Delta t_{CFD}}{2} \\
= & - \sum_{j=0}^{N_{CFD}-1} \sum_{i=0}^{N_{vib}} \int_{S_{wi}} \frac{1}{m'} z \Big|_{t_{vib}^{i,j}} \left(a_{vib}^{i} \frac{\delta p_{load}}{\delta b_n}\Big|_{t_{CFD}^{j}} + (a_{vib}^{i} - 1) \frac{\delta p_{load}}{\delta b_n}\Big|_{t_{CFD}^{j+1}} \right) dS \Delta t_{vib} \\
& + \int_{S_{wi}} \frac{1}{m'} z \Big|_{t_{vib}^{0,0}} \frac{\delta p_{load}}{\delta b_n}\Big|_{t_{CFD}^{0}} dS \, \frac{\Delta t_{CFD}}{2} \\
& + \int_{S_{wi}} \frac{1}{m'} z \Big|_{t_{vib}^{0,N_{CFD}}} \frac{\delta p_{load}}{\delta b_n}\Big|_{t_{CFD}^{N_{CFD}}} dS \, \frac{\Delta t_{CFD}}{2}
\end{aligned} \tag{3.45}
$$

The difference between eq. 3.44 and eq. 3.45 is that the latter takes into account the adjoint deflection computed at every vibration time step and not only at the time steps that coincide with the CFD ones which, as observed during the verification, leads to numerical errors. It is, thus, important to use eq. 3.45 in order to ensure the accuracy of the sensitivity derivative term, eq. 3.20 .

The interior of the SAE body is meshed using the snappyHexMesh functionality of OpenFOAM which leads to an appropriate for acoustics mesh, as shown in fig. 3.3. The finite area mesh on the window is practically the boundary mesh of the interior. The grid resolution is 10mm, apart from a refinement region in the window cavity, which has a resolution of 5mm. The time step used for the solutions of the bending wave and the wave equations are 10^{-7} and 5×10^{-6} respectively. Moreover, the window thickness is $h = 3.15mm$, the window density $2700kg/m^3$ and the damping coefficients $\eta_1 = 2 \cdot 10^6\, s$, $\eta_2 = 200\, s^{-1}$ and $\eta_3 = 0$.

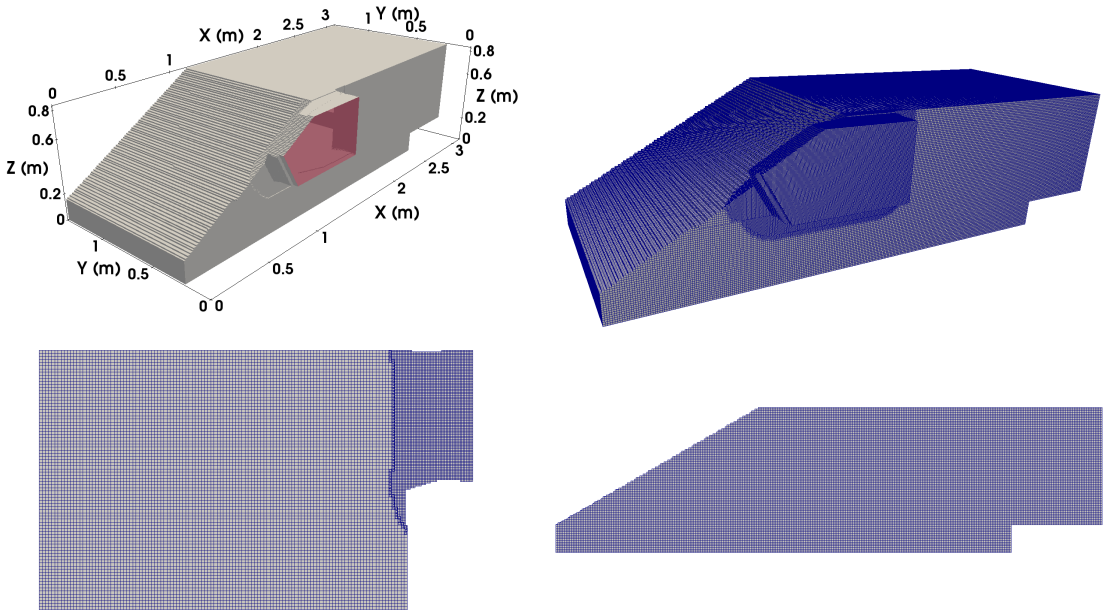

Figure 3.3: SAE Type 4 geometry: Interior model (top left) and computational mesh (top right). Cross sections at $x = 1.2m$ (bottom-left) and at $y = 0.8$ (bottom-right) show the refinement region in the window cavity and the geometry details that are an accurate representation of the original physical model.

3.5 Verification of the Method against Finite Differences

The accuracy of the computed sensitivity derivatives with the adjoint method presented in this chapter is verified here against Finite Differences (FD). The adjoint wave equation, adjoint bending wave equation and adjoint vibro-acoustic model are verified separately.

Adjoint Wave Equation

To verify the adjoint wave equation, a synthetic plane wave is given as an input for the window deflection, in the form of

$$w(x,z,t) = A\sum_{f} sin\left(2\pi f\left(\frac{x}{a_0}+\frac{z}{a_0}-t\right)\right) \tag{3.46}$$

where A is the amplitude, x and z are the corresponding cartesian coordinates on the window and f is a frequency, in the range between 800Hz and 4kHz, with $\Delta f = 10Hz$. Eq. 3.46 is used in eq. 2.23 and the interior sound field is

computed for a time window of $T_s = 0.3s$, based on the typical procedure used and presented in chapter 6. The objective function, eq. 3.4 , is integrated over the same time window, $T_{of} = T_s = 0.3s$, for a receiver placed near the driver's ear, as seen in fig. 3.4. The adjoint wave equation is solved and, then, the sensitivity derivatives w.r.t. the amplitude A of the plane wave are computed with eq. 3.42 , where term $\delta w/\delta b_n$ is calculated analytically. The derivatives of J_{int} w.r.t. A are computed also with central Finite Differences, where a step size equal to $10^{-6}D$ is chosen, so that the FD gradient value is independent of the step size. The adjoint SD and the FD show good agreement, with a relative error of 0.13%.

Adjoint Bending Wave Equation

Similarly, in order to verify the adjoint bending wave equation, a synthetic plane wave is imposed as a pressure load on the side window,

$$p_{load}(x,z,t) = A\sum_f sin\left(2\pi f\left(\frac{x}{a_0}+\frac{z}{a_0}-t\right)\right) \tag{3.47}$$

with parameters A and f defined as before. The vibrational response of the window is simulated for $T_s = 0.3s$, over which the objective function eq. 3.22 is integrated. The derivative of J_{vib} w.r.t. the A is computed using the sensitivity derivative expression of eq. 3.38 , where the term $\delta p_{load}/\delta b_n$ is calculated analytically. The FD derivative is also computed, with a central difference scheme for a step size equal to 10^{-6}. Again the adjoint SD show a good agreement, with a relative error of 0.12%. The discretization of the SD term used here, is the one presented in eq. 3.45 . In case eq. 3.44 is used the relative error increases to more than 10%, hence, it is important to use the former formulation.

Adjoint Vibroacoustic model

Finally, the coupled vibroacoustic model and its adjoint are verified against FD. The input given by eq. 3.47 is imposed on the window and both its vibrational response and interior propagation are simulated for a time window of $T_s = 0.3s$. The objective function is integrated for $T_{of} = T_s = 0.3s$. The gradient of J_{int} w.r.t. the amplitude A of the pressure load computed with the adjoint method is compared to a central FD scheme, yielding a relative error of 0.34%.

In addition, a second verification case is investigated for adjoint vibro-acoustic model, where the input pressure load is given by

$$p_{load} = ap_{ac} \tag{3.48}$$

where p_{ac} is the radiated acoustic pressure from the vehicle's mirror to the window, computed numerically with a CFD simulation and the Kirchhoff Integral acoustic analogy, as described in chapter 2. The multiplier a is the design variable of the problem with an initial value equal to 1. The derivative of J_{int} w.r.t. a computed with the adjoint method, eq. 3.38 , is compared to FD and shows a good agreement with a relative error of 0.16%.

The results of the verification of the sensitivity derivatives computed with the adjoint method developed in this chapter for the vibroacoustic model are summarized in table 3.1. The accuracy of the continuous adjoint method for the vehicle interior propagation is quite satisfactory and the method can be incorporated in larger adjoint aeroacoustic chains that include the adjoints to sound radiation and flow solutions in order to perform aeroacoustic optimization in vehicles.

	Sound propagation	Window Vibration	Coupled Problem	Coupled Problem 2
Finite Differences	2.4394E-15	1.13122E-21	1.52641E-16	4.25274E-11
Continuous Adjoint	2.4391E-15	1.12984E-21	1.52124E-16	4.24584E-11
Relative Error (%)	0.013	0.12	0.34	0.16

Table 3.1: Comparison between objective function gradient values computed with the continuous adjoint method and finite differences.

3.6 Applications

This section presents two applications of the developed adjoint method on the SAE body test case. To keep a focus only on the vibro-acoustic phenomena and their adjoint, the pressure load on the window is induced by the sound radiation from a dipole source in a moving medium, rather than by a fully developed turbulent flow. Two different cases are considered.

3.6.1 Ellipsoid Mirror

In this test case, the mirror of the SAE body is replaced by an ellipsoid surface, as seen in fig. 3.5. The dipole source is placed on the ellipsoid surface so that its directivity vector is aligned with the surface normal and the radiated acoustic pressure from the dipole source on the window is given analytically by

$$p'(\vec{x},t) = -\rho_0 \left(\frac{\partial \phi}{\partial t} + U_i \frac{\partial \phi}{\partial x_i} \right) \quad \text{for } i = 1,2,3 \tag{3.49}$$

where ρ_0 is the air density, U_i the vehicle and mean flow velocity components and ϕ the acoustic potential

$$\phi(\vec{x},t) = \frac{\partial}{\partial x_i}\left(\frac{A}{4\pi R^*}e^{i\omega\left(t-\frac{R^+}{c_0}\right)}\right)d_i \tag{3.50}$$

with amplitude A and directivity vector $\vec{d}$. Variables R^+ and R^* are related to the distance R_i between the dipole and each receiver point where the induced pressure is computed and take the convection of the sound waves by the mean flow velocity into account[100],

$$\begin{aligned} R^+ &= \frac{-M_{0,i}R_i + R^*}{\beta^2} \\ R^* &= \sqrt{(M_{0,i}R_i)^2 + \beta^2 R^2} \end{aligned} \tag{3.51a}$$

where $M_{0,i} = U_i/a_0$, a_0 the speed of sound and $\beta = \sqrt{1-M_0^2}$.

The dipole's position is given by the analytical expression of the ellipsoid surface

$$\begin{aligned} X_{dip} &= X_c + a\,\mathrm{cos}k\,\mathrm{cos}l \\ Y_{dip} &= Y_c + b\,\mathrm{cos}k\,\mathrm{sin}l \\ Z_{dip} &= Z_c + c\,\mathrm{sin}k \end{aligned} \tag{3.52}$$

where k and l are the ellipsoid's parameters, with $-\frac{\pi}{2} \leq k \leq \frac{\pi}{2}$ and $-\pi \leq l \leq \pi$.

The optimization aims at finding the optimal position of the dipole source on the ellipsoid that yields the minimum interior noise pressure at a receiver near the driver's ear, seen in fig. 3.5. By differentiating eqs. 3.49 ,3.50 and 3.52, a closed form expression is derived for the derivative of the pressure load w.r.t. the design variables in expression 3.38.

A line search strategy is used for updating the design variables, starting from the initial value $\vec{b}_{init} = (0\ 0)$. The quasi-Newton BFGS method is used for computing the search direction and an interpolation based algorithm for choosing an appropriate step length [103]. Four optimization cycles are performed in total and the objective function is reduced by 34.3%. As seen in fig. 3.6, the optimization algorithm moves the dipole source so that the window area affected by sound radiation is minimized. This leads eventually to a decrease of interior pressure level and, thus, J_{int}.

3.6.2 Orientation of the SAE Mirror

In this application, the usteady pressure distribution on the SAE mirror is computed analytically for $T_s = 0.3s$, using eq. 3.49 for a dipole source positioned at the initial coordinates presented in section 3.6.1, given by eq. 3.52 for $k = 0$ and $l = 0$. This pressure field is stored and used in eq. 2.15 to numerically compute the sound radiation on the side window of the SAE body. For this section, the Kirchhoff Integral is treated as a black-box in order to put emphasis only on the vibroacoustic model.

Keeping the unsteady pressure distribution on the mirror fixed during the optimization, the optimal orientation of the mirror is sought, targeting at minimum interior pressure near the driver's ear, fig. 3.10. The mirror geometry is displaced as a rigid body during the optimization and the x-,y- and z-orientation of the mirror axis are the design variables of the optimization problem. In this case, the derivative $\delta p_{load}/\delta b_n$ in eq. 3.42 is computed with FD.

In total, three optimization cycles are performed, after which the obtained mirror orientation is rather impractical, as seen in fig. 3.10, which is primarily due to the fact that no geometrical constraints are imposed. The goal of this application is, however, to demonstrate the ability of the adjoint vibroacoustic model to compute accurate gradients for gradient-based optimization problems. This is achieved, as the objective function is reduced by 39%. The mirror is deflected away from the window, so that the sound radiation from the mirror is pointing in a different direction.

3.7 Conclusions

In this chapter, the continuous adjoint method for a vibroacoustic model, which predicts the vehicle interior noise induced by a pressure load on the side window, was formulated. The primal equations include the bending wave equation, which simulates the vibrational response of the window to the pressure load, and the wave equation, which describes the sound radiation inside the car cabin. The adjoint to the state equations and the corresponding boundary conditions which couple the two equations are derived.

The method was verified with finite differences and applied to interior noise reduction in a generic vehicle model, the SAE body. In this case, the pressure load was induced by the sound radiation from a dipole source located at the area of the side mirror and the optimization algorithm searched for the optimal position of the source. It was shown that the developed method computes gradients with sufficient accuracy and therefore can be integrated into larger aeroacoustic chains, in which the pressure load on the window is computed by solving different sets of equations, such as the Navier-Stokes equations. This integration follows in the next chapters.

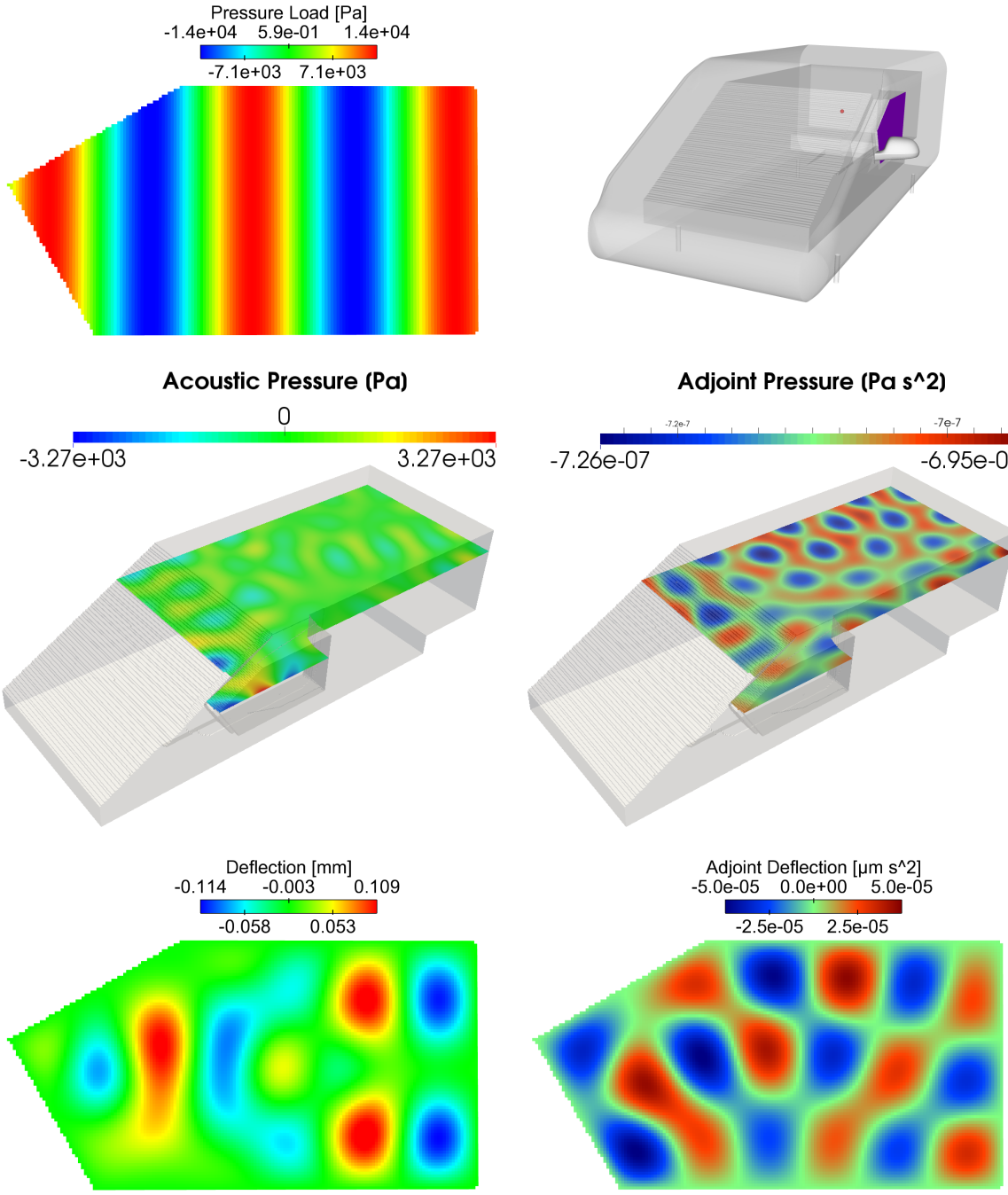

Figure 3.4: Verification of the adjoint solution, using a plane wave as an input either for the bending wave or wave equation. The plane wave is a synthesis of frequencies between 500Hz and 5kHz and the 1000Hz component is shown, top-left. The instantaneous solutions of the wave and adjoint wave equations in the vehicle interior are presented (middle-left and right, respectively). The instantaneous solutions of the bending wave and adjoint bending wave equation are presented (bottom-left and right, respectively).

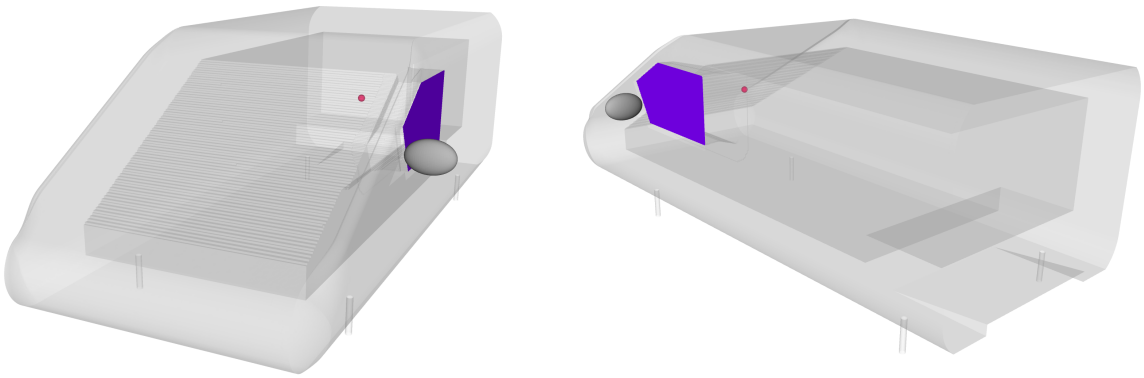

Figure 3.5: Ellipsoid mirror on the SAE body: A dipole source is allowed to move on the ellipsoid surface which replaced the mirror. The optimization target is to reduce the perceived noise at the point near the driver's ear (red point).

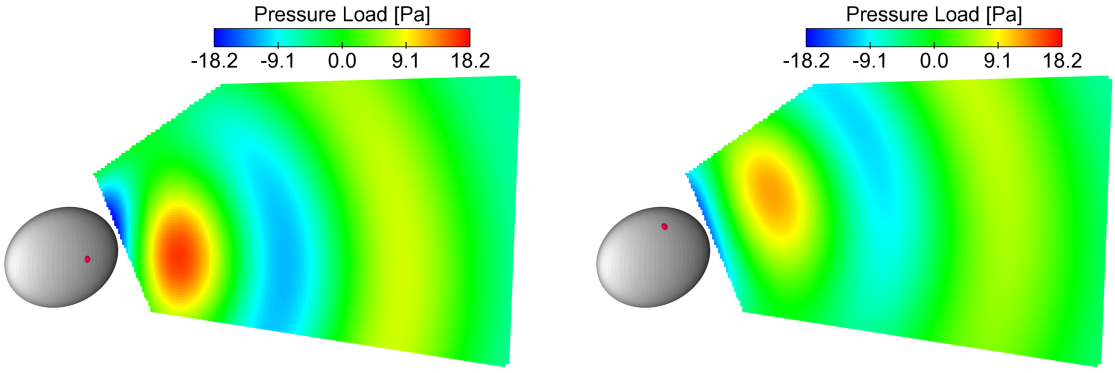

Figure 3.6: Minimizing interior noise of the SAE body: Pressure load on the window is induced by a dipole source which moves on the surface of the ellipsoid resembling a mirror, with directivity normal to the surface. A comparison between the starting (bottom-left) and the optimal (bottom-right) dipole position is presented. The instantaneous pressure load p' (top row) induced by the dipole source (red point) and acts on a smaller area of the window in the optimized case. The amplitude of the acoustic pressure in the interior is also reduced by 34% for the optimal position of the source.

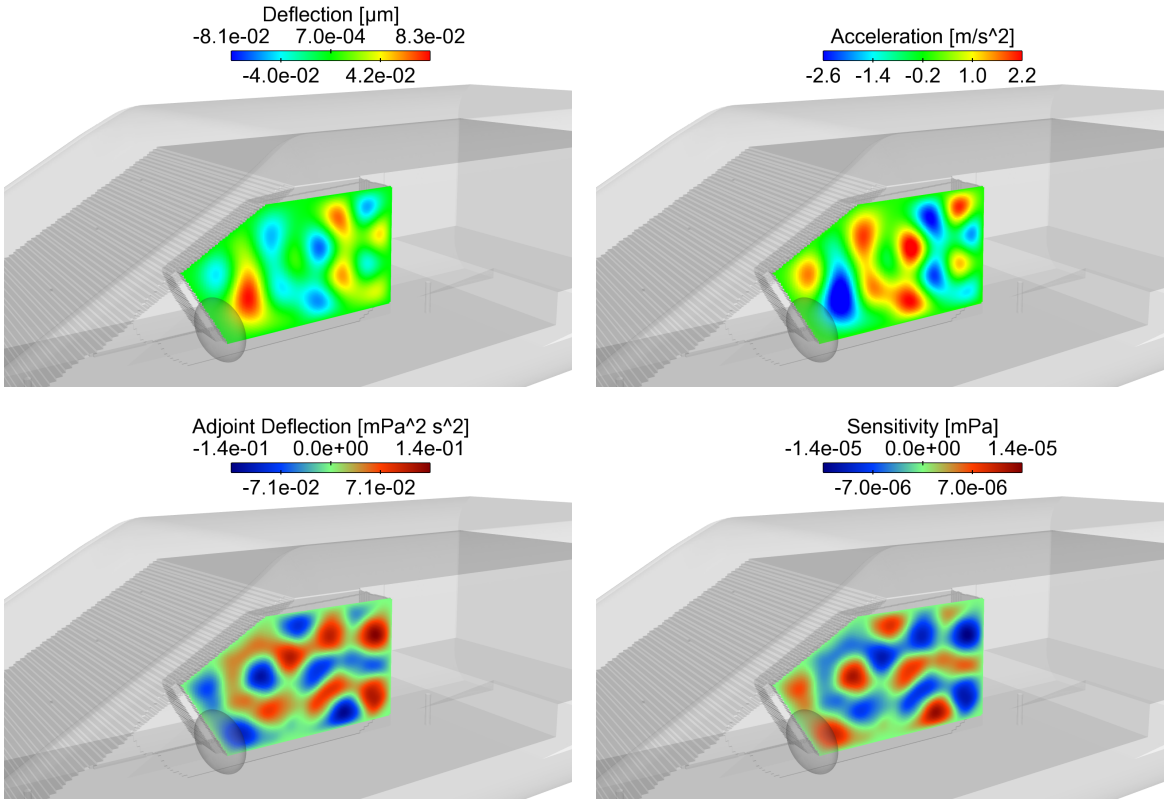

Figure 3.7: Minimizing the interior noise of the SAE body: Instantaneous fields of deflection (top-left) and acceleration (top-right) of the window, as well as adjoint deflection (bottom-left) and sensitivity (bottom-right) computed at the first optimization cycle.

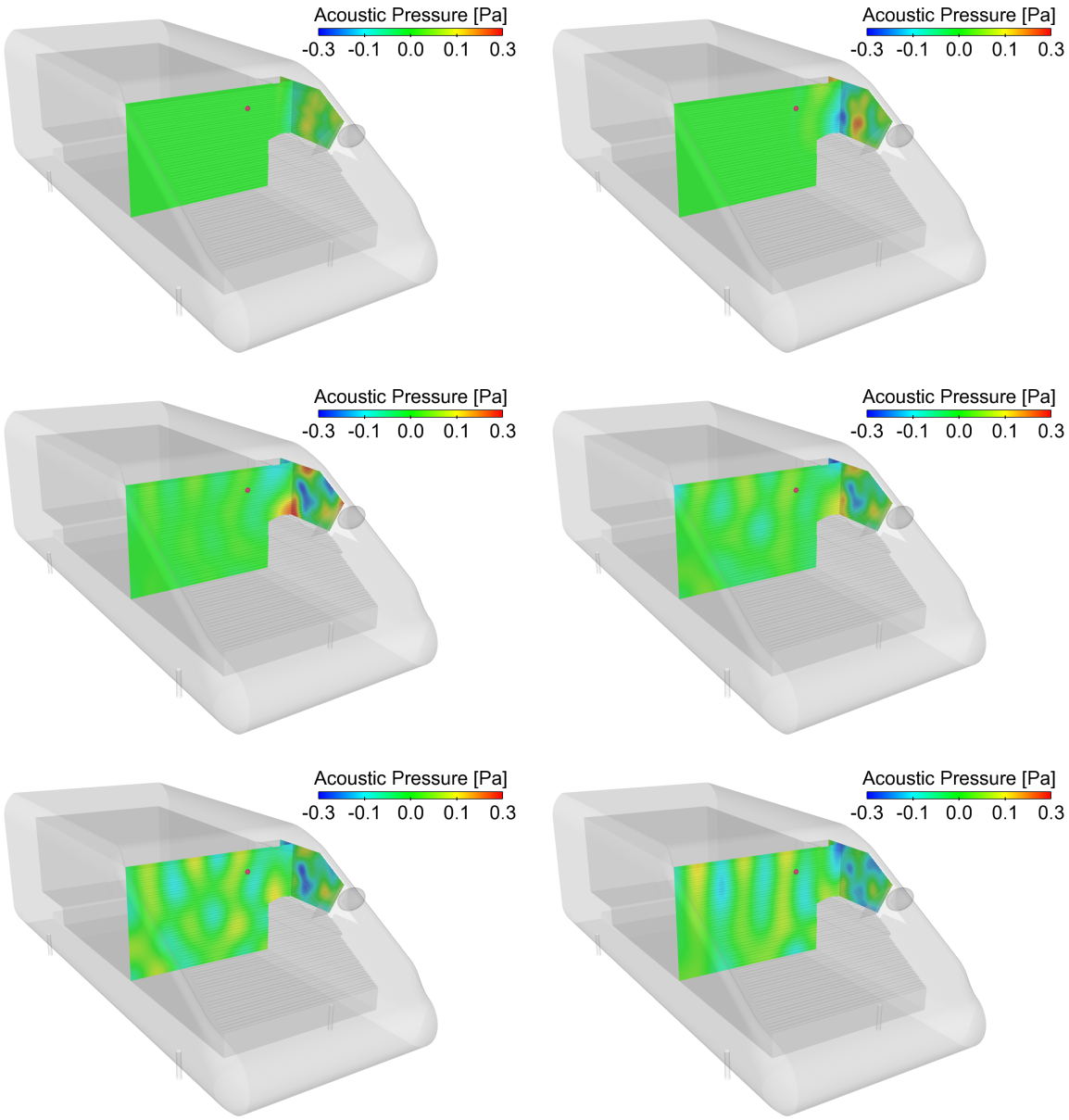

Figure 3.8: Minimizing the interior noise of the SAE body: Six equidistant ($\Delta t = 10^{-3}s$) time snapshots during the sound radiation in the interior, computed at the first optimization cycle. Sound waves generated by the window vibration propagate to the interior and are partly reflected by the vehicle interior walls.

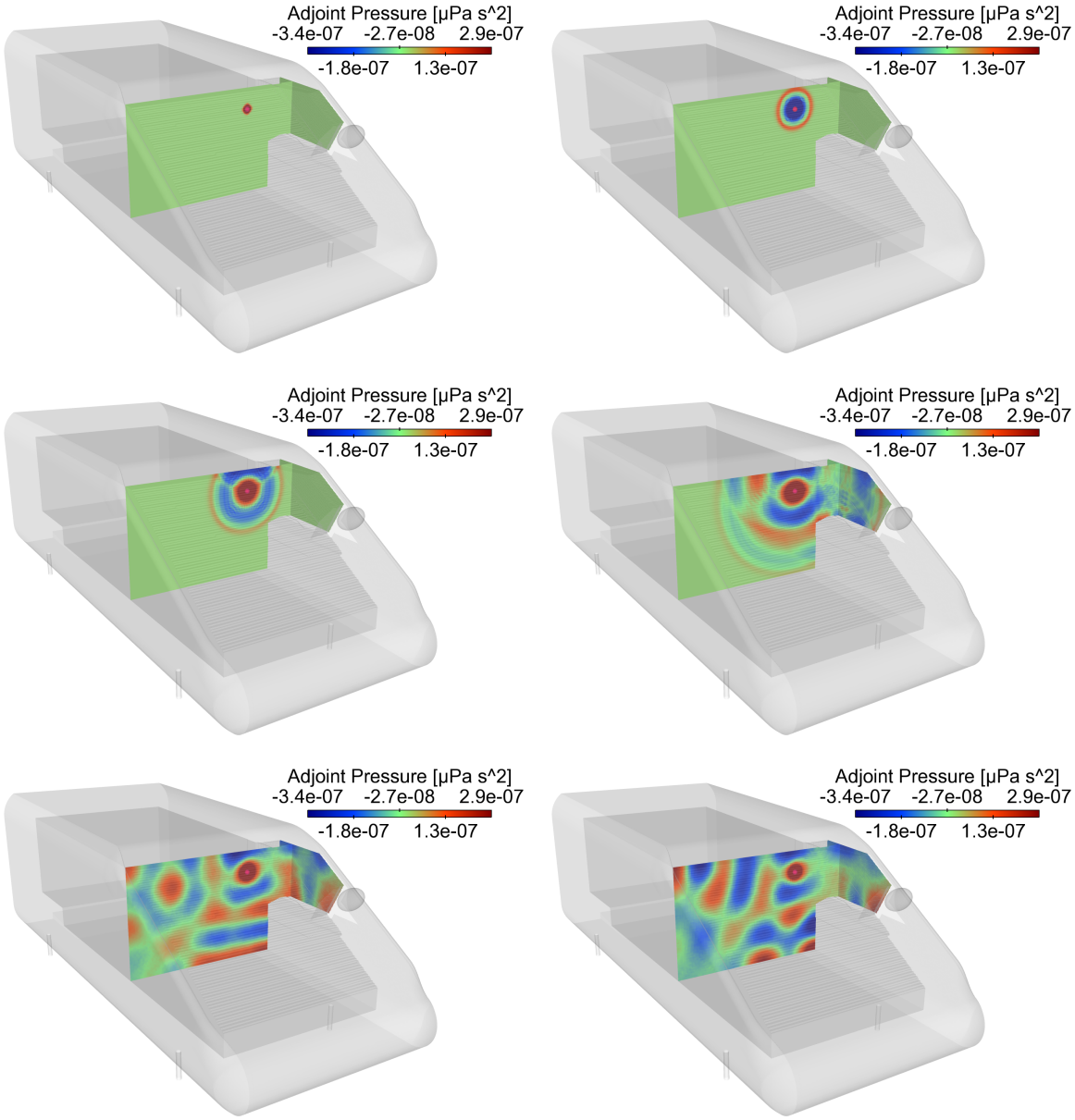

Figure 3.9: Minimizing the interior noise of the SAE body: Six equidistant ($\Delta t = 10^{-3}s$) time snapshots of the computed adjoint pressure. The point where the objective function is defined (red point) acts as a monopole source for the adjoint wave equation. The adjoint pressure fluctuations propagate to the interior and reach the window. The second time derivative of the presented field at the window is the source for the adjoint bending wave equation.

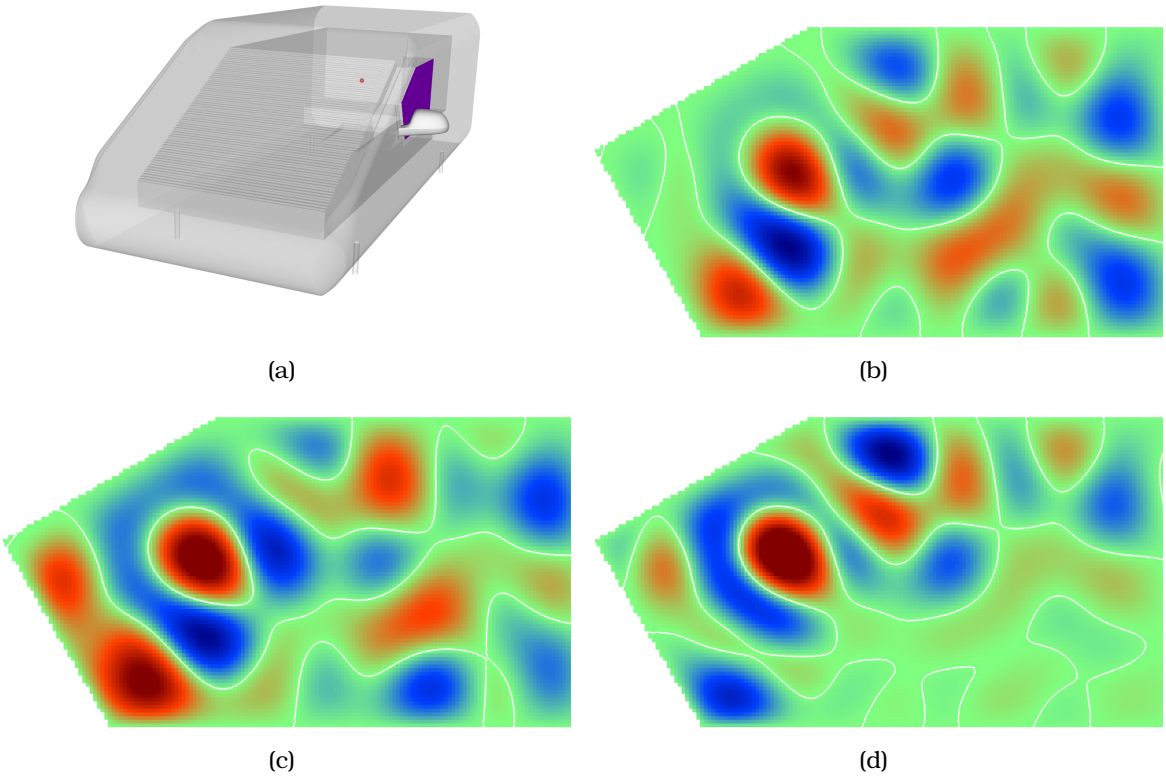

(a) (b)

(c) (d)

Figure 3.10: Minimizing the interior noise of the SAE body: Pressure load on the window is induced by an unsteady pressure distribution and are kept constant during the optimization. This distribution was computed by the same dipole source as in section 3.6.1. The optimization procedure aims to find the optimal orientation of the mirror, so that the interior pressure near the driver's ear (a, red point) is reduced. The window sensitivities w.r.t. to the x-, y- and z- orientation of the mirror axis are shown in b,c and d respectively. These are used along with the term $\frac{\delta p_{load}}{\delta b_n}$ computed with FD, to compute the final gradient of J.

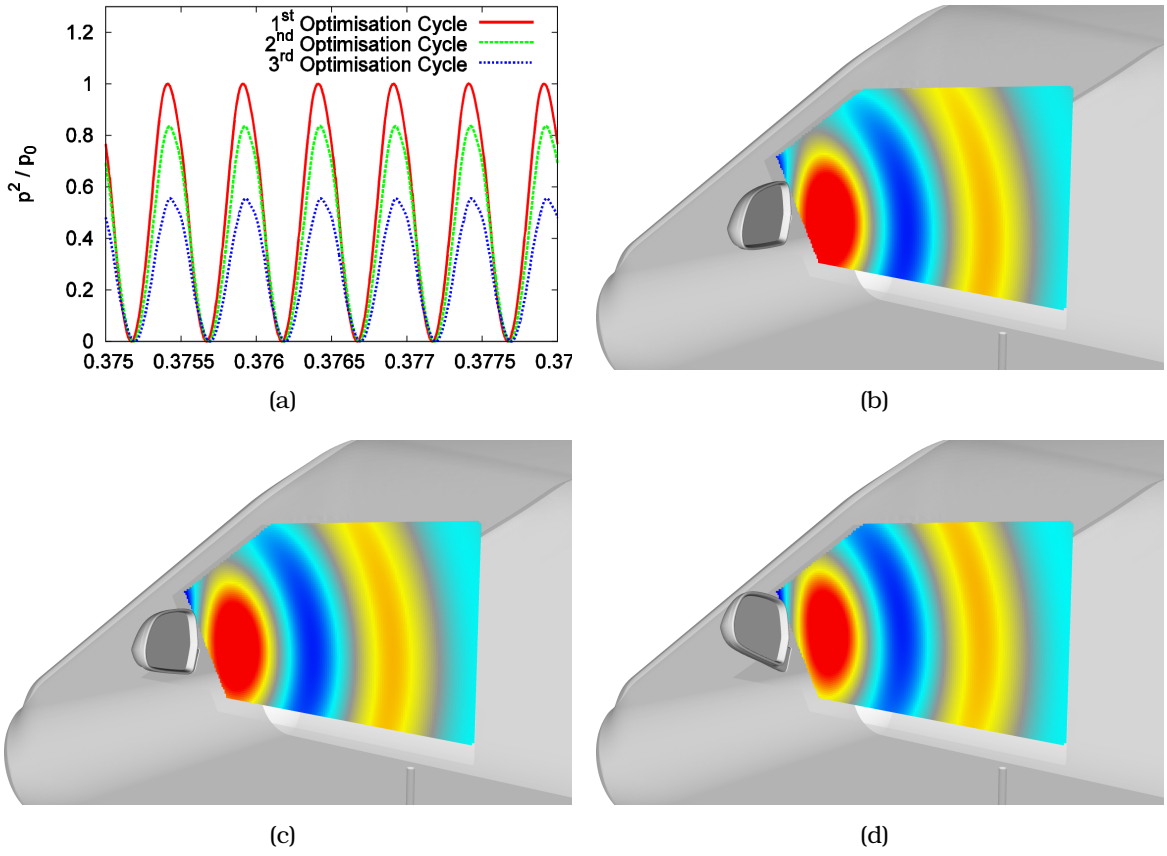

Figure 3.11: Minimizing the interior noise of the SAE body: The computed acoustic pressure and mirror orientation for three optimization cycles are shown in e,f,g and h.

Chapter 4

Continuous Adjoint Formulation for Flow-Induced Sound Radiation - Theory

This chapter focuses on the development of the continuous adjoint method in the exterior domain of the noise prediction chain for vehicles, where noise is generated and radiated to the side window. To predict flow-induced sound radiation from a body in free-stream, the process presented in chapter 2 is followed, where an incompressible Improved Delayed Detached Eddy Simulation is firstly performed. The generated noise is then propagated with the Kirchhoff Integral method, which uses the pressure distribution on the body surface to compute the sound pressure at selected receivers.

The continuous adjoint method for the aforementioned process is developed and presented for the first time in the corresponding literature. In the adjoint process, the differentiated Kirchhoff Integral is used to compute the boundary condition of the adjoint velocity on the body surface and, then, the unsteady adjoint equations are solved backwards in time. It should be noted that the time window over which the simulation is performed and the time window over which the objective function is evaluated do not coincide. This is reflected on the adjoint boundary condition along the body and the time integration of the sensitivity derivatives (SD).

During the optimization process, a set of n design variables b_n, are updated and the parameterized geometry is modified accordingly. The interior nodes of the computational grid must be displaced as well in order to maintain mesh quality. Two grid displacement models are considered in this thesis, one utilizing an algebraic relation between the design variables and the interior nodes displacement and another one that solves the Laplace equation to propage the boundary displacement into the interior nodes. To ensure the consistency of the continuous adjoint-based gradients with the complete primal procedure, grid sensitivities (GS) are taken into account and corresponding adjoint grid displacement equations along with an additional term in the expression of the sensitivity derivatives

are derived. The incorporation of the grid displacement equations during the mathematical development of the continuous adjoint method was firstly proposed in [71], where the significance of grid sensitivities in accurately computing the adjoint derivatives (in continuous adjoint) was demonstrated.

Two different objective functions are considered in this chapter, one that minimizes pressure fluctuation on the radiating body and another one that minimizes the radiated acoustic pressure at a specified set of receivers. The corresponding boundary conditions and sensitivity derivative expession are presented.

4.1 On the Derivatives of Quantities Defined in the Exterior Domain

In contrast to the interior domain presented in 3, the shape and grid of which remains independent of the design variables b_n, the exterior domain contains the parameterized wall boundary, S_{W_P}, which is modified during the optimization and affects any physical quantity computed in this domain. This should carefully be taken into account during the differentiation process.

Here, a distinction is made between symbols $\delta/\delta b_n$ and $\partial/\partial b_n$; the former is used to denote the total derivative of an arbitrary quantity Φ and represents the total change in Φ by varying b_n whereas the latter is used to denote the partial derivative which represents the change in Φ caused by changes in the state variables without taking space deformation into account.

The total derivative w.r.t. b_n of any quantity $\Phi_{ext}\big(b_n, \vec{x}(b_n)\big)$ in the exterior domain is expanded as [115]

$$\frac{\delta \Phi_{ext}}{\delta b_n} = \left.\frac{\partial \Phi_{ext}}{\partial b_n}\right|_x + \left.\frac{\partial \Phi_{ext}}{\partial x_i}\right|_b \frac{\delta x_i}{\delta b_n} \tag{4.1}$$

where the subscripts on the right of each vertical bar are quantities that remain constant during differentiation. The first term on the r.h.s. of eq. 4.1 expresses the derivative of Φ_{ext} at a fixed location, by ignoring the effect of b_n on x_i. The second term accounts for space changes at the same node (grid displacements, in the discrete sense) following changes in b_n for a fixed field of Φ_{ext}.

In the sound radiation test cases, the physical quantities on the body surface that contribute to the radiated acoustic pressure are expressed at the retarted time τ, eq. 2.15 , which itself depends on the distance between the sound sources and the receivers. This distance is not a constant quantity during the optimization, since the sound radiating boundary is modified. Therefore, the total derivative of quantities $\Phi_{ext}\Big(b_n, \vec{x}(b_n), \tau\big(x(b_n)\big)\Big)$ expressed on such surface boundaries is

enhanced to account for these changes as

$$\frac{\delta_s \Phi_{ext}}{\delta b_n} = \left.\frac{\delta \Phi_{ext}}{\delta b_n}\right|_{\tau} + \frac{\partial \Phi_{ext}}{\partial \tau}\frac{\delta \tau}{\delta b_n} \tag{4.2a}$$

$$= \underbrace{\left.\frac{\partial \Phi_{ext}}{\partial b_n}\right|_{x,\tau}}_{T_1} + \underbrace{\left.\frac{\partial \Phi_{ext}}{\partial x_i}\right|_{b,\tau}\frac{\delta x_i}{\delta b_n}}_{T_2} + \underbrace{\left.\frac{\partial \Phi_{ext}}{\partial \tau}\right|_{b,x}\left.\frac{\partial \tau}{\partial x_i}\right|_{b}\frac{\delta x_i}{\delta b_n}}_{T_3} \tag{4.2b}$$

The first term on the r.h.s. of eq. 4.2a expresses the derivative of Φ_{ext} at a fixed retarted time τ, as if body shape changes do not affect τ, despite changes in distances; it is expanded as in eq. 4.1 and leads to terms T_1 and T_2 of eq. 4.2b. The second term on the r.h.s. of eq. 4.2a, term T_3 in eq. 4.2b, indicates changes in Φ_{ext} because of a change in τ, caused by a change in the relative position between the modified source point and the fixed receiver. Whenever Φ_{ext} is not expressed at the retarted time, T_3 vanishes.

Since $\partial/\partial b_n$ takes into account only changes in the flow variables at the unperturbated flow domain and excludes changes in the shape/volume and time of the flow domain, the following permutations are allowed

$$\frac{\partial}{\partial b_n}\left(\frac{\partial \Phi_{ext}}{\partial x_i}\right) = \frac{\partial}{\partial x_i}\left(\frac{\partial \Phi_{ext}}{\partial b_n}\right) \tag{4.3a}$$

$$\frac{\partial}{\partial b_n}\left(\frac{\partial \Phi_{ext}}{\partial t}\right) = \frac{\partial}{\partial t}\left(\frac{\partial \Phi_{ext}}{\partial b_n}\right) \tag{4.3b}$$

$$\frac{\delta}{\delta b_n}\left(\frac{\partial \Phi_{ext}}{\partial t}\right) = \frac{\partial}{\partial t}\left(\frac{\delta \Phi_{ext}}{\delta b_n}\right) \tag{4.3c}$$

To derive eq. 4.3c, the total derivative of the time derivative of Φ_{ext} w.r.t. b_n is expanded and yields

$$\frac{\delta}{\delta b_n}\left(\frac{\partial \Phi_{ext}}{\partial t}\right) = \frac{\partial}{\partial b_n}\left(\frac{\partial \Phi_{ext}}{\partial t}\right) + \frac{\partial}{\partial x_j}\left(\frac{\partial \Phi_{ext}}{\partial t}\right)\frac{\delta x_j}{\delta b_n} + \frac{\partial^2 \Phi_{ext}}{\partial t^2}\frac{\partial \tau}{\partial x_j}\frac{\delta x_j}{\delta b_n} \tag{4.4}$$

where the vertical bars indicating the constant quantities are omitted.

The time derivative of the total derivative of Φ_{ext} w.r.t. b_n yields

$$\frac{\partial}{\partial t}\left(\frac{\delta \Phi_{ext}}{\delta b_n}\right) = \frac{\partial}{\partial t}\left(\frac{\partial \Phi_{ext}}{\partial b_n} + \frac{\partial \Phi_{ext}}{\partial x_i}\frac{\delta x_i}{\delta b_n} + \frac{\partial \Phi_{ext}}{\partial t}\frac{\partial \Phi_{ext}}{\partial \tau}\frac{\partial \tau}{\partial x_i}\right)$$

$$= \frac{\partial}{\partial t}\left(\frac{\partial \Phi_{ext}}{\partial b_n}\right) + \frac{\partial}{\partial t}\left(\frac{\partial \Phi_{ext}}{\partial x_j}\right)\frac{\delta x_j}{\delta b_n} + \frac{\partial^2 \Phi_{ext}}{\partial t^2}\frac{\partial \tau}{\partial x_j}\frac{\delta x_j}{\delta b_n} \tag{4.5}$$

It is apparent that eqs. 4.4 and 4.5 are equal.

Although the spatial or time differentiation and the partial differentiation w.r.t. b_n permute, this is not the case for the total differentiation, where the following identity can easily be proved, similarly to eq. 4.3c ,

$$\frac{\delta}{\delta b_n}\left(\frac{\partial \Phi}{\partial x_j}\right) = \frac{\partial}{\partial x_j}\left(\frac{\delta \Phi}{\delta b_n}\right) - \frac{\partial \Phi}{\partial x_k}\frac{\partial}{\partial x_j}\left(\frac{\delta x_k}{\delta b_n}\right) \tag{4.6}$$

4.2 Grid Displacement Models

In order to modify the geometry during the optimization, a volumetric B-Splines method is used that relates the surface displacement with a user-defined set of control points [90], based on Splines basis-functions. In each optimization step, the derivative of the examined objective function w.r.t. the control points coordinates is computed and used to displace the control points [113]. This displacement is then translated to a surface deformation.

Afterwards, the interior nodes of the computational grid must be displaced too in order to maintain mesh quality. The grid displacement model can be based either on an explicit/algebraic relation between the design variables and the interior grid nodes, or on the solution of additional PDEs which propagate the boundary deformation into the grid interior. A representative of both methods is presented in this thesis:

1. Volumetric B-Splines: the same method used to deform the geometry can be used to compute the interior grid nodes displacement[113], given by

$$R_i^{Bspl} = x_i - M_i = 0\ ,\ i = 1, 2, 3 \tag{4.7}$$

   where x_i are the Cartesian coordinates of the grid nodes and $M_i(b_n)$ is a closed-form expression that yields the grid nodes coordinates based on the coordinates of the control points, which are the design variables b_n . Although, in this thesis, M_i is based on splines basis-functions formulation, any other algebraic model could be used instead, without any change in the formulation that follows. This approach is straight-forward and efficient in terms of computational time and implementation complexity. As shown in section 4.3.5, it leads to a sensitivity derivatives expression which is a synthesis of field and surface integrals. Therefore, the visualization of the objective function gradients on the surface, namely the surface sensitivity map, is not possible.

2. Laplace equations: the displacement of interior nodes is derived by solving

the Laplace PDEs

$$R_i^{lap} = \frac{\partial^2 m_i}{\partial x_j^2} = 0 \ , \ i = 1, 2, 3 \tag{4.8}$$

where m_i are the Cartesian displacements of the grid nodes. Along S_{W_P}, m_i are known from the current optimization step, while $m_i = 0$ on the remaining boundaries, $S \setminus S_{W_P}$, which are not affected by the optimization. This approach may lead to a sensitivity derivatives expression expressed only on the parameterized surface. Therefore, it is suitable for the visualization with sensitivity maps. The latter is especially useful for industrial cases, where the most sensitive regions of the geometry must be identified either to adjust the parameterization or to give insight to the designers and engineers into areas of potential interest.

The influence of the grid displacement must be taken into account for the gradient computation to be consistent in a numerical sense with the primal procedure. Therefore, the grid displacement equations, denoted as R_i^m in the general case, will be included in the augmented objective function, defined later. In section 4.3 it is shown that their contribution is an additional adjoint grid displacement equation and an addition term in the sensitivity derivatives expression, later denoted as Grid Sensitivities (GS). Section 4.3.6 presents the adjoint formulation for the two aforementioned grid displacement models.

4.3 The Adjoint Formulation to the Unsteady Navier-Stokes Equations

The continuous adjoint formulation for the Navier-Stokes equations has been extensively covered in the literature [112, 108, 115, 72, 85]. In this section, only an extended summary of the mathematical development to derive the adjoint equations, initial conditions and boundary conditions is presented.

4.3.1 The Objective Function and its Differentiation

The mathematical development considers only objective functions defined on wall boundaries which are parameterized and deformed during the optimization. Formulations for several other objective functions can be found in [112, 115, 72].

A generic objective function defined along the parameterized wall boundaries,

J_{W_P}, can be written as

$$J_{W_P} = \int_{T_{of}} \int_{S_{W_P}} F_{W_i}\left(\vec{x}, \Phi_{ext}\left(b_n, \vec{x}(b_n), \tau\left(\vec{x}(b_n)\right)\right)\right) n_i dS dt \tag{4.9}$$

where Φ_{ext} is any quantity defined in the exterior domain Ω_{ext}, b_n are the design variabes affecting this quantity and τ is the retarted time.

Throughout this thesis, letter J is used to denote an objective function with its name as subscript and F is used to denote the corresponding integrand of J.

The differentiation of J_{W_P} follows the chain rule and eqs. 4.2a and 4.2b and reads

$$\begin{aligned}
\frac{\delta J_{W_P}}{\delta b_n} &= \int_{T_{of}} \int_{S_{W_P}} \left(\frac{\partial F_{W_i}}{\partial x_j}\frac{\delta x_j}{\delta b_n} + \frac{\partial F_{W_i}}{\partial \Phi_{ext}}\frac{\delta \Phi_{ext}}{\delta b_n} + \frac{\partial F_{W_i}}{\partial \Phi_{ext}}\frac{\partial \Phi_{ext}}{\partial \tau}\frac{\delta \tau}{\delta b_n} \right) dS dt \\
&+ \int_{T_{of}} \int_{S_{W_P}} F_{W_i}\frac{\delta (n_i dS)}{\delta b_n} dt \qquad (4.10a) \\
&= \int_{T_{of}} \int_{S_{W_P}} \left(\frac{\partial F_{W_i}}{\partial x_j}\frac{\delta x_j}{\delta b_n} + \frac{\partial F_{W_i}}{\partial \Phi_{ext}}\frac{\partial \Phi_{ext}}{\partial b_n} + \frac{\partial F_{W_i}}{\partial \Phi_{ext}}\frac{\partial \Phi_{ext}}{\partial x_j}\frac{\delta x_j}{\delta b_n} + \frac{\partial F_{W_i}}{\partial \Phi_{ext}}\frac{\partial \Phi_{ext}}{\partial \tau}\frac{\partial \tau}{\partial x_j}\frac{\delta x_j}{\delta b_n} \right) dS dt \\
&+ \int_{T_{of}} \int_{S_{W_P}} F_{W_i}\frac{\delta (n_i dS)}{\delta b_n} dt \qquad (4.10b)
\end{aligned}$$

The augmented objective function L for the Navier-Stokes equations is defined as the sum of J_{W_P} and the time and space integrals of the product of the primal residuals and the adjoint variable fields

$$L = J_{W_P} + \int_{T_s} \int_{\Omega_{ext}} \left(u_i R_i^v + q R^p\right) d\Omega dt + \int_{\Omega_{ext}} m_i^a R_i^m d\Omega \tag{4.11}$$

where T_s is the time window over which the primal equations, eqs. 2.1 and 2.2, are solved, u_i, q, m_i^a are the adjoint to the velocity v_i, pressure p and grid displacement m_i, respectively. An adjoint turbulence field could have been introduced as in previous works [146, 114, 73]. However, the frozen turbulence assumption is made in this thesis and eddy viscosity is considered to be independent of changes in the design variables and, thus, $\delta\nu_t/\delta b_n = \partial\nu_t/\partial b_n = 0$. Results presented in sections 5.2 and 5.3 support this assumption for the cases examined in this thesis.

Time windows T_{of} and T_s, as defined in eqs. 4.10b and 4.11 respectively, do not necessarily coincide. In order to exclude transient phenomena occurring in the beginning of unsteady flow simulations, the flow equations are usually solved for a large time window T_s. After a sufficient interval of time, the integration

of the objective function begins and is performed for a time window T_{of} being a part of time window T_s. This is why the general case in which T_s and T_{of} do not coincide is presented. Section 5.3.2 investigates further the selection of the two time windows by means of adjoint sensitivity maps on the side mirror of the SAE Body.

The differentiation of eq. 4.11 yields

$$\begin{aligned}\frac{\delta L}{\delta b_n} = \frac{\delta J_{W_P}}{\delta b_n} &+ \frac{\delta}{\delta b_n}\left(\int_{T_S}\int_{\Omega_{ext}} \left(u_i R_i^v + q R^p\right) d\Omega dt\right) \\ &+ \frac{\delta}{\delta b_n}\int_{\Omega_{ext}} m_i^a R_i^m d\Omega \end{aligned} \tag{4.12}$$

4.3.2 Differentiation of the Unsteady Navier-Stokes Equations

The second term on the r.h.s. of eq. 4.12 is further developed as

$$\begin{aligned}\frac{\delta}{\delta b_n}\left(\int_{T_S}\int_{\Omega_{ext}} \left(u_i R_i^v + q R^p\right) d\Omega dt\right) &= \int_{T_S}\int_{\Omega_{ext}} \left(u_i \frac{\delta R_i^v}{\delta b_n} + q\frac{\delta R^p}{\delta b_n}\right) d\Omega dt \\ &+ \int_{T_S}\int_{\Omega_{ext}} \left(u_i R_i^v + q R^p\right)\frac{\delta d\Omega}{\delta b_n} dt \end{aligned} \tag{4.13}$$

The total derivatives of the residuals of the Navier-Stokes equations w.r.t. b_n yield

$$\frac{\delta R^p}{\delta b_n} = \underbrace{-\frac{\delta}{\delta b_n}\left(\frac{\partial v_j}{\partial x_j}\right)}_{T_1} \tag{4.14}$$

and

$$\frac{\delta R_i^u}{\delta b_n} = \underbrace{\frac{\delta}{\delta b_n}\left(\frac{\partial v_i}{\partial t}\right)}_{T_2} + \frac{\partial v_i}{\partial x_j}\frac{\delta v_j}{\delta b_n} + \underbrace{v_j\frac{\delta}{\delta b_n}\left(\frac{\partial v_i}{\partial x_j}\right)}_{T_3} - \underbrace{\frac{\delta}{\delta b_n}\left(\frac{\partial \tau_{ij}}{\partial x_j}\right)}_{T_4} + \underbrace{\frac{\delta}{\delta b_n}\left(\frac{\partial p}{\partial x_i}\right)}_{T_5} \tag{4.15}$$

After substituting eqs. 4.14 and 4.15 into eq. 4.13, the corresponding integrals of the underbraced terms are further expanded using the Green-Gauss theorem

and eq. 4.6 ,

$$
\begin{aligned}
T_1 : -\int_{T_s}\int_{\Omega_{ext}} q\frac{\delta}{\delta b_n}\left(\frac{\partial v_j}{\partial x_j}\right) d\Omega\, dt &= \int_{T_s}\int_{\Omega_{ext}} q\frac{\partial}{\partial x_i}\left(\frac{\delta v_i}{\delta b_n}\right) d\Omega\, dt \\
&- \int_{T_s}\int_{\Omega_{ext}} q\frac{\partial v_i}{\partial x_k}\frac{\partial}{\partial x_i}\left(\frac{\delta x_k}{\delta b_n}\right) d\Omega\, dt \\
&= -\int_{T_s}\int_{\Omega_{ext}} \frac{\partial q}{\partial x_i}\frac{\delta v_i}{\delta b_n} d\Omega\, dt + \int_{T_s}\int_{S_{ext}} q\frac{\delta v_i}{\delta b_n} n_i dS dt \\
&- \int_{T_s}\int_{\Omega_{ext}} q\frac{\partial v_i}{\partial x_k}\frac{\partial}{\partial x_i}\left(\frac{\delta x_k}{\delta b_n}\right) d\Omega\, dt
\end{aligned} \tag{4.16}
$$

$$
T_2 : \int_{T_s}\int_{\Omega_{ext}} u_i\frac{\partial}{\partial t}\left(\frac{\delta v_i}{\delta b_n}\right) d\Omega dt = -\int_{T_s}\int_{\Omega_{ext}} \frac{\partial u_i}{\partial t}\frac{\delta v_i}{\delta b_n} d\Omega\, dt + \int_{\Omega_{ext}} u_i\frac{\delta v_i}{\delta b_n} d\Omega\Big|_{t_{start}}^{t_{end}} \tag{4.17}
$$

$$
\begin{aligned}
T_3 : \int_{T_s}\int_{\Omega_{ext}} u_i v_j\frac{\delta}{\delta b_n}\left(\frac{\partial v_i}{\partial x_j}\right) d\Omega\, dt &= \int_{T_s}\int_{\Omega_{ext}} u_i v_j\frac{\partial}{\partial x_j}\left(\frac{\delta v_i}{\delta b_n}\right) d\Omega\, dt \\
&- \int_{T_s}\int_{\Omega_{ext}} u_i v_j\frac{\partial v_i}{\partial x_k}\frac{\partial}{\partial x_j}\left(\frac{\delta x_k}{\delta b_n}\right) d\Omega\, dt \\
&= -\int_{T_S}\int_{\Omega_{ext}} \frac{\partial u_i}{\partial x_j} v_j\frac{\delta v_i}{\delta b_n} d\Omega\, dt + \int_{T_s}\int_{S_{ext}} u_i v_j n_j\frac{\delta v_i}{\delta b_n} dS dt \\
&- \int_{T_s}\int_{\Omega_{ext}} u_i v_j\frac{\partial v_i}{\partial x_k}\frac{\partial}{\partial x_j}\left(\frac{\delta x_k}{\delta b_n}\right) d\Omega\, dt
\end{aligned} \tag{4.18}
$$

$$
\begin{aligned}
T_4 : \int_{T_s}\int_{\Omega_{ext}} -u_i\frac{\delta}{\delta b_n}\left(\frac{\partial \tau_{ij}}{\partial x_j}\right) d\Omega\, dt &= -\int_{T_s}\int_{\Omega_{ext}} u_i\frac{\partial}{\partial x_j}\left(\frac{\delta \tau_{ij}}{\delta b_n}\right) d\Omega\, dt \\
&+ \int_{T_s}\int_{\Omega_{ext}} u_i\frac{\partial \tau_{ij}}{\partial x_k}\frac{\partial}{\partial x_j}\left(\frac{\delta x_k}{\delta b_n}\right) d\Omega\, dt \\
&= \int_{T_s}\int_{\Omega_{ext}} \frac{\partial u_i}{\partial x_j}\frac{\delta \tau_{ij}}{\delta b_n} d\Omega\, dt - \int_{T_s}\int_{S_{ext}} u_i n_j\frac{\delta \tau_{ij}}{\delta b_n} dS dt \\
&+ \int_{T_s}\int_{\Omega_{ext}} u_i\frac{\partial \tau_{ij}}{\partial x_k}\frac{\partial}{\partial x_j}\left(\frac{\delta x_k}{\delta b_n}\right) d\Omega\, dt
\end{aligned} \tag{4.19}
$$

$$
\begin{aligned}
T_5 : \int_{T_s}\int_{\Omega_{ext}} u_i \frac{\delta}{\delta b_n}\left(\frac{\partial p}{\partial x_i}\right) d\Omega\, dt &= \int_{T_s}\int_{\Omega_{ext}} u_i \frac{\partial}{\partial x_i}\left(\frac{\delta p}{\delta b_n}\right) d\Omega\, dt \\
&- \int_{T_s}\int_{\Omega_{ext}} u_i \frac{\partial p}{\partial x_k}\frac{\partial}{\partial x_i}\left(\frac{\delta x_k}{\delta b_n}\right) d\Omega\, dt \\
&= -\int_{T_s}\int_{\Omega_{ext}} \frac{\partial u_i}{\partial x_i}\frac{\delta p}{\delta b_n} d\Omega\, dt + \int_{T_s}\int_{S_{ext}} u_i n_i \frac{\delta p}{\delta b_n} dS dt \\
&- \int_{T_s}\int_{\Omega_{ext}} u_i \frac{\partial p}{\partial x_k}\frac{\partial}{\partial x_i}\left(\frac{\delta x_k}{\delta b_n}\right) d\Omega\, dt
\end{aligned}
\tag{4.20}
$$

4.3.3 Field Adjoint Equations and Initial Conditions

By substituting eqs. 4.16 into 4.20 and 4.13, the expression of the derivative of L yields

$$
\begin{aligned}
\frac{\delta L}{\delta b_n} &= \int_{T_s}\int_{\Omega_{ext}} \left\{ -\frac{\partial u_i}{\partial t} - v_j\frac{\partial u_i}{\partial x_j} + u_j\frac{\partial v_j}{\partial x_i} - \frac{\partial \tau^a_{ij}}{\partial x_j} + \frac{\partial q}{\partial x_i} \right\} \frac{\delta v_i}{\delta b_n} d\Omega\, dt \\
&- \int_{T_s}\int_{\Omega_{ext}} \left\{ \frac{\partial u_i}{\partial x_i} \right\} \frac{\delta p}{\delta b_n}\, d\Omega\, dt \\
&+ \int_{\Omega_{ext}} u_i \frac{\delta v_i}{\delta b_n} d\Omega \Big|_{t_{end}} - \int_{\Omega_{ext}} u_i \frac{\delta v_i}{\delta b_n} d\Omega \Big|_{t_{start}} \\
&+ \int_{T_s}\int_{S_{ext}} \left\{ u_i v_j n_j - q n_i + \tau^a_{ij} n_j \right\} \frac{\delta v_i}{\delta b_n} dS dt \\
&+ \int_{T_s}\int_{S_{ext}} \left\{ u_i n_i \right\} \frac{\delta p}{\delta b_n} dS dt + \int_{T_s}\int_{S_{ext}} \left\{ - u_i n_j \right\} \frac{\delta \tau_{ij}}{\delta b_n} dS dt \\
&+ \int_{T_{of}}\int_{S_{W_P}} \left(\frac{\partial F_{W_i}}{\partial p}\frac{\delta p}{\delta b_n} + \frac{\partial F_{W_i}}{\partial p}\frac{\partial p}{\partial t}\frac{\partial \tau}{\partial x_j}\frac{\delta x_j}{\delta b_n} + \frac{\partial F_{W_i}}{\partial x_j}\frac{\delta x_j}{\delta b_n} \right) n_i dS dt \\
&+ \int_{T_{of}}\int_{S_{W_P}} F_{W_i} \frac{\delta(n_i dS)}{\delta b_n} dt \\
&+ \int_{T_s}\int_{\Omega_{ext}} \left\{ - u_i v_j \frac{\partial v_i}{\partial x_k} - u_j \frac{\partial p}{\partial x_k} - \tau^a_{ij}\frac{\partial v_i}{\partial x_k} + u_i \frac{\partial \tau_{ij}}{\partial x_k} + q\frac{\partial v_j}{\partial x_k} \right\} \frac{\partial}{\partial x_j}\left(\frac{\delta x_k}{\delta b_n}\right) d\Omega\, dt \\
&+ \frac{\delta}{\delta b_n}\int_{\Omega_{ext}} m^a_i R^m_i d\Omega
\end{aligned}
\tag{4.21}
$$

where $\tau^{\alpha}_{ij} = (\nu + \nu_t)\left(\frac{\partial u_i}{\partial x_j} + \frac{\partial u_j}{\partial x_i}\right)$ is the adjoint stress tensor.

In order to avoid the computation of $\delta v_i/\delta b_n$, $\delta p/\delta b_n$ in the field integrals on the r.h.s. of eq. 4.21 , their coefficients are set to zero, deriving so the unsteady

adjoint Navier-Stokes equations

$$R^q = -\frac{\partial u_j}{\partial x_j} = 0 \tag{4.22}$$

$$R^u_i = -\frac{\partial u_i}{\partial t} + u_j\frac{\partial v_j}{\partial x_i} - \frac{\partial (v_j u_i)}{\partial x_j} + \frac{\partial q}{\partial x_i} - \frac{\partial \tau^a_{ij}}{\partial x_j} = 0\ ,\ i = 1,2,3 \tag{4.23}$$

Eq 4.22 is the adjoint continuity equation whereas eqs. 4.23 are the adjoint momentum equations. The unsteady field adjoint equations draw the usual similarity with the primal ones, with a divergence-free adjoint velocity expressed by eq. 4.22 and the adjoint momentum equation enhanced with the non-conservative adjoint transpose convection term, $u_j\frac{\partial u_j}{\partial x_i}$.

An important difference is that the unsteady adjoint equations are solved backwards in time. This is imposed by the derived initial condition, during the differentiation of the temporal derivative of the Navier-Stokes equations. The corresponding terms are the third and fourth field integrals on the r.h.s. of eq. 4.21 which are expressed either at the start, t_{start}, or at the end, t_{end}, of the simulation. The primal velocities are fixed and independent of b_n, thus its total variation is zero and the first of the aforementioned terms vanishes. By setting the adjoint velocity at t_{end} equal to zero, the second term is eliminated, resulting to the initial condition of the adjoint solution at the end

$$u_i = 0 \text{ for } t = t_{end}\ ,\ i = 1,2,3 \tag{4.24}$$

4.3.4 Adjoint Boundary Conditions

After satisfying the adjoint Navier-Stokes equations and their initial conditions, the remaining terms in eq. 4.21 yield

$$\begin{aligned}
\frac{\delta L}{\delta b_n} &= \int_{T_s}\int_{S_{ext}} \left\{ u_i v_j n_j - q n_i + \tau^a_{ij} n_j \right\} \frac{\delta v_i}{\delta b_n} dS dt \\
&+ \int_{T_s}\int_{S_{ext}} \left\{ u_i n_i \right\} \frac{\delta p}{\delta b_n} dS dt + \int_{T_s}\int_{S_{ext}} \left\{ -u_i n_j \right\} \frac{\delta \tau_{ij}}{\delta b_n} dS dt \\
&+ \int_{T_{of}}\int_{S_{W_P}} \left(\frac{\partial F_{W_i}}{\partial p}\frac{\delta p}{\delta b_n} + \frac{\partial F_{W_i}}{\partial p}\frac{\partial p}{\partial t}\frac{\partial \tau}{\partial x_j}\frac{\delta x_j}{\delta b_n} + \frac{\partial F_{W_i}}{\partial x_j}\frac{\delta x_j}{\delta b_n} \right) n_i dS dt \\
&+ \int_{T_{of}}\int_{S_{W_P}} F_{W_i}\frac{\delta (n_i dS)}{\delta b_n} dt \\
&+ \int_{T_s}\int_{\Omega_{ext}} \left\{ -u_i v_j \frac{\partial v_i}{\partial x_k} - u_j\frac{\partial p}{\partial x_k} - \tau^a_{ij}\frac{\partial v_i}{\partial x_k} + u_i\frac{\partial \tau_{ij}}{\partial x_k} + q\frac{\partial v_j}{\partial x_k} \right\} \frac{\partial}{\partial x_j}\left(\frac{\delta x_k}{\delta b_n}\right) d\Omega\, dt
\end{aligned}$$

(4.25)

Inlet Boundaries, S_I

At the exterior domain inlet boundary S_I, a zero Dirichlet condition is imposed on $\vec{v}$, whereas a zero Neumann on p. Since the inlet is fixed and independent of b_n, $\frac{\delta u_i}{\delta b_n} = \frac{\partial u_i}{\partial b_n} = \frac{\delta x_i}{\delta b_n} = 0$. Consequently, the first integral in eq. 4.25 vanishes.

The remaining terms expressed along S_I yields

$$\int_{T_s}\int_{S_I}\left\{u_i n_i\right\}\frac{\delta p}{\delta b_n}dSdt + \int_{T_s}\int_{S_I}\left\{-u_i n_j\right\}\frac{\delta \tau_{ij}}{\delta b_n}dSdt \tag{4.26}$$

and are eliminated by imposing a zero Dirichlet condition for the adjoint velocity

$$u_{\langle n\rangle} = 0 \tag{4.27a}$$
$$u^l_{\langle t\rangle} = 0\,,\ l = 1,2 \tag{4.27b}$$

where $u_{\langle n\rangle} = u_i n_i$ and $v^l_{\langle t\rangle} = v_i t^l_i\,,\ l = 1,2$

In addition, no boundary condition for q is derived by eliminating any of the boundary integrals along S_I, so a zero Neumann boundary condition is imposed

$$\frac{\partial q}{\partial x_i}n_i = 0 \tag{4.28}$$

Outlet boundaries, S_O

At the outlet boundary of the exterior domain, S_O, a zero Dirichlet condition is imposed on p, whereas a zero Neumann on $\vec{v}$. The outlet is also geometrically fixed and, thus, independent of b_n. Consequently, the second integral of eq. 4.25 vanishes.

The remaining expression along S_O yields

$$\int_{T_s}\int_{S_O}\left\{u_i v_j n_j - q n_i + \tau^a_{ij} n_j\right\}\frac{\delta v_i}{\delta b_n}dSdt + \int_{T_s}\int_{S_O}\left\{-u_i n_j\right\}\frac{\delta \tau_{ij}}{\delta b_n}dSdt \tag{4.29}$$

The second term of expression 4.29 can be neglected, since the outlet boundary is placed far enough so that the velocity profile's uniformity is independent of b_n.

The integrand of the remaining term must now be eliminated. However, there are 4 unknown quantities, the three components of u_i and q, but only three equations. Consequently, one of these must be extrapolated from the interior field

and here, this is the normal adjoint velocity [112]. The integrand is then multiplied with the normal and tangential to the surface vectors, n_i and t_i respectively, and the boundary conditions for the adjoint pressure and the tangential components of the adjoint velocity along S_O are derived

$$q = u_{\langle n \rangle} v_{\langle n \rangle} + 2(\nu + \nu_t) \frac{\partial u_{\langle n \rangle}}{\partial x_i} n_i \tag{4.30}$$

$$u^l_{\langle t \rangle} v_{\langle n \rangle} + (\nu + \nu_t) \left(\frac{\partial u^l_{\langle t \rangle}}{\partial x_i} n_i + \frac{\partial u_{\langle n \rangle}}{\partial x_i} t^l_i \right) = 0 \tag{4.31}$$

where $v_{\langle n \rangle} = v_i n_i$ and $v^l_{\langle t \rangle} = v_i t^l_i \,,\ l = 1, 2$

Parameterized & Unparameterized wall boundaries, S_{W_P} & S_W

The primal conditions on wall boundaries are similar to the ones used along S_I, that is a Dirichlet for $\vec{v}$ and a zero Neumann for q.

For the unparameterized wall boundaries, the same terms of eq. 4.25 vanish, due to $\delta v_i / \delta b_n = \delta x_i / \delta b_n = 0$ and the boundary conditions are derived, which are the same as eqs. 4.27 and 4.28.

For the parameterized boundaries however, the remaining terms expressed along S_{W_P} yield

$$\begin{aligned}
&\int_{T_s} \int_{S_{W_P}} \left\{ u_i n_i + \frac{\partial F_{W_i}}{\partial p} n_i H(t - t_{of}) \right\} \frac{\delta p}{\delta b_n} dS dt + \int_{T_s} \int_{S_{W_P}} \left\{ - u_i n_j \right\} \frac{\delta \tau_{ij}}{\delta b_n} dS dt \\
+ &\int_{T_s} \int_{S_{W_P}} u_k n_k \tau_{ij} \frac{\delta (n_i n_j)}{\delta b_n} dS dt \\
+ &\int_{T_{of}} \int_{S_{W_P}} \left(\frac{\partial F_{W_i}}{\partial p} \frac{\partial p}{\partial t} \frac{\partial \tau}{\partial x_j} \frac{\delta x_j}{\delta b_n} + \frac{\partial F_{W_i}}{\partial x_j} \frac{\delta x_j}{\delta b_n} \right) n_i dS dt \\
+ &\int_{T_{of}} \int_{S_{W_P}} F_{W_i} \frac{\delta (n_i dS)}{\delta b_n} dt
\end{aligned} \tag{4.32}$$

where H is the Heaviside function and t_{of} is the starting time of the objective function integration window T_{of}. Note that an additional term arises, the third integral of expression 4.32, which contributes to the sensitivity derivatives [115], along with the last two integrals of expression 4.32.

The multipliers of eq. 4.32 are set to zero and the boundary conditions for the

wall boundaries are derived

$$u_{\langle n \rangle} = -\frac{\partial F_{W_i}}{\partial p} n_i H(t - t_{of}) \tag{4.33a}$$

$$u^l_{\langle t \rangle} = 0\ ,\ l = 1, 2 \tag{4.33b}$$

and

$$\frac{\partial q}{\partial x_i} n_i = 0 \tag{4.34}$$

4.3.5 Sensitivity Derivatives Expression

After satisfying the field adjoint equations, eq. 4.22 and 4.23, along with their initial, eq. 4.24, and boundary conditions, eq. 4.27 to eq. 4.34, the remaining terms in the expression of the augmented function derivatives read

$$\begin{aligned}
\frac{\delta L}{\delta b_n} = & \int_{T_S}\int_{\Omega_{ext}} \left\{ - u_i v_j \frac{\partial v_i}{\partial x_k} - u_j \frac{\partial p}{\partial x_k} - \tau^a_{ij} \frac{\partial v_i}{\partial x_k} + u_i \frac{\partial \tau_{ij}}{\partial x_k} + q \frac{\partial v_j}{\partial x_k} \right\} \frac{\partial}{\partial x_j}\left(\frac{\delta x_k}{\delta b_n}\right) d\Omega\, dt \\
& + \int_{T_s}\int_{S_{W_P}} u_k n_k \tau_{ij} \frac{\delta(n_i n_j)}{\delta b_n} dS dt \\
& + \int_{T_{of}}\int_{S_{W_P}} \left(\frac{\partial F_{W_i}}{\partial p} \frac{\partial p}{\partial t} \frac{\partial \tau}{\partial x_j} \frac{\delta x_j}{\delta b_n} + \frac{\partial F_{W_i}}{\partial x_j} \frac{\delta x_j}{\delta b_n} \right) n_i dS dt \\
& + \int_{T_{of}}\int_{S_{W_P}} F_{W_i} \frac{\delta(n_i dS)}{\delta b_n} dt \\
& + \frac{\delta}{\delta b_n} \int_{\Omega_{ext}} m^a_i R^m_i d\Omega
\end{aligned} \tag{4.35}$$

The first term on the r.h.s. of eq. 4.35 can further be expanded as

$$\begin{aligned}
& \int_{T_S}\int_{\Omega_{ext}} \left\{ - u_i v_j \frac{\partial v_i}{\partial x_k} - u_j \frac{\partial p}{\partial x_k} - \tau^a_{ij} \frac{\partial v_i}{\partial x_k} + u_i \frac{\partial \tau_{ij}}{\partial x_k} + q \frac{\partial v_j}{\partial x_k} \right\} \frac{\partial}{\partial x_j}\left(\frac{\delta x_k}{\delta b_n}\right) d\Omega\, dt \\
= & - \int_{T_S}\int_{\Omega_{ext}} \frac{\partial}{\partial x_j} \left\{ - u_i v_j \frac{\partial v_i}{\partial x_k} - u_j \frac{\partial p}{\partial x_k} - \tau^a_{ij} \frac{\partial v_i}{\partial x_k} + u_i \frac{\partial \tau_{ij}}{\partial x_k} + q \frac{\partial v_j}{\partial x_k} \right\} \frac{\delta x_k}{\delta b_n} d\Omega\, dt \\
& + \int_{T_s}\int_{S_{W_P}} \left\{ \underbrace{-u_i v_j n_j \frac{\partial v_i}{\partial x_k}}_{\vec{v}=0} \underbrace{- u_j n_j \frac{\partial p}{\partial x_k}}_{u_{\langle n \rangle} = -\frac{\partial F_{W_i}}{\partial p} n_i} - \tau^a_{ij} \frac{\partial v_i}{\partial x_k} + u_i \frac{\partial \tau_{ij}}{\partial x_k} n_j + q \frac{\partial v_j}{\partial x_k} n_j \right\} \frac{\delta x_k}{\delta b_n} dS dt
\end{aligned}$$

$$
\begin{aligned}
= \; - \; & \int_{T_S}\int_{\Omega_{ext}} \frac{\partial}{\partial x_j}\Big\{ - u_i v_j \frac{\partial v_i}{\partial x_k} - u_j \frac{\partial p}{\partial x_k} - \tau_{ij}^a \frac{\partial v_i}{\partial x_k} + u_i \frac{\partial \tau_{ij}}{\partial x_k} + q\frac{\partial v_j}{\partial x_k}\Big\}\frac{\delta x_k}{\delta b_n} d\Omega \, dt \\
+ \; & \int_{T_s}\int_{S_{W_P}} \Big\{ \frac{\partial F_{W_i}}{\partial p}\frac{\partial p}{\partial x_k} n_i - \tau_{ij}^a \frac{\partial v_i}{\partial x_k} n_j + u_i \frac{\partial \tau_{ij}}{\partial x_k} n_j + q\frac{\partial v_j}{\partial x_k} n_j \Big\}\frac{\delta x_k}{\delta b_n} dS dt
\end{aligned}
\tag{4.36}
$$

The field integral on the r.h.s. of eq. 4.36 is used in the development of term $\frac{\delta}{\delta b_n}\int_{\Omega_{ext}} m_i^a R_i^m d\Omega$ of eq. 4.35, which leads to the adjoint grid displacement equations, solved along with the aforementioned adjoint equations, as well as to the grid sensitivities term, $G.S.$, which contributes to the sensitivity derivatives expression. The development of these terms follows in the next section, 4.3.6.

After substituting the remaining surface integral of eq. 4.36 into eq. 4.35, the final expression of the sensitivity derivatives yields

$$
\begin{aligned}
\frac{\delta L}{\delta b_n} = & \int_{T_s}\int_{S_{W_P}} \Big\{ -\tau_{ij}^a \frac{\partial v_i}{\partial x_k} n_j + u_i \frac{\partial \tau_{ij}}{\partial x_k} n_j + q\frac{\partial v_j}{\partial x_k} n_j \Big\}\frac{\delta x_k}{\delta b_n} dS dt \\
& + \int_{T_s}\int_{S_{W_P}} u_k n_k \tau_{ij} \frac{\delta(n_i n_j)}{\delta b_n} dS dt \\
& + \int_{T_{of}}\int_{S_{W_P}} \left(\frac{\partial F_{W_i}}{\partial p}\left(\frac{\partial p}{\partial t}\frac{\partial \tau}{\partial x_j} + \frac{\partial p}{\partial x_j} \right) + \frac{\partial F_{W_i}}{\partial x_j} \right)\frac{\delta x_j}{\delta b_n} n_i dS dt \\
& + \int_{T_{of}}\int_{S_{W_P}} F_{W_i} \frac{\delta(n_i dS)}{\delta b_n} dt \\
& + G.S.
\end{aligned}
\tag{4.37}
$$

4.3.6 Adjoint Grid Displacement & Grid Sensitivities

The adjoint grid displacement equations and the grid sensitivities term depend on the grid displacement model that is utilized, and the derivation for the models investigated in this thesis follow. The significance of incorporating the adjoint grid displacement equations is demonstrated in sections 5.2 and 5.3, where the objective function derivatives are computed with and without the grid displacement term.

Volumetric B-Splines

For the case of the volumetric B-Splines model that relies on algebraic expressions to compute the interior grid node displacements, eq. 4.7, the differentiation of the

model yields

$$\begin{aligned}\frac{\delta}{\delta b_n}\int_{\Omega_{ext}} m_i^a R_i^{bspl} d\Omega &= \int_{\Omega_{ext}} m_i^a \frac{\delta R_i^{bspl}}{\delta b_n} d\Omega + \underbrace{\int_{\Omega_{ext}} m_i^a R_i^{bspl} \frac{\delta(d\Omega)}{\delta b_n}}_{=0} \\ &= \int_{\Omega_{ext}} m_i^a \frac{\delta x_i}{\delta b_n} d\Omega - \int_{\Omega_{ext}} m_i^a \frac{\delta M_i}{\delta b_n} d\Omega \end{aligned} \tag{4.38}$$

The second term on the r.h.s. of eq. 4.38 includes the derivative of the algebraic relation between the interior displacement and the design variables.

The r.h.s. of eq. 4.38 is grouped with the remaining field integral on the r.h.s. of eq. 4.36 and yields the expression

$$\begin{aligned}&\int_{\Omega_{ext}} \left\{ m_i^a - \int_{T_s} \frac{\partial}{\partial x_j} \left(-u_i v_j \frac{\partial v_i}{\partial x_k} - u_j \frac{\partial p}{\partial x_k} - \tau_{ij}^a \frac{\partial v_i}{\partial x_k} + u_i \frac{\partial \tau_{ij}}{\partial x_k} + q \frac{\partial v_j}{\partial x_k} \right) dt \right\} \frac{\delta x_i}{\delta b_n} d\Omega \\ &- \int_{\Omega_{ext}} m_i^a \frac{\delta M_i}{\delta b_n} d\Omega \end{aligned} \tag{4.39}$$

By seting the multiplier of $\delta x_i / \delta b_n$ to zero, the adjoint grid displacement equation is derived

$$R_k^{m^a} = m_k^a - \int_{T_s} \frac{\partial}{\partial x_j} \left\{ -u_i v_j \frac{\partial v_i}{\partial x_k} - u_j \frac{\partial p}{\partial x_k} - \tau_{ij}^a \frac{\partial v_i}{\partial x_k} + u_i \frac{\partial \tau_{ij}}{\partial x_k} + q \frac{\partial v_j}{\partial x_k} \right\} dt = 0, \, k = 1, 2, 3 \tag{4.40}$$

Eq. 4.40 is an algebraic equation, too. Since the primal and adjoint fields are time-dependent, the source term in the steady adjoint grid displacement equation, eq. 4.40 , includes one time integral over T_s. During the solution of eqs. 4.22 and 4.23, contributions from the computed primal/adjoint velocity and pressure fields are accumulated in time to obtain the source term of eqs. 4.40 . Then, eq. 4.40 can be solved at a post-processing step, once per optimization cycle, in order to compute the adjoint grid displacements m_i^a, $i = 1, 2, 3$.

After the computation of m_i^a, the remaining terms yield the grid sensitivities expression

$$G.S. = -\int_{\Omega_{ext}} m_i^a \frac{\delta M_i}{\delta b_n} d\Omega \tag{4.41}$$

Eq. 4.41 is a field integral that represents the impact that a change in the design variables has on the interior nodes coordinates.

Although this approach is straightforward and efficient to use during the optimization, the field integral cannot be transformed to a surface integral and,

therefore, it is not possible to represent the derivative of the objective function on the parameterized surface by means of a sensitivity map.

Laplace Equations

In case the Laplace equations are used for the grid displacement of the interior nodes, the mathematical development is [71]

$$\begin{aligned}\frac{\delta}{\delta b_n}\int_{\Omega_{ext}} m_i^a R_i^{lap} d\Omega \;&=\; \int_S m_i^a n_j \frac{\partial}{\partial x_j}\left(\frac{\delta x_i}{\delta b_n}\right) dS - \int_{S_{W_P}} \frac{\partial m_i^a}{\partial x_j} n_j \frac{\delta x_i}{\delta b_n} dS \\ &+\; \int_{\Omega_{ext}} \frac{\partial^2 m_i^a}{\partial x_j^2}\frac{\partial m_i}{\partial b_n} d\Omega + \underbrace{\int_{S_{W_P}} m_i^a R_i^m n_k \frac{\delta x_k}{\delta b_n} dS}_{=0}\end{aligned} \tag{4.42}$$

For the third term on the r.h.s. of eq. 4.38, the identity $\frac{\partial m_i}{\partial b_n} = \frac{\delta x_i}{\delta b_n}$ is used [72] and the term is grouped with the remaining field integral on the r.h.s. of eq. 4.36, yielding the expression

$$\begin{aligned}&\int_{\Omega_{ext}} \left\{ \frac{\partial^2 m_i^a}{\partial {x_j}^2} - \int_{T_s} \frac{\partial}{\partial x_j}\left(-u_i v_j \frac{\partial v_i}{\partial x_k} - u_j \frac{\partial p}{\partial x_k} - \tau_{ij}^a \frac{\partial v_i}{\partial x_k} + u_i \frac{\partial \tau_{ij}}{\partial x_k} + q\frac{\partial v_j}{\partial x_k}\right) dt \right\} \frac{\delta x_i}{\delta b_n} d\Omega \\ +\; &\int_S m_i^a n_j \frac{\partial}{\partial x_j}\left(\frac{\delta x_i}{\delta b_n}\right) dS - \int_{S_{W_P}} \frac{\partial m_i^a}{\partial x_j} n_j \frac{\delta x_i}{\delta b_n} dS\end{aligned} \tag{4.43}$$

By seting the multiplier of $\delta x_i/\delta b_n$ to zero, the adjoint grid displacement equations are derived

$$\begin{aligned}R_k^{m^a} &= \frac{\partial^2 m_k^a}{\partial x_j^2} - \int_{T_s} \frac{\partial}{\partial x_j}\left\{ u_i v_j \frac{\partial v_i}{\partial x_k} + u_j \frac{\partial p}{\partial x_k} + \tau_{ij}^a \frac{\partial v_i}{\partial x_k} - u_i \frac{\partial \tau_{ij}}{\partial x_k} - q\frac{\partial v_j}{\partial x_k}\right\} dt \\ &= 0\;,\; k = 1,2,3\end{aligned} \tag{4.44}$$

Similarly to the grid displacement model, the adjoint grid displacement equation is a Poisson equation, using a time integral of the primal and adjoint fields as a source term. The boundary conditions $m_i^a = 0,\; i = 1,2,3$ are imposed along S, [71].

After the computation of m_i^a, the remaining terms yield the grid sensitivities expression

$$G.S. = -\int_{S_{W_P}} \frac{\partial m_i^a}{\partial x_j} n_j \frac{\delta x_i}{\delta b_n} dS \tag{4.45}$$

The SD expression with eq. 4.45 now includes only surface integrals and can be, thus, represented with a sensitivity map.

4.3.7 Objective Function for Minimizing Pressure Fluctuations

As discussed in chapter 2, noise generation is associated with pressure fluctuations on radiating bodies. Thus, an objective function that could potentially suppress noise targets at minimizing the pressure fluctuations on the body surface and reads

$$J_{pfluc} = \frac{1}{T_{of}} \int_{T_{of}} \int_{S_{W_P}} (p - \overline{p})^2 dt dS = \frac{1}{T_{of}} \int_{T_{of}} \int_{S_{W_P}} p'^2 dt dS \tag{4.46}$$

The differentiation of eq. 4.46 w.r.t. b_n yields

$$\begin{aligned} \frac{\delta J_{pfluc}}{\delta b_n} &= \int_{T_{of}} \int_{S_{W_P}} \underbrace{\frac{2}{T_{of}} p'}_{\frac{\partial F_{pfluc}}{\partial p}} \underbrace{\left(\frac{\partial p}{\partial b_n} + \frac{\partial p}{\partial x_i} \frac{\delta x_i}{\delta b_n} \right)}_{\frac{\delta p}{\delta b_n}} dS dt \\ &+ \frac{1}{T_{of}} \int_{T_{of}} \int_{S_{W_P}} p'^2 \frac{\delta dS}{\delta b_n} dt \end{aligned} \tag{4.47}$$

For $J_{W_P} = J_{pfluc}$, the boundary condition on the wall, eq. 4.33a , yields

$$u_{\langle n \rangle} = -\frac{2}{T} p' H(t - t_{of}) \tag{4.48a}$$

$$u^l_{\langle t \rangle} = 0 \, , \; l = 1, 2 \tag{4.48b}$$

The sensitivity derivative expression for J_{pfluc}, based on eq. 4.37 , yields

$$\begin{aligned} \frac{\delta J_{pfluc}}{\delta b_n} = &\int_{T_s} \int_{S_{W_P}} \left\{ -\tau^a_{ij} \frac{\partial v_i}{\partial x_k} n_j + u_i \frac{\partial \tau_{ij}}{\partial x_k} n_j + q \frac{\partial v_j}{\partial x_k} n_j \right\} \frac{\delta x_k}{\delta b_n} dS dt \\ &+ \int_{T_s} \int_{S_{W_P}} u_k n_k \tau_{ij} \frac{\delta (n_i n_j)}{\delta b_n} dS dt \\ &+ \frac{2}{T} \int_{T_{of}} \int_{S_{W_P}} p' \frac{\partial p}{\partial x_i} \frac{\delta x_i}{\delta b_n} dt \\ &+ \frac{1}{T} \int_{T_{of}} \int_{S_{W_P}} p'^2 \frac{\delta (dS)}{\delta b_n} dt \\ &+ G.S. \end{aligned} \tag{4.49}$$

The grid sensitivities term is derived either by solving eq. 4.40 to compute eq. 4.41 , if volumetric B-Splines are used for the interior grid displacement, or by solving eq. 4.44 to compute eq. 4.45 , if the Laplace equations are used.

4.4 The Adjoint Method to Flow-Induced Sound Radiation

An objective function related to sound radiation is investigated in this section and the adjoint boundary conditions and sensitivity derivatives expressions are presented.

4.4.1 Objective Function for Radiated Noise and its Differentiation

The Kirchhoff Integral method, eq. 2.15 , is considered for the adjoint derivation. Its input is the pressure distribution on the body surface, p, and its output the radiated acoustic pressure p_{ac} at the receivers. A suitable objective function for shape optimization targeting minimal noise is defined as the time-averaged squared acoustic pressure fluctuation

$$J_{KI} = \frac{1}{T_{of}} \int_{T_{of}} (p_{ac} - \overline{p_{ac}})^2 dt = \frac{1}{T_{of}} \int_{T_{of}} p'^2_{ac} dt \tag{4.50}$$

In case a set of receivers is studied, the objective function is simply the sum of the r.h.s. integrals of eq. 4.50 over all receivers. For the sake of readability, only one receiver is considered for the mathematical development, although the verification and application test cases include more than one.

The differentiation of eq. 4.50 w.r.t. b_n yields

$$\frac{\delta J_{KI}}{\delta b_n} = \frac{2}{T_{of}} \int_{T_{of}} p'_{ac} \frac{\delta p_{ac}}{\delta b_n} dS dt \tag{4.51}$$

4.4.2 Differentiation of the Kirchhoff Integral

The derivative of the acoustic pressure on the r.h.s. of eq. 4.51 , is expanded further based on eq. 2.15

$$\frac{\delta p_{ac}}{\delta b_n} = \frac{\rho}{4\pi} \int_{S_W} \left[\frac{\delta g_{ret,i}}{\delta b_n} \hat{n}_i dS + g_{ret,i} \frac{\delta (\hat{n}_i dS)}{\delta b_n} \right] \tag{4.52}$$

As the integrand of eq. 4.52 is expressed at the retarded time τ, the derivative of $g_{ret,i}$ is developed according to eq. 4.2b as

$$\begin{aligned}\frac{\delta}{\delta b_n}\left(\frac{\hat{r}_i}{R^2}p\right) &= \left[\left(3\hat{r}_i\hat{r}_j\frac{\delta x_j}{\delta b_n}-\frac{\delta x_i}{\delta b_n}\right)\frac{1}{R^3}\right]p \\ &+ \frac{\hat{r}_i}{R^2}\left[\frac{\partial p}{\partial b_n}+\frac{\partial p}{\partial x_j}\frac{\delta x_j}{\delta b_n}+\frac{\partial p}{\partial t}\frac{\hat{r}_j}{a_0}\frac{\delta x_j}{\delta b_n}\right]\end{aligned} \tag{4.53}$$

and

$$\begin{aligned}\frac{\delta}{\delta b_n}\left(\frac{\hat{r}_i}{a_0 R}\frac{\partial p}{\partial t}\right) &= \left[\left(2\hat{r}_i\hat{r}_j\frac{\delta x_j}{\delta b_n}-\frac{\delta x_i}{\delta b_n}\right)\frac{1}{a_0R^2}\right]\frac{\partial p}{\partial t} \\ &+ \frac{\hat{r}_i}{a_0 R}\left[\frac{\partial}{\partial b_n}\left(\frac{\partial p}{\partial t}\right)+\frac{\partial^2 p}{\partial t\partial x_j}\frac{\delta x_j}{\delta b_n}+\frac{\partial^2 p}{\partial t^2}\frac{\hat{r}_j}{a_0}\frac{\delta x_j}{\delta b_n}\right]\end{aligned} \tag{4.54}$$

where p and its derivatives are expressed at τ.

By substituting eqs. 4.53 and 4.54 into 4.52, the derivative of the acoustic pressure radiated to a receiver from a source surface S_w w.r.t. the design variables b_n is given by

$$\begin{aligned}\frac{\delta p_{ac}}{\delta b_n}(t,\vec{x}_{rec}) &= \frac{\rho}{4\pi}\int_{S_W}(3\hat{r}_i\hat{n}_i\hat{r}_j-\hat{n}_j)\frac{1}{R^3}p\Big|_{ret}\frac{\delta x_j}{\delta b_n}dS \\ &+ \frac{\rho}{4\pi}\int_{S_W}(2\hat{r}_i\hat{n}_i\hat{r}_j-\hat{n}_j)\frac{1}{a_0R^2}\frac{\partial p}{\partial t}\Big|_{ret}\frac{\delta x_j}{\delta b_n}dS \\ &+ \frac{\rho}{4\pi}\int_{S_W}\frac{\hat{r}_i\hat{n}_i}{R}\left(\frac{1}{R}\frac{\partial p}{\partial x_j}\Big|_{ret}+\frac{1}{a_0}\frac{\partial^2 p}{\partial t\partial x_j}\Big|_{ret}\right)\frac{\delta x_j}{\delta b_n}dS \\ &+ \frac{\rho}{4\pi}\int_{S_W}\frac{\hat{r}_i\hat{n}_i\hat{r}_j}{a_0R}\left(\frac{1}{R}\frac{\partial p}{\partial t}\Big|_{ret}+\frac{1}{a_0}\frac{\partial^2 p}{\partial t^2}\Big|_{ret}\right)\frac{\delta x_j}{\delta b_n}dS \\ &+ \frac{\rho}{4\pi}\int_{S_W}\left[\frac{\hat{r}_i\hat{n}_i}{R^2}\frac{\delta p}{\delta b_n}\Big|_{ret}+\frac{\hat{r}_i\hat{n}_i}{a_0R}\frac{\partial}{\partial t}\left(\frac{\delta p}{\delta b_n}\right)\Big|_{ret}\right]dS \\ &+ \frac{\rho}{4\pi}\int_{S_W}g_{ret,i}\frac{\delta(\hat{n}_i dS)}{\delta b_n}\end{aligned} \tag{4.55}$$

On the r.h.s. of eq. 4.55 , the time-varying flow quantities $p, \partial p/\partial t,\ \partial^2 p/\partial t^2$ as well as their partial derivatives w.r.t. the design variables are expressed at the retarted time τ which depends on the distance between the receiver and the corresponding sender.

The final expression of the sensitivity derivatives of J_{KI} w.r.t. b_n, can now be

written for a set of N_R receivers, by substituting eq. 4.55 into eq. 4.51 ,

$$
\begin{aligned}
\frac{\delta J_{KI}}{\delta b_n} &= \int_{T_{of}}\int_{S_{W_P}} \frac{\rho}{2\pi T_{of}} \sum_{r=1}^{N_R} p_{ac}^{r\prime} \left(3\hat{r}_i\hat{n}_i\hat{r}_j - \hat{n}_j\right) \frac{1}{R^3} p\Big|_{ret} \frac{\delta x_j}{\delta b_n} dSdt \\
&+ \int_{T_{of}}\int_{S_{W_P}} \frac{\rho}{2\pi T_{of}} \sum_{r=1}^{N_R} p_{ac}^{r\prime} \left(2\hat{r}_i\hat{n}_i\hat{r}_j - \hat{n}_j\right) \frac{1}{a_0 R^2} \frac{\partial p}{\partial t}\Big|_{ret} \frac{\delta x_j}{\delta b_n} dSdt \\
&+ \int_{T_{of}}\int_{S_{W_P}} \frac{\rho}{2\pi T_{of}} \sum_{r=1}^{N_R} p_{ac}^{r\prime} \frac{\hat{r}_i\hat{n}_i}{R} \left(\frac{1}{R}\frac{\partial p}{\partial x_j}\Big|_{ret} + \frac{1}{a_0}\frac{\partial^2}{\partial t \partial x_j}\Big|_{ret}\right) \frac{\delta x_j}{\delta b_n} dSdt \\
&+ \int_{T_{of}}\int_{S_{W_P}} \frac{\rho}{2\pi T_{of}} \sum_{r=1}^{N_R} p_{ac}^{r\prime} \frac{\hat{r}_i\hat{n}_i\hat{r}_j}{a_0 R} \left(\frac{1}{R}\frac{\partial p}{\partial t}\Big|_{ret} + \frac{1}{a_0}\frac{\partial^2 p}{\partial t^2}\Big|_{ret}\right) \frac{\delta x_j}{\delta b_n} dSdt \\
&+ \int_{T_{of}}\int_{S_{W_P}} \frac{\rho}{2\pi T_{of}} \sum_{r=1}^{N_R} p_{ac}^{r\prime} \left[\frac{\hat{r}_i\hat{n}_i}{R^2}\frac{\delta p}{\delta b_n}\Big|_{ret} + \frac{\hat{r}_i\hat{n}_i}{a_0 R}\frac{\partial}{\partial t}\left(\frac{\delta p}{\delta b_n}\right)\Big|_{ret}\right] dSdt \\
&+ \int_{T_{of}}\int_{S_{W_P}} \frac{\rho}{2\pi T_{of}} \sum_{r=1}^{N_R} p_{ac}^{r\prime} g_{ret,i}^{r} \frac{\delta(\hat{n}_i dS)}{\delta b_n} dt
\end{aligned}
\tag{4.56}
$$

where $p_{ac}^{r\prime}$, $\hat{r}^r$ and R^r refer to the corresponding receiver r during the summation. The sum of the integrands of the first two terms on the r.h.s. of eq. 4.56 denote part $\frac{\partial F_{KI}}{\partial x_j}\frac{\delta x_j}{\delta b_n}$ of the total derivative of the objective function, eq. 4.10b . The integrand of the third term is the $\frac{\partial F_{KI}}{\partial p}\frac{\partial p}{\partial x_j}$ and the integrand of the fourth term is $\frac{\partial F_{KI}}{\partial p}\frac{\partial p}{\partial t}\frac{\partial \tau}{\partial x_j}\frac{\delta x_j}{\delta b_n}$. The fifth term is further expanded, in order for this to take the form of $\frac{\partial F_{KI}}{\partial p}\frac{\delta p}{\delta b_n}$, as follows

$$
\begin{aligned}
&\int_{T_{of}}\int_{S_{W_P}} \frac{\rho}{2\pi T_{of}} \sum_{r=1}^{N_R} p_{ac}^{r\prime} \left[\frac{\hat{r}_i\hat{n}_i}{R^2}\frac{\delta p}{\delta b_n}\Big|_{ret} + \frac{\hat{r}_i\hat{n}_i}{a_0 R}\frac{\partial}{\partial t}\left(\frac{\delta p}{\delta b_n}\right)\Big|_{ret}\right] dSdt \\
= &\int_{T_{of}}\int_{S_{W_P}} \frac{\rho}{2\pi T_{of}} \sum_{r=1}^{N_R} p_{ac}^{r\prime} \frac{\hat{r}_i\hat{n}_i}{R^2}\frac{\delta p}{\delta b_n}\Big|_{ret} dSdt + \int_{S_W} \frac{\rho}{2\pi T_{of}} \sum_{r=1}^{N_R} \int_{T_{of}} p_{ac}^{r\prime} \frac{\hat{r}_i\hat{n}_i}{a_0 R}\frac{\partial}{\partial t}\left(\frac{\delta p}{\delta b_n}\right)\Big|_{ret} dtdS \\
= &\int_{T_{of}}\int_{S_{W_P}} \frac{\rho}{2\pi T_{of}} \sum_{r=1}^{N_R} p_{ac}^{r\prime} \frac{\hat{r}_i\hat{n}_i}{R^2}\frac{\delta p}{\delta b_n}\Big|_{ret} dSdt - \int_{S_{W_P}} \frac{\rho}{2\pi T_{of}} \sum_{r=1}^{N_R} \int_{T_{of}} \frac{\partial p_{ac}^{r\prime}}{\partial t} \frac{\hat{r}_i\hat{n}_i}{a_0 R}\frac{\delta p}{\delta b_n}\Big|_{ret} dtdS \\
&+ \int_{S_{W_P}} \frac{\rho}{2\pi T_{of}} \sum_{r=1}^{N_R} \left[p_{ac}^{r\prime} \frac{\hat{r}_i^r\hat{n}_i}{a_0 R}\frac{\delta p}{\delta b_n}\right]_{t_{of}}^{t_{of}+T_{of}} dS \\
= &\int_{T_{of}}\int_{S_{W_P}} \frac{\rho}{2\pi T_{of}} \sum_{r=1}^{N_R} \left(p_{ac}^{r\prime} \frac{\hat{r}_i^r\hat{n}_i}{R^{r\,2}} + \frac{\partial p_{ac}^{r\prime}}{\partial t}\frac{\hat{r}_i^r\hat{n}_i}{a_0 R}\right) \frac{\delta p}{\delta b_n}\Big|_{ret} dSdt
\end{aligned}
$$

$$
\begin{aligned}
&+\int_{S_{W_P}} \frac{\rho}{2\pi T_{of}} \sum_{r=1}^{N_R} \left[p'^{r}_{ac} \frac{\hat{r}^r_i \hat{n}_i}{a_0 R} \frac{\delta p}{\delta b_n}\bigg|_{ret} \right]_{t_{of}}^{t_{of}+T_{of}} dS \\
= &\int_{T_{of}} \int_{S_{W_P}} \frac{\rho}{2\pi T_{of}} \sum_{r=1}^{N_R} \left[p'^{r}_{ac} \frac{\hat{r}^r_i \hat{n}_i}{R^{r\,2}} + \frac{\partial p'^{r}_{ac}}{\partial t} \frac{\hat{r}^r_i \hat{n}_i}{a_0 R} \right]_{adv} \frac{\delta p}{\delta b_n} dS dt \\
&+\int_{S_{W_P}} \frac{\rho}{2\pi T_{of}} \sum_{r=1}^{N_R} \left[p'^{r}_{ac}\bigg|_{adv} \frac{\hat{r}^r_i \hat{n}_i}{a_0 R} \frac{\delta p}{\delta b_n} \right]_{t_{of}}^{t_{of}+T_{of}} dS
\end{aligned}
\tag{4.57}
$$

where in the last integral on the r.h.s. of eq. 4.57 the advance time is introduced, $\tau^{adv} = t + \frac{r}{c}$, at which p'^{r}_{ac} and $\partial p'^{r}_{ac}/\partial t$ are expressed. This way, $\delta p/\delta b_n$ is expressed at t and can be grouped with the remaining multipliers of $\delta p/\delta b_n$ derived by differentiating the Navier-Stokes equations, in order to derive the boundary condition on the parameterized wall, as shown later.

4.4.3 Adjoint Boundary Condition on the Wall & Sensitivity Derivatives Expression

In sound radiaton problems, the adjoint equations remain unchanged (eqs. 4.23 and 4.22). The condition on the wall boundary of the radiating body depends, however, on the objective function. For $J_{W_P} = J_{KI}$ and using eq. 4.57 , the boundary condition for u_i, eq. 4.33a , yields

$$
\begin{aligned}
u_{\langle n \rangle} &= -\sum_{r=1}^{N_R} \frac{\rho}{2\pi T_{of}} \left[\frac{\hat{r}_j \hat{n}_j}{R^2} p'_{ac} - \frac{\hat{r}_j \hat{n}_j}{a_0 R} \frac{\partial p'_{ac}}{\partial t} \right]_{adv} H(t - t_{of}) \\
&\quad - \sum_{r=1}^{N_R} \frac{\rho}{2\pi T_{of}} p'^{r}_{ac} \frac{\hat{r}^r_i \hat{n}_i}{a_0 R}\bigg|_{t_{of}}^{t_{of}+T_{of}} \qquad (4.58a) \\
u^l_{\langle t \rangle} &= 0\,,\ l = 1, 2 \qquad (4.58b)
\end{aligned}
$$

The adjoint velocity has a constant direction that is normal to the surface and its instantaneous value at t depends on the acoustic pressure, computed at the advanced time $\tau^{adv} = t + \frac{r}{c}$. During the primal solution, the acoustic pressure and its temporal derivative at any receiver at time t are computed based on the contributions of the time instants at retarted time τ. Conversely, the acoustic pressure and its time derivative contributing to the adjoint boundary condition at a time instant t are expressed at the "adjoint retarted" time, which is, in fact, an advanced time τ^{adv}, given that the adjoint simulation runs backwards this time. Details about the algorithmic implementation can be found in section 5.1.2. Furthermore, since eq. 4.58 involves the differentiation of the objective function,

it is valid only for the time window T_{of} and has no contribution, i.e. $u_i = 0$, at any other time instant of T_s. Finally, numerical experiments showed that the second term on the r.h.s. of eq. 4.58a , expressed only at the start and end of the J_{KI} time window can be neglected with no impact on the accuracy of the sensitivity derivatives.

The sensitivity derivative expression for J_{KI}, based on eqs. 4.37 and 4.56 yields

$$
\begin{aligned}
\frac{\delta J_{KI}}{\delta b_n} = & \int_{T_s}\int_{S_{W_P}} \left\{ -\tau_{ij}^a \frac{\partial v_i}{\partial x_k} n_j + u_i \frac{\partial \tau_{ij}}{\partial x_k} n_j + q \frac{\partial v_j}{\partial x_k} n_j \right\} \frac{\delta x_k}{\delta b_n} dSdt \\
& + \int_{T_s}\int_{S_{W_P}} u_k n_k \tau_{ij} \frac{\delta (n_i n_j)}{\delta b_n} dSdt \\
& + \int_{T_{of}}\int_{S_{W_P}} \frac{\rho}{2\pi T_{of}} \sum_{r=1}^{N_R} p_{ac}^{r\,\prime} \left(3\hat{r}_i \hat{n}_i \hat{r}_j - \hat{n}_j\right) \frac{1}{R^3} p \Big|_{ret} \frac{\delta x_j}{\delta b_n} dSdt \\
& + \int_{T_{of}}\int_{S_{W_P}} \frac{\rho}{2\pi T_{of}} \sum_{r=1}^{N_R} p_{ac}^{r\,\prime} \left(2\hat{r}_i \hat{n}_i \hat{r}_j - \hat{n}_j\right) \frac{1}{a_0 R^2} \frac{\partial p}{\partial t} \Big|_{ret} \frac{\delta x_j}{\delta b_n} dSdt \\
& + \int_{T_{of}}\int_{S_{W_P}} \frac{\rho}{2\pi T_{of}} \sum_{r=1}^{N_R} p_{ac}^{r\,\prime} \frac{\hat{r}_i \hat{n}_i}{R} \left(\frac{1}{R} \frac{\partial p}{\partial x_j} \Big|_{ret} + \frac{1}{a_0} \frac{\partial^2}{\partial t \partial x_j} \Big|_{ret} \right) \frac{\delta x_j}{\delta b_n} dSdt \\
& + \int_{T_{of}}\int_{S_{W_P}} \frac{\rho}{2\pi T_{of}} \sum_{r=1}^{N_R} p_{ac}^{r\,\prime} \frac{\hat{r}_i \hat{n}_i \hat{r}_j}{a_0 R} \left(\frac{1}{R} \frac{\partial p}{\partial t} \Big|_{ret} + \frac{1}{a_0} \frac{\partial^2 p}{\partial t^2} \Big|_{ret} \right) \frac{\delta x_j}{\delta b_n} dSdt \\
& + \int_{T_{of}}\int_{S_{W_P}} \frac{\rho}{2\pi T_{of}} \sum_{r=1}^{N_R} p_{ac}^{r\,\prime} g_{ret,i}^r \frac{\delta (\hat{n}_i dS)}{\delta b_n} dt \\
& + G.S
\end{aligned}
\tag{4.59}
$$

The first two integrals indicate geometry changes which affect directly the flow and, consequently, the pressure distribution and noise creation on the body. The following four integrals on the r.h.s. of eq. 4.59 are associated with the directivity of the sound field and how this is affected by geometry changes. It is important to point out the difference in the integration time windows of the sensitivity derivative terms; the first two are integrated over the simulation window T_s whereas the last three over the objective function window T_{of}. Finally, the grid sensitivities term is derived either by solving eq. 4.40 to compute eq. 4.41 , if volumetric B-Splines are used for the interior grid displacement, or by solving eq. 4.44 to compute eq. 4.45 , if the Laplace equations are used.

4.5 Conclusions

The formulation of the continuous adjoint method for flow-induced sound radiation with the Kirchhoff Integral is presented in this chapter for the first time in the literature. To predict the near- and far-field sound radiation from a body in free-stream, an incompressible flow computation with IDDES is performed, to resolve the noise creation phenomena, followed by the sound pressure propagation with the Kirchhoff Integral method, which uses the hydrodynamic pressure and its time derivative computed on the Kirchhoff surface, coinciding with the body's boundary.

Furthermore, in the primal unsteady simulations, two time windows are commonly defined; T_s, where the flow equations are solved and T_{of}, placed at the end of T_s, where the objective function is evaluated. Their distinction was taken into account in the adjoint development and the derivation of the sensitivity derivative expression. Chapter 5 sheds light upon their influence on the SD and the optimization solution.

In order to take the impact of interior grid node displacement into account, grid displacement models were incorporated in the mathematical development. This gave rise to the adjoint grid displacement equations (aGDE) as well as a Grid Sensitivity (GS) term. Two different displacement models were considered; the first model is based on volumetric B-Splines to displace the geometry and the interior grid nodes whereas the second uses the Laplace equations to propagate an already computed geometry displacement into the grid interior. The former results in an algebraic adjoint grid displacement equation, similar to the primal one, and in a field integral SD term. In this case, the computation of the aGDE and the GS term are performed in a straightforward manner, since grid sensitivities are computed analytically with the volumetric B-Splines model. However, since the GS term is a field term, the visualization of the grid sensitivities with a sensitivity map is not possible. On the other hand, the Laplace model results in an Poisson aGDE. The GS term is expressed at the parameterized surface so this approach proved to be advantageous for various investigations that followed in the thesis. The significance of the GS term in the SD expression is demonstrated in chapter 5.

Chapter 5

Continuous Adjoint Formulation for Flow-Induced Sound Radiation - Applications

This chapter focuses on the implementation, verification and application of the continuous adjoint method for flow-induced noise radiation, developed in chapter 4. The primal analysis utilizes an IDDES of the external flow and the Kirchhoff Integral (KI) acoustic analogy to propagate noise from a radiating body to a specified set of receivers. The adjoint method includes the differentiated Kirchhoff Integral and the unsteady adjoint Navier-Stokes equations.

Firstly, the implementation of the KI method is presented. In order to take adjoint requirements into account, such as storing the primal acoustic pressure, the original KI code used in [68] is significantly enhanced. A few practical issues are also discussed to facilitate the development of similar approaches in the future.

The verification of adjoint gradients is typically performed by comparing the computed values with the ones computed with a Finite Differences (FD) scheme. For unsteady turbulent flows, this process may be dubious due to the fact that the convergence of the FD gradients is not always guaranted [145]. In fact, the longer the simulation/integration time windows are and the more turbulent the flow is (thus increasing its chaotic nature) the more difficult is to compute converged and, thus, accurate FD. Therefore, a simpler test case is selected to verify the accuracy of the proposed method that investigates the turbulent flow around a 3D cylinder. The accuracy of the adjoint gradients of the two objective functions defined in chapter 4, targeting at minimum pressure fluctuations on the radiating body and at minimum radiated pressure at the receivers, is demonstrated in section 5.2.

In section 5.3, the method is applied to optimize the shape of the side mirror the SAE body w.r.t. the sound radiation to the vehicle's side window. Firstly, a sensitivity map analysis is conducted to investigate the influence the sensitivity derivative integration time window has on its computation but, also, to prove the importance of including the adjoint grid displacement equations. Afterwards, an

optimization of the side mirror is performed, targeting at minimizing the radiated flow-induced sound at a number of receivers on the vehicle's side window, which is associated to the cabin noise level [68].

5.1 Implementation

This section describes some practical issues of the Kirchhoff Integral (KI) algorithm, as well as the unsteady adjoint solution.

5.1.1 Kirchhoff Integral Method

The KI solver and its adjoint were programmed as a stand-alone library in the OpenFOAM© environment, are version independent and can be practically used with any CFD solver, provided there is an interface to read the pressure input.

Different approaches have been proposed in the literature on the algorithmic implementation for aspects such as retarted-/forward-time or memory handling, [88]. In this thesis, the KI algorithm is developed by taking the requirements of the adjoint/differentiated KI into consideration. Among other processes, the following variables must be computed requiring a time stencil of several time steps: pressure time derivative, acoustic pressure, acoustic pressure fluctuation and its time derivative and the multipliers for the adjoint sensitivities. Storing all the necessary variables to memory and performing the aforementioned computations modularly, after the CFD simulation is finished, deemed to be advantageous compared to an in situ computation. The complexity of the algorithm highly increases when so many computations must be performed on-the-fly and makes the algorithm less versatile to future enhancements, such as the filtering process described in 7.

In order to deal with the excessive memory load, the coordinates as well as the computed field values at both the sources and receivers are distributed to all processors. It should be made clear that the KI kernel does not utilize the same grid decomposition as the CFD solver but distributes evenly the stored values to all available processors. Therefore, in this section the process of "distributing" concerns the gathering of all information from the CFD decomposition to the master processor and, then, scattering it to the processors based on the KI decomposition.

For the primal KI, eq. 2.15 is computed, which requires the pressure field and its time derivative on the radiating body. During the primal solution, the surface hydrodynamic pressure, p, is distributed over all processors and stored. After the flow simulation has ended, the pressure field is used to compute the time derivative with an 8^{th} order central differences scheme. In this thesis' applications, the number of sources greatly exceeds the number of receivers, therefore

the sources are distributed over all processors. This has no impact on the computational time, as it is constant regardless of distributing the receivers or the sources. However, in terms of memory, distributing the sources leads to less memory load per processor.

At this point, all necesssary fields, p and $\partial p/\partial t$, are computed and distributed to all processors. As seen in fig. 5.1, a forward-time approach is used to compute the KI, which computes the contribution of all sources at a CFD iteration (time step) to p_{ac} of all receivers at corresponding future time instants. The KI algorithm marches through the source time steps (practically the CFD time steps) and for each source-receiver pair computes the forward time that the sound waves have reached the receiver. This time does not necessarily coincide with any of the receiver's time steps and is, thus, linearly interpolated to its adjacent time steps.

The computation of p_{ac} at a receiver at a time instant t requires the sum of the contribution from all sources, which stems from different time steps in the past; the time that a sound wave needs to reach from the source to the receiver depends on their distance, $\tau = r_i/a_0$. Therefore, the complete computation of p_{ac} at t lasts for a specific number of time steps which is determined by the difference of the longest ($t_{max}/\Delta t$) and the shortest ($t_{min}/\Delta t$) time between the receiver and the sources, defined by the longest and shortest distances respectively. If more than one receivers are examined, this time window is practically the range between the minimum t_{min} and the maximum t_{max}. When the simulation reaches the time instant $t-t_{min}+\Delta t$, the computation of p_{ac} at all receivers for t is completed and p_{ac} can be distributed to all processors in order to reduce the memory requirements per processor.

The adjoint KI algorithm, fig. 5.2, follows the same exact procedure only that the contributions are from the receivers to the sources. Marching through the source time steps, the future time instants are found where the source had contributed to the receivers, during the primal KI computations. Then, the contribution of the adjoint acoustic pressure at the affected receivers is added to the sources.

5.1.2 Unsteady Primal & Adjoint Navier-Stokes

The primal and adjoint flow simulations are performed in the OpenFOAM© environment. The flow equations are solved using the standard transient incompressible solver *pisoFoam*. A blending convection scheme is utilized [132] which based on wall distance, velocity gradient and eddy viscosity, switches between a low-dissipative linear scheme in the vorticity dominated LES (finely resolved) regions and a numerically robust upwind-biased scheme in irrotational and RANS (coarsely-resolved) regions.

The adjoint equations are solved with an in-house adjoint solver using the PISO algorithm with two outer correction iterations when needed,to better converge the

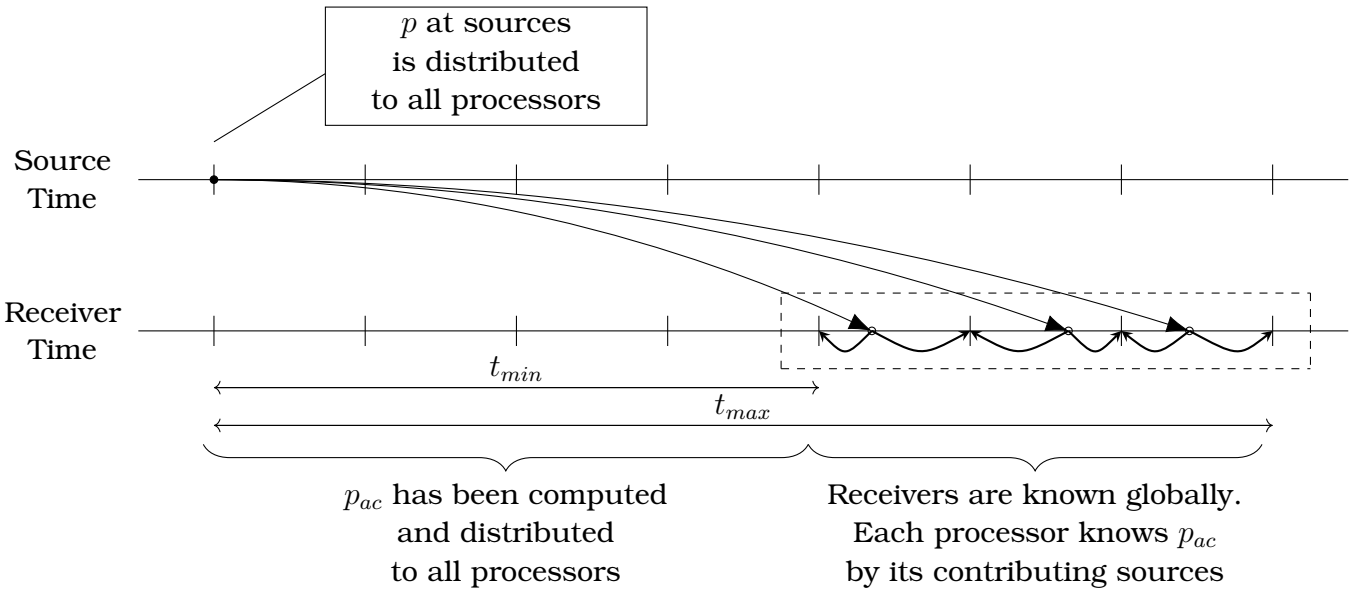

Figure 5.1: Forward-time computation of the KI between one source and one receiver. In dashed boxes is the time stencil where the acoustic pressure of all receivers are known by all processors. In other time steps, this information is evenly distributed among all processors.

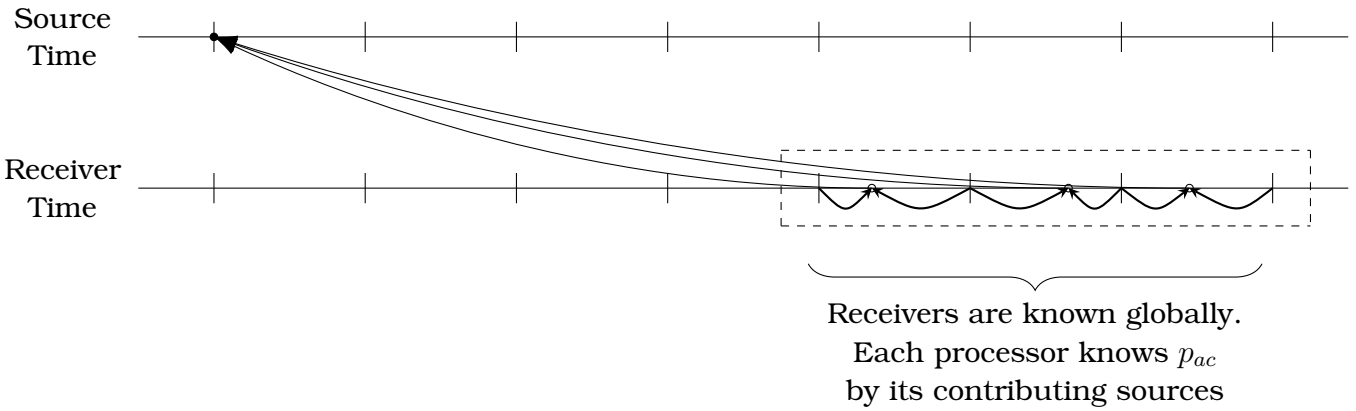

Figure 5.2: Backward-time computation of the adjoint KI between one receiver and one source. The information distribution among the processors follows the rules of the primal KI computation.

adjoint momentum equations. For the convection term in the adjoint solution, a second-order downwind scheme is used. In case of convergence instabilities that usually occur in industrial applications, a first-order scheme is used for the convection term and a dissipative limited scheme for the spatial gradient discretization of the so-called Adjoint Transposed Convection term, $u_j \frac{\partial v_j}{\partial x_i}$, in the adjoint momentum equation, eq. 4.23 .

As seen in eq. 4.23 , the instantaneous primal velocities are needed for the backward time integration of the adjoint solution. Since storing all time steps requires a great amount of memory, the binomial checkpointing technique is used [139], where only a set of time steps, the so-called checkpoints, is stored. During the adjoint solution, if the primal flow fields are not available, the primal equations are solved again starting from the latest stored checkpoint. The recomputation time depends on the number of checkpoints and the total iterations. In this thesis, 60 checkpoints are used for the SAE Body where a total of 58800 time steps are simulated, leading to an additional recomputation cost of 2.3 times the cost of a complete unsteady primal computation, during the adjoint solution.

5.2 Verification

The accuracy of the computed sensitivity derivatives with the adjoint method presented in this chapter is verified here against gradients computed with FD. In this section, an additional test case is considered that investigates the 3D turbulent flow around a cylinder. As explained later, this is to ensure the accuracy of the FD gradients, since they are prone to numerical errors for large time integrations of turbulent/chaotic flows. The mesh independency study for this test case as well as its setup is presented in appendix A.

The differentiation of the Kichhoff Integral is firstly tested, verifying the geometric sensitivities, the constituent terms of $\frac{\delta J_{KI}}{\delta b_n}$, eq. 4.56 , that do not include the derivative $\delta p / \delta b_n$. To do so, the flow fields computed for each test case are kept "frozen" during the investigation and, therefore, $\delta p / \delta b_n = 0$. Afterwards, the adjoint derivatives for flow problems are considered.

5.2.1 Kirchhoff Integral - Geometric Sensitivities

5.2.1.1 3D Cylinder - Verification with Finite Differences

The first test case examines the sound radiation from the flow around an isolated 3D cylinder, and uses the KI to propagate the noise from the unsteady pressure distribution on the cylinder to 120 receivers placed at 15D distance on the z-Plane crossing the middle of the cylinder, fig. 5.3.

The pressure distribution on the cylinder over a period of $T = 10s$ is stored and used for the KI computation. The flow field is considered frozen and independent of the cylinder's geometry during the optimization, thus $\delta p/\delta b_n = 0$, and the fifth integral on the r.h.s. of eq. 4.56 vanishes.

The cylinder surface is morphed using volumetric B-Splines, [113]. A set of 8 control points around the cylinder is selected, as shown in fig. 5.3, and the design variables are the x- and y- coordinates of each control point, thus 16 in total.

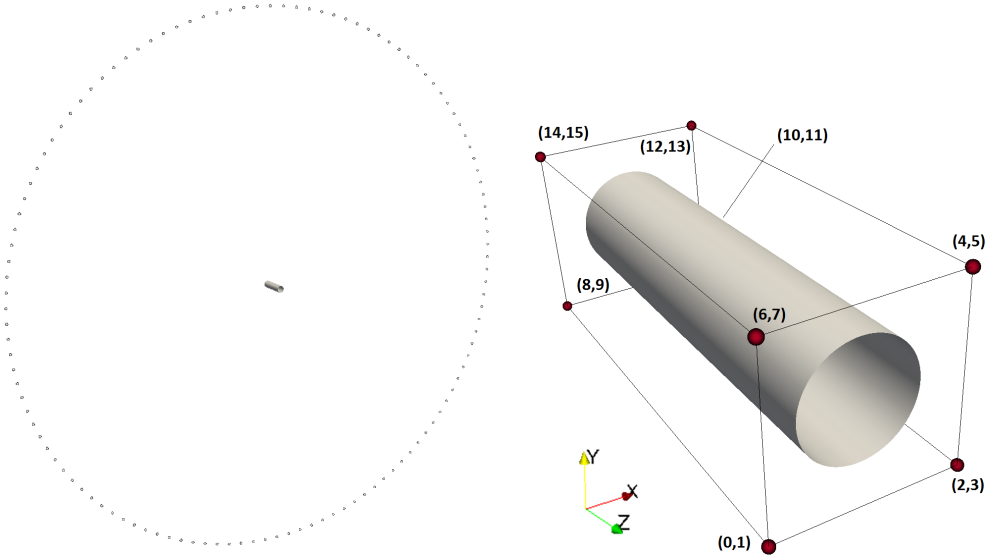

Figure 5.3: 3D Cylinder - Verification with FD: Distribution of 120 receivers around the cylinder (left). The volumetric B-Splines control points (right) deform the cylinder's surface for the FD verification.

The derivatives of eq. 4.50 at the receivers w.r.t. b_n are computed with central differences, where a step size equal to $10^{-6}D$ is chosen, after conducting a study on independence of the step size. For each perturbation, the cylinder geometry is modified by the morpher and, afterwards, keeping the same unsteady distribution, the sound radiation from the updated geometry is evaluated.

The gradients of J_{KI} are also computed with the expression of the differentiated KI, eq. 4.56, and the comparison with the FD gradient is presented in fig. 5.4 showing an excellent agreement. In addition, the SD is decomposed in its different components, where term $\frac{\partial J_{KI}}{\partial x_i}\frac{\delta x_i}{\delta b_n}$ is denoted as *dJdx*, term $\frac{\partial J_{KI}}{\partial p}\left(\frac{\partial p}{\partial x_i}+\frac{\partial p}{\partial t}\frac{\partial \tau}{\partial x_i}\right)\frac{\delta x_i}{\delta b_n}$ as *dJdp* and the one including $\frac{\delta(n_i dS)}{\delta b_n}$ as *dndSdb*. The latter is the most important term in this test case.

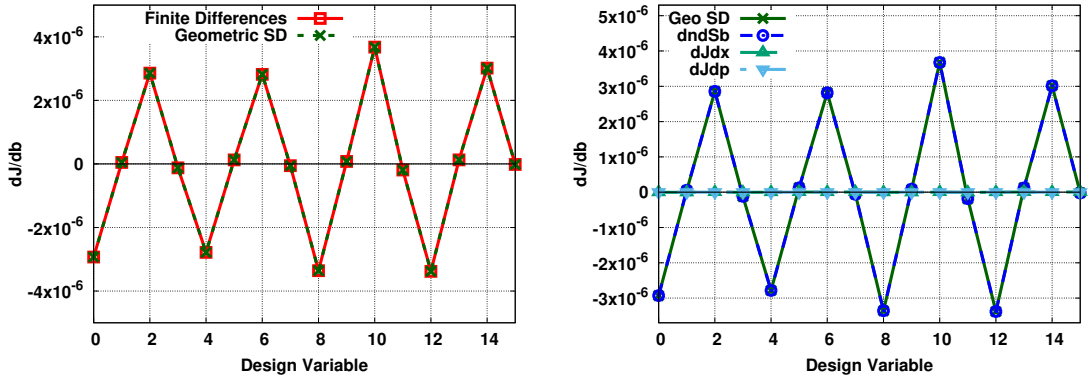

Figure 5.4: 3D Cylinder - Verification with FD: Comparison of the geometric sensitivities of J_{KI} computed with FD and the adjoint method (left). The contribution of each term of eq. 4.56 is shown on the right.

5.2.1.2 3D Cylinder - "Frozen Flow" Optimization

In this section, an optimization is performed on the cylinder, during which the flow is kept "frozen", as described in section 5.2.1.1. In order to allow for greater surface deformations, a new parameterization is used where 9 control points on the z-plane crossing the cylinder middle are allowed to vary, as shown in fig. 5.5.

Using steepest descent with a fixed step in each optimization cycle, the sound radiation of the cylinder at the receivers is completely suppressed, fig. 5.5. Of course, this does not mean that there is no radiation at all; as seen in the history of the cylinder surface during the optimization, fig. 5.6, the new shape has most of its face normals at a near-right angle with the z-plane where the receivers are placed, so that the directivity towards the receivers (term $\hat{r}_i \hat{n}_i$ in eq. 2.15) is set to zero.

5.2.1.3 SAE Body - Verification with Finite Differences

The approach of section 5.2.1.1 is followed to verify the geometric sensitivities on the SAE Body. The unsteady pressure distribution on the mirror is computed with the IDDES methodology, as discussed in chapter 2 and in section 5.1 and then stored for the study that follows.

A set of volumetric B-Splines control points are placed around the neck of the mirror which is the most sensitive region for aeroacoustics, as presented in section 5.3. In total 75 control points are used, as shown in fig. 5.7, $5 \times 3 \times 5$ in the x-, y- and z-direction, respectively, and only the internal ones are allowed to move in x- and z- direction, giving rise to 18 design variables.

The receivers are distributed uniformly on the side window on a structured grid of 1 cm, not coinciding with the CFD surface grid nodes, leading to a total number of 10000.

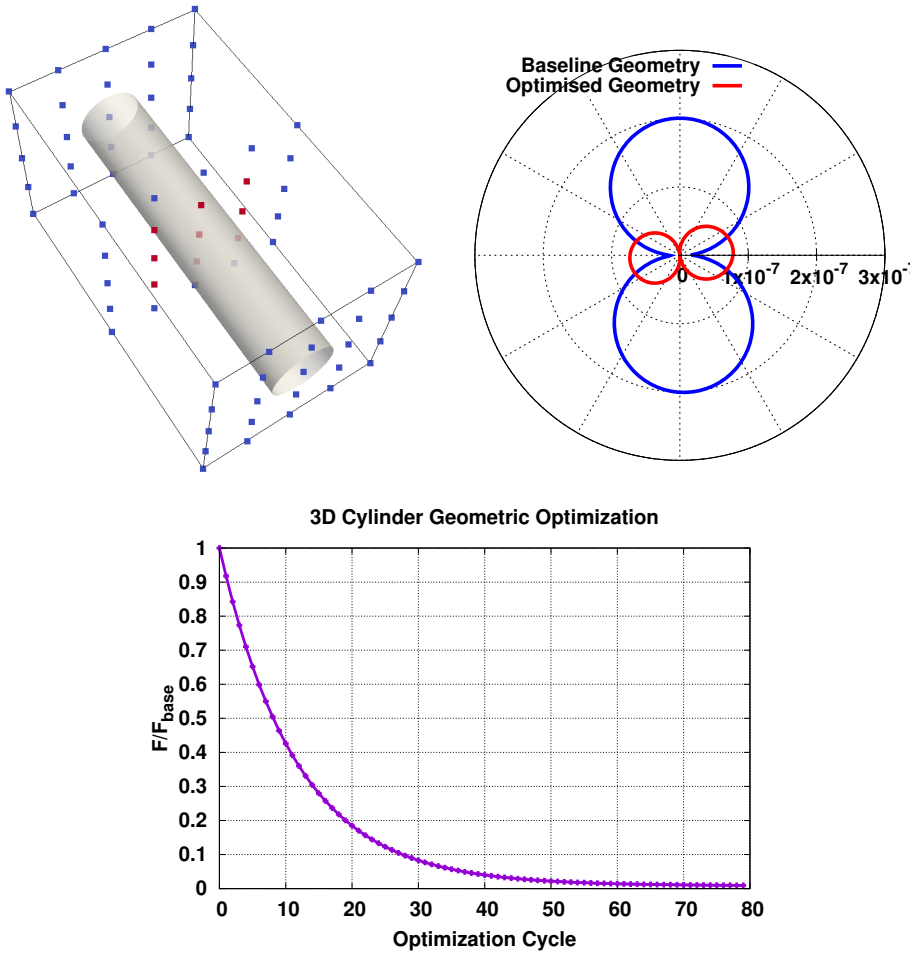

Figure 5.5: 3D cylinder optimization with fixed (frozen) flow: a 5×5×3 control box parameterizes the cylinder surface (top-left), where only interior control points (red squares) are allowed to vary during the optimization. The directivity (top-right) for the baseline (blue) and optimal (red) geometry is also presented. The optimization algorithm converged after around 82 optimization cycles (bottom).

The gradient of J_{KI} w.r.t. the design variables is computed firstly with a central FD scheme, and afterwards with eq. 4.55. The two methods are in excellent agreement, as depicted in fig. 5.8. In this case, both the variation of the normal component and area of each element as well as $\frac{\partial J_{KI}}{\partial x_i}\frac{\delta x_i}{\delta b_n}$ are significantly contributing to the gradient value.

5.2.1.4 SAE Body - "Frozen Flow" Optimization

Here, an optimization is performed to find the shape of the mirror that radiates less noise to the side window, assuming that the sound sources are fixed (recall that

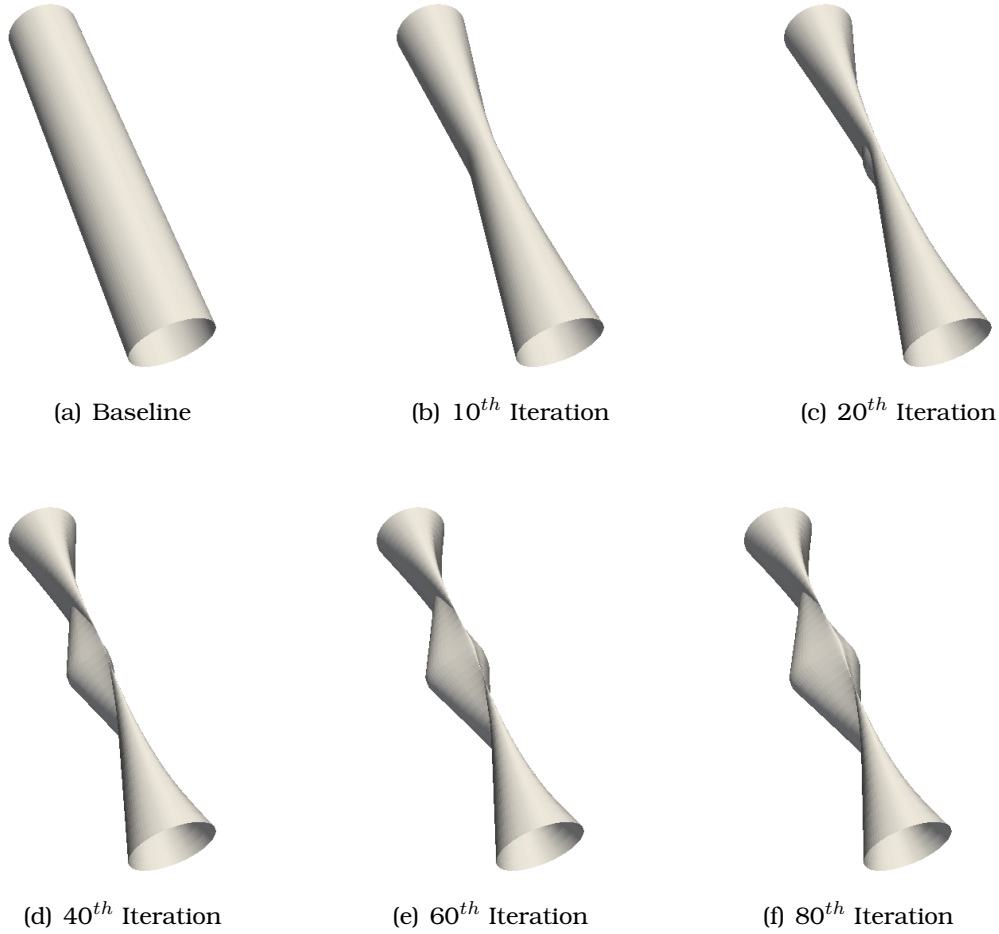

(a) Baseline (b) 10^{th} Iteration (c) 20^{th} Iteration

(d) 40^{th} Iteration (e) 60^{th} Iteration (f) 80^{th} Iteration

Figure 5.6: 3D cylinder optimization with fixed (frozen) flow: Shape of the cylinder for several optimization steps.

the unsteady pressure distribution remains "frozen" throught the optimization). The same volumetric B-Splines control box is used for the mirror parameterization, however, more points are used this time, $8 \times 4 \times 8$ in x-, y- and z- direction respectively, as shown in fig. 5.9.

After 19 optimization cycles, the objective function is reduced by around 20% and the optimization is terminated because the mirror shape quality deteriorated as seen in fig. 5.10. It must be noted however that this reduction does not represent the actual one, if flow changes were taken into consideration and the sources on the mirror were recomputed for each updated geometry. In fact, the flow field of the geometry of the 1^{st} optimization cycle is evaluated again and yielded 1.4% increase in J_{KI}.

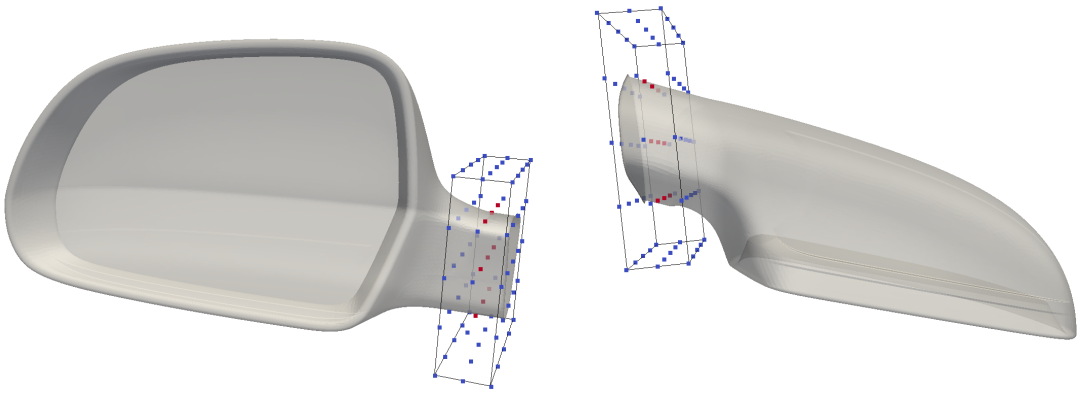

Figure 5.7: SAE Body - Verification with FD: a 5×3×5 control box parameterizes the mirror surface and the derivative of the interior control points (red squares) w.r.t. their x- and z coordinates are compared with FD.

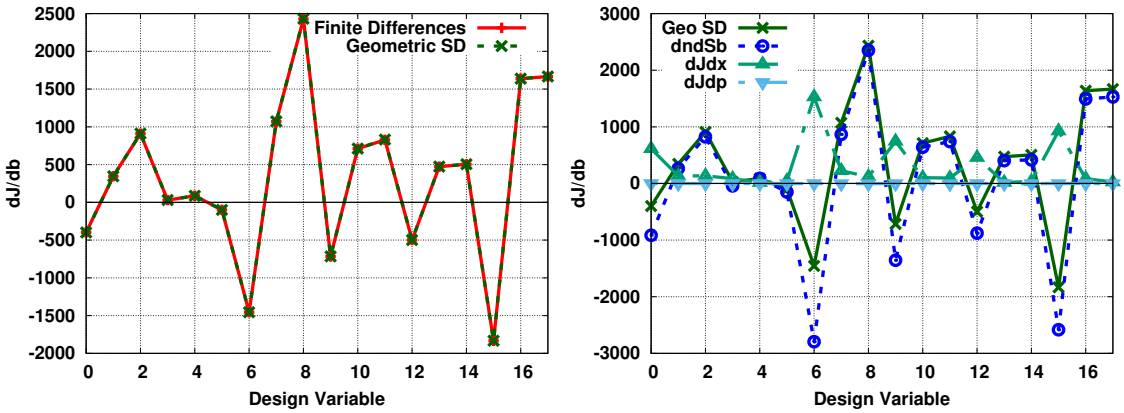

Figure 5.8: SAE Body - Verification with FD: Comparison of the geometric sensitivities of J_{KI} computed with FD and the adjoint method (left). The contribution of each term of eq. 4.55 is shown on the right.

5.2.2 Unsteady Adjoint Flow Sensitivities

This section verifies the accuracy of the adjoint flow derivatives computed with the proposed method. For the unsteady adjoint method, as the integration time of J increases, the accuracy of the FD derivatives deteriorates, often to the order of the sensitivity itself, due to round-off errors [145]. In addition, for complex industrial cases, such as the SAE body, the values of the FD gradients do not converge as the step size decreases. Therefore, to make FD as accurate as possible, the verification is conducted for the 3D turbulent flow around the cylinder.

Two objective function are investigated targeting at pressure fluctuations minimization, eq. 4.46 computed over the cylinder's surface, and radiated acoustic pressure minimization, eq. 4.50 computed at the 120 receivers around the cylin-

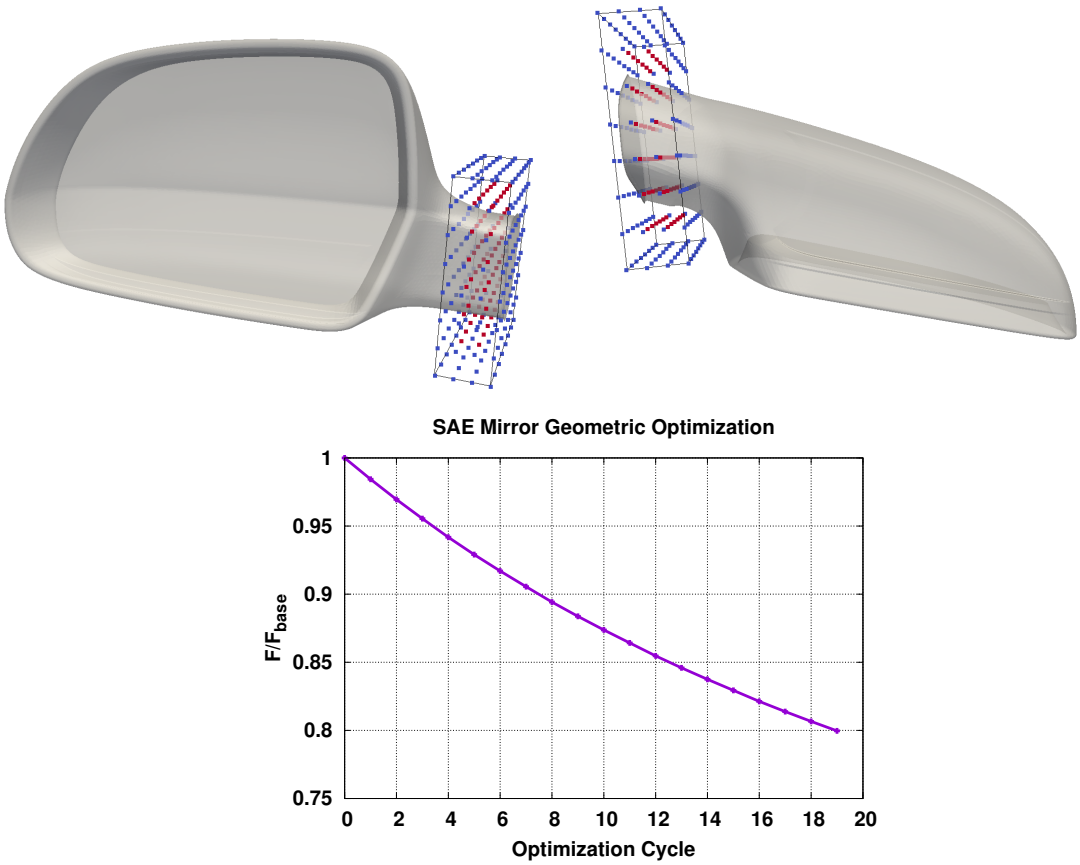

Figure 5.9: Optimization of the SAE mirror with fixed (frozen) flow: A set of volumetric-Splines control points is defined around the neck of the mirror (top) and only interior points (red squares) are allowed to vary during the optimization. The optimization terminates after 19 optimization cycles, as the mirror geometry's quality started deteriorating.

der defined previously, (section 5.2.1.1, fig. 5.3). The primal procedure computes the flow for $T_s = 10s$, starting from a stored initial condition of a flow field with fully developed vortex shedding. The corresponding objective function is integrated over the same time window, thus $T_{of} = T_s = 10s$.

To modify the cylinder surface, the volumetric B-Splines control points presented in section 5.2.1.1 are used and their x and y coordinates are the design variables b_n, as shown in fig. 5.3. The derivatives of the objective function w.r.t. b_n are computed with central differences, where a step size equal to $10^{-6}D$ is chosen, after conducting a study on independence of the step size. For each perturbation, the cylinder geometry is modified by the morpher and, afterwards, these displacements are propagated into the interior of the grid either with the volumetric B-Splines morpher, eq. 4.7 , or by solving the Laplace equations, eqs. 4.8 . Then, the objective function is computed again, leading to two sets of derivatives

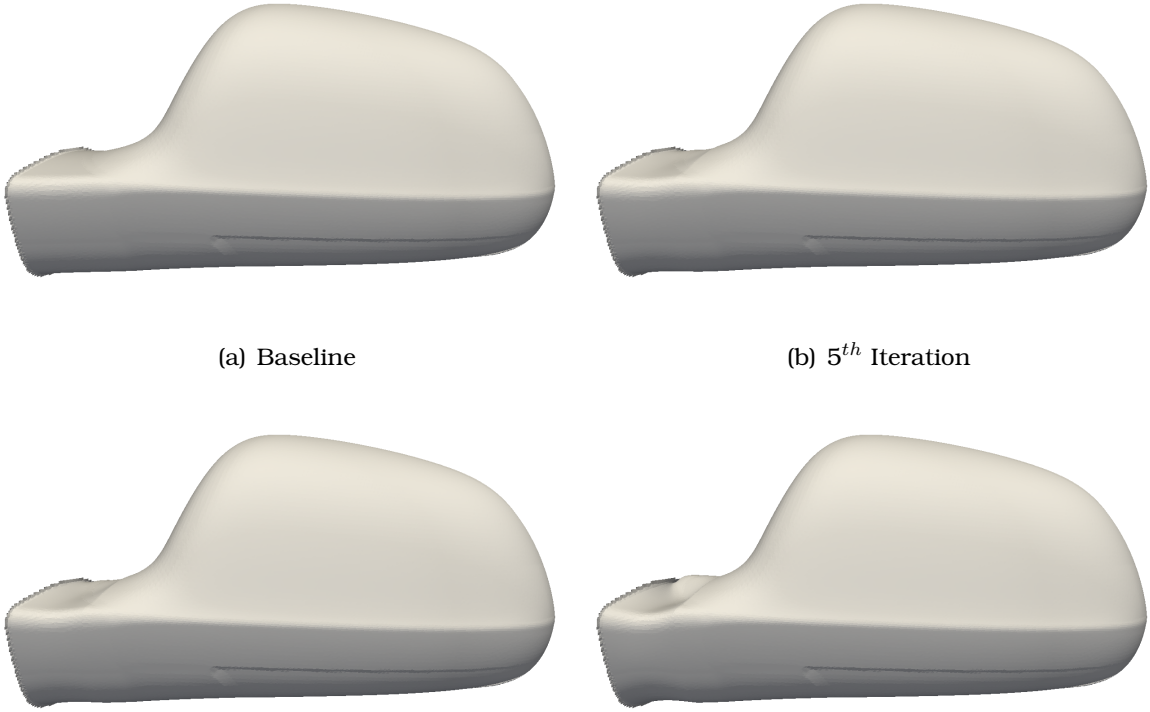

(a) Baseline

(b) 5^{th} Iteration

(c) 10^{th} Iteration

(d) 15^{th} Iteration

Figure 5.10: Optimization of the SAE mirror with fixed (frozen) flow: Shape of the cylinder during the optimization, which is terminated after 19 optimization cycles, as the mirror geometry's quality started deteriorating.

per objective function in total. It should be noted that, depending on the mesh resolution, the two grid displacement methods should converge to the same value of gradient, since the impact of interior nodes on the derivative of the objective function reduces.

The developed adjoint method is used to obtain the sensitivities of J_{pfluc} and J_{KI} w.r.t. b_n, and the grid sensitivities are computed using eqs. 4.40 and 4.41 and eqs. 4.44 and 4.45. A snapshot of the adjoint flow targeting at minimizing J_{KI} is presented in fig. 5.11.

In figs. 5.12 and 5.13, the sensitivity derivatives values for J_{pfluc} and J_{KI} respectively computed with FD are plotted against the ones computed with the adjoint method. Firstly, it is clear that the adjoint gradients are in a very good agreement with FD. To emphasize the importance of the grid sensitivities, the SD without the corresponding term is also plotted and it is observed that the accuracy of the SD strongly deteriorates.

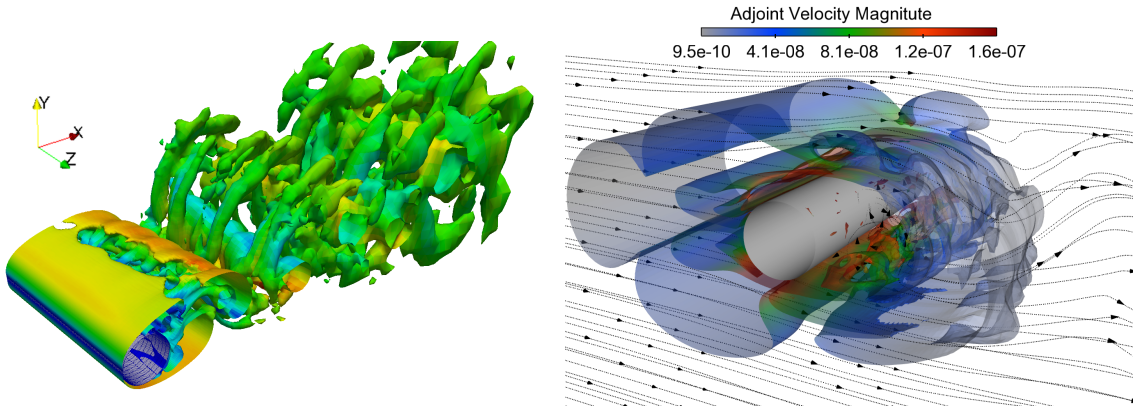

Figure 5.11: Turbulent flow around a 3D cylinder for Re=500. Left: Instantaneous flow structure visualized by the isosurface of $Q = \frac{1}{8}\left(\|\nabla v - (\nabla v)^T\|^2 - \|\nabla v + (\nabla v)^T\|^2\right) = 10^{-1}s^{-2}$ and colored according to the velocity magnitude. Right: Adjoint vorticity iso-surfaces colored by the adjoint velocity magnitude (s^{-3}). Black lines are the primal velocity streamlines.

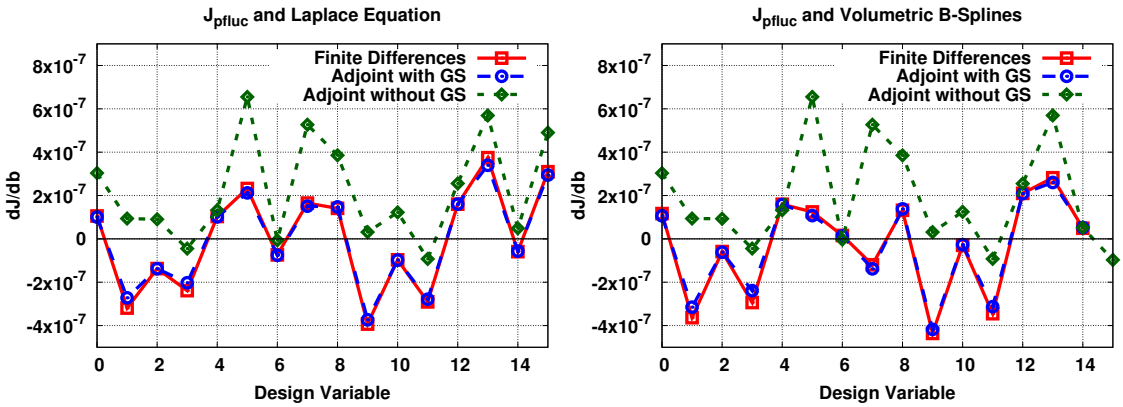

Figure 5.12: Turbulent flow around a 3D cylinder for Re=500: Comparison of the derivative of J_{pfluc} computed with FD and the adjoint method using the Laplace equation (left) and the volumetric B-Splines (right) as a grid displacement model. In both cases, it seen that neglecting the grid sensitivities term (GD) is detrimental to the accuracy of the sensitivity derivatives.

5.3 Applications

In this section, the proposed adjoint-based optimization is applied to minimize the flow-induced sound radiation from the side mirror of the SAE body, presented in chapter 2, to the vehicle's side window. Cabin noise is related to the acoustic load on the window, so its minimization is a first step towards interior noise reduction.

The KI is computed over the mirror surface, and its accuracy relies solely on that of the pressure predicted over the surface. For this reason, the grid in this

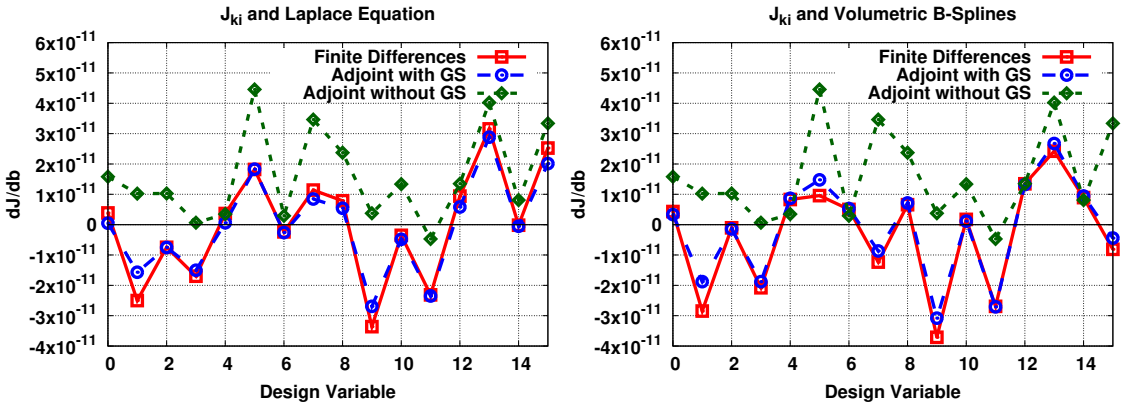

Figure 5.13: Turbulent flow around a 3D cylinder for Re=500: Comparison of the derivative of J_{KI} computed with FD and the adjoint method using the Laplace equation (left) and the volumetric B-Splines (right) as a grid displacement model.

region as well as in areas that strongly affect the flow around the mirror, such as the A-pillar region, is fine enough to resolve the vortex structures and capture possible flow separations.

The unstructured computational grid used in this thesis, fig. 5.14, is generated with the snappyHexMesh tool of OpenFOAM© and comprises around 80 million cells, with a grid resolution of 1mm on and around the mirror that results in 120000 faces-senders on the mirror surface. In addition, 15 layers are used within the first 3mm, yielding an average $y+$ of the first cell center off the wall of around 1. 10000 receivers on the window are distributed uniformly on a structured surface grid of 1 cm, which does not coincide with the CFD surface grid nodes.

The flow computation with IDDES is performed for a total of $T_s = 1.3s$; the first $0.9s$ is the initial transient phase and this is why a bigger time step is used compared to the remaining simulation, $\Delta t = 5 \times 10^{-5}$ instead of $\Delta t = 2 \times 10^{-5}$; the flow-induced noise radiation from the mirror is then assessed starting at $t_{of} = 1s$, for $T_{of} = 0.3s$.

The A-pillar vortex and the mirror wake at a flow velocity of 40 m/s, computed numerically, are shown in fig. 5.15 (bottom-left). The interaction of these two typical vehicle flow structures leads to strong pressure fluctuation on the mirror and, consequently, noise generation and radiation to all directions and towards the vehicle side window, fig. 5.15 (bottom-right).

5.3.1 On the time integration of the unsteady adjoint problem

Flow-induced noise from the side mirror is computed according to the aforementioned procedure. According to the mathematical formulation presented in section 4.3, the adjoint problem must be solved for the time window of the primal simu-

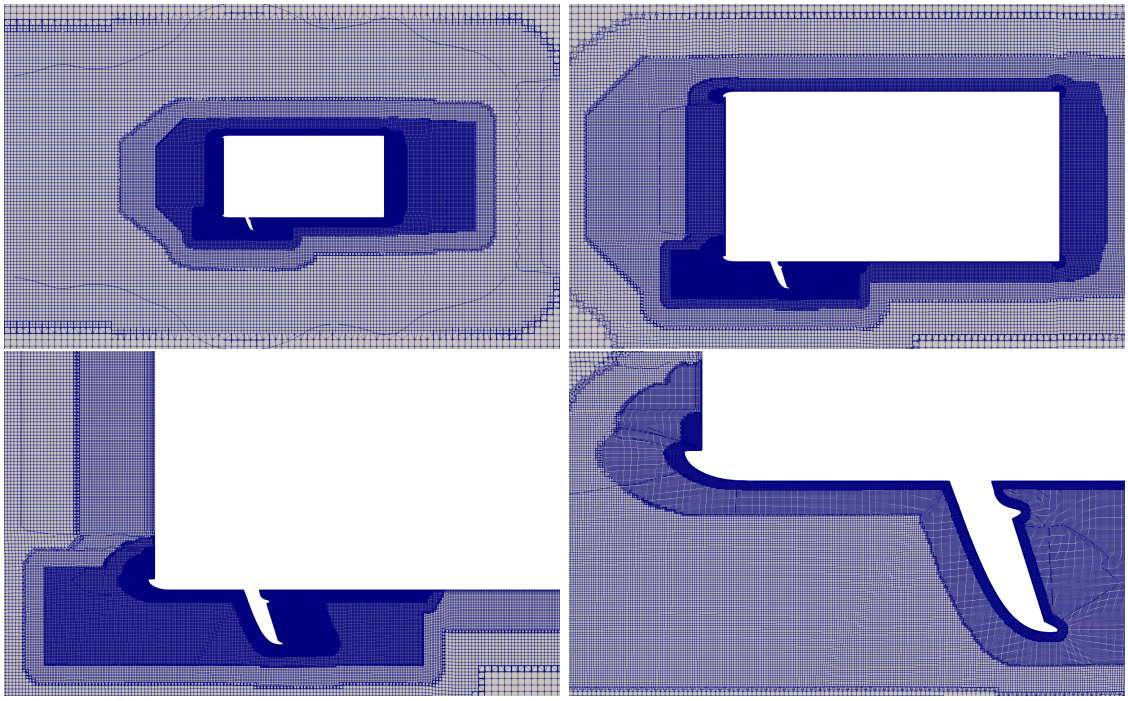

Figure 5.14: Computational grid for the exterior domain of the SAE Body: different refinement layers around the car and the mirror at cross-section plane normal to the z-axis. The finest resolution is $1mm$ in the region around the side mirror.

lation T_s, in conformity to the time integrals in eq. 6.1 during which the residuals of the unsteady equations are satisfied. As shown in fig. 5.16, the boundary condition of eq. 4.58 is acting only on T_{of}. This means that, as the adjoint is solved backwards in time, the source in the adjoint equations takes non-zero values only until $t = t_{of}$ and is set to zero afterwards; thus, the adjoint fields start decaying until the end of the adjoint simulation, $t = 0s$. This is depicted in fig. 5.17, where the adjoint flow statistics of a simulation performed over T_s, later referred to as approach A, is presented.

5.3.2 Sensitivity map analysis

A sensitivity map analysis is performed here to compare the approach for tackling the unsteady adjoint problem proposed in section 4.3 with a different approach, which appears intuitively to be equivalent. The computed sensitivity map on the side mirror of the SAE body stands for the derivatives of the objective function w.r.t. the normal surface displacement, eq. 4.59 with $\frac{\delta x_i}{\delta b_n} = n_i$, and gives insight into the local geometry changes that may contribute to performance improvement.

The two approaches examined are summarized below:

- *Approach A* computes the primal flow for a total of $T_s = 1.3s$ and integrates

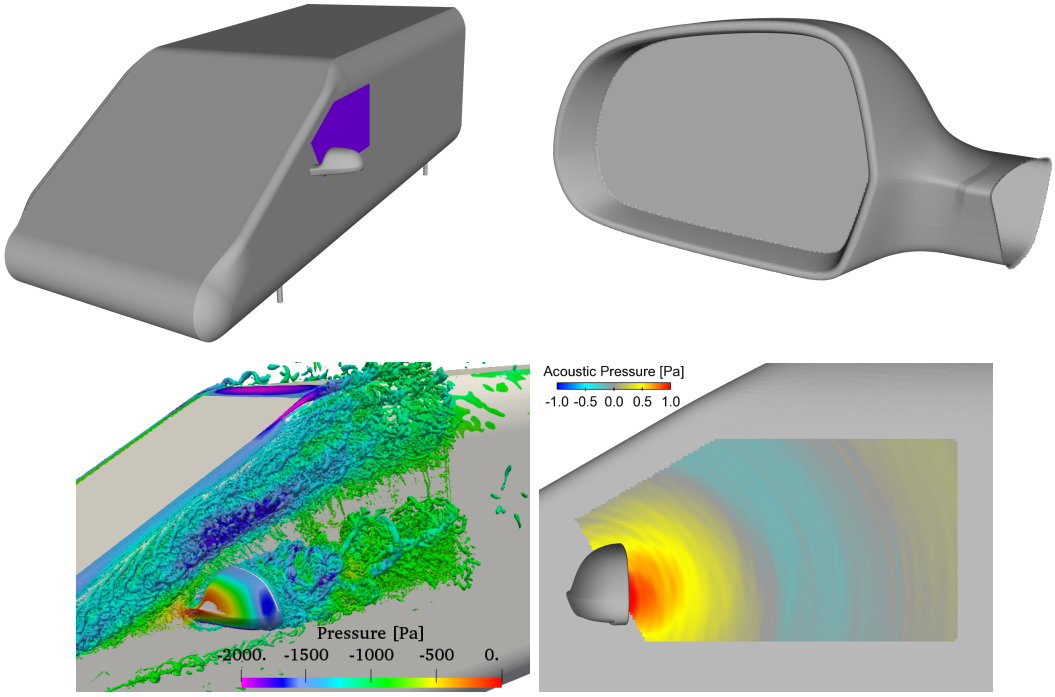

Figure 5.15: Geometry of the SAE body and numerical simulation of the flow-induced sound radiation: The CAE model of the SAE body and the tested mirror are shown. The area marked in purple is the vehicle's side window, where 10000 receivers are placed and the radiated acoustic pressure is numerically computed. The unsteady flow is computed with an IDDES and the instantaneous flow structure visualized by the isosurface of $Q = \frac{1}{8}\left(\|\nabla v - (\nabla v)^T\|^2 - \|\nabla v + (\nabla v)^T\|^2\right) = 5 \cdot 10^5 s^{-2}$ and colored according to the velocity magnitude is presented (bottom-left). The radiated acoustic pressure at the receivers lying over the window is computed using the Kirchhoff Integral method (bottom-right).

the objective function for the last $T_{of} = 0.3s$ of T_s. The adjoint equations are then solved for $T_s = 1.3s$ and the adjoint velocity boundary condition along the side mirror is given by eq. 4.58 only during the first $T_{of} = 0.3s$ of the adjoint simulation; afterwards, this is set to zero until the end of the simulation. Time integrals of eqs. 4.59 , 4.44 and 4.45 are computed at the time windows marked in the provided formulas.

- *Approach B*, starting from $t = t_{of} = 1s$, computes the primal flow and J for the remaining time, $T_{of} = 0.3s$. The objective function value computed in the first optimization cycle is obviously the same as in approach A. However, the adjoint solution and the sensitivity derivative terms are computed only over T_{of}. This is consistent with the adjoint velocity boundary condition, eq. 4.58 , as long as the initial field of each primal simulation during the optimization

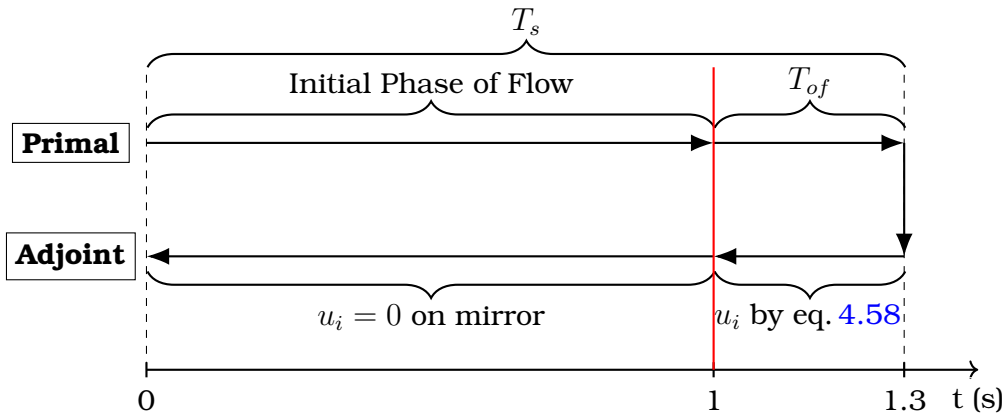

Figure 5.16: Time windows of primal and adjoint analysis. The sensitivity derivatives, eq. 4.59, are integrated during the solution of the adjoint equations for the corresponding time window in which each time integral is defined.

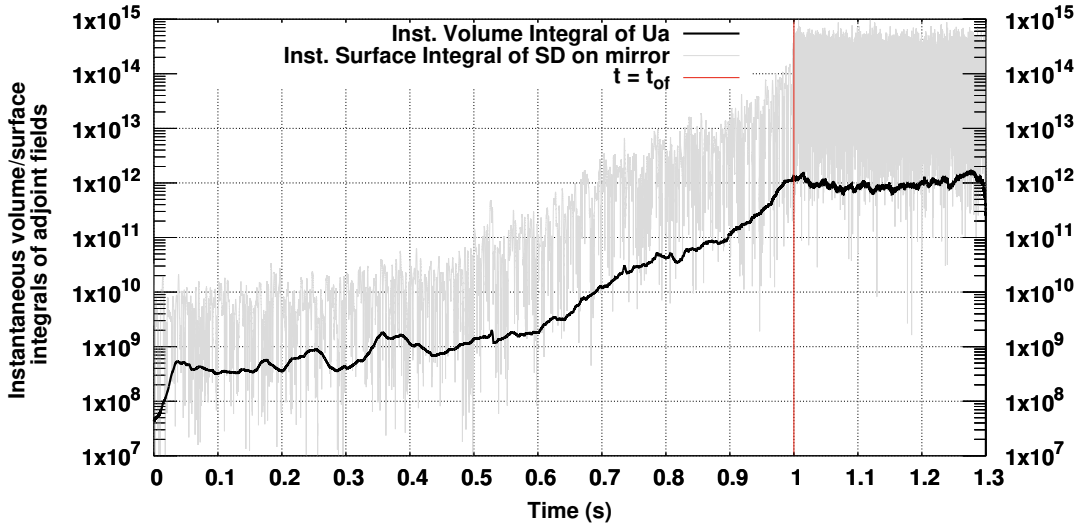

Figure 5.17: Adjoint flow statistics for flow-induced sound reduction on the SAE body: The time integration of J starts at $t_{of} = 1s$ (red vertical line) and is performed over the last $T_{of} = 0.3s$. The sum of the first two instantaneous surface integrals of eq. 4.59 (*SD*) is an indication of the impact this time step has on the objective function variation. As expected, J is influenced mostly by time instants belonging to T_{of}, after which the order of magnitude drops significantly.

is kept the same and, thus, independent of the design variables, so that $\delta v_i / \delta b_n \big|_{t_{start}} = 0$.

The total wall-clock time for the sensitivity derivatives computation was around $145hrs$ and $71hrs$, for approaches A and B respectively, without accounting for the additional overhead for grid displacement and data management. The wall-

	Approach A	Approach B
Primal Flow	23.15	12.82
Kirchhoff Integral	0.28	0.25
Adjoint Kirchhoff Integral	0.56	0.58
Adjoint Incl. Primal Recomputations	120.49	57.20
Total Time	145.24	70.54

Table 5.1: Wall-clock time (in hours) of each step of the primal and adjoint procedure for approaches A and B: computations performed on 960 CPUs.

clock time cost for the individual parts of the primal and adjoint procedures is presented in detail in table 5.1.

The two aeroacoustic sensitivity maps computed with approaches A and B are shown in fig. 5.18(a) and fig. 5.18(b) respectively. For both approaches, two main sensitive areas appear, the mirror neck and the casing of the mirror glass. In fig. 5.19, two cross sections over these two areas are presented. High sensitivities can be seen on the downwind edges of both the upper and lower side of the neck. As seen in fig. 5.19(c), flow separation occurs in this area, which creates pressure fluctuations that in turn generate and radiate noise. Similarly, on the edges around the casing of the mirror glass, the flow is disturbed by the geometry curvature or specific design features, such as the small step on the underside of the mirror, fig. 5.19(d).

Although high sensitivity values appear on the same areas for both approaches, differences arise on the way the mirror surface should be displaced. More distinctly, on the upper side of the mirror neck, approach A suggests an outward displacement on the part up to the downwind edge, where the sign changes and this area should be pushed inwards. On the contrary, approach B is dominated by an inward displacement on the upper side, with a small area of outward normal displacement in between.

A morphing step was performed to show how this difference on the sensitivity maps translates to changes in the objective function. The mirror was parameterized using the volumetric B-Splines method, similarly to section 5.2. 256 control points, 8, 4 and 8 in the x-, y- and z-direction, respectively, are used to define the part of the mirror geometry to be morphed. As seen in fig. 5.20, the control box surrounds the neck of the mirror which is the area with the highest potential in improvement. The placement of the bounding box is acceptable from the design point of view as well, as areas important for rain water management, such as the mirror glass casing, are left intact. During the morphing, only the internal control points are allowed to move in all three directions, giving rise to 216 design variables in total and the maximum displacement of the surface was $1mm$.

The morphed geometries are presented in fig. 5.21 and the difference between the two approaches can be seen. The objective function for the two geometries was

evaluated again. The objective functions are reduced by 17% and 22% respectively, thus, in each respective optimization problem the geometry was displaced to the right direction. An additional primal run was performed using approach A for the morphed mirror of approach B. The obtained value yielded a reduced objective function by 11%, a smaller reduction than that observed with approach A. In fig. 5.22, the time-averaged squared acoustic pressure fluctuation radiated to the side window from the baseline and the two optimized mirror geometries is presented. This practically stands for the integrand of J_{KI}, eq. 4.50, plotted for each receiver on the side window and the reduction is indeed bigger for approach A.

Consequently, this study shows, through the comparison of the sensitivity maps, that Approach B does not guarantee that the correct optimization problem, as defined by the benchmark procedure (approach A), is solved. This would be the case, if the integration time of approach B was sufficiently long, which would require, however, an a-priori and case-dependent "trial and error" investigation.

In addition, the significance of the proposed method that includes the grid displacement in its formulation can also be clearly visualized in fig. 5.18(c). Similarly to section 5.2.2 and fig. 5.13, the sensitivity map computed based on the formulation without the grid sensitivities term in the sensitivity derivatives expression is presented. According to this map, an additional area on the top part of the mirror neck must be pushed inwards. These sensitivities guide in fact the optimization to the opposite direction, compared to the one that improved the objective function, as shown in the one-step displacement of fig. 5.21(a).

5.3.3 Optimization of the Side Mirror of the SAE Vehicle Targeting at Minimizing Acoustic Pressure at the Window

The side mirror of the SAE body, is optimized in this section, using approach A, as presented in section 5.3.2. Memory requirements of the individual parts for each optimization cycle are presented in fig. 5.23. After the computation of the derivatives of J w.r.t. the control points, their coordinates are updated and the geometry and internal grid are morphed.

Three optimization cycles are performed with an approximate cost of 20 days on 960 CPUs. After this, the optimization process is terminated, since another cycle would exceed the allowed overall cost from the industrial point of view. The averaged squared acoustic pressure fluctuation computed over the receivers on the side window, as defined in eq. 4.50, is reduced by 35%. The optimization history and the total computational cost per optimization cycle is shown in table 5.2.

The maximum displacement is around 2.6mm and the total geometry displacement, projected on the normal direction is presented in fig. 5.24. In fig. 5.25, the

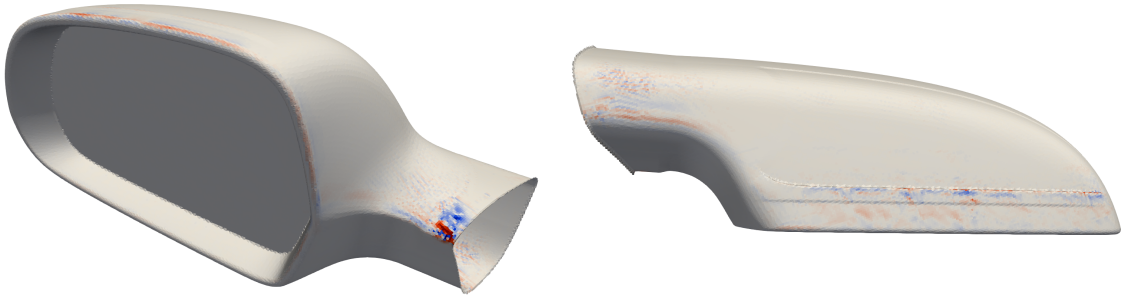

(a) Approach A

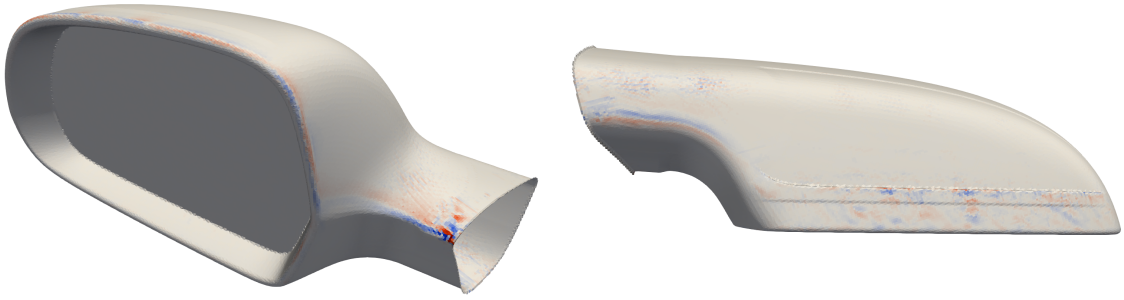

(b) Approach B

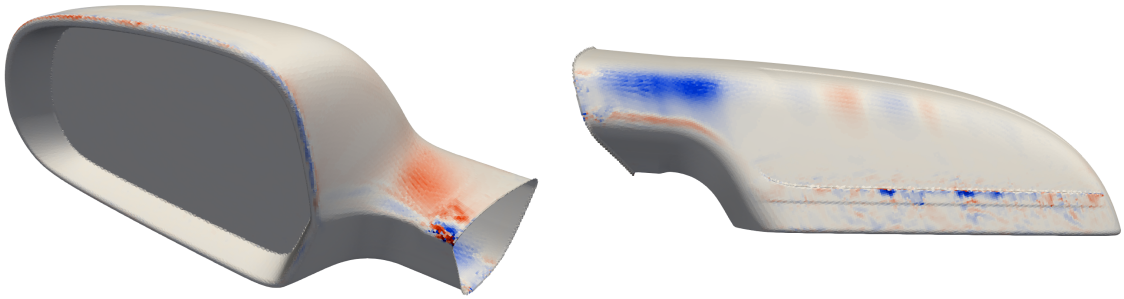

(c) Approach B without grid sensitivities

Figure 5.18: Flow-induced sound reduction on the SAE body: Adjoint sensitivity maps targeting at minimum the radiated sound to the vehicle side window. Red areas must be pushed inwards whereas blue areas must be pulled outwards in order to minimize the objective function.

objective function J at each receiver placed on the side window is presented, as computed for the starting and optimized mirror geometry. The radiated sound has decreased in magnitude which is associated to the influence the geometry change has on the flow and, thus, on sound generation. Moreover, by looking at the iso-lines of the squared acoustic pressure on the window, it is seen that the

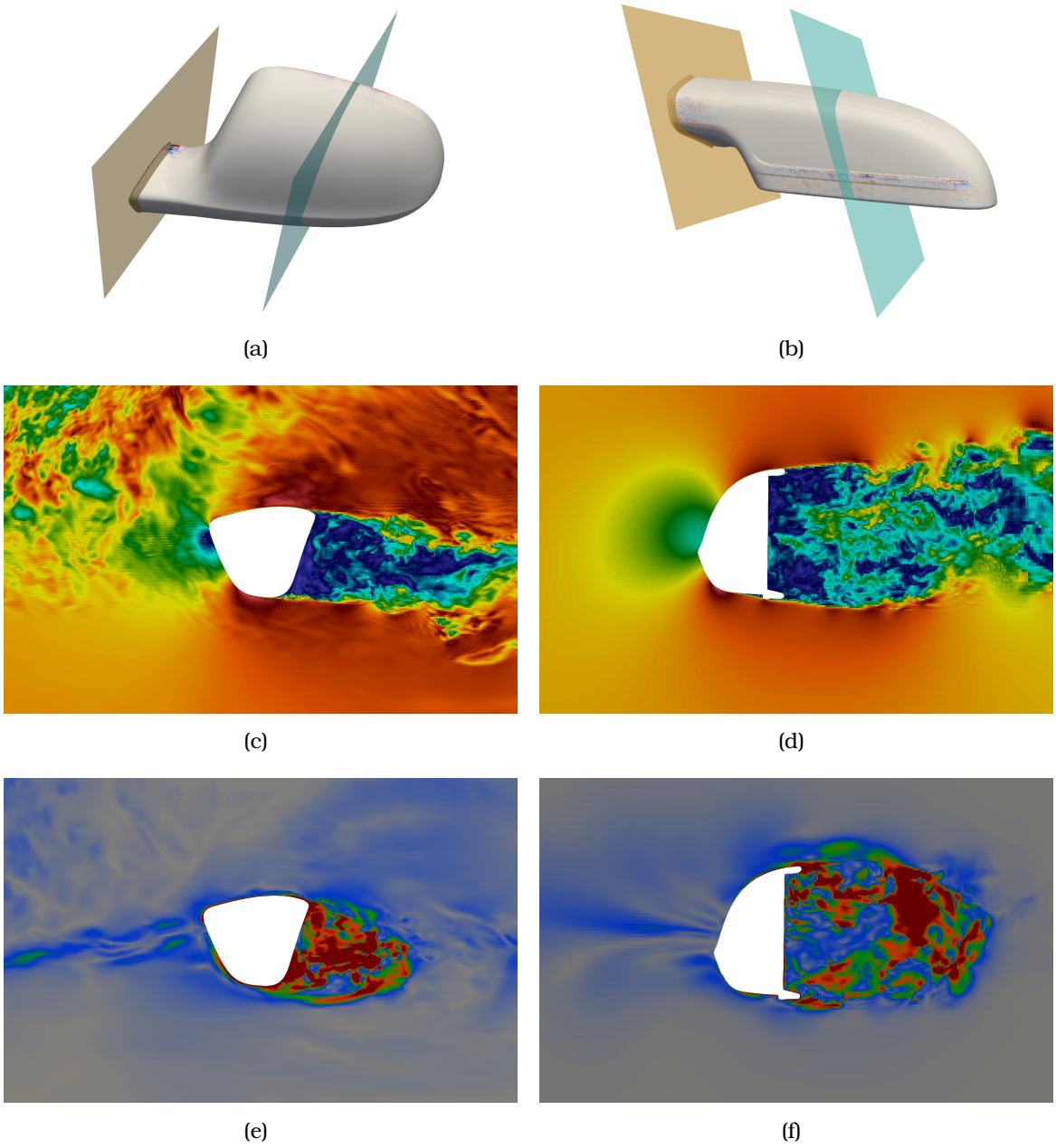

Figure 5.19: Flow-induced sound reduction on the SAE body: Two cross-sections over the mirror are presented. The first section covers the area around the mirror neck (depicted with the orange plane, first row), whereas the second the area around the casing of the mirror glass (depicted with the blue plane, first row). Primal (second row) and adjoint (third row) velocity magnitudes are shown for the mirror neck (left) and casing (right) cross-sections.

directivity of the generated sound field of the optimized mirror shape has moved

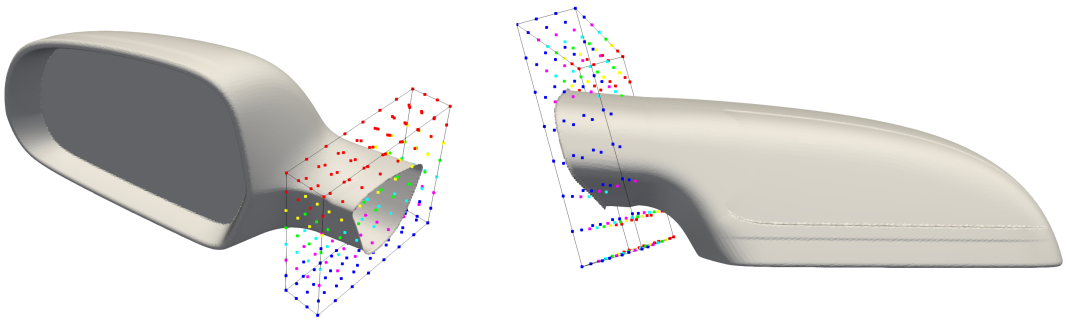

Figure 5.20: Flow-induced sound reduction on the SAE body: Bounding box of the control points of the volumetric B-Splines method used to parameterize the mirror. The control points are coloured based on their z-coordinate and, during the optimization loop, only the internal points are allowed to vary.

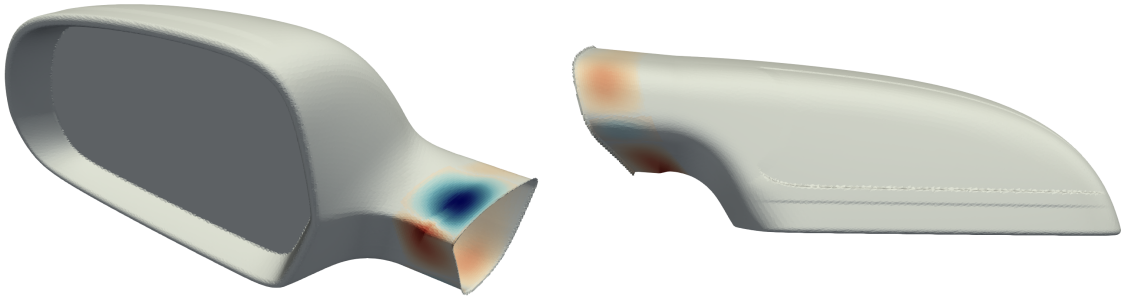

(a) Approach A

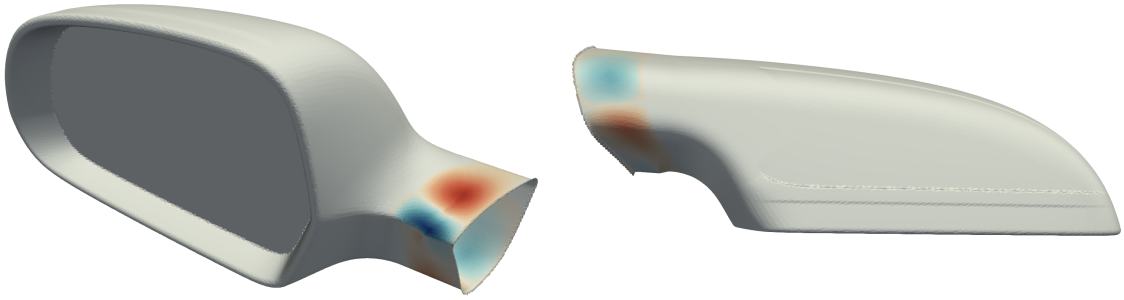

(b) Approach B

Figure 5.21: Flow-induced sound reduction on the SAE body: Normal displacement after one morphing step with the volumetric B-splines method. Red areas were pushed inwards whereas blue areas were pulled outwards, in order to minimize the objective function.

upwind, affecting in this way less the area of the window.

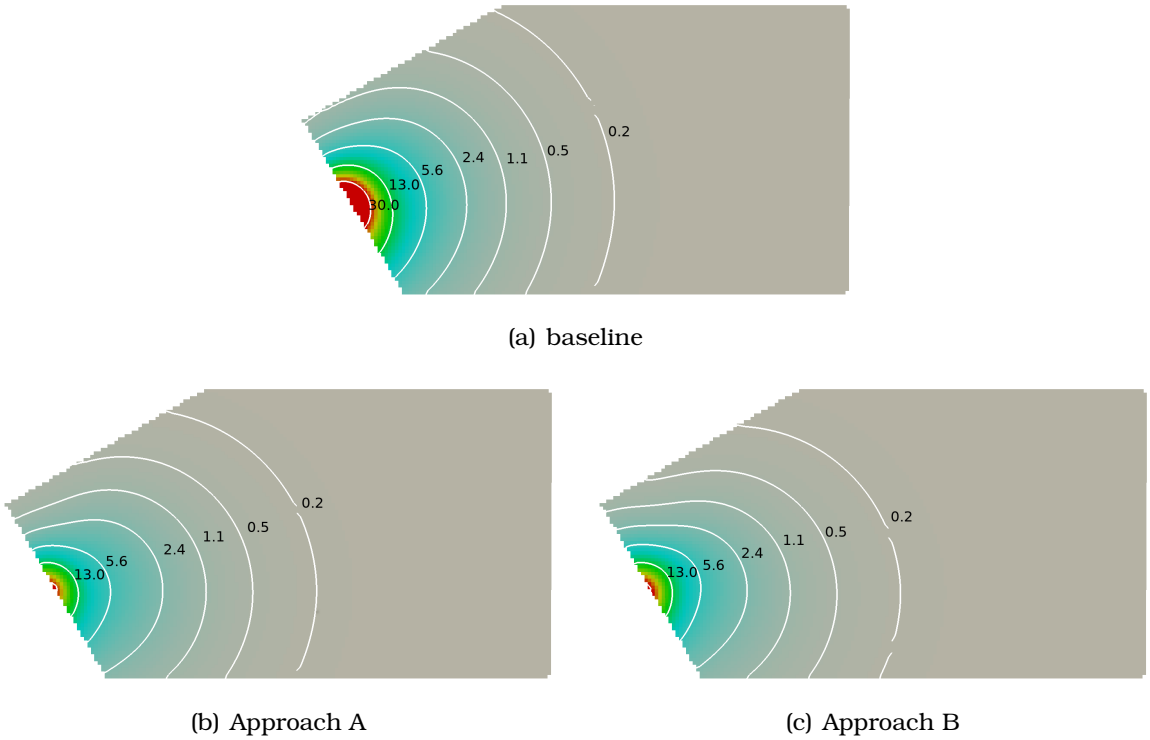

(a) baseline

(b) Approach A

(c) Approach B

Figure 5.22: Flow-induced sound reduction on the SAE body: Time-averaged squared acoustic pressure fluctuation radiated to the side window from the baseline (top) and the optimized mirror with approaches A and B. Both optimized geometries are assessed with a flow computation for $T_s = 1.3s$, during which the objective function is computed over the last $T_{of} = 0.3s$.

	$\frac{\Delta J_{iter}}{J_{base}}\%$	Wall-Clock Time (days)
Baseline	-	6.05
1^{st} Iteration	17.1%	6.17
2^{nd} Iteration	25.3%	6.33
3^{rd} Iteration	35.2%	1.07
	Total time	19.62

Table 5.2: Optimization results and wall-clock time per iteration on 960 CPUs. The primal and adjoint simulations as well as the geometry modification were performed during the 1^{st} and 2^{nd} iteration and taken into account in wall-clock time. Only the primal simulation was performed at the last iteration in order to assess the gain in performance.

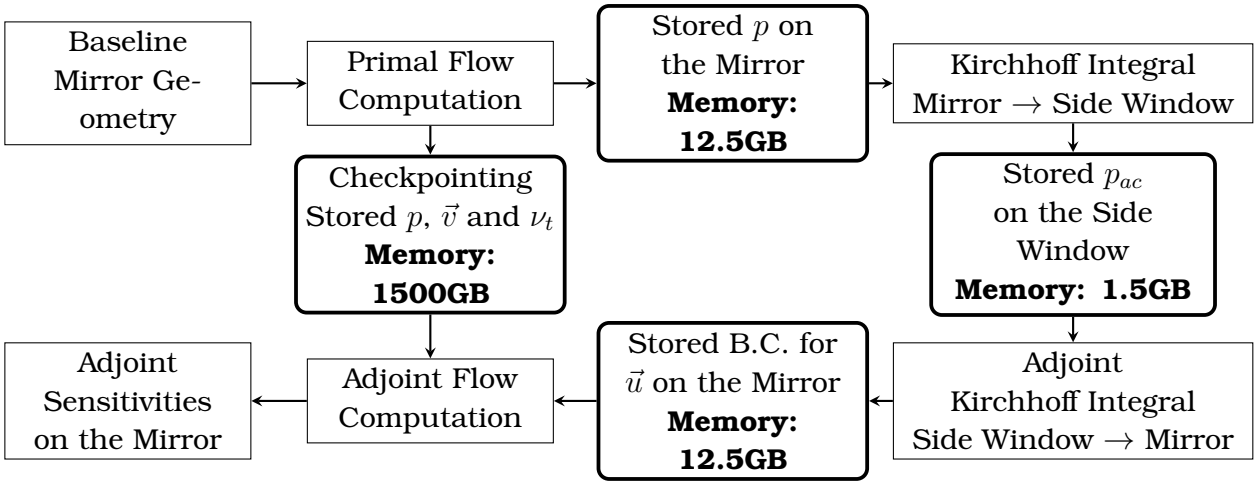

Figure 5.23: Overview of the primal and adjoint procedure for each optimization cycle. Square boxes indicate a simulation/computation, while rounded boxes in bold indicate fields stored in memory.

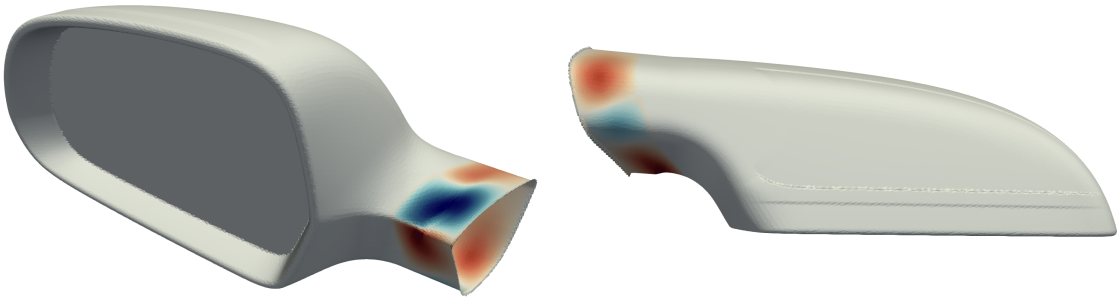

Figure 5.24: Flow-induced sound reduction on the SAE body: Total normal displacement performed during the optimization (top view left, bottom view right). Red areas indicate an inward displacement whereas blue areas an outward. With a maximum displacement of 2.6mm, the time-averaged squared acoustic pressure fluctuation radiated from the mirror to the side window is reduced by 35%.

5.4 Conclusions

In this chapter, the unsteady continuous adjoint method was verified for unsteady turbulent flows and was applied in complex, real-world problems. The efficiency and accuracy of the proposed method is demonstrated not only for a mid-size academic test case but also for a large-scale problem, the generic SAE body. In a 3D turbulent flow around a cylinder, a good agreement between the gradients computed with adjoint and FD was achieved. It was shown that, in aeroacoustic shape optimization problems, it is important to incorporate grid displacement equations in the adjoint formulation, in order to account for grid sensitivities.

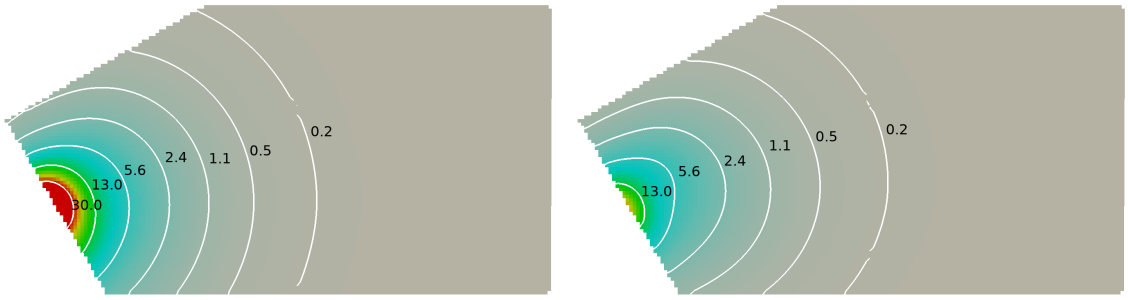

Figure 5.25: Flow-induced sound reduction on the SAE body: Time-averaged squared acoustic pressure fluctuation radiated to the side window from the starting (left) and the optimized (right) mirror. The optimization reduced the radiated sound magnitude and also pushed its directivity upwind, to have a smaller influence on the window.

Otherwise, the sensitivity derivative computation is prone to inacurracies.

In the mathematical formulation of chapter 4, a distinction between the time window T_s of the flow simulation and the time window T_{of} over which the objective function is evaluated was taken into account. To investigate the impact they have on the SD, a sensitivity map analysis was conducted for minimizing flow-induced noise radiation from the side mirror of the SAE body to its side window. It was demonstrated that, in order for the adjoint gradients to be consistent with the primal problem, the adjoint equations must not be integrated only along the objective function window. The adjoint boundary conditions that depend on the objective function, here the adjoint velocity on the body, are imposed during T_{of} and, afterwards, are set to zero for the remaining time, while the magnitude of the adjoint fields decays. Solving the adjoint equations only for T_{of} computes different gradient values which do not guarantee to solve the same optimization problem.

Based on these findings, three optimization cycles are performed and the obtained optimized shape of the mirror of the SAE body was displaced by a maximum of 2.6mm. The objective function, the time averaged squared sound pressure at the vehicle's side window, was minimized by 35%.

Chapter 6

The Continuous Adjoint Formulation to Vehicle Aeroacoustics - Complete Chain

During the early development phase of the car design, aeroacoustic engineers introduce changes to the baseline mirror geometry in order to reduce objective functions such as J_{int}, eq. 3.4 , and, consequently, to improve the aeroacoustic performance of the vehicle. However, this is not a straightforward task. Although specific noise phenomena such as tonal noise have been identified and tackled, there is still no clear connection between mirror geometry changes and their effect on broadband noise.

A numerical tool that can potentially provide an insight to engineers is that of a sensitivity map; it is effectively the gradient of the objective function with respect to the normal displacement of each node on the computational mesh on the mirror and shows the magnitude and direction of the displacement of each node in the normal direction, which results in an improvement of the aforementioned objective function. In other words, it indicates which regions of the vehicle mirror should be pulled outwards and which inwards, in order to achieve a reduction of the interior noise level. Moreover, this sensitivity map can be used in conjuction with a morphing tool to drive a numerical optimization which, after several optimization cycles, can provide a better mirror shape.

This chapter formulates the continuous adjoint method to the complete noise prediction chain based on the developments presented in chapters 3 and 4, in order to efficiently compute the aeroacoustic sensitivity map on the mirror. Afterwards, the proposed adjoint aeroacoustic framework is applied to optimize the side mirror of the SAE body and also to extract useful conclusions on the influence that each step of the noise prediction chain has on interior pressure level.

6.1 The Generic Augmented Objective Function and the Derived Coupled Systems

In this chapter all four objective functions, J_{int}, J_{vib}, J_{KI} and J_{pfluc}, as defined in chapters 3 and 4, are taken into consideration during the continuous adjoint development. In addition, the augmented objective function L includes the time and space integral of the residuals of all equations defined in the previous chapters multiplied with their respective adjoint variables.

The augmented objective function expression reads

$$\begin{aligned} L &= J_{int} + \int_{T_{S_{int}}} \int_{\Omega_{int}} q_{int} R^{p_{int}} d\Omega dt \\ &+ J_{vib} + \int_{T_{S_{int}}} \int_{S_{wi}} z R^{w} dS dt \\ &+ J_{KI} + \int_{T_{S_{int}}} \int_{S_{wi}} q_{ac} R^{p_{ac}} dS dt \\ &+ J_{pfluc} + \int_{T_{S_{ext}}} \int_{\Omega_{ext}} \left(u_i R_i^v + q R^p\right) d\Omega dt \end{aligned} \tag{6.1}$$

On the r.h.s. of eq. 6.1 , R^p and R_i^v are the residuals of the flow continuity and momentum equations, eqs. 2.1 and 2.2 respectively, solved in the domain Ω_{ext} outside the vehicle, $R^{p_{ac}}$ is the Kirchhoff Integral equation, eq. 2.15 , R^w is the residual of the bending wave equation solved on the side window S_{wi} and $R^{p_{int}}$ is the residual of the wave equation solved in the domain Ω_{int} inside the vehicle. The adjoint variables appearing on the r.h.s. of eq. 6.1 are the adjoint velocity and pressure, defined in section 4.3.2 as $\vec{u}$ and q, the adjoint acoustic pressure, defined later on in this chapter as q_{ac}, the adjoint deflection, defined in section 3.2 as z and the adjoint interior pressure, defined in section 3.1 as q_{int}. In addition, windows $T_{S_{int}}$ and $T_{S_{ext}}$ correspond to the simulation time for the interior and exterior domain respectively. The formulation of eq. 6.1 includes all four objective functions, defined in the previous chapters, in order to present the mathematical development that follows in a generic way. In the applications of section 6.3, only one objective function will be considered at a time, although, a multi-objective optimization targeting at any combination of J_{int}, J_{vib}, J_{KI} and J_{pfluc} would be possible.

The total derivative of L w.r.t. b_n yields

$$\frac{\delta L}{\delta b_n} = \frac{\delta J_{int}}{\delta b_n} + \int_{T_{S_{int}}} \int_{\Omega_{int}} q_{int} \frac{\delta R^{p_{int}}}{\delta b_n} d\Omega dt$$

$$
\begin{aligned}
&+ \quad \frac{\delta J_{vib}}{\delta b_n} + \int_{T_{S_{int}}} \int_{S_{wi}} z \frac{\delta R^w}{\delta b_n} dS dt \\
&+ \quad \frac{\delta J_{KI}}{\delta b_n} + \int_{T_{S_{int}}} \int_{S_{wi}} q_{ac} \frac{\delta R^{p_{ac}}}{\delta b_n} dS dt \\
&+ \quad \frac{\delta J_{pfluc}}{\delta b_n} + \int_{T_{S_{ext}}} \int_{\Omega_{ext}} \left(u_i \frac{\delta R_i^v}{\delta b_n} + q \frac{\delta R^p}{\delta b_n} \right) d\Omega dt \\
&+ \quad \int_{T_{S_{ext}}} \int_{\Omega_{ext}} \left(u_i R_i^v + q R^p \right) \frac{\delta d\Omega}{\delta b_n} dt
\end{aligned} \tag{6.2}
$$

The development of individual terms in eq. 6.2 follows the same procedure presented in the previous chapters and the resulting expression yields

$$
\begin{aligned}
\frac{\delta L}{\delta b_n} \quad = \quad & \int_{T_{S_{int}}} \int_{\Omega_{int}} R^{q_{int}} \frac{\delta p_{int}}{\delta b_n} d\Omega dt + \int_{T_{S_{int}}} \int_{S_{wi}} \left(R^z \frac{\delta w}{\delta b_n} + R^{q_{ac}} \frac{\delta p_{ac}}{\delta b_n} \right) dS dt \\
& + \int_{T_{S_{ext}}} \int_{\Omega_{ext}} \left(R^{u_i} \frac{\delta v_i}{\delta b_n} + R^q \frac{\delta p}{\delta b_n} \right) d\Omega dt \\
& + \int_{\Omega_{int}} \left[I_1^{q_{int}} \frac{\partial}{\partial t} \left(\frac{\delta p_{int}}{\delta b_n} \right) + I_2^{q_{int}} \frac{\delta p_{int}}{\delta b_n} \right]_{t_{end}} d\Omega \\
& + \int_{S_{wi}} \left[I_1^z \frac{\delta}{\delta b_n} \left(\frac{\partial w}{\partial t} \right) + I_2^z \frac{\delta w}{\delta b_n} \right]_{end} dS + \int_{\Omega_{ext}} I^{u_i} \frac{\delta u_i}{\delta b_n} \bigg|_{end} d\Omega \\
& + \int_{T_{S_{int}}} \int_{S_{int}} B^{q_{int}} \frac{\delta p_{int}}{\delta b_n} dS dt + \int_T \int_L B^z \frac{\delta w}{\delta b_n} dl dt \\
& + \int_{T_{S_{ext}}} \int_{S_{ext}} \left(B^{u_i} \frac{\delta v_i}{\delta b_n} + B^q \frac{\delta p}{\delta b_n} + B^{\tau_{ij}^a} \frac{\delta \tau_{ij}}{\delta b_n} \right) dS dt \\
& + \quad S.D.
\end{aligned} \tag{6.3}
$$

On the r.h.s. of eq. 6.3, $R^{q_{int}}$, R^z, R^{u_i} and R^q are the residuals of the adjoint equations, as defined in eqs. 3.15, 3.33, 4.23 and 4.22, respectively. Terms $I_i^{q_{int}}$, I_i^z and I^{u_i} are the initial conditions for the wave, bending wave and flow problems, eqs. 3.16, 3.34 and 4.24 respectively. Finally, terms $B^{q_{int}}$, B^z and B^u stand for the boundary conditions, as defined in sections 3.1.3, 3.2.3 and 4.3.4 respectively. Term $S.D.$ stands for the sensitivity derivatives and is discussed later on.

The residual of the equation for the adjoint acoustic pressure on the window, $R^{q_{ac}}$, is derived by the following development, where the sensitivity derivatives term of the bending wave equation, eq. 3.38, is used along with the KI expression

for p_{ac}, eq. 2.15 ,

$$\begin{aligned}
&\int_{T_s}\int_{S_{wi}}\left[-\frac{1}{m'}z\frac{\delta p_{ac}}{\delta b_n}+\frac{\partial J_{KI}}{\partial p_{ac}}\frac{\delta p_{ac}}{\delta b_n}+q_{ac}\frac{\delta R^{p_{ac}}}{\delta b_n}\right]dSdt\\
=&\int_{T_s}\int_{S_{wi}}\left[-\frac{1}{m'}z\frac{\delta p_{ac}}{\delta b_n}+\frac{\partial J_{KI}}{\partial p_{ac}}\frac{\delta p_{ac}}{\delta b_n}+q_{ac}\frac{\delta p_{ac}}{\delta b_n}-q_{ac}\frac{\delta}{\delta b_n}\left(\frac{1}{4\pi}\int_{S_{mir}} g_{ret,i}\,\hat{n}_i dS\right)\right]dSdt\\
=&\int_{T_s}\int_{S_{wi}}\left[\left(-\frac{1}{m'}z+q_{ac}+\frac{\partial J_{KI}}{\partial p_{ac}}\right)\frac{\delta p_{ac}}{\delta b_n}-q_{ac}\frac{\delta}{\delta b_n}\left(\frac{1}{4\pi}\int_{S_{mir}} g_{ret,i}\,\hat{n}_i dS\right)\right]dSdt
\end{aligned} \tag{6.4}$$

The multiplier of $\delta p_{ac}/\delta b_n$ in the first term on the r.h.s. of eq. 6.4 is set to zero to derive the equation for the adjoint acoustic pressure, q_{ac},

$$R^{q_{ac}} = q_{ac} - \frac{1}{m'}z + \frac{\partial J_{KI}}{\partial p_{ac}} = 0 \tag{6.5}$$

This is the coupling equation between the interior and exterior domain, where the adjoint deflection on the window is transformed to the adjoint acoustic pressure. The latter is then propagated to the mirror with the adjoint Kirchhoff Integral.

The second term on the r.h.s. of eq. 6.4 is expanded as presented in section 4.4.2 and yields

$$\begin{aligned}
&-\int_T\int_{S_{mir}} q_{ac}\frac{\delta}{\delta b_n}\left(\frac{1}{4\pi}\int_{S_{mir}} g_{ret,i}\,\hat{n}_i dS\right)dSdt\\
=&-\int_T\int_{S_{mir}}\int_{S_{win}}\frac{\rho q_{ac}}{4\pi}\frac{\partial g_{ret,j}}{\partial p}\frac{\delta p}{\delta b_n}\hat{n}_j dSdSdt\\
&-\int_T\int_{S_{mir}}\int_{S_{win}}\frac{q_{ac}}{4\pi}\frac{\partial g_{ret,j}}{\partial x_i}\frac{\delta x_i}{\delta b_n}\hat{n}_j dSdSdt\\
&-\int_T\int_{S_{mir}}\int_{S_{win}}\frac{q_{ac}}{4\pi}g_{ret,j}\frac{\delta \hat{n}_j dS}{\delta b_n}dSdt
\end{aligned} \tag{6.6}$$

The first term of eq. 6.6 is grouped with another surface integral expressed on the mirror boundary, derived from the differentiation of the pressure term in the Navier-Stokes equations,

$$\begin{aligned}
&-\int_T\int_{S_{mir}}\int_{S_{win}}\frac{\rho q_{ac}}{4\pi}\frac{\partial g_{ret,j}}{\partial p}\frac{\delta p}{\delta b_n}\hat{n}_j dSdSdt+\int_T\int_{S_{mir}} u_i n_i\frac{\delta p}{\delta b_n}dSdt\\
=&\int_T\int_{S_{mir}}\left(u_i n_i-\int_{S_{win}}\frac{\rho q_{ac}}{4\pi}\frac{\partial g_{ret,i}}{\partial p}\hat{n}_i dS\right)\frac{\delta p}{\delta b_n}dSdt
\end{aligned} \tag{6.7}$$

To avoid computing $\delta p/\delta b_n$, its multipliers are set to zero and the boundary condition for the adjoint velocity is derived

$$u_i = \int_{S_{win}} \frac{\rho}{4\pi} \left[\frac{\hat{r}_j \hat{n}_j}{R^2} q_{ac} + \frac{\hat{r}_j \hat{n}_j}{a_0 R} \frac{\partial q_{ac}}{\partial t} \right]_{adv} dS\, n_i \tag{6.8}$$

Note that eq. 6.8 is only a generalized form of eq. 4.58 presented in chapter 4 for sound radiation problems. In case only J_{KI} is considered, without taking into account the interior part of the vehicle (thus $z = 0$), eq. 6.5 yields $q_{ac} = -2p'_{ac}$ and eq. 6.8 takes the form of eq. 4.58 .

Finally, the second and third terms on the r.h.s. of eq. 6.6 contribute along with terms derived from the differentiation of the Navier-Stokes equations and the grid sensitivities to the sensitivity derivatives expression, referred to as $S.D.$. The latter is practically the same with the one presented in chapter 4, section 4.4.3, which is repeated here for the sake of completeness,

$$\begin{aligned}
\frac{\delta L}{\delta b_n} = & \int_{T_s} \int_{S_{W_P}} \left\{ -\tau^a_{ij} \frac{\partial v_i}{\partial x_k} n_j + u_i \frac{\partial \tau_{ij}}{\partial x_k} n_j + q \frac{\partial v_j}{\partial x_k} n_j \right\} \frac{\delta x_k}{\delta b_n} dS dt \\
& + \int_{T_s} \int_{S_{W_P}} u_k n_k \tau_{ij} \frac{\delta (n_i n_j)}{\delta b_n} dS dt \\
& + \int_{T_{of}} \int_{S_{W_P}} \frac{\rho}{2\pi T_{of}} \sum_{r=1}^{N_R} p^{r\prime}_{ac} \left(3\hat{r}_i \hat{n}_i \hat{r}_j - \hat{n}_j\right) \frac{1}{R^3} p \Big|_{ret} \frac{\delta x_j}{\delta b_n} dS dt \\
& + \int_{T_{of}} \int_{S_{W_P}} \frac{\rho}{2\pi T_{of}} \sum_{r=1}^{N_R} p^{r\prime}_{ac} \left(2\hat{r}_i \hat{n}_i \hat{r}_j - \hat{n}_j\right) \frac{1}{a_0 R^2} \frac{\partial p}{\partial t} \Big|_{ret} \frac{\delta x_j}{\delta b_n} dS dt \\
& + \int_{T_{of}} \int_{S_{W_P}} \frac{\rho}{2\pi T_{of}} \sum_{r=1}^{N_R} p^{r\prime}_{ac} \frac{\hat{r}_i \hat{n}_i}{R} \left(\frac{1}{R} \frac{\partial p}{\partial x_j} \Big|_{ret} + \frac{1}{a_0} \frac{\partial^2}{\partial t \partial x_j} \Big|_{ret} \right) \frac{\delta x_j}{\delta b_n} dS dt \\
& + \int_{T_{of}} \int_{S_{W_P}} \frac{\rho}{2\pi T_{of}} \sum_{r=1}^{N_R} p^{r\prime}_{ac} \frac{\hat{r}_i \hat{n}_i \hat{r}_j}{a_0 R} \left(\frac{1}{R} \frac{\partial p}{\partial t} \Big|_{ret} + \frac{1}{a_0} \frac{\partial^2 p}{\partial t^2} \Big|_{ret} \right) \frac{\delta x_j}{\delta b_n} dS dt \\
& + \int_{T_{of}} \int_{S_{W_P}} \frac{\rho}{2\pi T_{of}} \sum_{r=1}^{N_R} p^{r\prime}_{ac} g^r_{ret,i} \frac{\delta (\hat{n}_i dS)}{\delta b_n} dt \\
& + G.S
\end{aligned} \tag{6.9}$$

where $G.S.$ is the grid sensitivity term, depending on the grid displacement model. In case the volumetric B-splines model is used, eq. 4.44 is solved along with the

adjoint equations, and

$$G.S. = -\int_{\Omega} m_i^a \frac{\delta M_i}{\delta b_n} d\Omega \tag{6.10}$$

In case the Laplace equations are solved to propagate the boundary movement into the grid interior, eqs. 4.44 is solved along with the adjoint equations and

$$G.S. = \frac{\partial m_i^a}{\partial x_j} n_j \frac{\delta x_i}{\delta b_n} dS \tag{6.11}$$

6.2 An Overview of the Continuous Adjoint Framework for Vehicle Aeroacoustic Optimization

This section presents an overview of the adjoint aeroacoustic framework and covers the practical aspects of its implementation. First of all, the numerical setup for the solution of each individual step are the ones presented in chapters 3 and 5, sections 3.4 and 5.1 respectively.

Regarding the adjoint integration time, the exact mathematical formulation is followed (approach A in chapter 5) and the primal simulation windows are used for the adjoint solution as well; the exterior flow is simulated for $T_{S_{ext}} = 1.3s$ and the sound radiation and interior domain equations for the last $T_{S_{int}} = 0.3s$. For J_{pfluc} and J_{KI}, the time window $T_{of} = 0.3s$ was used whereas for J_{vib} and J_{int} $T_{of} = 0.3s$. All objective function windows are located at the end of $T_{S_{ext}}$ and $T_{S_{int}}$.

The steps performed in order to assess the aeroacoustic performance of the vehicle and compute the continuous adjoint sensitivities on the side mirror are summarized below:

1. Solve the Navier-Stokes equations in the exterior domain, eqs. 2.2 , 2.1, 2.3, over $T_{S_{ext}}$.

2. Store the hydrodynamic pressure time-series on the mirror, p, over the last $T_{of} = 0.3s$.

3. Using p, compute the radiated acoustic pressure, p_{ac}, on the window using the KI, eq. 2.15 .

4. Using the acoustic load p_{ac}, solve the bending wave equation on the window, eq. 2.16 , over $T_{S_{int}}$.

5. Using the window acceleration as input, eq. 2.23 , solve the wave equation in the interior domain, eq. 2.22 , to compute p_{int}, over T_{of}.

6. Compute objective function J_{int}, over T_{of}.

7. Solve the adjoint wave equation, eq. 3.15 , over T_{of}.

8. Using q_{int} on the window, solve the adjoint bending wave equation, eq. 3.33 , over T_{of}.

9. Compute the adjoint velocity boundary condition on the mirror, eq. 6.8 , with q_{ac}, eq. 6.5 , over T_{of}.

10. Solve the adjoint Navier-Stokes, eqs. 4.23 and 4.22, over $T_{S_{ext}}$.

11. Solve the adjoint grid displacement equation, eq. 4.44 or eq. 4.40 .

12. Compute the sensitivity derivatives, using expression eqs. 6.9 , using the corresponding G.S. term, eq. 6.10 or 6.11 respectively.

It has to be noted that the presented methods for the exterior domain (solution of Navier-Stokes equation and KI) and for the interior domain (solution of bending wave and wave equations) are implemented in different OpenFOAM versions, due to the fact that, at the time this thesis was conducted, versions which included the Finite Area functionality were not compatible with the versions that included the required libraries for the external flow analysis. Therefore, the interior and exterior domains are examined separately, by two different processes/executables and an additional I/O interface based on file exchange was developed. In additon, the exterior domain is decomposed in 960 CPUs, significantly more than the 12 CPUs in which the interior domain is decomposed.

As seen in fig. 6.1, the external flow and sound radiation are firstly simulated. The primal fields u_i, $\partial u_i/\partial t$, p, ν_t and $\partial \nu_t/\partial t$ are stored to be used by the adjoint flow solver at the last step of the chain. Only instantaneous fields at 60 time steps at the corresponding checkpointings are stored. In addition, the acoustic pressure on the window is stored and read by the interior process at its start.

The window vibration and interior propagation are then simulated and the interior pressure near the driver's ear is stored. The adjoint solution in the interior follows, using p_{int} in the source term of the adjoint wave equation, which leads to the computation and storing of the adjoint deflection time-series on the window. This concludes this interior process and the second and last part of the exterior process begins.

The stored adjoint deflection and primal flow fields are read and the adjoint KI is used to "radiate" the adjoint acoustic pressure from the window to the side mirror, in order to compute the adjoint boundary condition for u_i. The adjoint flow is then simulated and the unsteady adjoint sensitivities as well as the adjoint grid displacement source term are integrated, according to the time windows over which the time integrals are defined.

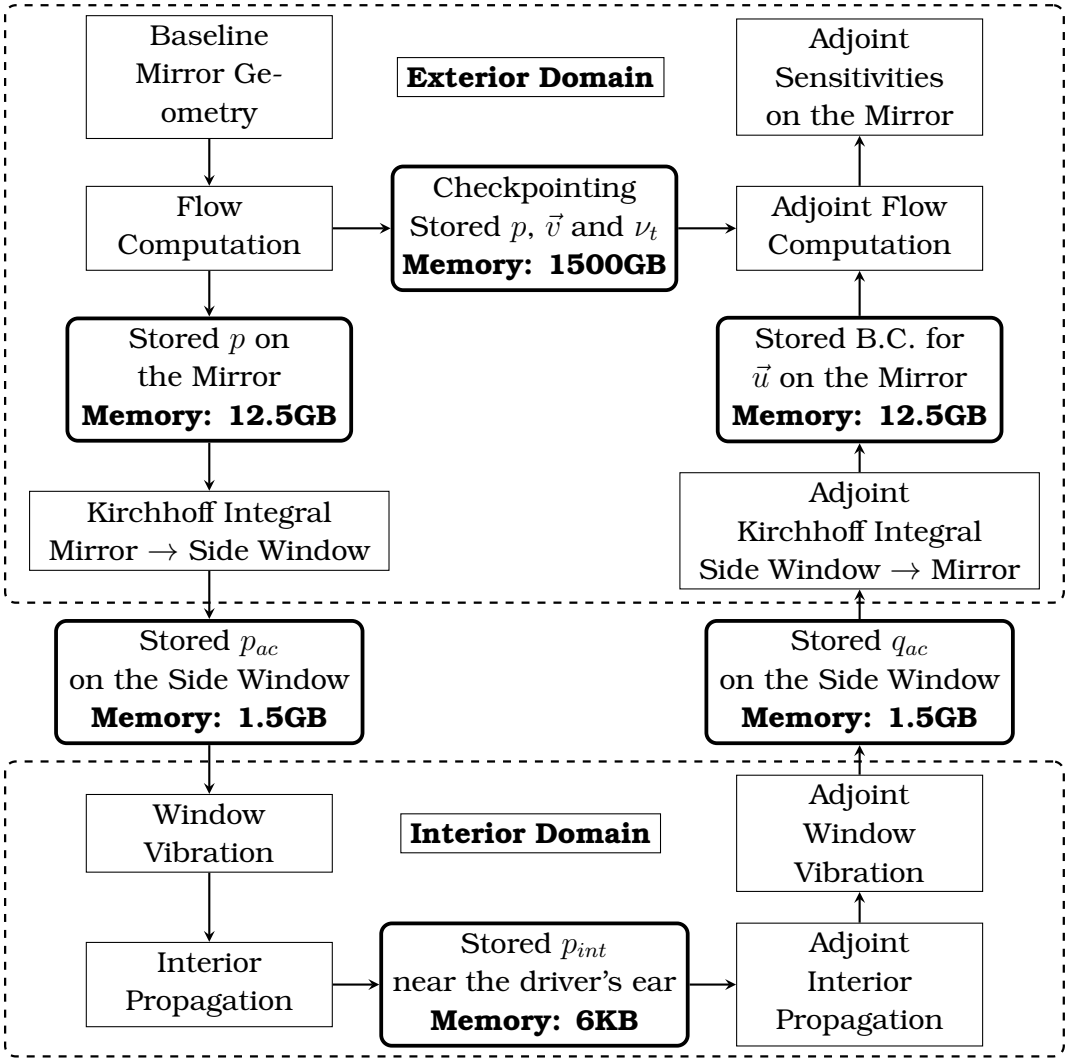

Figure 6.1: Continuous adjoint framework for vehicle aeroacoustic optimization: Flowchart of memory requirements for stored fields.

6.3 Applications

This section presents the application of the developed continuous adjoint framework to compute the aeroacoustic sensitivities that take the complete primal aeroacoustic chain into consideration. Firstly, the side mirror of the SAE body is optimized w.r.t. the interior pressure level. Secondly, an analysis is conducted to investigate the influence that the optimization with regard to an objective function defined at each individual step of the primal procedure has on the objective function defined in the interior.

6.3.1 Optimization of the Side Mirror of the SAE Vehicle Targeting at Interior Pressure Level Minimization

In this section an optimization is performed taking into account all four steps of flow-induced noise generation and propagation into the vehicle interior. The objective function aims at reducing the interior pressure fluctuations, J_{int}, at a point near the driver's ear, as seen in fig. 3.5.

The results of the wind noise prediction process can be seen in fig. 6.2. The strong hydrodynamic pressure fluctuations on the mirror create noise that radiates to all directions and meets the side window. Its vibrational response to the acoustic load generates, in turn, sound waves that propagate to the cabin.

Upon computation of the primal chain steps, the adjoint equations are solved, backwards in time and in reverse order, and snapshots of the solution are presented in fig. 6.3. At the point near the driver's ear there is a monopole source acting, which is the input for the wave equation. The variation of the objective function propagates in the vehicle interior and excites the window to adjoint vibration. The adjoint acoustic pressure on the window, connected to its adjoint deflection, is radiated from the side window towards the vehicle mirror, where it contributes to the boundary condition of the adjoint velocity. The latter flows in the external computational domain through the boundary condition on the mirror and is convected backwards in time by the primal velocity field. By the end of the simulation, the aeroacoustic adjoint sensitivity map is computed, as seen in fig. 6.4(c); it indicates the optimal normal direction in which the mirror geometry should be deformed, in order to achieve a reduction in the wind noise transmission to the driver's ear and thus improve the aeroacoustic performance of the vehicle.

In fig. 6.4, sensitivity maps computed at the first optimization cycle with and without the grid sensitivities are compared (fig. 6.4(a) and fig. 6.4(c) respectively). To enable the plotting of the adjoint derivatives on the surface, the Laplacian equations are used as the grid displacement model. Similarly to the sensitivities for

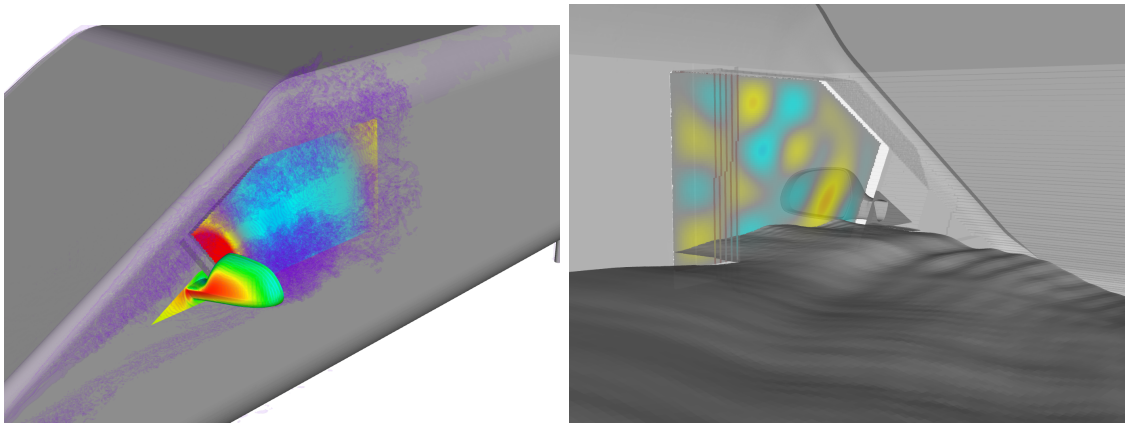

Figure 6.2: The continuous adjoint method for shape optimization in vehicle aeroacoustics: Snapshots of the wind noise prediction chain: On the left, the solution in the exterior domain is presented. The flow in the region of focus is described by the A-pillar and mirror vortices, here shown by the iso-surface (magenta) of $Q = \frac{1}{8}\left(\|\nabla v - (\nabla v)^T\|^2 - \|\nabla v + (\nabla v)^T\|^2\right) = 10^{-1}s^{-2}$. On the right, the vibrational response of the window is depicted. In the interior, a surface at $z = 1.1m$ is elevated based on p_{int} values to represent the propagation of sound waves in the interior compartment.

sound radiation presented in 4, the inclusion of grid sensitivities, eq. 6.4(b) has a great impact on the computed sensitivities, fig. 6.4(c). As demonstrated in section 5.2, the addition of this term ensures the accuracy of the adjoint derivatives.

The wall-clock time required for each individual step is presented in table 6.1. Comparing the times required for this simulation with table 5.1 in chapter 5, it is observed that the solution of the adjoint Navier-Stokes equations in the case of the complete chain has a reduced duration, compared to the solution of the same equations where the source term is the one of the sound radiation. This occurs because the pressure correction step required fewer steps to converge, leading to around 25% less time per iteration.

To perform an optimization cycle, the volumetric B-Splines tool is used for both the surface and interior mesh displacements, therefore eqs. 4.40 and 6.10 are used for the grid sensitivities. The total adjoint sensitivities are computed for the user-defined control points and their coordinates are updated based on steepest descent. Afterwards, the new coordinates of the surface and interior nodes are computed with eq. 4.7 .

The displacement projected in the normal direction for the first and third optimization cycle are presented in fig. 6.5. In total, a 14.1% reduction in the interior pressure at the selected receiver was achieved. The objective function convergence and the required wall-clock time for each optimization cycle is presented in table 6.2.

The impact that the optimized geometry has on several primal fields of the

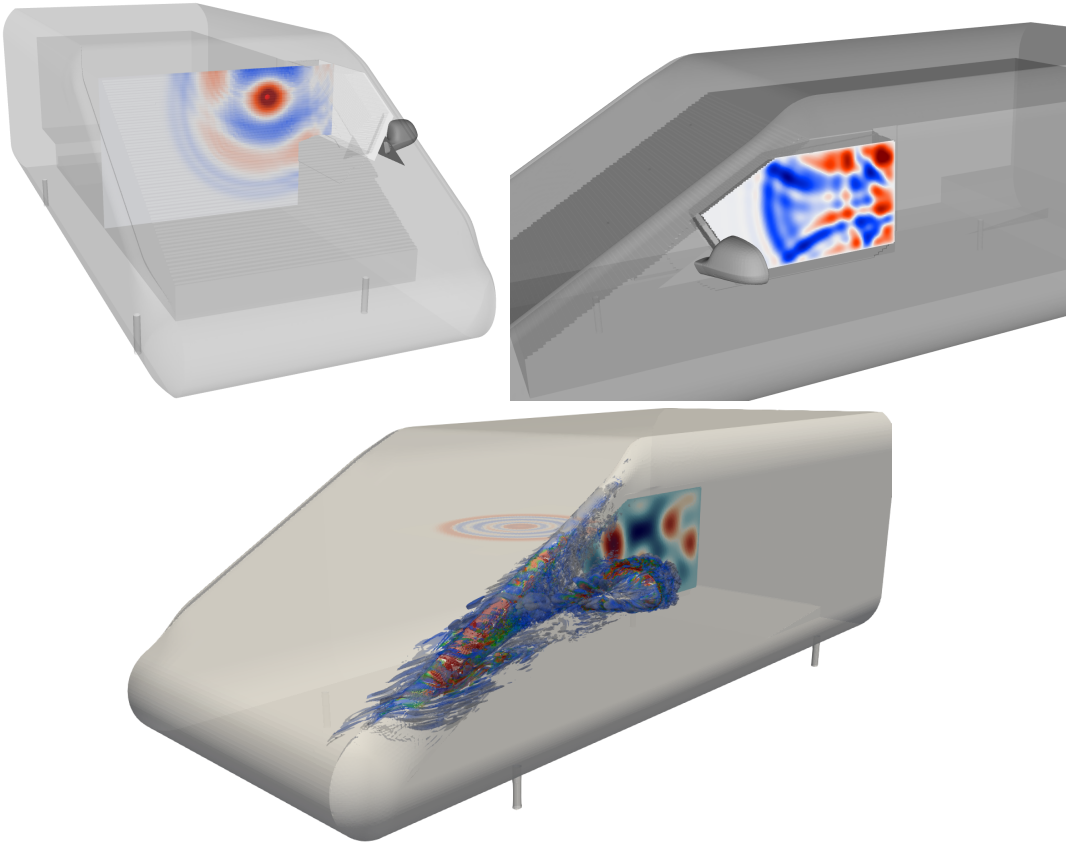

Figure 6.3: The continuous adjoint method for shape optimization in vehicle aeroacoustics: Snapshots of the continuous adjoint chain in the interior. The adjoint wave equation is solved first in the interior and the source term is a monopole at the position where the objective function is defined, here at the red spot near the driver's ear (left). After having propagated the adjoint solution into the interior, it reaches the side window and excites it to adjoint vibration (right).

aeroacoustic chain is presented in fig. 6.6. First of all, a reduction of the squared acoustic pressure fluctuation is observed. This in turns excites the side window at a smaller magnitude and, as a consequence, the squared deflection fluctuation and acceleration of the window are minimized. With a reduced vibrational response of the window, the generated sound waves are reduced as well and the interior pressure level computed near the driver's ear is minimized.

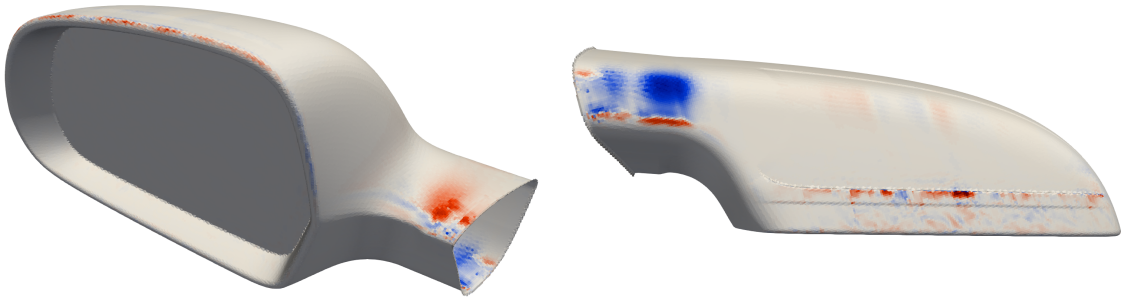

(a) Without grid sensitivities

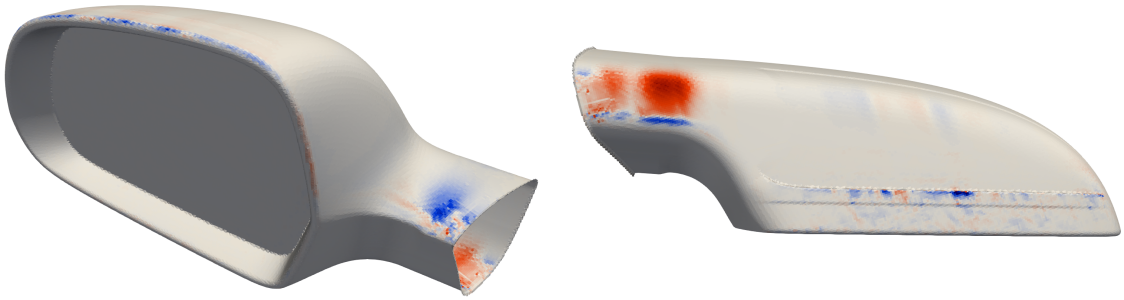

(b) Grid sensitivities term, eq. 6.11

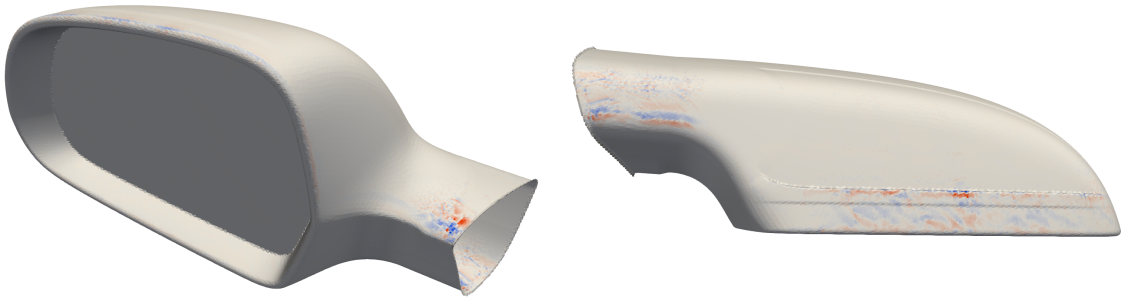

(c) With grid sensitivities: (a) + (b)

Figure 6.4: Interior noise reduction for the SAE body: Sensitivity maps targeting at minimum the interior noise. Red areas must be pushed inwards whereas blue areas must be pulled outwards in order to minimize the objective function. They take into consideration all four steps of the aeroacoustic chain: unsteady flow, sound radiation, window vibration, interior propagation.

Primal Flow (hrs)	23.32
Kirchhoff Integral (hrs)	0.28
Vibration and Interior Propagation (hrs)	6.33
Adjoint Vibration and Interior Propagation (hrs)	4.41
Adjoint Kirchhoff Integral (hrs)	0.61
Adjoint Incl. Primal Recomputations (hrs)	113.81
Total Time (hrs)	148.76

Table 6.1: Wall-clock time of each step of the primal and adjoint procedure for the complete chain. The primal and adjoint flow and KI are computed at 960 CPUs, whereas the primal and adjoint vibration and interior propagation are computed at 12 CPUs. Time needed for data management, such as uploading/downloading to/from the cluster, is not included.

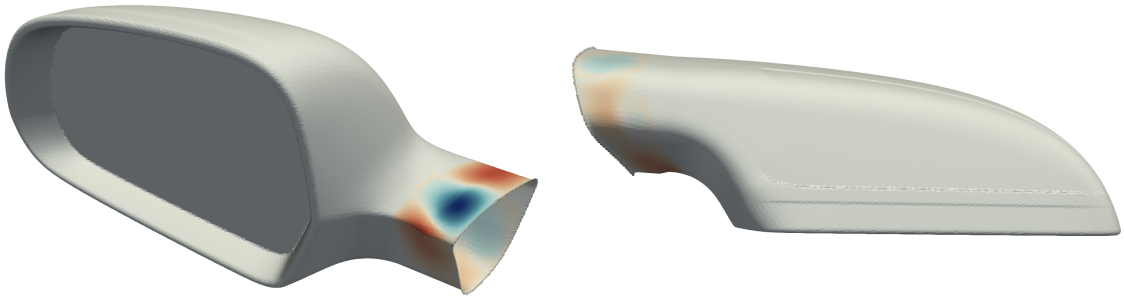

(a) Total displacement after 1 morphing step

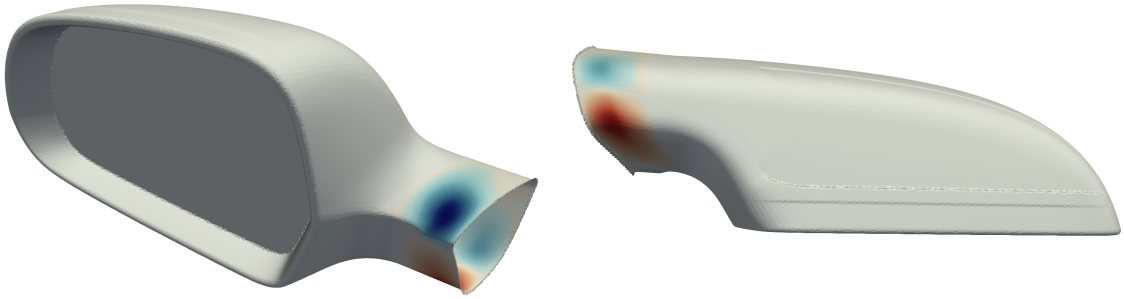

(b) Total displacement after 3 morphing steps

Figure 6.5: Interior noise reduction for the SAE body: Total normal displacement after one morphing step (top) and after three (bottom). Red areas were pushed inwards, whereas blue areas were pulled outwards, in order to minimize the objective function.

6.3.2 Investigation of the Impact of each Step of the Aeroacoustic Chain on Interior Noise

The noise prediction chain is a series of steps, where the output of each individual step is the input to the following one. Therefore, one could argue that the

	$\frac{J_{iter}}{J_{base}}\%$	Computational Time (days)
Baseline	-	6.20
1^{st} Iteration	11.8%	6.08
2^{nd} Iteration	13.9%	6.80
3^{rd} Iteration	14.1%	1.25
	Total time	20.33

Table 6.2: Interior noise reduction on the SAE body: Optimization results and wall-clock time per iteration on 960 CPUs. The primal and adjoint simulations as well as the geometry modification were performed during the 1^{st} and 2^{nd} iteration and taken into account in wall-clock time. Only the primal simulation was performed at the last iteration in order to assess the gain in performance.

suppression of the output of one step would eventually reduce the output of the last step. For instance, based on this rationale, performing a shape optimization for mirror pressure fluctuation would consistently result in minimizing interior noise.

A closer look at the KI, eq. 2.15, indicates that the radiated pressure at a receiver is the weighted integral of the contributions of all surface sources on the mirror. This means that the reduction in the unweighted integral, J_{pfluc}, does not necessarily translate to a reduction in the radiated acoustic pressure, unless the pressure fluctuation magnitude of all sources reduces simultaneously.

This section investigates the influence that an optimization with regard to each individual step of the noise prediction chain has on the interior sound pressure level. The four noise-related objective functions expressed at different stages of the aforementioned simulation chain were defined in chapters 3 and 4 and are J_{int}, J_{vib}, J_{KI} and J_{pfluc}. For each objective function, the respective steps, as defined in section 6.2, are performed to compute the corresponding sensitivity map:

- Pressure Fluctuations: Step 1 is performed and, then, J_{pfluc} is computed. Afterwards, steps 9, 10, 11 and 12 are performed to compute the adjoint sensitivity map.
- Acoustic Pressure: Steps 1,2 and 3 are performed and, then, J_{KI} is computed. Afterwards, steps 9, 10, 11 and 12 are performed to compute the adjoint sensitivity map.
- Window Vibration: Steps 1,2,3 and 4 are performed and, then, J_{vib} is computed. Afterwards, steps 8, 9, 10, 11 and 12 are performed to compute the adjoint sensitivity map.
- Interior Pressure Level: All steps 1-12 are performed.

The four computed sensitivity maps are presented in fig. 6.7. The most sensitive areas of the mirror appear to be the upper and lower sides of the mirror neck. This is expected since, as explained in chapter 5, these are the regions where flow separates and, hence, strong pressure fluctuations, occur. However, in the case presented in fig. 6.7(a), the lower side seems to be of less important for J_{pfluc}, since the magnitude there is considerably smaller than at the other objective functions. Moreover, there are significant differences on the sign of the sensitivities, where positive (red) indicate a need for an inward displacement, whereas negative (blue) an outward one.

To quantify the actual difference of the sensitivity maps and the corresponding reductions in the objective functions, a single step optimization is performed. The baseline mirror geometry is deformed at a fixed maximum displacement of $1mm$ once per sensitivity map and four new shapes are obtained. The geometry displacement for each new geometry is presented in fig. 6.8, where the smooth normal surface displacement depicts the differences more clearly.

For each new mirror geometry, the noise prediction chain is repeated and the four objective functions at the different stages are evaluated anew. The objective function values that each of the four new mirror geometries yields are presented in table 6.3. Firstly, the objective function that each optimization step is actually targeting at is reduced (diagonal of the table). However, a reduction in one step, does not necessarily translate to a reduction in the following steps. The biggest reduction achieved in the interior is performed indeed by targeting at the respective function, J_{int}. Table 6.3 demonstrates that there is not a clear correlation between the stages of the noise prediction chain. For instance, a minimization of the mirror pressure fluctuations does not necessarily correspond to a minimization of the radiated acoustic pressure on the window, although this does not have a negative impact on the interior pressure level. Therefore, the incorporation of all four steps in the adjoint chain is important in order to guarantee a reduction in the interior pressure level.

6.4 Conclusions

In this chapter, the continuous adjoint formulation for an existing multi-disciplinary framework for wind noise prediction in vehicles was presented. This includes an unsteady IDDES flow simulation to compute the hydrodynamic pressure on the mirror, the dominant noise source that is investigated, the KI formulation to extract and radiate the acoustic components from the mirror to the vehicle side window, a structural vibration simulation to compute the window vibration and the interior propagation simulation, to compute the interior acoustic pressure field.

The continuous adjoint formulations presented in chapters 3 and 4 were combined to develop a multi-disciplinary adjoint framework for vehicle aeroacoustic

	Change in Objective Function			
Targeted Objective Function	Pressure Fluctuations	Acoustic Pressure	Window Vibration	Interior Pressure Level
Pressure Fluctuations	-14%	+2%	-8%	-2%
Acoustic Pressure	-9%	-17%	+13%	-7%
Window Vibration	-3%	-5%	-6%	-7%
Interior Pressure Level	-5%	-7%	-5%	-12%

Table 6.3: Investigation of the influence of the noise prediction steps in vehicle aeroacoustic adjoint optimization: Impact that a geometry change has on the four different stages of the noise prediction chain (columns 2 to 5). Each row represents a different mirror geometry improved with regard to the objective function defined in column 1.

optimization. After the computation of each step of the primal and adjoint process chains, it is possible to obtain the aeroacoustic adjoint sensitivity map on the mirror. It takes the physics of all noise creation and transmission mechanisms into consideration and it provides guidance to the aeroacoustic engineer for the optimal normal deformation of the mirror that will improve the aeroacoustic performance of the vehicle. It is, practically, the first time that the unsteady continuous adjoint method is applied to a multi-disciplinary industrial problem of high complexity. The aeroacoustic sensitivity map offers an alternative for engineers to gain insight into vehicle aeroacoustics, and it can also be used in an optimization loop, in order to iteratively find the optimal mirror shape for minimum interior sound pressure level.

However, it must be pointed out, that the computational cost of the method remains an issue. Although the storage of the primal field is reduced by using checkpointing , there is still a trade-off between memory needs and computation time. Moreover, the implementation of an objective function in the frequency domain would also be advantageous for an aeroacoustic investigation, which is presented in chapter 7.

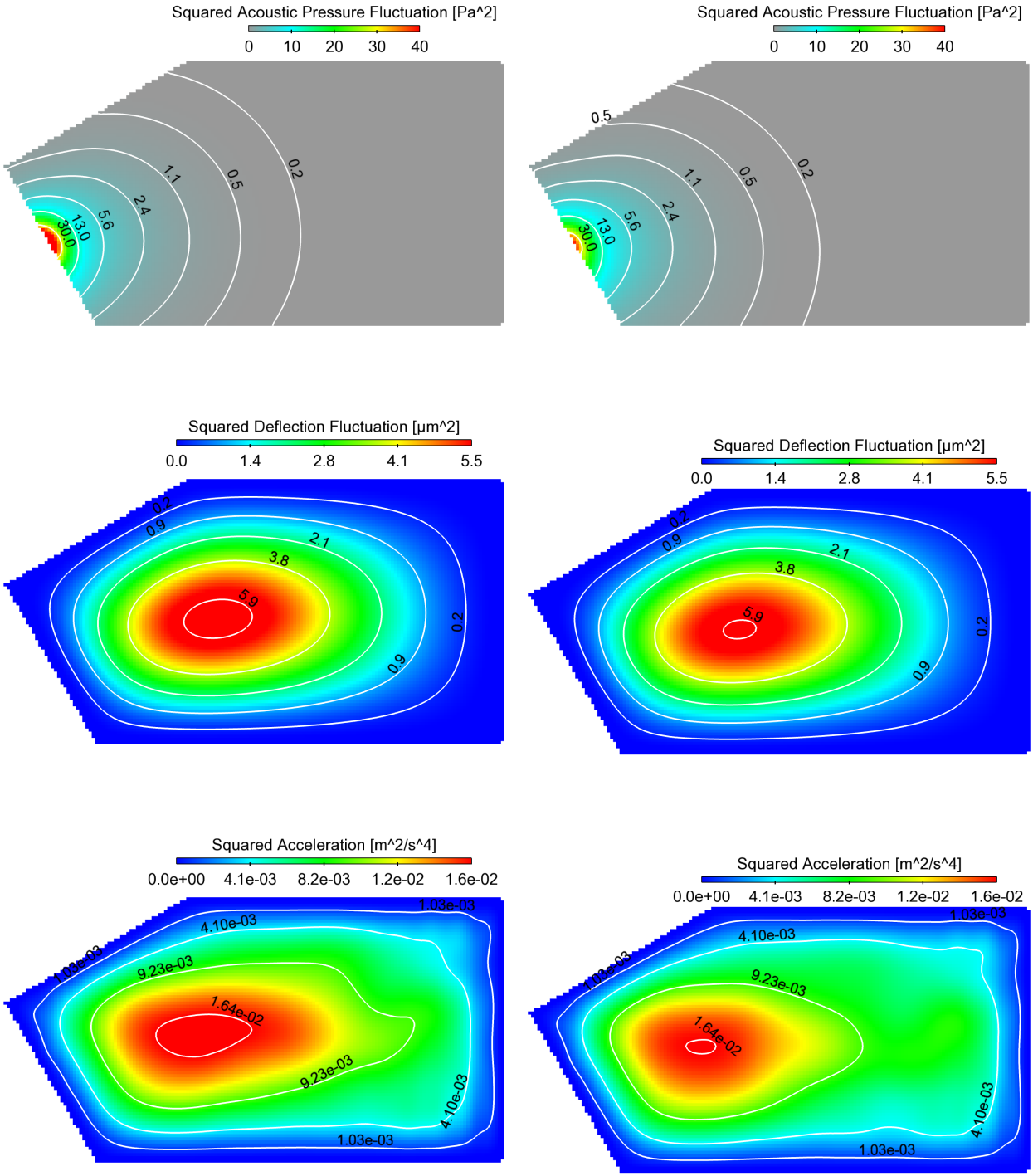

Figure 6.6: Interior noise reduction on the SAE body: Time-averaged squared fields computed on the window for the baseline (left column) and optimized (right column) mirror geometry. The optimized shape affects the window in a different way so that interior pressure level computed at a point near the driver's ear is reduced.

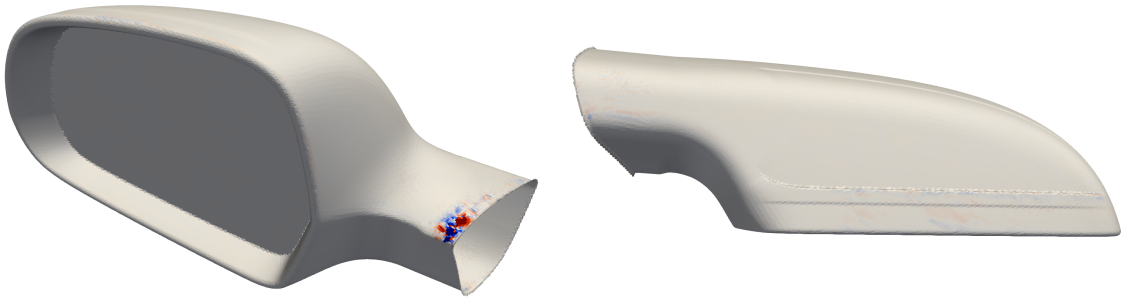

(a) Minimizing pressure fluctuations, J_{pfluc}

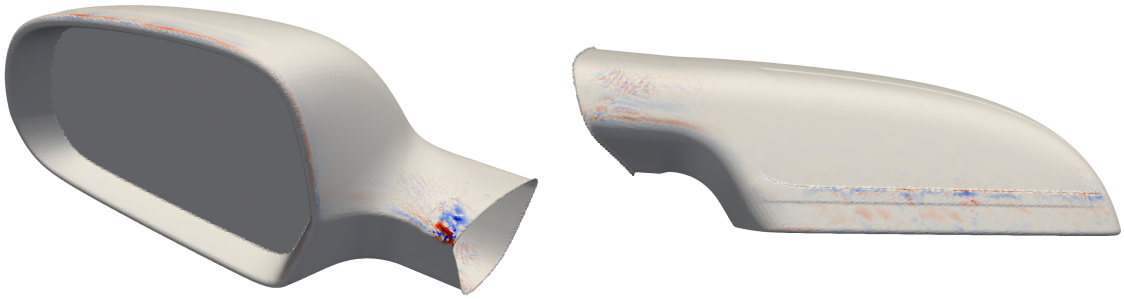

(b) Minimizing acoustic pressure, J_{KI}

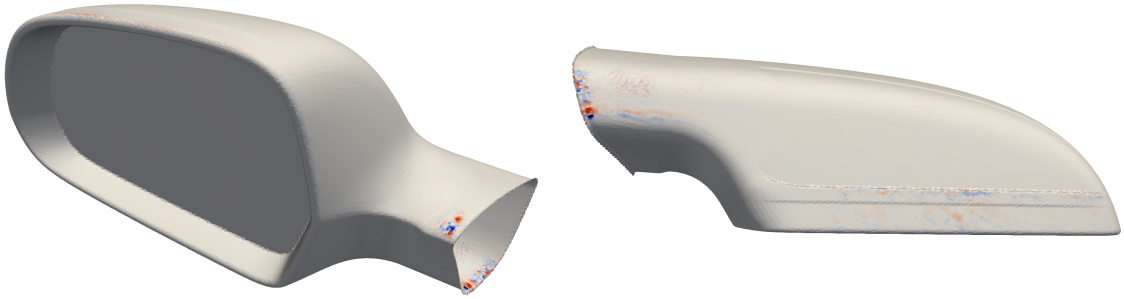

(c) Minimizing window vibration, J_{vib}

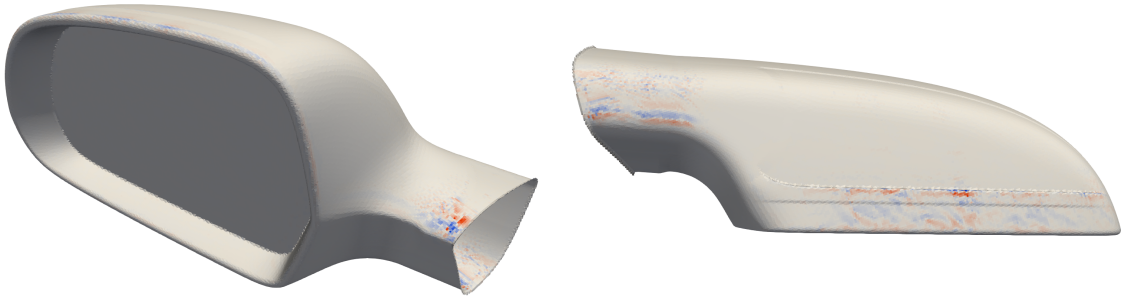

(d) Minimizing interior pressure level, J_{int}

Figure 6.7: Investigation of the influence of the noise prediction steps on vehicle aeroacoustic adjoint optimization: Sensitivity maps targeting at different objective functions expressed at different stages of the noise prediction chain. Red areas must be pushed inwards whereas blue areas must be pulled outwards in order to minimize the corresponding objective function.

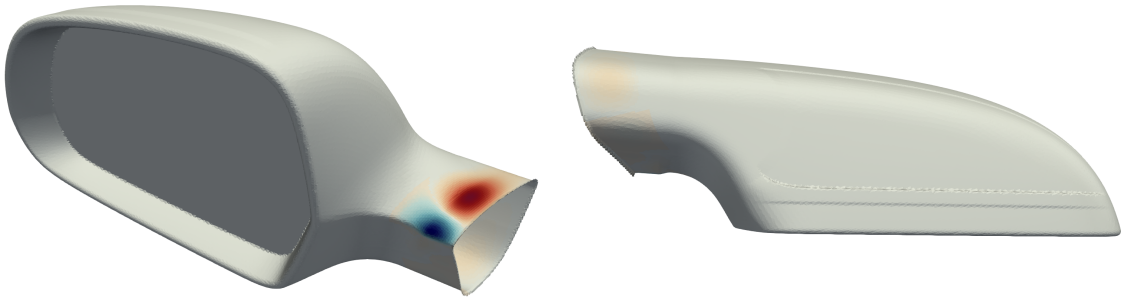

(a) Minimizing pressure fluctuations, J_{pfluc}

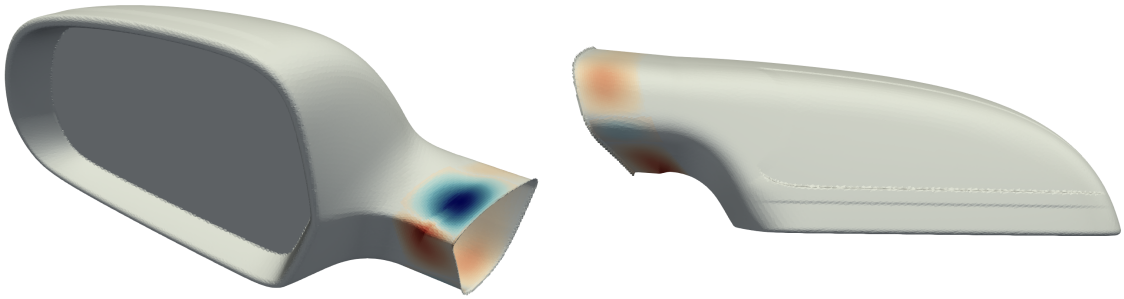

(b) Minimizing acoustic pressure, J_{KI}

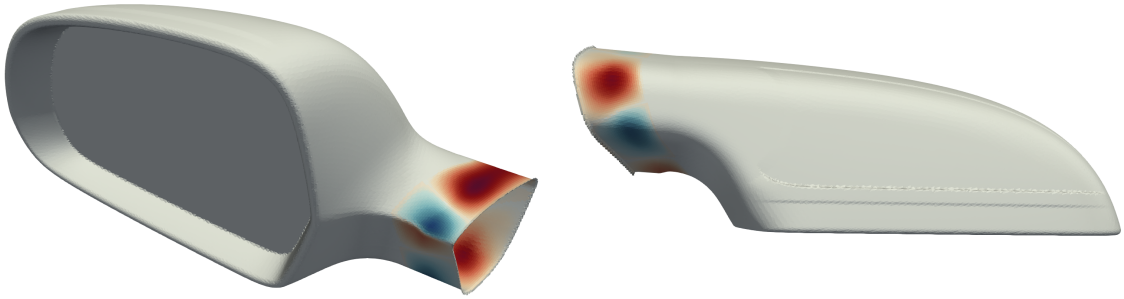

(c) Minimizing window vibration, J_{vib}

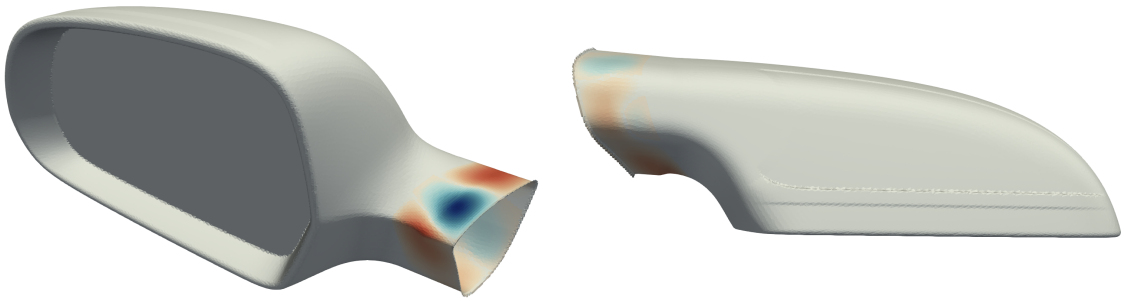

(d) Minimizing interior pressure level, J_{int}

Figure 6.8: Investigation of the influence of the noise prediction steps in vehicle aeroacoustic adjoint optimization: Geometry displacement based on sensitivity maps targeting at different objective functions. Red areas were pushed inwards, whereas blue areas were pulled outwards, in order to minimize the objective function.

Chapter 7

Sensitivities in the Frequency Domain

In the previous chapters, the mirror of the SAE body was optimized with regard to several objective functions which are related to flow-induced noise generation and propagation to the vehicle interior. In fact, in chapter 5 the radiated acoustic pressure on the window was reduced by 35%, whereas in chapter 6 the interior acoustic pressure at a point near the driver's ear was reduced by 14%. The objective function computation and, thus, its reduction concerns the complete frequency spectrum. Due to the fact that low frequencies have a greater energy content, the optimization is rather biased towards lower frequencies.

The One-Third Octave Sound Pressure Level (SPL) of p_{int} computed at a point in the vehicle interior near the driver's ear for the baseline and optimized mirror geometry is presented in fig. 7.1. Although the optimization was successfull in minimizing the overall interior pressure fluctuations, this reduction was obtained mostly from the dominating low frequencies. More energy is contained in this range and, therefore, a smaller change has a greater impact on the objective function. On the other hand, vehicle aeroacoustics are more relevant for a frequency range of $800 - 4000 Hz$. In this chapter, a frequency domain approach is proposed, so that the optimization can target specific frequency ranges.

7.1 Considered Approaches

Two approaches are considered to investigate the optimization problem in the frequency domain. The first one decomposes the time series of the variables to be integrated in the objective function in the frequency domain, using the Fourier Transform, and performs the integration afterwards over a given frequency range. The second approach uses a signal processing filter to remove unwanted frequency components from the pressure time-series on the mirror. The rest of the primal and adjoint chain remain unchanged, making this approach attractive in terms of non-intrusiveness and versatility. For these practical reasons, although both

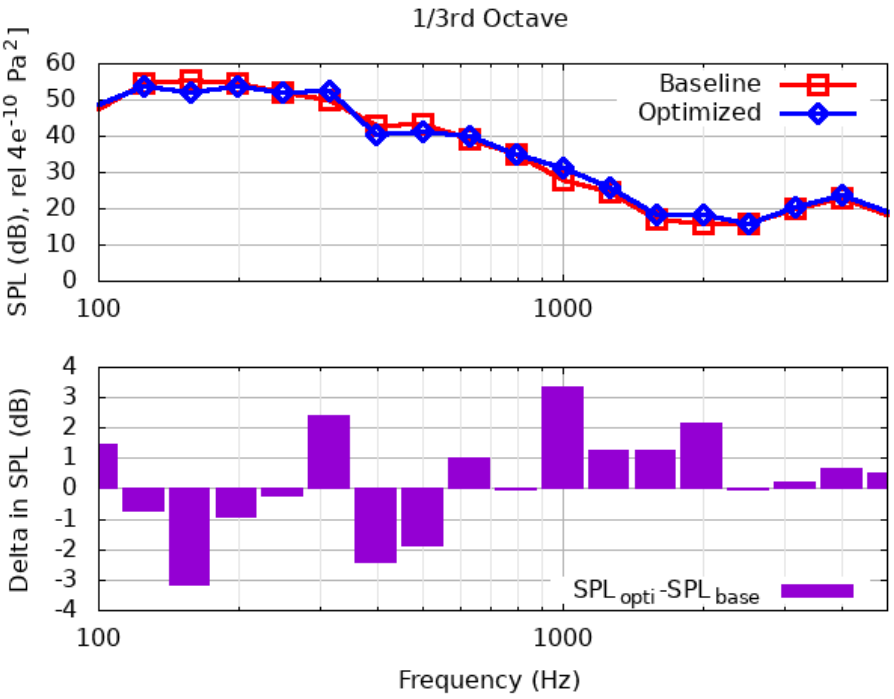

Figure 7.1: Sound Pressure Level in the interior near the driver's ear computed for the baseline mirror geometry (red curve) and the optimized (blue) obtained in section 6.3.1.

approaches are formulated, only the signal filtering is implemented and applied to the SAE test case.

7.1.1 Objective Function with Fourier Transform

This approach introduces an objective function in the frequency domain by transforming the time signal of the considered variable with the Fourier Transform. A suitable expression would be

$$J_{FT} = \int_{f_{min}}^{f_{max}} \left\| \hat{\Phi}(f) \right\|^2 df = \int_{f_{min}}^{f_{max}} \left(R_{\hat{\Phi}}^2 + I_{\hat{\Phi}}^2 \right) df \tag{7.1}$$

where f_{min} and f_{max} are the lower and upper bounds respectively of the considered frequency range and $\hat{\Phi}(f)$ is the Fourier Transform of $\Phi(t)$

$$\hat{\Phi}(f) = \int_{-\infty}^{\infty} \Phi(t) e^{-i2\pi ft} dt$$

$$= \underbrace{\int_{-\infty}^{\infty} \Phi(t) \cos(2\pi f\, t)\, dt}_{R_{\hat{\Phi}}} \underbrace{- \int_{-\infty}^{\infty} \Phi(t) \sin(2\pi f\, t)\, dt}_{I_{\hat{\Phi}}} \tag{7.2}$$

The differentiation of J_{FT} w.r.t. b_n yields

$$\begin{aligned}
\frac{\delta J_{FT}}{\delta b_n} &= \int_{f_{min}}^{f_{max}} \left(2R_{\hat{\Phi}} \frac{\delta R_{\hat{\Phi}}}{\delta b_n} + 2I_{\hat{\Phi}} \frac{\delta I_{\hat{\Phi}}}{\delta b_n} \right) df \\
&= \int_{f_{min}}^{f_{max}} \left(2R_{\hat{\Phi}} \int_{-\infty}^{\infty} \frac{\delta \Phi(t)}{\delta b_n} \cos(2\pi f\, t)\, dt + 2I_{\hat{\Phi}} \int_{-\infty}^{\infty} \frac{\delta \Phi(t)}{\delta b_n} \sin(2\pi f\, t)\, dt \right) df \\
&= \int_{-\infty}^{\infty} \underbrace{\int_{f_{min}}^{f_{max}} \left(2R_{\hat{\Phi}} \cos(2\pi f\, t) + 2I_{\hat{\Phi}} \sin(2\pi f\, t) \right) df}_{\frac{\partial J_{FT}}{\partial \Phi}} \frac{\delta \Phi(t)}{\delta b_n} dt
\end{aligned} \tag{7.3}$$

The expansion of eq. 7.3 can now be coupled with any boundary condition or source term of the aeroacoustic chain, as explained in chapters 3 and 4. For instance, in case Φ is the interior pressure at a point near the driver's ear, p_{int}, then eq. 7.3 is used to obtain the source term on the r.h.s. of eq. 3.15, which yields

$$\frac{\partial J_{FT}}{\partial p_{int}} H(t - t_{of}) = \int_{f_{min}}^{f_{max}} \left(2R_{\hat{p}_{int}} \cos(2\pi f\, t) + 2I_{\hat{p}_{int}} \sin(2\pi f\, t) \right) df\, H(t - t_{of}) \tag{7.4}$$

where

$$R_{\hat{p}_{int}}(f) = \int_{-\infty}^{\infty} p_{int}(t) \cos(2\pi f\, t)\, dt \tag{7.5}$$

and

$$I_{\hat{p}_{int}}(f) = - \int_{-\infty}^{\infty} p_{int}(t) sin(2\pi f\, t)\, dt \tag{7.6}$$

This approach is objective function-dependent and must be tailored to any defined objective function that must be computed in the frequency domain.

7.1.2 Filtering

In this approach, the signal processing method of filtering is considered and the signal (time-series) of pressure is filtered at an early stage of the noise prediction chain, in order to remove frequency components that are not relevant to the

investigation. Therefore, once the filter is implemented, no additional code enhancement is required, neither for the computation of the objective function, nor for its differentiation and the adjoint chain.

The time-domain operation that has an equivalent effect to filtering is convolution [52], which combines two signals to generate a third one. If the first signal is the acoustic signal and the second one is the impulse response of a filter, then the result of convolution is a filtered signal.

This is expressed mathematically as

$$\Phi^{filt}(t) \triangleq \int_{t_s}^{t_e} \Phi(\tau)\mathscr{F}(t-\tau)d\tau \tag{7.7}$$

where $\mathscr{F}$ is the filter function, $\Phi(t)$ is the signal, in this thesis the time-series of p_{ac}, and t_s and t_e are the start and end of the signal respectively.

Moreover, the "inverted" signal can be defined as

$$\Phi^*(t) \triangleq \Phi(t_s + t_e - t) = \Phi(t^*) \tag{7.8}$$

which is practically the signal Φ backwards, that is the time-series of Φ starting at t_e and ending at t_s. In addition, the following identity is useful for the mathematical development that follows,

$$\Phi^{filt-}(t) \triangleq \int_{t_s}^{t_e} \Phi(\tau)\mathscr{F}(\tau-t)d\tau \tag{7.9}$$

Eq. 7.9 is further developed using eq. 7.8 and the substitution $\tau = t_s + t_e - u$

$$\begin{aligned}
\Phi^{filt-}(t) &= \int_{t_s}^{t_e} \Phi(\tau)\mathscr{F}(\tau-t)dt \\
&= -\int_{t_e}^{t_s} \Phi(t_s+t_e-u)\mathscr{F}(t_s+t_e-t-u)du \\
&= \int_{t_s}^{t_e} \Phi^*(u)\mathscr{F}(t^*-u)du \\
&= \Phi^{*filt}(t^*)
\end{aligned} \tag{7.10}$$

The last expression on the r.h.s. of eq. 7.10 denotes the inverted outcome of the filtering of the inverted Φ. Practically, the time-signal Φ is firstly inverted, then filtered and then inverted again.

In the aeroacoustic framework, the variable that is filtered is the radiated

acoustic pressure as computed with the KI and yields

$$p_{ac}^{filt}(t) = \int_{T_{of}} p_{ac}(\tau)\mathscr{F}(t-\tau)dt \tag{7.11}$$

For the solution of the bending wave equation, eq. 2.16, the source term $p_{load} = p_{ac}^{filt}$ is used. The following steps of the noise prediction process remain unaffected. This time, however, they contain only the filtered frequencies that are of interest.

The influence of the filtering in the adjoint process is seen by taking eq. 3.42 into consideration, where $p_{load} = p_{ac}^{filt}$

$$\begin{aligned}
\frac{\delta L_{int}}{\delta b_n} &= -\int_T \int_{S_{wi}} \frac{1}{m'} z(t) \frac{\delta p_{load}}{\delta b_n}(t) dS dt \\
&= -\int_T \int_{S_{wi}} \frac{1}{m'} z(t) \frac{\delta p_{ac}^{filt}}{\delta b_n}(t) dS dt \\
&= -\int_T \int_{S_{wi}} \frac{1}{m'} z(t) \int_T \frac{\delta p_{ac}(\tau)}{\delta b_n} \mathscr{F}(t-\tau) d\tau dS dt \\
&= -\int_T \int_{S_{wi}} \frac{1}{m'} \underbrace{\left(\int_T z(t)\mathscr{F}(t-\tau)dt \right)}_{z^{filt-}} \frac{\delta p_{ac}}{\delta b_n}(\tau) dS d\tau
\end{aligned} \tag{7.12}$$

where z^{filt-}, as shown in eq. 7.10, is the inverted outcome of the filtering of inverted z. Practically the time-signal of the adjoint deflection is inverted, filtered and then inverted again, in order to be used for the adjoint KI. Substituting eq. 7.12 in eq. 6.4 yields

$$\begin{aligned}
&\int_{T_s} \int_{S_{wi}} \left[-\frac{1}{m'} z^{filt-} \frac{\delta p_{ac}}{\delta b_n} + \frac{\partial J_{KI}}{\partial p_{ac}} \frac{\delta p_{ac}}{\delta b_n} + q_{ac} \frac{\delta R^{p_{ac}}}{\delta b_n} \right] dS dt \\
= &\int_{T_s} \int_{S_{wi}} \left[\left(-\frac{1}{m'} z^{filt-} + q_{ac} + \frac{\partial J_{KI}}{\partial p_{ac}} \right) \frac{\delta p_{ac}}{\delta b_n} - q_{ac} \frac{\delta}{\delta b_n} \left(\frac{1}{4\pi} \int_{S_{mir}} g_{ret,i}\, \hat{n}_i dS \right) \right] dS dt
\end{aligned} \tag{7.13}$$

and consequently

$$R^{q_{ac}} = q_{ac} - \frac{1}{m'} z^{filt-} + \frac{\partial J_{KI}}{\partial p_{ac}} = 0 \tag{7.14}$$

In this approach, p_{ac} is filtered, in order to maintain only the frequency components of interest. In the adjoint chain, the same filtering process is performed for the adjoint deflection, this time backwards. The main advantage of this method is that it is less intrusive (the filtering for both the primal and adjoint signals is

easily added as an additional function) and thus very versatile. The primal and adjoint process of the aeroacoustic framework remain the same.

In addition, by filtering the signal early on in the process chain, any objective function defined afterwards can be computed for the desired frequency range automatically, without the need for implementing the Fourier Transform.

7.2 Implementation

The implementation of a digital filter can be specified by the difference equation [104] which is a formula for computing an output sample at time n based on past and present input samples and past output samples in the time domain

$$\begin{aligned} y(n) &= b_0 x(n) + b_1 x(n-1) + \cdots + b_M x(n-M) \\ &\quad - a_1 y(n-1) - \cdots - a_N x(n-N) \\ &= \sum_{i=0}^{M} b_i (x(n-1) - \sum_{j=1}^{N} a_j y(n-j) \end{aligned} \tag{7.15}$$

where x is the input signal, y is the output (filtered) signal and $b_i,\ i = 0, ..., M$ and $a_i,\ i - 1, ..., N$ are coefficients that depend on the filter. The b_i coefficients are called feedforward coefficients whereas the a_i are called feedback coefficients, since they allow for the use of past output samples, $y(n-j)$, a process called feedback. A filter is called recursive or infinite-impulse-response (IIR) filter when $a_i \neq 0$ for some $i > 0$. When there is no feedback ($a_i = 0, \forall i > 0$), the filter is called nonrecursive or finite-impulse-response (FIR) digital filter.

The Butterworth filter is used in this thesis, which is designed to have a frequency response as flat as possible in the passband [20]. The feedforward and feedback coefficients required for the filtering process, eq. 7.15 , can be computed using any signal-processing tool, such as GNU Octave [2] or MATLAB® [1]. Although this process is out of the scope of this thesis, a short description of an algorithm that computes these coefficients follows:

1. Given the desired filter order, the poles of the normalized analog Butterworth filter for cut-off frequency $\omega_c = 1 rad/s$ are firstly computed [20, 140].

2. Given the desired cut-off frequencies, the upper and lower bounds of the desired frequency range, the poles of the analog Butterworth filter are computed in the complex Laplace domain [116].

3. Using the bilinear transform, the poles are transformed from the complex Laplace domain to the z-domain and the analog filter is converted to a digital one [105, 87].

4. The poles and zeros are converted to polynomials with the coefficients b_i and a_i and the transfer function in the z-domain yields the general form

$$Y(z) = \frac{b_0 + b_1 z^{-1} + ... + b_M z^{-M}}{1 + a_1 z^{-1} + ... + a_N z^{-N}} X(z) \tag{7.16}$$

where X(z) and Y(z) is the z-transform of the input Φ and output Φ^{filt} signal respectively.

7.3 Applications

In this section, the filtering process is applied to compute sensitivity maps for several frequency ranges. Firstly, the objective function-based analysis study presented in section 6.3.2 is repeated for a frequency range between $800 - 4000Hz$. Afterwards, in order to demonstrate the influence that the selected frequency range has on the sensitivity derivatives, the sensitivity maps for the $1/3^{rd}$ frequency bands in the aforementioned frequency range are computed.

7.3.1 Frequency Range 800-4000Hz

In this study, a 4^{th}-order bandpass Butterworth filter is used to filter p_{ac} in the range of $800 - 4000Hz$. As explained in the previous section and seen in fig. 7.2, the filtering process is performed after the KI and, correspondingly, the adjoint filtering process is performed before the adjoint KI.

The interior SPL computed for the filtered signal is presented in fig. 7.3, where it is seen that the amplitude at frequencies lower than 800Hz and higher than 4000Hz has significantly decreased and, thus, these do not affect the optimization.

Similarly to section 6.3.2, a sensitivity map is computed for the noise-related objective functions defined in the previous chapters and, this time, only a specific frequency range is considered. Since the filtering process is performed after the KI computation, the pressure fluctuations on the mirror are not taken into account as an objective function. Therefore, three sensitivity maps are computed targeting at minimizing the acoustic pressure at the window, J_{KI} in eq. 4.50 , the window vibration, J_{vib} in eq. 3.22 and the interior pressure level near the driver's ear, J_{int} in eq. 3.4 .

The three computed sensitivity maps are presented in fig. 7.4. Similarly to section 6.3.2, the mirror geometry is displaced by $1mm$, fig. 7.5 and the aeroacoustic process is performed again. The newly computed objective functions for each geometry are presented in table 7.1. Compared to the results of table 6.3, obtained for the complete frequency spectrum, in this frequency range it is clearer

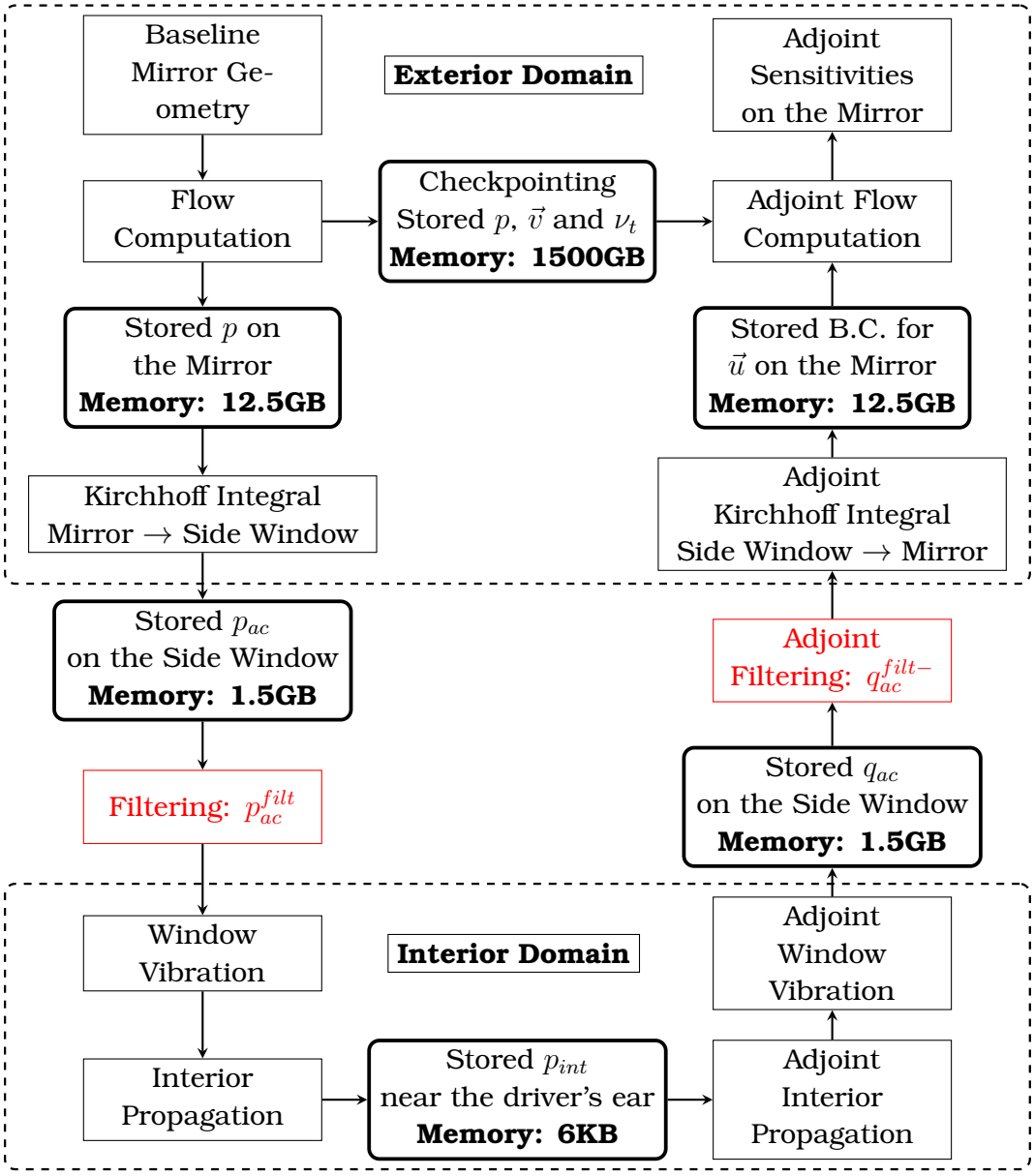

Figure 7.2: Continuous adjoint framework for vehicle aeroacoustic optimization with filering: Flowchart of memory requirements for stored variables

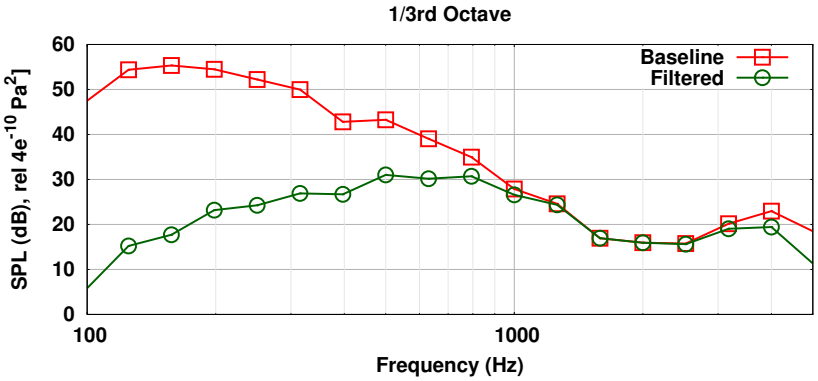

Figure 7.3: Sound Pressure Level in the interior near the driver's ear computed for the baseline geometry, with (green curve) and without (red curve) filtering.

that the minimization of one step in the noise prediction chain does not translate to a minimization of the steps that follow. Therefore, the incorporation of all four steps in the adjoint chain is important in order to guarantee a reduction in the interior pressure level.

	Computed Objective Function		
Targeted Objective Function	Acoustic Pressure	Window Vibration	Interior Pressure Level
Acoustic Pressure	-2.7%	+0.1%	+2%
Window Vibration	+3.9%	-1.8%	-2.9%
Interior Pressure Level	+7.0%	2.2%	-5.0%

Table 7.1: Investigation of the influence of the noise prediction steps for vehicle aeroacoustic adjoint optimization using filtering for 800-4000Hz: Impact that a geometry change has on the four different stages of the noise prediction chain (columns 2 to 4). Each row represents a different mirror geometry improved with regard to the objective function defined in column 1.

7.3.2 One Third Octave Bands Between 800-4000Hz

This section investigates further the frequency dependency of the sensitivity maps and how these are affected by targeting different frequency ranges. Specifically, the desired frequency range $800 - 4000Hz$ is divided to its third-octave frequency bands, as presented in table 7.2. For each band, a different sensitivity map is computed, firstly for minimizing the acoustic pressure on the window and afterwards for minimizing interior pressure.

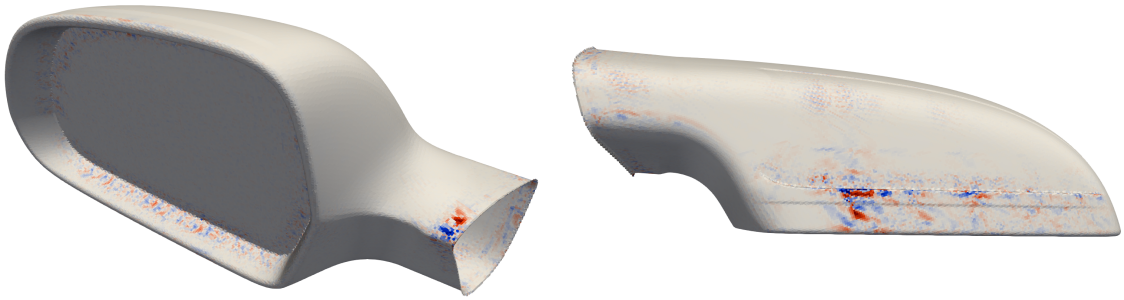

(a) Minimizing acoustic pressure, J_{KI}

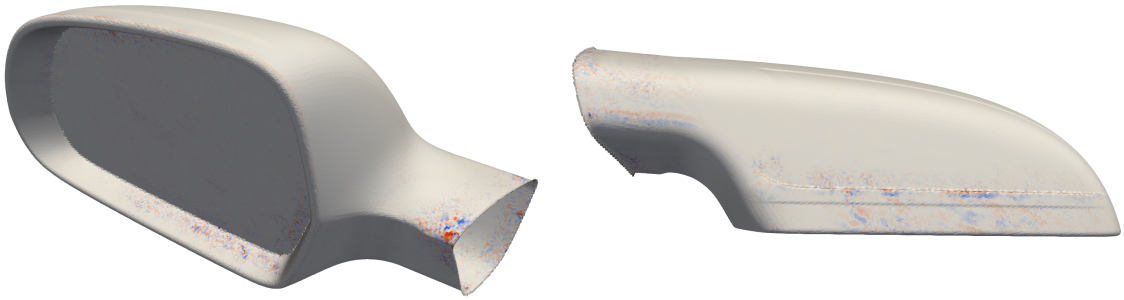

(b) Minimizing window vibration, J_{vib}

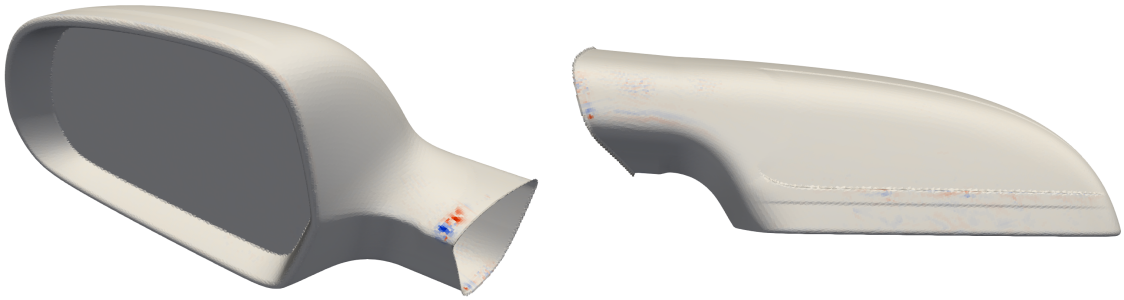

(c) Minimizing interior pressure level, J_{int}

Figure 7.4: Investigation of the influence of the noise prediction steps for vehicle aeroacoustic adjoint optimization using filtering for 800-4000Hz: Sensitivity maps targeting at different objective functions expressed at different stages of the noise prediction chain. Red areas must be pushed inwards whereas blue areas must be pulled outwards in order to minimize the corresponding objective function.

Minimization of acoustic pressure on the window

In figs 7.6 and 7.7, the sensitivity maps for acoustic pressure minimization on the window, computed for the eight one-third frequency bands in the range 800-4000Hz are presented. In addition, the displacement according to these maps is

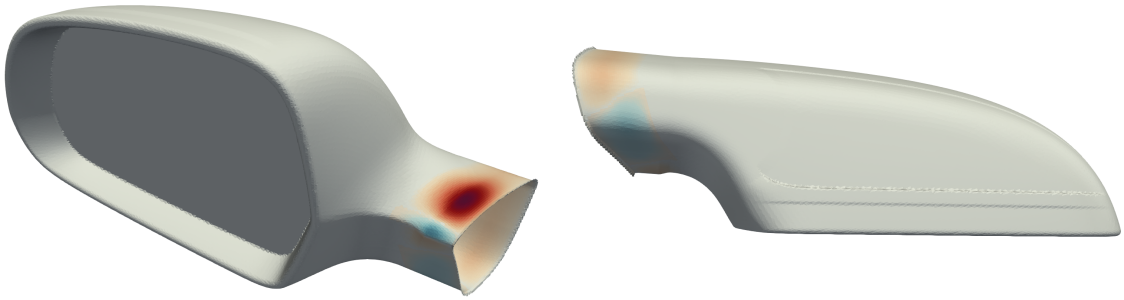

(a) Minimizing acoustic pressure, J_{KI}

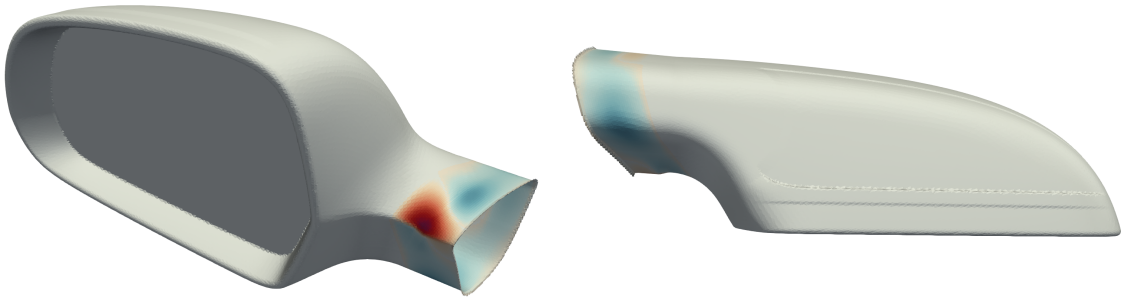

(b) Minimizing window vibration, J_{vib}

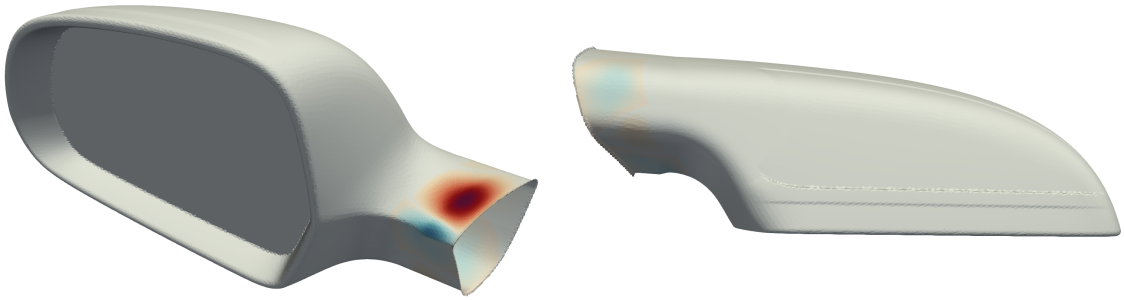

(c) Minimizing interior pressure level, J_{int}

Figure 7.5: Investigation of the influence of the noise prediction steps for vehicle aeroacoustic adjoint optimization using filtering for 800-4000Hz: Geometry displacement based on sensitivity maps targeting at different objective functions defined in the noise prediction chain.

presented in figs 7.8 and 7.9, where the differences are more clear.

For frequencies up to 1413Hz, a sensitivity indicating an outward displacement dominates the upper side of the mirror neck, whereas above this frequency the sensitivity sign changes, apart from the downwind edge which remains the same up to 2818Hz. Changes w.r.t. frequency ranges are stronger, on the lower

1/3 Octave Bands		
Lower Band Limit (Hz)	Nominal Band Limit (Hz)	Upper Band Limit (Hz)
708	800	891
891	1000	1122
1122	1250	1413
1413	1600	1778
1778	2000	2239
2239	2500	2818
2818	3150	3548
3548	4000	4467

Table 7.2: Lower, upper and nominal frequencies for one-third octave bands.

side of the mirror, where there is no easily identifiable trend. In addition, at the last two frequency bands of the adjoint sensitivities, numerical noise is becoming more apparent. This is due to the fact that the energy content is quite small at these high frequencies, and the magnitude of numerical errors of the adjoint method becomes more significant.

Minimization of interior pressure level

Similarly, in figs 7.10 and 7.11, the sensitivity maps for interior noise minimization, computed for the eight one-third frequency bands in the range 800-4000Hz are presented. The corresponding displacements are presented in figs 7.12 and 7.13.

A similar pattern is observed on the upper side of the mirror neck for frequency ranges between 708-891Hz and 1122-2239Hz, where an outward displacement for most of the upper region and an inward for the most downwind edge, are indicated as optimal. These sensitivities are opposite from the sensitivity map computed without filtering, presented in fig. 6.5(a). This means that the optimization in section 6.3.1 was on the opposite direction from the optimal one required for frequencies between 700-2000Hz. This can be actually observed in fig. 7.1, where the baseline geometry performs better for this range than the optimal.

7.4 Conclusions

This chapter enhanced the continuous adjoint aeroacoustic framework presented in chapter 6 with a signal filtering process in order to compute sensitivity maps for specific frequency ranges. Specifically the Butterworth filter was utilized and its adjoint was formulated and implemented.

Two studies were presented, both focusing in the frequency range between

800-4000Hz which is of interest for vehicle aeroacoustic test cases. Firstly, the influence that each step of the noise prediction chain has on interior pressure level was investigated. It was demonstrated, both by means of sensitivity maps and by a one-step morphing of the mirror geometry, that the minimization of an objective function early in the aeroacoustic process does not translate to a reduction in the interior pressure level. This lack of correlation between the several steps was more obvious in the aforementioned frequency range than in the complete frequency spectrum, presented in chapter 6.

Moreover, the proposed continuous adjoint method was applied to compute a sensitivity map for each one-third frequency band in the range 800-4000Hz, for two objective functions, J_{KI} and J_{int}. This study demonstrated that, for both objective functions, each frequency band required a different change in the mirror surface geometry. Therefore, the reduction in the interior pressure level for an extended frequency range can practically be seen as a multi-objective optimization, where different frequencies may compete with each other.

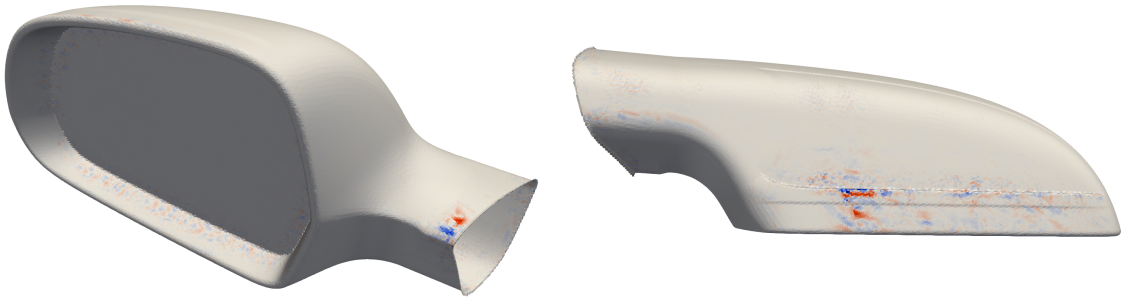

(a) Frequency Range: 708 Hz - 891 Hz

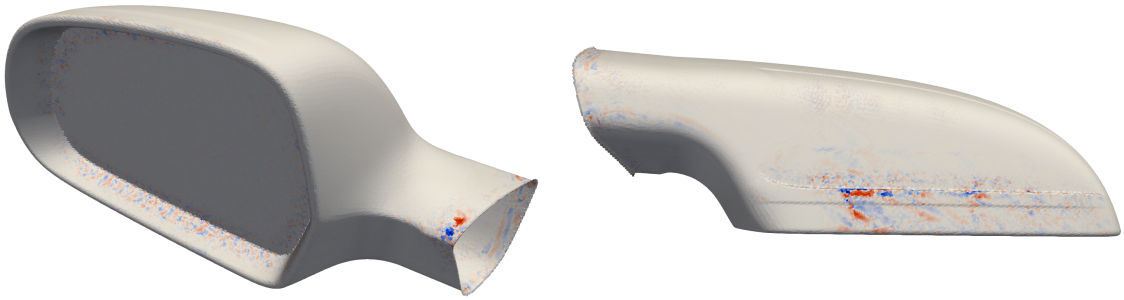

(b) Frequency Range: 891 Hz - 1122 Hz

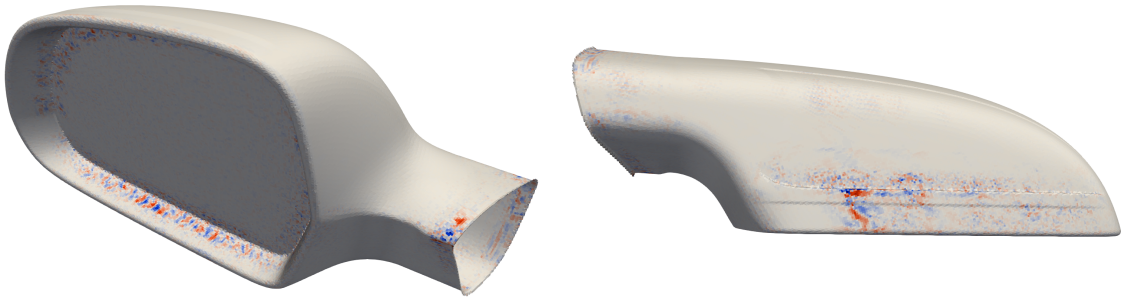

(c) Frequency Range: 1122 Hz - 1413 Hz

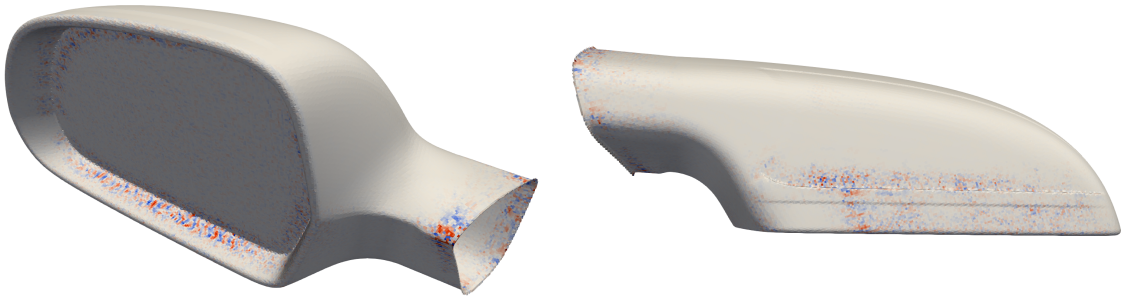

(d) Frequency Range: 1413 Hz - 1778 Hz

Figure 7.6: Minimization of acoustic pressure on the vehicle's window: Sensitivity maps computed for different one-third octave frequency bands.

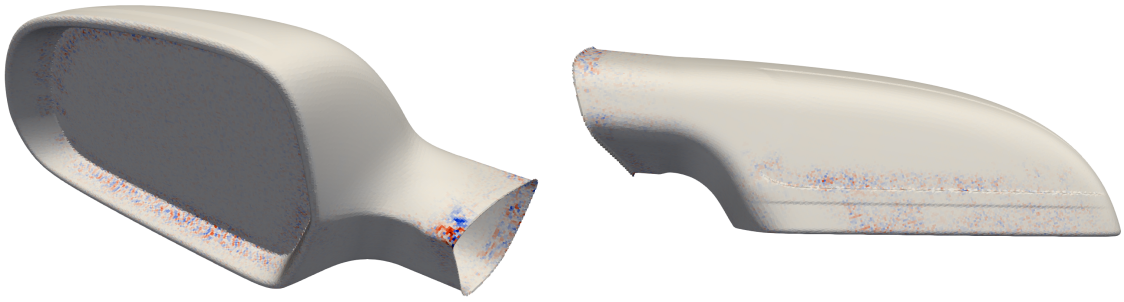

(a) Frequency Range: 1778 Hz - 2239 Hz

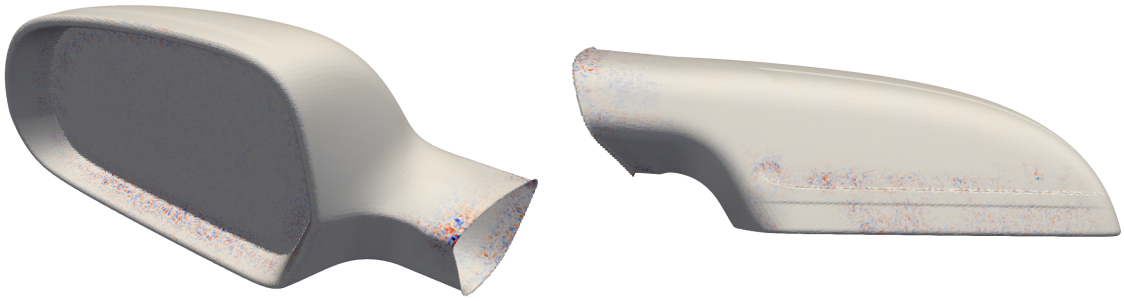

(b) Frequency Range: 2239 Hz - 2818 Hz

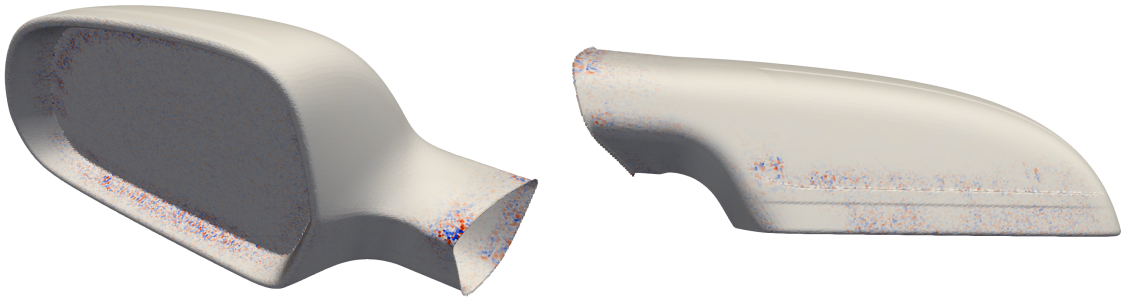

(c) Frequency Range: 2818 Hz - 3548 Hz

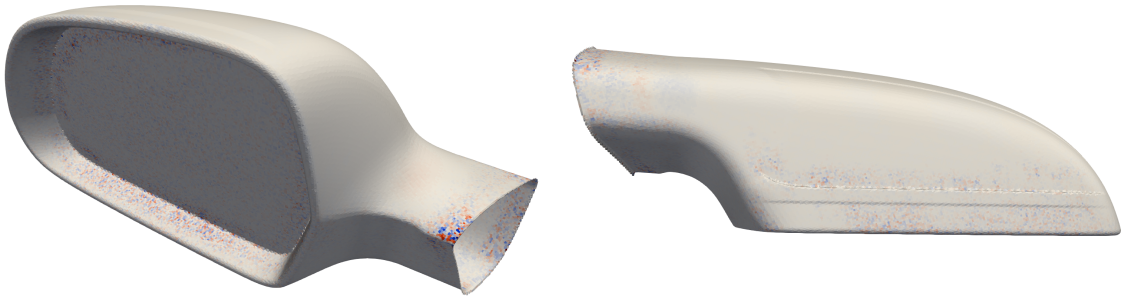

(d) Frequency Range: 3548 Hz - 4467 Hz

Figure 7.7: Minimization of acoustic pressure on the vehicle's window: Sensitivity maps computed for different one-third octave frequency bands.

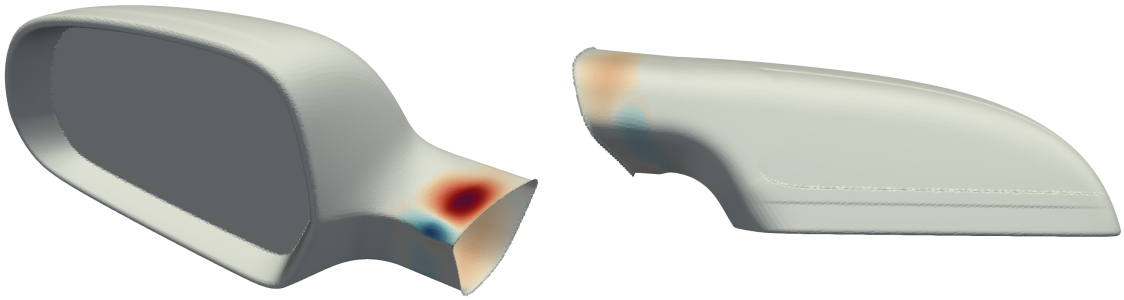

(a) Frequency Range: 708 Hz - 891 Hz

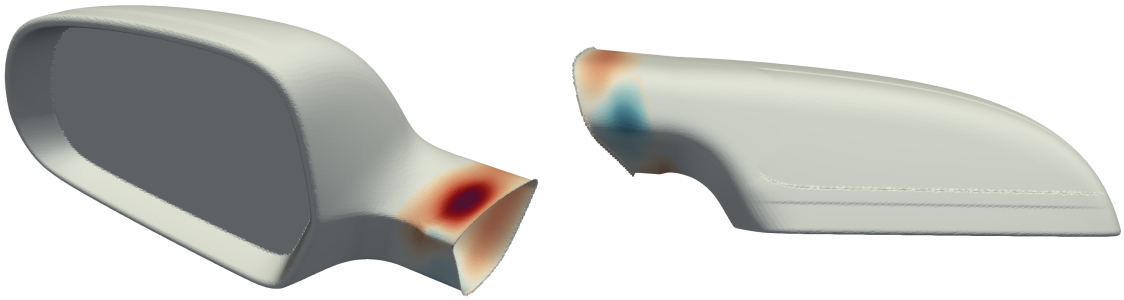

(b) Frequency Range: 891 Hz - 1122 Hz

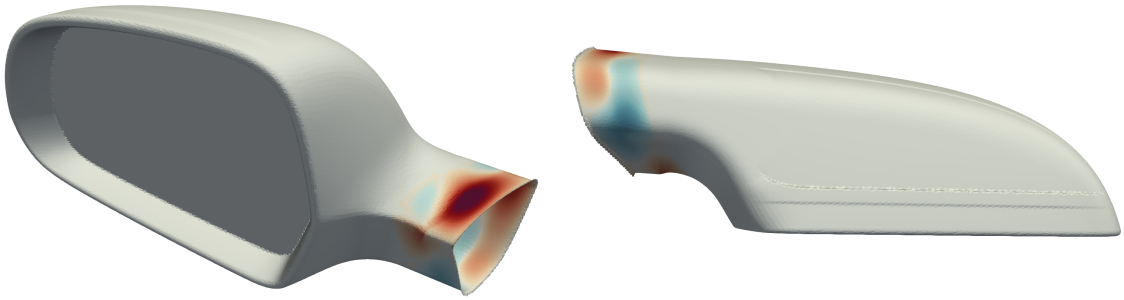

(c) Frequency Range: 1122 Hz - 1413 Hz

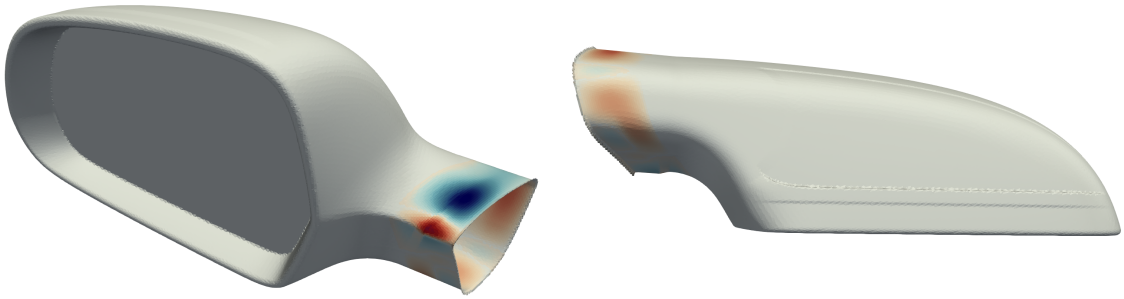

(d) Frequency Range: 1413 Hz - 1778 Hz

Figure 7.8: Minimization of acoustic pressure on the vehicle's window: Geometry displacement based on sensitivity maps computed for different one-third octave frequency bands.

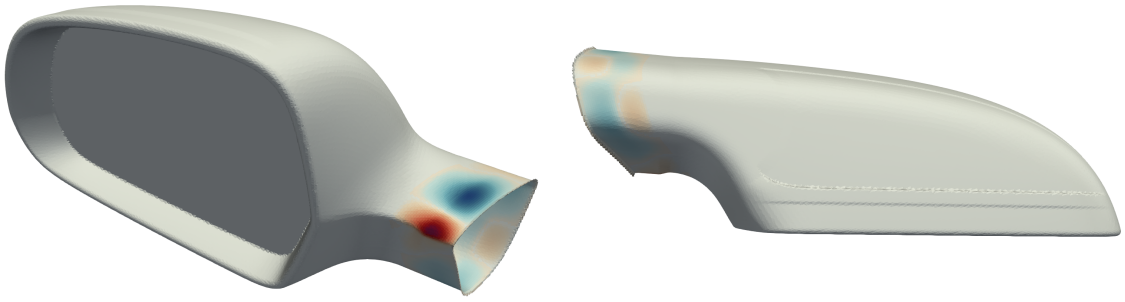

(a) Frequency Range: 1778 Hz - 2239 Hz

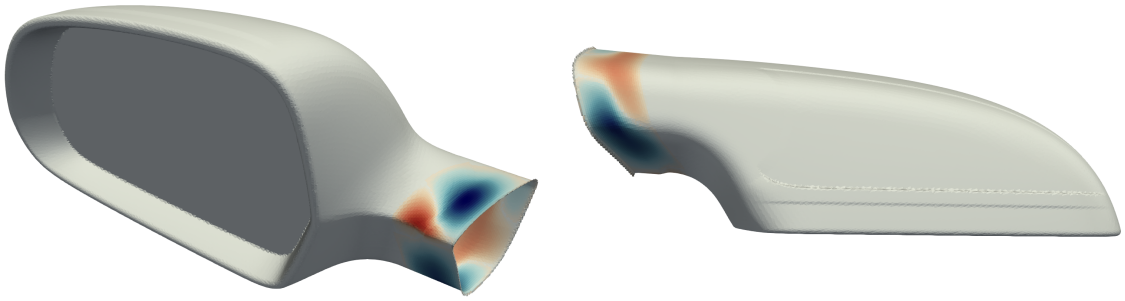

(b) Frequency Range: 2239 Hz - 2818 Hz

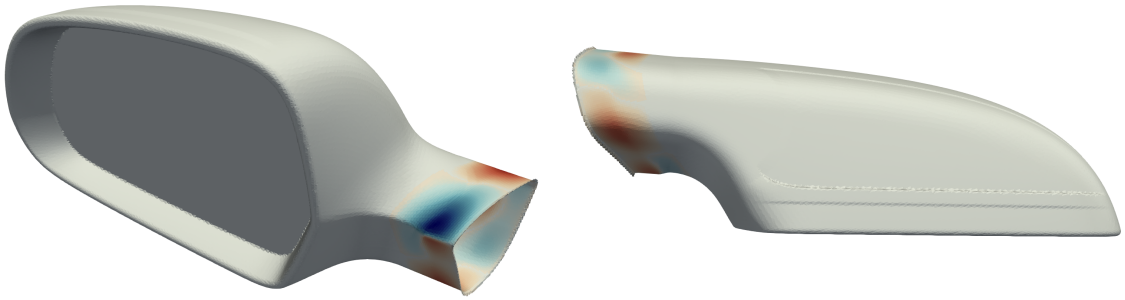

(c) Frequency Range: 2818 Hz - 3548 Hz

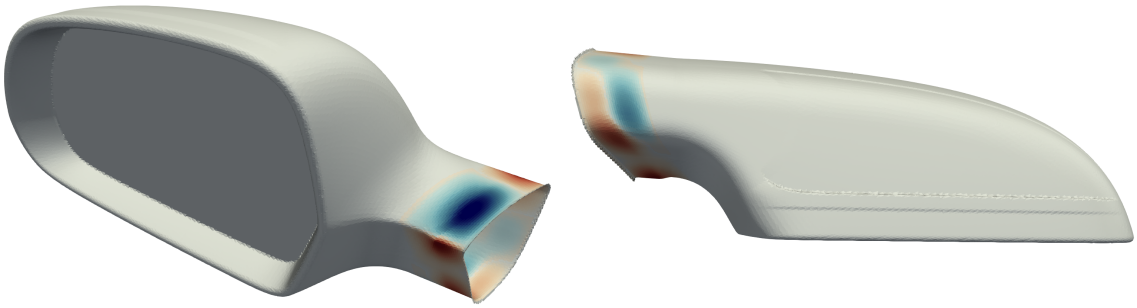

(d) Frequency Range: 3548 Hz - 4467 Hz

Figure 7.9: Minimization of acoustic pressure on the vehicle's window: Geometry displacement based on sensitivity maps computed for different one-third octave frequency bands.

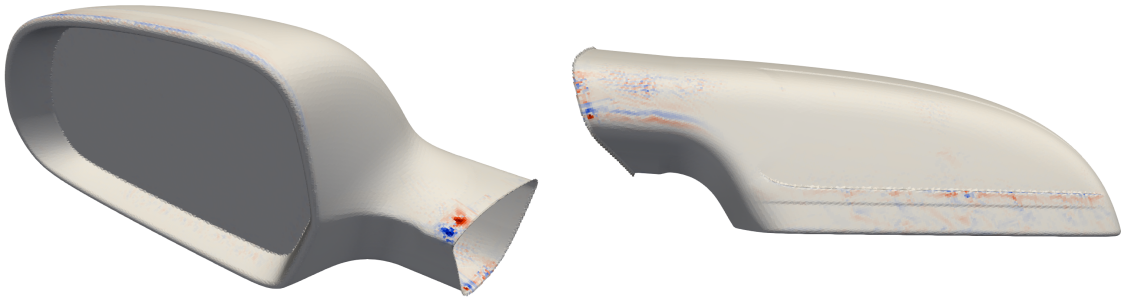

(a) Frequency Range: 708 Hz - 891 Hz

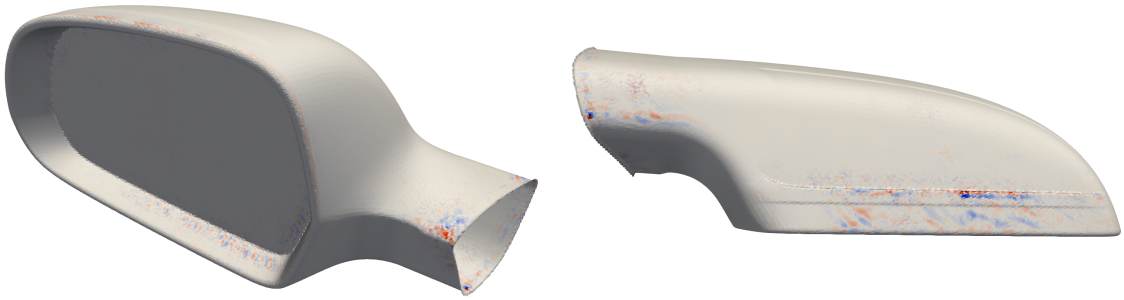

(b) Frequency Range: 891 Hz - 1122 Hz

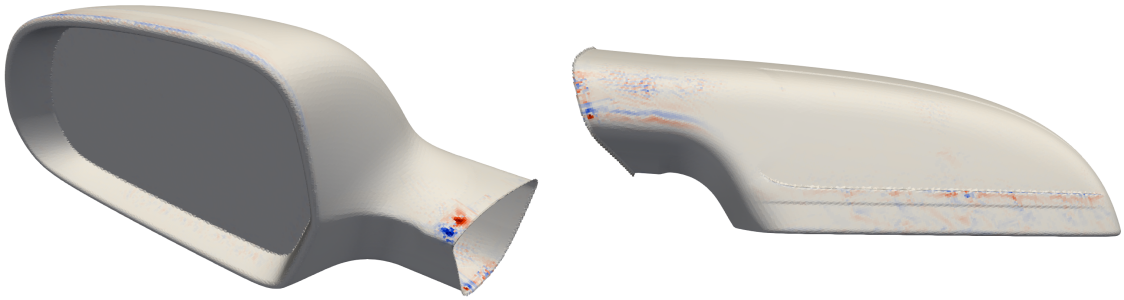

(c) Frequency Range: 1122 Hz - 1413 Hz

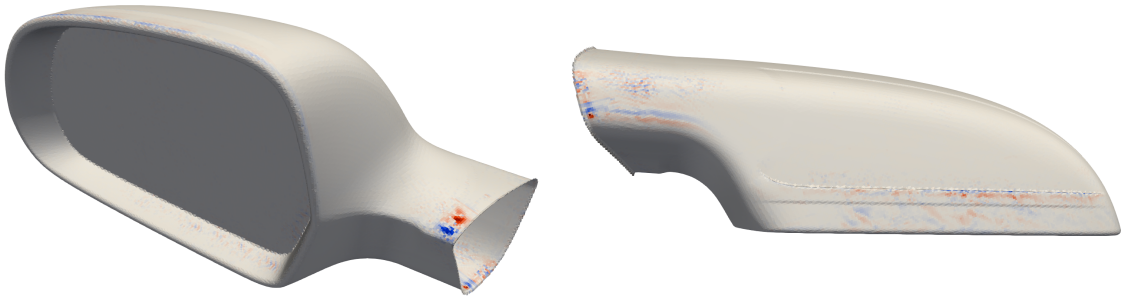

(d) Frequency Range: 1413 Hz - 1778 Hz

Figure 7.10: Targeting at minimization of interior acoustic pressure near driver's ear: Sensitivity maps computed for different one-third octave frequency bands.

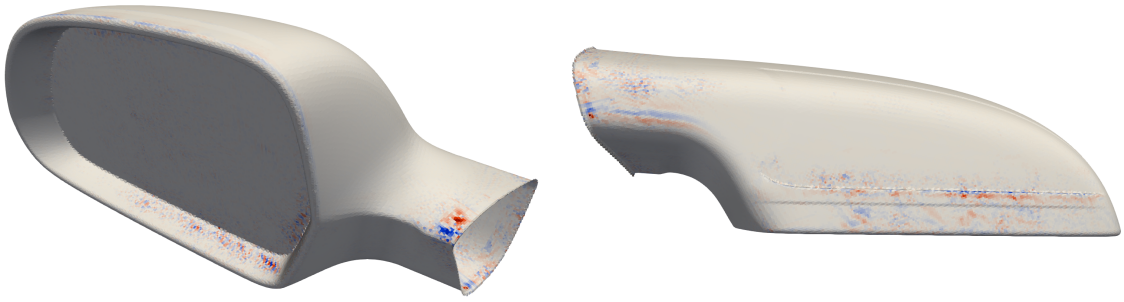

(a) Frequency Range: 1778 Hz - 2239 Hz

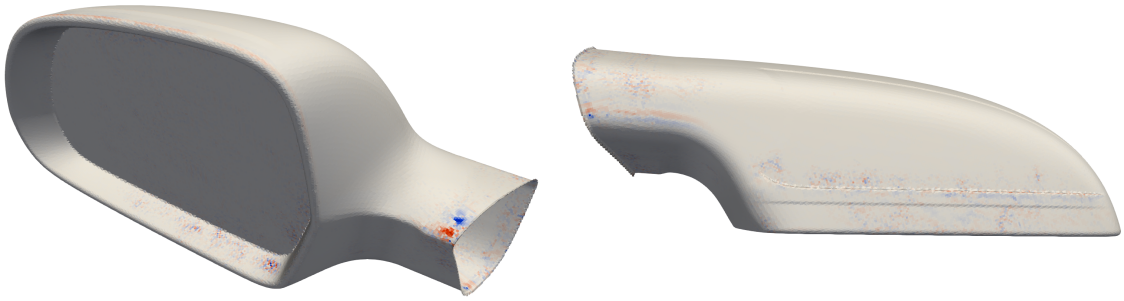

(b) Frequency Range: 2239 Hz - 2818 Hz

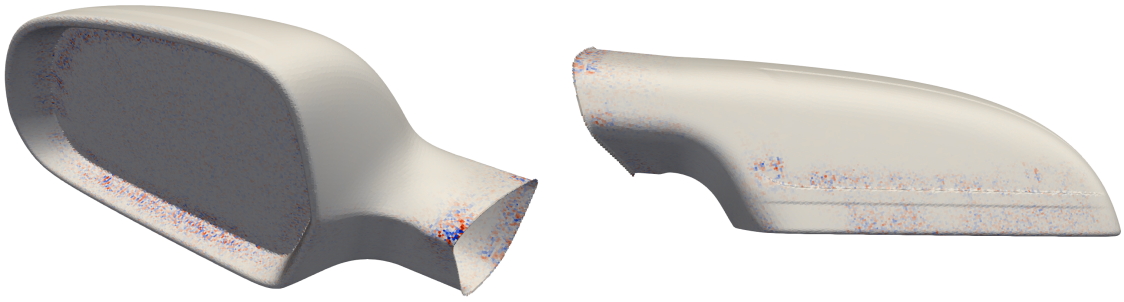

(c) Frequency Range: 2818 Hz - 3548 Hz

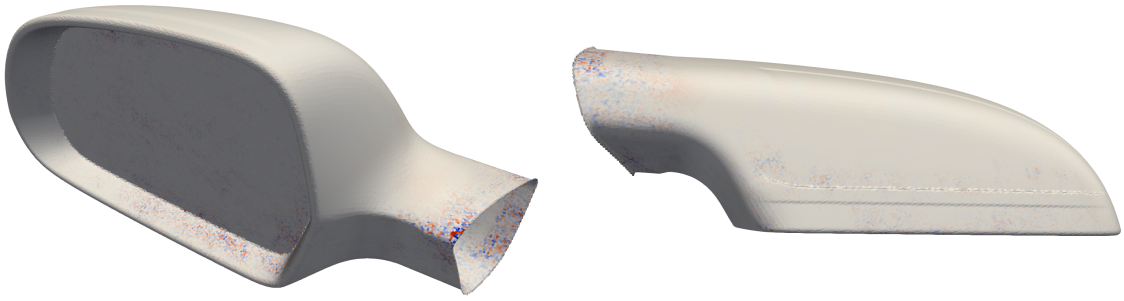

(d) Frequency Range: 3548 Hz - 4467 Hz

Figure 7.11: Targeting at minimization of interior acoustic pressure near driver's ear: Sensitivity maps computed for different one-third octave frequency bands.

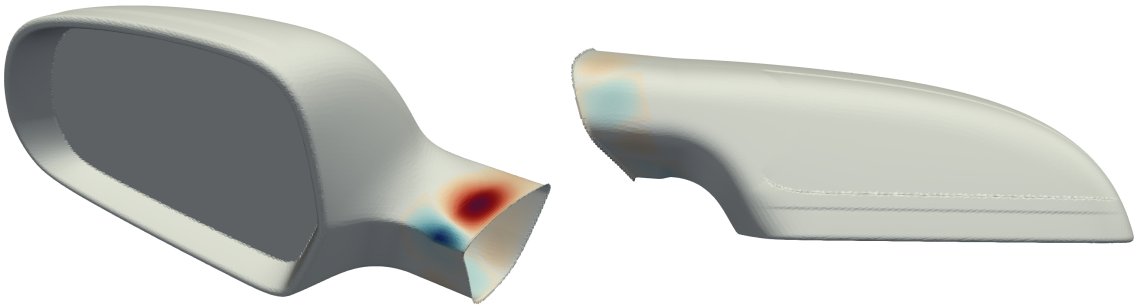

(a) Frequency Range: 708 Hz - 891 Hz

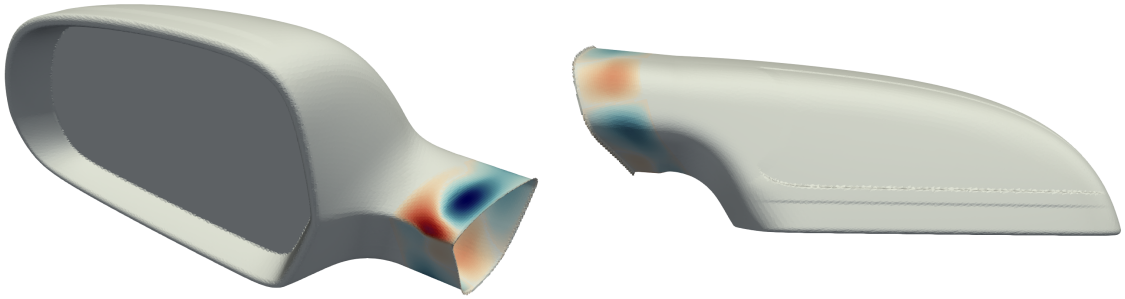

(b) Frequency Range: 891 Hz - 1122 Hz

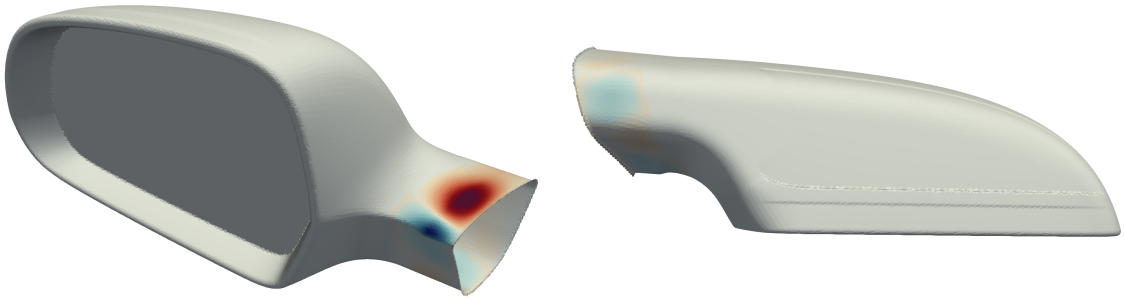

(c) Frequency Range: 1122 Hz - 1413 Hz

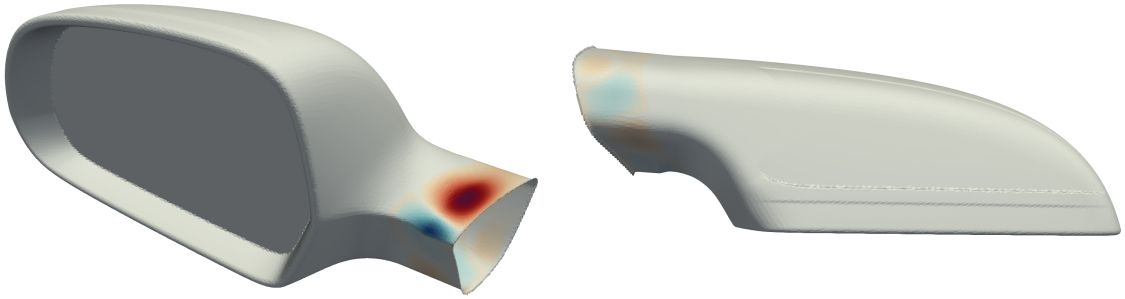

(d) Frequency Range: 1413 Hz - 1778 Hz

Figure 7.12: Targeting at minimization of interior acoustic pressure near driver's ear: Geometry displacement based on sensitivity maps computed for different one-third octave frequency bands.

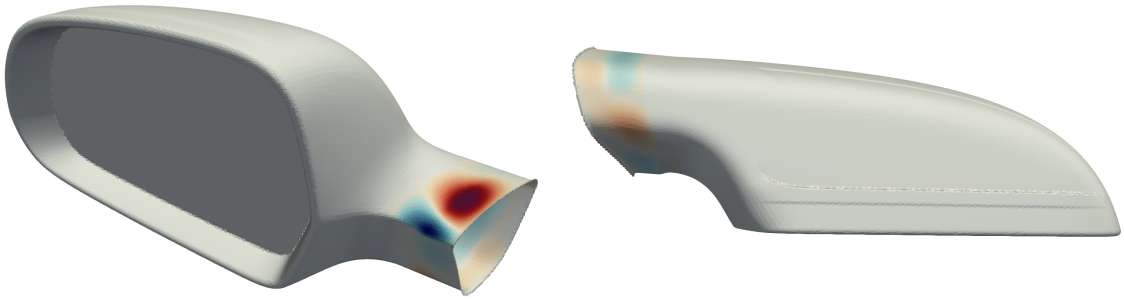

(a) Frequency Range: 1778 Hz - 2239 Hz

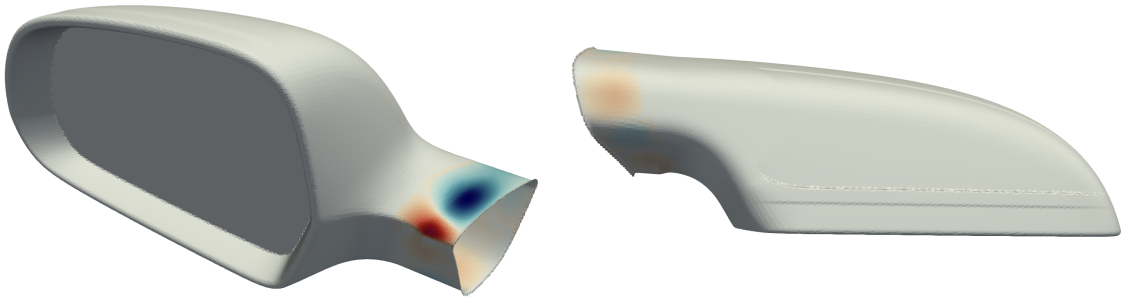

(b) Frequency Range: 2239 Hz - 2818 Hz

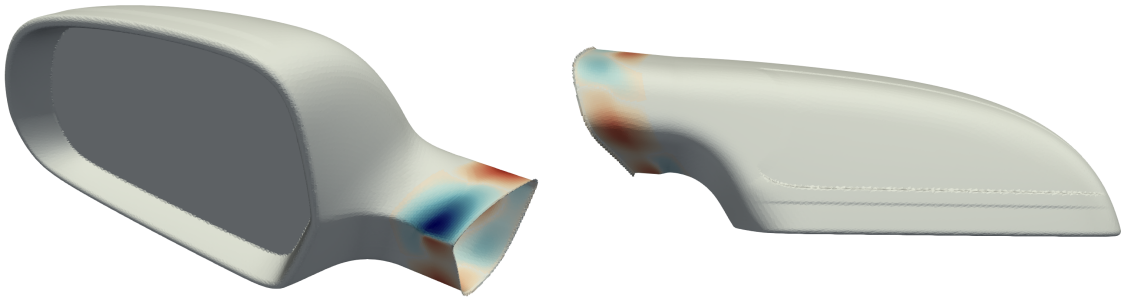

(c) Frequency Range: 2818 Hz - 3548 Hz

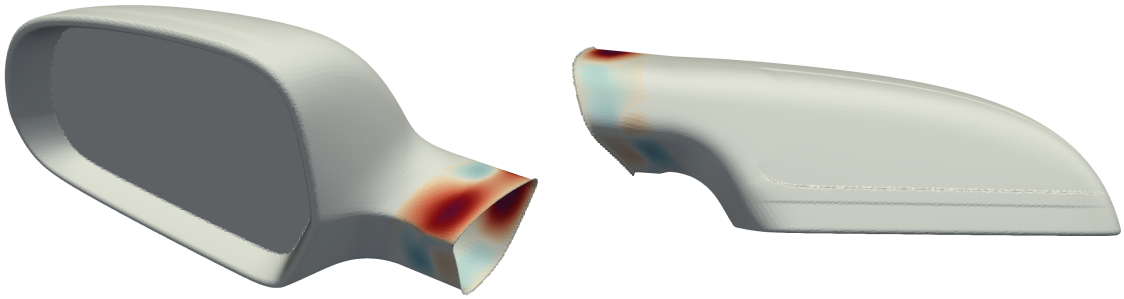

(d) Frequency Range: 3548 Hz - 4467 Hz

Figure 7.13: Targeting at minimization of interior acoustic pressure near driver's ear: Geometry displacement based on sensitivity maps computed for different one-third octave frequency bands.

Chapter 8

Closure-Conclusions

This doctoral thesis aimed at formulating and developing the continuous adjoint method to an existing framework for automotive aeroacoustics. The programming of the proposed method was carried out using the open-source CFD toolbox OpenFOAM© and was applied to minimize the wind noise transmission into the interior of the SAE body, a generic vehicle. In the next paragraphs, the presented developments and the conclusions drawn in each chapter are summarized.

In Chapter 2, the constituent parts of the noise prediction chain for vehicle aeroacoustics were presented. The equations governing the physical mechanisms of noise creation and transmission to the interior as well as their coupling were described. These were the starting point for the continuous adjoint development in the following chapters. In order to demonstrate the accuracy of the primal analysis and to give an overview of the challenges faced at aeroacoustic design, the results of the experimental validation of the aforementioned process performed by Kabat vel Job [68] were summarized here with kind permission of Volkswagen Group Research.

To formulate the continuous adjoint method, the aforementioned framework was split in two domains; the exterior domain includes the flow-induced noise generation and radiation to the window whereas the interior domain includes the vibroacoustic model for window vibration and interior wave propagation. These systems were firstly examined separately and were afterwards coupled to propose the continuous adjoint chain for vehicle aeroacoustic optimization.

In Chapter 3, the adjoint to the vibroacoustic model was developed. Here, the adjoint wave and bending wave equations, their boundary and initial conditions, their coupling and the sensitivity derivatives (SD) expression were derived. The SD expression on the window w.r.t. input pressure load can be either used directly if there is an analytical expression of the load or used to couple the vibroacoustic model to the external flow simulation, where the input pressure load is computed. It was demonstrated that in order to ensure the accuracy of the SD expression/coupling term on the side window, its discretization must be derived

based on a discrete adjoint perspective, in this thesis with hand-differentiation. Specifically, the source term of the bending wave equation, namely the pressure load obtained by the CFD solution, is expressed at the CFD time steps which do not coincide to those of the bending wave solution. The differentiation of this term contributes to the SD/coupling term on the window and using an ordinary discretization scheme neglects several time steps of the adjoint deflection, becoming so prone to numerical errors. The interior propagation and window deflection were firstly verified separately against Finite Differences (FD), using a synthetic wave as an input, parameterized by its amplitude. Afterwards the adjoint coupled vibroacoustic model was verified against FD, using the aforementioned synthetic wave as an input and also using an actual acoustic pressure field, computed with CFD/CAA. In all cases, the adjoint gradients showed a very good agreement with the FD and the adjoint vibroacoustic model can be coupled to any simulation chain that computes the exterior flow and sound radiation to the window.

In Chapter 4, the continuous adjoint method was formulated for the Navier-Stokes equations and the Kirchhoff Integral acoustic analogy. The unsteady adjoint Navier-Stokes equations, their boundary and initial conditions and the adjoint Kirchhoff Integral were derived. In order to take the impact of interior grid node displacement into account, grid displacement models were incorporated in the mathematical development. This gave rise to the adjoint grid displacement equations (aGDE) as well as a Grid Sensitivity (GS) term. Two different displacement models were considered in this thesis. The first model is based on volumetric B-Splines to displace the geometry and the interior grid nodes whereas the second one uses the Laplace equations to propagate an already computed geometry displacement into the grid interior. The former results in an algebraic adjoint grid displacement equation, similar to the primal one, and in a field integral SD term. In this case, the computation of the aGDE and the GS term are performed in a straightforward manner, since grid sensitivities are computed analytically with the volumetric B-Splines model. However, since the GS term is a field term, the visualization of the grid sensitivities with a sensitivity map is not possible. The Laplace equation on the other hand results in an Poisson aGDE. Since the GS term is expressed as a surface integral along the parameterized surface, it can be visualized with a sensitivity map so this approach proved to be advantageous for various investigations that followed in the thesis.

Chapter 4 also laid emphasis upon the time window T_s over which the simulation is performed and the time window T_{of} over which the objective function is evaluated. These do not necessarily coincide which is reflected on the adjoint boundary condition along the noise radiating body as well as on the time integration of the sensitivity derivatives. It was demonstrated in chapter 5 that, in order for the adjoint gradients to be consistent with the primal problem, the adjoint equations must not be integrated only along T_{of}. The adjoint boundary conditions that depend on the objective function are imposed during T_{of} and, af-

terwards, are set to zero for the remaining time, while the magnitude of the adjoint fields decays. A comparative study by means of sensitivity maps on the mirror of the SAE body targeting at minimizing flow-induced noise radiation at the vehicle's window showed that solving the adjoint equations only for T_{of} computes different gradient values which do not guarantee to solve the same optimization problem.

Chapter 5 focused on the verification of the proposed adjoint method for flow-induced sound radiation. Due to the fact that for long and turbulent flow simulations it is difficult to compute converged and, thus, accurate FD, a simpler test case was selected that investigates the turbulent flow around a 3D cylinder. Firstly, the differentiated geometric terms of the Kirchhoff Integral were verified against FD by perturbing the design variables while keeping the flow "frozen" and showed an excellent agreement. Afterwards, the flow SD were verified against FD targeting at minimizing pressure fluctuations on the cylinder as well as radiated acoustic pressure at receivers placed around the cylinder. In both cases, the adjoint SD showed a very good agreement with the FD. In addition, the significance if incorporating the grid displacement model in the adjoint formulation was demonstrated. The proposed method was then applied to optimize the mirror of the SAE body so as to reduce the radiated acoustic pressure on its side window. Three optimization cycles were performed and the obtained optimized shape of the mirror was displaced by a maximum of 2.6mm. The objective function, the time average of the squared sound pressure at the vehicle's side window, was minimized by 35%.

After the development of the continuous adjoint method to the interior and exterior domain, Chapter 6 coupled the two domains to present the adjoint aeroacoustic chain to efficiently compute the aeroacoustic sensitivity map on the side mirror of vehicles; it indicates the optimal normal direction in which the mirror geometry should be deformed, in order to achieve a reduction in the wind noise transmission to the driver's ear and thus improve the aeroacoustic performance of the vehicle. The proposed adjoint aeroacoustic framework was used to optimize the side mirror of the SAE body and, after three optimization cycles, yielded a 14.1% reduction in the interior SPL. Afterwards, an investigation into the influence that an optimization with regard to each individual step of the noise prediction chain has on the interior sound pressure level was conducted. Four noise-related objective functions expressed at different stages of the aforementioned simulation chain were used, targeting at minimizing

1. pressure fluctuations on the side mirror
2. acoustic pressure fluctuations on the side window
3. window deflection
4. interior pressure fluctuations near the driver's ear.

A sensitivity map was computed for each of these objective functions and the baseline geometry was modified based on these maps, yielding four new geome-

tries. The steps of the aeroacoustic framework were simulated again for each one of new geometries to compute the new objective function value at each step. It was observed that a reduction in one step, did not necessarily translate to a reduction in the following steps meaning that is not a clear correlation between the stages of the noise prediction chain. Consequently, the incorporation of all four steps in the adjoint chain is important in order to guarantee a reduction in the interior pressure level.

The aforementioned 14% reduction in interior noise achieved in Chapter 6 concerned the complete frequency spectrum. Due to the fact that low frequencies have a greater energy content, the optimization is rather biased towards those. Since vehicle aeroacoustics are more relevant for a frequency range of $800 - 4000Hz$, Chapter 7 proposed a frequency domain approach, so that the optimization can target at specific frequency ranges. A Butterworth filter was implemented at an early stage of the noise prediction chain in order to maintain only the frequency components of interest. Therefore, no additional code enhancement is required, neither for the computation of the objective function, nor for its differentiation and the adjoint chain. The influence that each step of the noise prediction chain has on interior pressure level was investigated, this time focusing only on the frequency range $800 - 4000Hz$. It was demonstrated that the lack of correlation between the several steps was more obvious in the aforementioned frequency range than in the complete frequency spectrum, presented in chapter 6. Finally, the proposed continuous adjoint method was applied to compute a sensitivity map for each one-third frequency band in the range 800-4000Hz, targeting at minimizing acoustic pressure at the SAE body's side window and its interior. It was shown that each frequency band required a different change in the mirror surface geometry. Therefore, the reduction of interior pressure level for an extended frequency range can be practically seen as a multi-objective optimization, where different frequencies may conflict with each other.

8.1 Novel Contributions

This PhD thesis has several novelties and findings. The main contributions are summarized below:

- Formulation, development and verification of the continuous adjoint method for an aeroacoustic prediction process which consists of an unsteady IDDES flow simulation and the Kirchhoff Integral method for sound propagation. This method was succesfully applied to a large scale problem investigating the flow-induced sound radiation from the side mirror of the SAE vehicle to its side window.

- Formulation, development and verification of the continuous adjoint method for a vibroacoustic model which consists of the bending wave and wave equa-

tions, used to predict the pressure-excited window vibration of a traveling vehicle and the interior propagation of sound waves.

- Development of a continuous adjoint framework for vehicle aeroacoustic optimization. It is the first time in the literature that aeroacoustic sensitivity maps are computed in automotive applications. These take all physical mechanisms of noise generation and transmission into account and are a powerful tool that provides an insight to the aeroacoustic engineers and designers into potential geometry modifications that can improve the aeroacoustic performance of a vehicle.

- The impact of the time windows over which the adjoint simulation is performed and the unsteady adjoint sensitivities are integrated have on the consistency of the computed sensitivities w.r.t. the primal procedure was demonstrated here for the first time in the literature of the unsteady adjoint method.

- The significance of incorporating grid displacement models in the mathematical formulation of the continuous adjoint method for aeroacoustic shape optimization problems was demonstrated.

- Development and implementation of the adjoint to the Butterworth filter. This enabled a straightforward way to compute sensitivity derivatives for specific frequency ranges. An alternative way would be to include the Fourier Transform in a time-domain objective function. The mathematical formulation and its differentiation were also presented in this thesis.

- Regarding vehicle aeroacoustics, it was demonstrated that there is no direct correlation between the four steps of the noise prediction chain. This means that, for instance, minimizing pressure fluctuations on the mirror will not necessarily result in a reduction of interior SPL. Therefore, during aeroacoustic design the complete aeroacoustic framework must be considered.

8.2 Publications, Talks & Seminars

Journal publications, conference papers and seminar talks resulted, thus far, from the research carried out in this thesis are listed below:

- C.S. Kapellos, E.M. Papoutsis-Kiachagias, K.C. Giannakoglou and M. Hartmann, *"The unsteady continuous adjoint method for minimizing flow-induced sound radiation"*, Journal of Computational Physics, Volume 392, 1 September 2019, Pages 368-384

- C.S. Kapellos and M. Hartmann, *"A Continuous Adjoint Framework for Vehicle Aeroacoustic Optimization"*, Internoise Conference, 25-29 August 2018, Chicago, USA

- C.S. Kapellos, *"Aeroacoustic optimization by means of sensitivity maps"*, German OpenFOAM User Meeting, February 2018, Braunschweig, Germany

- C.S. Kapellos, *"Adjoint Theory & Solver in OpenFOAM"*, German OpenFOAM User Meeting, March 2017 & February 2018, Braunschweig, Germany

- C.S. Kapellos and M. Hartmann, *"A continuous adjoint approach for vehicle interior noise reduction"*, ECCOMAS Congress, June 2016, Crete, Greece

Journal publications, conference papers and talks resulted from research carried out during this thesis in the field of adjoint optimization and parameterization are listed below:

- D. Agarwal, C. Kapellos, T. Robinson and C. Armstrong, *"Using Parametric effectiveness for efficient CAD-based adjoint optimization"*, Computer-Aided-Design and Applications, Volume 16, Issue 4, Pages 703-719, 2019

- D. Agarwal, T. Robinson, C. Armstrong and C. Kapellos, *"Enhancing CAD-based shape optimization by automatically updating the CAD model's parameterization"*, Structural and Multidisciplinary Optimization, Volume 59, Issue 5, Pages 1639{1654, 2018

- D. Agarwal, C. Kapellos, T. Robinson, C. Armstrong, *"Using parametric effectiveness for efficient CAD-based automotive design driven by adjoint sensitivity maps"*, EUROGEN 2017, September 2017, Madrid

- C. Kapellos, P. Alexias and E. De Villers, *"Das Adjungiertenverfahren in der Fahrzeugoptimierung unter Verwendung eines Sphärizität-basierten Morphers"*, *"The adjoint method for automotive optimisation using a Sphericity based morpher"*, NAFEMS CFD Seminar, October 2016, Wiesbaden

- D. Agarwal, C. Kapellos, T. Robinson, C. Armstrong, *"Parametric CAD model based shape optimization using adjoint functions"*, 11th ASMO UK/ ISSMO/ NOED2016, July 2016, Munich, Germany

- C.S. Kapellos, I.S. Kavvadias, E.M. Papoutsis-Kiachagias and K.C. Giannakoglou, *"A contribution to the unsteady continuous adjoint method for the optimization of jet-based flow control systems"*, EUROGEN 2015, September 2015, Glasgow, UK

8.3 Future Work

- The proposed adjoint aeroacoustic framework can be applied to several vehicle geometries, together with wind tunnel experiments, in order to extract more information regarding noise creation mechanisms. In addition, the synergy of the adjoint method with a noise source localization method [36] may prove to be useful.

- Several approaches have been proposed to minimize the excessive computational cost of the unsteady adjoint method, either by compressing the primal time-series needed for the adjoint method [136, 111], or by increasing computational time but reducing memory requirements [109], or by solving the unsteady equation forward in time [107]. However, none of these has reached the maturity to be applied to large-scale problems. Therefore, large memory requirements and the long simulation times of the unsteady adjoint method remain a challenge that must be addressed.

- The proposed adjoint method for flow-induced sound radiation problems can be extended to sound pollution problems from motorways to the surrounding enviroment. The design variables of such a problem would be the design of noise-absorbing structures or the integration of vegetation (trees etc.).

- The development of the adjoint vibroacoustic model enables the investigation into optimizing cabin components in order to suppress interior noise propagation. Feasibility studies for active noise control systems in vehicle interior, for example in the form of actuators on the window to cancel out the propagating bending waves, can be now conducted.

Appendix A

Turbulent flow around a 3D Cylinder, Re=500

In chapter 5, a simpler test case was used in order to verify the adjoint derivatives, due to the less computational time it required. In this case, the turbulent flow around an isolated 3D cylinder and the flow-induced sound radiation is investigated.

The Reynolds number based on the cylinder diameter $D = 0.1m$ is $Re_D = 500$; in this case, the wake exhibits fully turbulent behavior for a cylinder spanwise length greater than π diameters [69]. In the case presented in this PhD thesis, the spanwise length of the cylinder is $4D$, with a far-field distance of the flow domain $15D$ and symmetry planes at the cylinder's edges.

A.1 Grid independence study

A grid independence study on the selection of a fine enough O-type structured grid is conducted at first, see table A.1. The time step is $5 \cdot 10^{-3}s$ and yields a Courant number between 0.3 and 0.7, the latter obtained on the finest grid. After the initial transient phase, 40 periods in total are considered to compute the mean and Root Mean Square (RMS) values of the drag and lift coefficients, table A.1. The resulting shedding frequency is about 0.3Hz, fig. A.1, and the Strouhal number about 0.214, which both belong into the experimental range according to [78] and [125]. The sound radiation from the cylinder is computed over the same 40 periods and the directivity pattern at 120 receivers placed at a distance of 15D on the Z-plane crossing the middle of the cylinder is shown in fig. A.1.

From table A.1 and fig. A.1 it is clear that the aerodynamic coefficient values as well as the sound radiation computed for Grid 2 are comparable to those computed over the finer Grids 3 and 4, at a smaller computational cost though. Therefore, Grid 2 is used in chapter 5 for the adjoint verification through comparisons with FD.

	Grid Nodes (circum. × radial × span)	Cells Number	y^+	$\overline{c_D}$	RMS c_D	RMS c_L
Grid 1	152 × 125 × 40	760K	0.127	1.216	0.037	0.381
Grid 2	208 × 165 × 40	1373K	0.099	1.197	0.052	0.345
Grid 3	318 × 247 × 40	3082K	0.066	1.206	0.039	0.350
Grid 4	318 × 247 × 60	4624K	0.063	1.204	0.047	0.330

Table A.1: Turbulent flow around a 3D cylinder at $Re_D = 500$, grid independence study.

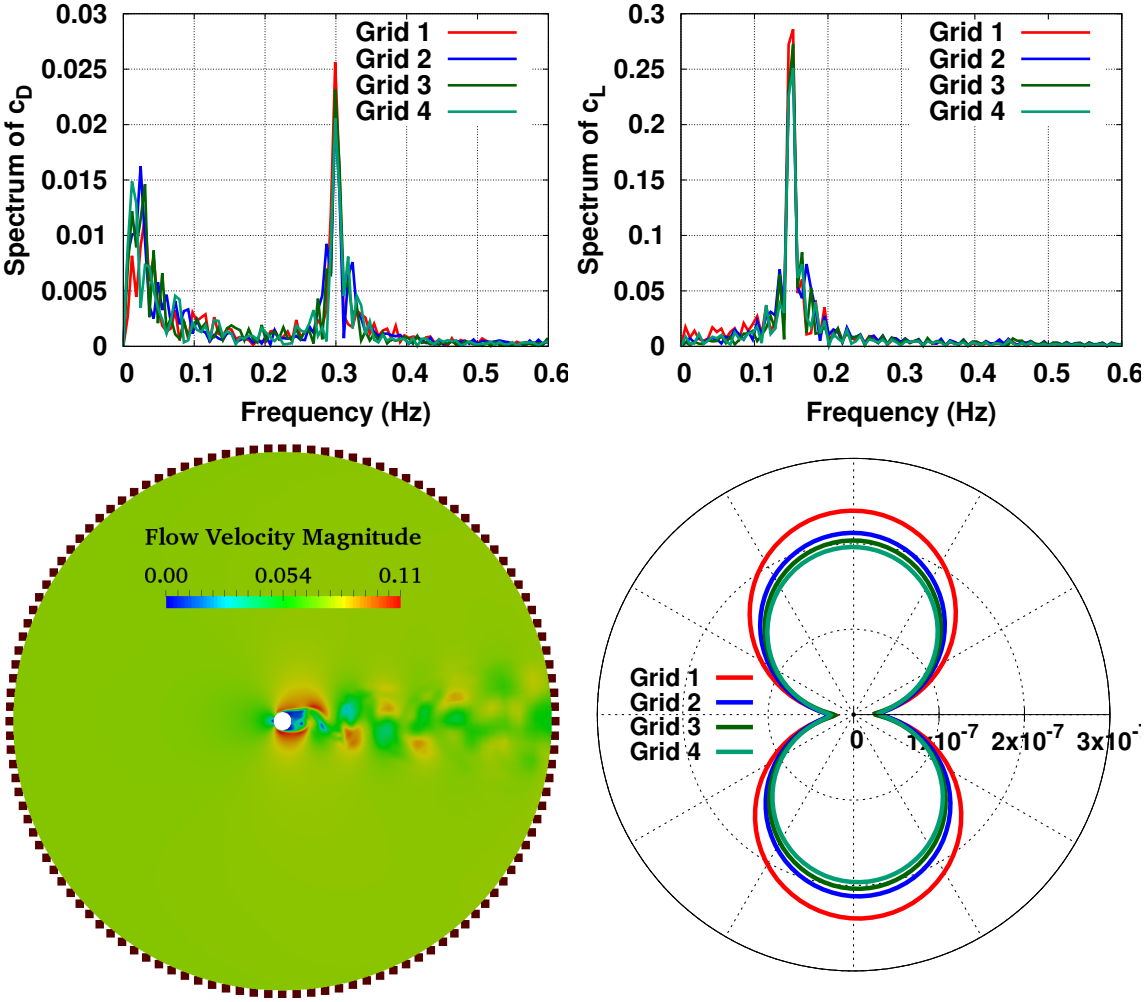

Figure A.1: Turbulent flow around a 3D cylinder at $Re_D = 500$, grid independence study: Comparison among the different grids (as in table A.1) examined for the drag (top-left) and lift (top-right) coefficient spectra and directivity patterns (bottom-right) at 120 receivers placed at a distance of 15D on the Z-plane crossing the middle of the cylinder span (dark squares, bottom-left).

Bibliography

[1] MATLAB and Statistics Toolbox Release 2012b, The MathWorks, Inc., Natick, Massachusetts, United States.

[2] www.gnu.org/software/octave.

[3] www.openfoam.com.

[4] E. Alba and JM. Troya. Analyzing synchronous and asynchronous parallel distributed genetic algorithms. Future Generation Computer Systems, 17(4):451–465, 2001.

[5] WK. Anderson and DL. Bonhaus. Aerodynamic design on unstructured grids for turbulent flows. NASA Technical Memorandum 112867, 1997.

[6] WK. Anderson and V. Venkatakrishnan. Aerodynamic design optimization on unstructured grids with a continuous adjoint formulation. AIAA Paper, 06(43), 1997.

[7] WK. Anderson and V. Venkatakrishnan. Aerodynamic design optimization on unstructured grids with a continuous adjoint formulation. Computers & Fluids, 28:443–480, 1999.

[8] L. Armijo. Minimization of functions having lipschitz continuous first partial derivatives. Pacific Journal of Mathematics, 16:1–3, 1966.

[9] J. Ask and L. Davidson. The sub-critical flow past a generic side mirror and its impact on sound generation and propagation. AIAA Paper 2006-2558, pages https://doi.org/10.2514/6.2006-2558.

[10] T. Bäck. Evolutionary Algorithms in Theory and Practice. Evolution Strategies, Evolutionary Programming, Genetic Algorithms. Oxford University Press, 1996.

[11] C. Bailly, C. Bogey, and O. Marsden. Progress in direct noise computation. International Journal of Aeroacoustics, 9:123–143, 2010.

[12] Seong R. Koh Beckett Y. Zhou, Nicolas R. Gauger and Wolfgang Schroeder. A discrete adjoint approach for trailing-edge noise minimization using porous material. Computational Methods in Applied Sciences, 36:351–365, 2015.

[13] DP. Bertsekas. Constrained Optimization and Lagrange Multiplier Methods, 1st edition. Athena Scientific, 1996.

[14] DP. Bertsekas. Nonlinear Programming, 2nd edition. Athena Scientific, 1999.

[15] C. Bischof, A. Carle, P. Khademi, and A. Mauer. The ADIFOR 2.0 system for the automatic differentiation of Fortran 77 programs. Report CRPC-TR94491, Center for Research and Parallel Computation, Rice University, 1994.

[16] D. Blanchet and A. Golota. Validation of a wind noise source characterization method for vehicle interior noise prediction. In International Conference on Noise and Vibration 2014, 2014.

[17] P.G. Bremner and M. Zhu. Recent progress using sea and cfd to predict interior wind noise. In SAE World Congress 2003-01-1705, Detroit, 2003.

[18] Kenneth S. Brentner and F. Farassat. Analytical comparison of the acoustic analogy and Kirchhoff formulation for moving surfaces. AIAA Journal, 36(8):1379–1386, 1998.

[19] Kenneth S. Brentner and F. Farassat. Modeling aerodynamically generated sound of helicopter rotors. Progress in Aerospace Sciences, 39(2-3):83–120, 2003.

[20] S. Butterworth. On the theory of filter amplifiers. Experimental Wireless and the Wireless Engineer, 7:536–541, 1930.

[21] RH. Byrd. Analysis of a symmetric rank-one trust region method. SIAM Journal on Optimization, 6(4), 1996.

[22] A. Garriga C. Spa and J. Escolano. Impedance boundary conditions for pseudo-time domain methods in room acoustics. Applied Acoustics, 71:402–410, 2010.

[23] Marie Cabrol, Yves Detandt, Michael Hartmann, and Alexandra Mutzke. A comparison between the effects of turbulent and acoustic wall pressure fluctuations inside a car. In AIAA Paper 2012-2202, 18th AIAA/CEAS Aeroacoustics Conference (33rd AIAA Aeroacoustics Conference), Colorado Springs, USA.

[24] A. Carnarius, F. Thiele, E. Ozkaya, A. Nemili, and NR. Gauger. Optimal control of unsteady flows using a discrete and a continuous adjoint approach. System Modeling and Optimization, IFIP Advances and Communication Technology, 391:318–327, 2013.

[25] T. Colonius. Modeling artificial boundary conditions for compressible flows. Annu. Rev. Fluid Mech., 36:315{345, 2004.

[26] T. Colonius and S. Lele. Computational aeroacoustics: progress on nonlinearproblems on sound generation. Progress in Aerospace Sciences, 40:345{415, 2004.

[27] F. Courty, A. Dervieux, B. Koobus, and L. Hascoët. Reverse automatic differentiation for optimum design: from adjoint state assembly to gradient computation. Optimization Methods and Software, 18(5):615–627, 2003.

[28] L. Cremer, M. Hecki, and B.A.T. Petersson. Structure-Borne Sound: Structural Vibrations and Sound Radiation at Audio Frequencies. Springer-Verlag, 2005.

[29] D.G. Crighton, A.P. Dowling, J.E. Ffowcs Williams, M. Heckl, and F.G. Leppington. Modern methods in analytical acoustics | Lecture Notes. Berlin: Springer, 1992.

[30] N. Curle. The influence of solid boundaries upon aerodynamic sound. Proceedings of the Royal Society of London, Series A 2314:505–514, 1955.

[31] L. Davis. Handbook of genetic algorithms. Van Nostrand Reinhold, 1991.

[32] H. Dechipre and M. Hartmann. Aeroacoustics simulation of an automotive a-pillar rain gutter. In 4th European Automotive Simulation Conference, Munich, Germany, 6-7 July 2009.

[33] T. Economon, F. Palacios, and J. Alonso. A coupled-adjoint method for aerodynamic and aeroacoustic optimization. In 12th AIAA Aviation Technology, Integration, and Operations (ATIO) Conference and 14th AIAA/ISSM, Indianapolis, Indiana, USA, 17 - 19 September 2012 2012.

[34] MA. El-Beltagy, PB. Nair, and AJ. Keane. Metamodeling techniques for evolutionary optimization of computationally expensive problems: Promises and limitations. In Genetic and Evolutionary Computation Conference - GECCO 1999. Morgan Kaufmann, San, Fransisco, USA, 27-30 June 1999.

[35] M. Elliot and J. Peraire. Constrained, multipoint shape optimization for complex 3D configurations. Aeronautical Journal, 102:365–376, 1998.

[36] D. Evans, M. Hartmann, and J. Delfs. Beamforming for point force surface sources in numerical data. Journal of Sound and Vibration, to appear in 2019.

[37] R. Ewert and W. Schroeder. Acoustic perturbation equation based on flow decomposition via source filtering. Journal of Computational Physics, 188:365–398, 2003.

[38] F. Farassat and M. Myers. Extension of kirchhoff's formula to radiation from moving surfaces. Journal of Sound and Vibration, 123(3):451–461, 1988.

[39] A. Fichtner, H.-P. Bunge, and H. Igel. The adjoint method in seismology, theory i. Physics of the Earth and Planetary Interiors, 157:86–104, 2006.

[40] R. Fletcher and C. M. Reeves. Function minimization by conjugate gradients. Computer Journal, 7:149–154, 1964.

[41] Roger Fletcher. Practical methods of optimization. New York: John Wiley & Sons, 1987.

[42] KC. Giannakoglou. Design of optimal aerodynamic shapes using stochastic optimization methods and computational intelligence. Progress in Aerospace Sciences, 38(1):43–76, 2002.

[43] M. Giles and N. Pierce. An introduction to the adjoint approach to design. Flow, Turbulence and Combustion, 65:393–415, 2000.

[44] MB. Giles, MC. Duta, JD. Muller, and NA. Pierce. Algorithm developments for discrete adjoint methods. AIAA Journal, 41(2), 2003.

[45] PE. Gill, W. Murray, and MH. Wright. Practical Optimization. Academic Press, 1981.

[46] B. Greschner, F. Thiele, M. C. Jacob, and D. Casalino. Prediction of sound generated by a rod-airfoil configuration using easm des and the generalised lighthill/fw-h analogy. Computers and Fluids, 37:402–413, 2008.

[47] A. Griewank. On automatic differentiation. Mathematical Programming: Recent Developments and Applications. Kluwer Academic Publishers, 1989.

[48] A. Griewank, D. Juedes, H. Mitev, J. Utke, O. Vogel, and A. Walther. ADOL-C: A package for the automatic differentiation of algorithms written in C/C++. ACM Transactions on Mathematical Software, 22(2):131–167, 1996.

[49] A. Griewank and A. Walther. Algorithm 799: Revolve: an implementation of checkpointing for the reverse or adjoint mode of computational differentiation. ACM Transactions on Mathematical Software (TOMS), 26(1):19–45, 2000.

[50] Ali H. Dawi and Rinie A.D. Akkermans. Spurious noise in direct noise computation with a finite volume method for automotive applications. International Journal of Heat and Fluid Flow, 72:243–256, 2018.

[51] J. Hardin and D.S. Pope. An acoustic/viscous splitting technique for computational aeroacoustics. Theoretical and Computational Fluid Dynamics, 6:323–340, 1994.

[52] J. Harrington and S. Cassidy. Techniques in Speech Acoustics. Springer Verlag, 1999.

[53] M. Hartmann, J. Ocker, T. Lemke, A. Mutzke, C. Schwarz, H. Tokuno, R. Toppinga, P. Unterlechner, and G. Wickern. Wind noise caused by the a-pillar and the side mirror flow of a generic vehicle model. In AIAA Paper 2012-2205, 18th AIAA/CEAS Aeroacoustics Conference (33rd AIAA Aeroacoustics Conference), Colorado Springs, USA.

[54] L. Hascoët, J. Utke, and U. Naumann. Cheaper adjoints by reversing address computations. Scientific Programming, 16(1):81–92, 2008.

[55] JA Hay, E Özkaya, and N Gauger, N Schönwald. Application of an adjoint caa solver for design optimization of acoustic liners. In 22nd AIAA/CEAS Aeroacoustics Conference, Lyon France, 30 May - 1 June 2016.

[56] P. He, C. Mader, J. Martins, and K. Maki. An aerodynamic design optimization framework using a discrete adjoint approach with openfoam. Computers & Fluids, 168, 04 2018.

[57] A. Hekmati, D. Ricot, and P. Druault. Vibroacoustic behavior of a plate excited by synthesized aeroacoustic pressure fields. In 16th AIAA/CEAS Aeroacoustic Conference, Vancouver, British Columbia, Canada, June 2010.

[58] F. Herrera, M. Lozano, and C. Moraga. Hierarchical distributed genetic algorithms. International Journal of of Intelligent Systems, 14(9):1099–1121, 1999.

[59] Moni Islam, Friedhelm Decker, Michael Hartmann, Anke Jaeger, Timo Lemke, Joerg Ocker, Volker Schwarz, Frank Ullrich, Bernd Crouse, Ganapathi Balasubramanian, and Fred Mendonca. Investigation of sunroof buffeting in an idealised generic vehicle model - Part I: Experimental results.

In 16 AIAA/CEAS Aeroacoustic Conference, Vancouver, British Columbia, Canada, 5-7 May 2008.

[60] Moni Islam, Friedhelm Decker, Michael Hartmann, Anke Jaeger, Timo Lemke, Joerg Ocker, Volker Schwarz, Frank Ullrich, Bernd Crouse, Ganapathi Balasubramanian, and Fred Mendonca. Investigation of sunroof buffeting in an idealised generic vehicle model - Part II: Numerical simulations. In 16 AIAA/CEAS Aeroacoustic Conference, Vancouver, British Columbia, Canada, 5-7 May 2008.

[61] S. Jakobsson and O. Amoignon. Mesh deformation using radial basis functions for gradient-based aerodynamic shape optimization. Computers & Fluids, 36:1119–1136, 2007.

[62] A. Jameson. Aerodynamic design via control theory. Journal of Scientific Computing, 3:233–260, 1988.

[63] A. Jameson. Optimum aerodynamic design using CFD and control theory. AIAA Paper, 17(29), 1995.

[64] A. Jameson and JJ. Alonso. Aerodynamic shape optimization techniques based on control theory. AIAA Paper, 23(58), 1998.

[65] A. Jameson and S. Kim. Reduction of the adjoint gradient formula in the continuous limit. In AIAA paper 2003-0040, 41th Aerospace Sciences Meeting and Exhibit, Reno, Nevada, January 2003.

[66] A. Jameson, NA. Pierce, and L. Martinelli. Optimum aerodynamic design using the Navier-Stokes equations. In AIAA paper 97-0101, 35th Aerospace Sciences Meeting and Exhibit, Reno, Nevada, 6-9 January 1997.

[67] Niklas Kuehl Juern Krueger and Thomas Rung. Adjoint volume-of-fluid approaches for the hydrodynamic optimisation of ships. Ship Technology Research, 65(1):47–68, 2018.

[68] A. Kabat vel Job, M. Hartmann, and J. Sesterhenn. Prediction of the interior noise level for automotive applications based on time-domain methods. In INTER-NOISE 2016, Hamburg, 2016.

[69] G. Karniadakis and G. Triantafyllou. Three-dimensional dynamics and transition to turbulence in the wake of bluff objects. Journal of Fluid Mechanics, 238:1–30, 1992.

[70] G. Karpouzas, E. Papoutsis-Kiachagias, T. Schumacher, E. De Villiers, K. Giannakoglou, and C. Othmer. Adjoint optimization for vehicle external aerodynamics. 7:1–7, 01 2016.

[71] I. Kavvadias, E. Papoutsis-Kiachagias, and K. Giannakoglou. On the proper treatment of grid sensitivities in continuous adjoint methods for shape optimization. Journal of Computational Physics, 301:1–18, 2015.

[72] IS. Kavvadias. Aerodynamic optimization for turbulent flows using adjoint methods and GPUs (in progress). PhD thesis, National Technical University of Athens.

[73] IS. Kavvadias, EM. Papoutsis-Kiachagias, G. Dimitrakopoulos, and KC. Giannakoglou. The continuous adjoint approach to the k–ω SST turbulence model with applications in shape optimization. Engineering Optimization, DOI:10.1080/0305215X.2014.979816, 2014.

[74] J. Kim, D. Bodony, and J.Freund. Adjoint-based control of loud events in a turbulent jet. Journal of Fluid Mechanics, 741:28–59, 2014.

[75] H.L. Atkins K.R. Meadows. Towards a highly accurate implementation of the Kirchhoff approach for computational aeroacoustics. Journal of Computational Acoustics, 4(2):225–241, 1996.

[76] N. Kroll, N. Gauger, J. Brezillon, R. Dwight, A. Fazzolari, D. Vollmer, K. Becker, H. Barnewitz, V. Schulz, and S. Hazra. Flow simulation and shape optimization for aircraft design. Journal of Computational and Applied Mathematics, 203:397–411, 2007.

[77] LD. Landau and EM. Lifshitz. Fluid Mechanics, Volume 6 of Course of Theoretical Physics. Pergamon Press, 1987.

[78] J. Lienhard. Synopsis of lift, drag and vortex frequency for rigid circular cylinder. College of Eng. Research Div. Bulletin 300, Technical Extension Service, Washington State University, 1966.

[79] M.J. Lighthill. On sound generated aerodynamically: I. general theory. Proceedings of the Royal Society of London, Series A 211:564–587, 1952.

[80] M.J. Lighthill. On sound generated aerodynamically: Ii. turbulence as a source. Proceedings of the Royal Society of London, Series A 222:1–32, 1954.

[81] D. Lim, YS. Ong, Y. Jin, B. Sendhoff, and BS. Lee. Efficient hierarchical parallel genetic algorithms using grid computing. Future Generation Computer Systems, 23(4):658–670, 2007.

[82] JL. Lions. Optimal control of systems governed by partial differential equations. Springer-Verlag, New York, 1971.

[83] B. Lokhande, S. Sovani, and J. Xu. Computational aeroacoustic analysis of a generic side view mirror. In SAE 2003 Noise & Vibration Conference and Exhibition, 2003.

[84] A.E.H. Love. On the smal free vibrations and deformations of elastic shells. Philosophical Transactions of the Royal Society, A(17):491–549, 1888.

[85] C. Lozano. Discrete surprises in the computation of sensitivities from boundary integrals in the continuous adjoint approach to inviscid aerodynamic shape optimization. Computers & Fluids, 56:118–127, 2012.

[86] D.G. Luenberger. Linear and Nonlinear Programming, 2nd edition. Kluwer Academic Publishers, 2003.

[87] Richard G. Lyons. Understanding Digital Signal Processing. Pearson, 2004.

[88] A. Lyrintzis. Surface integral methds in Computational Aeroacoustics - From the CFD near-field to the (acoustic) far-field. International Journal of Aeroacoustics, 2(2):95–128, 2003.

[89] K. Mani and D. Mavriplis. Unsteady discrete adjoint formulation for two-dimensional flow problems with deforming meshes. AIAA Journal, 46:1351–1364, 2008.

[90] MJ. Martin, E. Andres, C. Lozano, and E. Valero. Volumetric b-splines shape parametrization for aerodynamic shape design. Aerospace Science and Technology, 37:26–37, 2014.

[91] J. Martins, J. Alonso, and J. Reuther. High-Fidelity Aerostructural Design Optimization of a Supersonic Business Jet. Journal of Aircraft, 41, 2004.

[92] D. Mavriplis. Discrete adjoint-based approach for optimization problems on three-dimensional unstructured meshes. AIAA, 45(4):740–750, 2007.

[93] Z. Michalewicz. Genetic Algorithms + Data Structures = Evolution Programs, 2nd edition. Springer-Verlag, Berlin Heidelberg, 1994.

[94] W. Moehring. A well posed acoustic analogy based on a moving acoustic medium. Presented at the Aeroacoustic Workshop, Dresden, 1999, 999.

[95] B. Mohammadi and O. Pironneau. Applied shape optimization for fluids. Oxford University Press, 2001.

[96] C. Munz, M. Dumbser, and S. Roller. Linearized acoustic perturbation equations for low mach number flow with variable density and temperature. Journal of Computational Physics, 224:352–364, 2007.

[97] S. Nadarajah and A. Jameson. A comparison of the continuous and discrete adjoint approach to automatic aerodynamic optimization. AIAA Paper, 06(67), 2000.

[98] S. Nadarajah and A. Jameson. Optimal control theory of unsteady flows using a time accurate method. AIAA Paper, 54(36), 2002.

[99] S. Nadarajah and A. Jameson. Optimum shape design for unsteady three-dimensional viscous flows using a nonlinear frequency-domain method. Journal of Aircraft, 44:1513–1527, 2007.

[100] A. Najafi-Yazdi, F. Bres, and L. Mongeau. An acoustic analogy formulation for moving sources in uniformly moving media. Proceedings of the Royal Society A: Mathematical, Physical and Engineering Sciences, 467, DOI:10.1098/rspa.2010.0172, 2010.

[101] JC Newman, WK. Anderson, and DL. Whitfield. Multidisciplinary sensitivity derivatives using complex variables. MSSU-COE-ERC-98-08, 1998.

[102] E. Nielsen and M. Park. Using an adjoint approach to eliminate mesh sensitivities in aerodynamic design. AIAA Journal, 44(5):948–953, 2006.

[103] J. Nocedal and S. Wright. Numerical Optimization. Springer-Verlag, 1999.

[104] A.V. Oppenheim and R.W. Schafer. Digital Signal Processing. Englewood Cliffs, NJ: Prentice-Hall, 1975.

[105] A.V. Oppenheim, R.W. Schafer, and J.R. Buck. Discrete-Time Signal Processing. Upper Saddle River, NJ: Prentice-Hall, 1999.

[106] C. Othmer. Adjoint methods for car aerodynamics. Journal of Mathematics in Industry, 4(6):https://doi.org/10.1186/2190–5983–4–6, 2014.

[107] D. Papadimitriou. In the forward in time solution of theunsteady adjoint equations. In 11th World Congress on Computational Mechanics (WCCM XI), Barcelona, Spain, July 21-25, 2014, 2014.

[108] D.I. Papadimitriou. Adjoint formulations for the analysis and design of turbomachinery cascades and optimal grid adaptation using a posteriori error analysis. PhD thesis, National Technical University of Athens, 2007.

[109] D.I. Papadimitriou. A two-step back{forth algorithm for the solution of the unsteady adjoint equations. International Journal of Computational Fluid Dynamics, 30(3):272–284, 2016.

[110] DI. Papadimitriou and KC. Giannakoglou. A continuous adjoint method with objective function derivatives based on boundary integrals for inviscid and viscous flows. Journal of Computers & Fluids, 36(2):325–341, 2007.

[111] V.S. Papageorgiou, K.D. Samouchos, and K.C. Giannakoglou. The Unsteady Continuous Adjoint Method Assisted by the Proper Generalized Decomposition Method, pages 109–125. 09 2019.

[112] E. Papoutsis and K. Giannakoglou. Continuous adjoint methods for turbulent flows, applied to shape and topology optimization: Industrial applications. Archives of Computational Methods in Engineering, pages http://dx.doi.org/10.1007/s11831–014–9141–9, 2014.

[113] E. Papoutsis-Kiachagias, N. Magoulas, J. Mueller, C. Othmer, and K. Giannakoglou. Noise reduction in car aerodynamics using a surrogate objective function and the continuous adjoint method with wall functions. Computers and Fluids, 122:223–232, 2015.

[114] E.M. Papoutsis-Kiachagias, A.S. Zymaris, I.S. Kavvadias, D.I. Papadimitriou, and K.C. Giannakoglou. The continuous adjoint approach to the k{e turbulence model for shape optimization and optimal active control of turbulent flows. Engineering Optimization, "DOI:10.1080/0305215X.2014.892595", 2014.

[115] M. Papoutsis{Kiachagias. Adjoint Methods for Turbulent Flows, Applied to Shape or Topology Optimization and Robust Design. PhD thesis, National Technical University of Athens, 2013.

[116] T.W. Parks and C. S. Burrus. Digital Filter Design. New York: John Wiley & Sons, 1987.

[117] V. Pascual and L. Hascoët. TAPENADE for C. In Selected papers from AD2008 Bonn, Lecture Notes in Computational Science and Engineering. Springer, 2008.

[118] J. Periaux and G. Winter. Genetic Algorithms In Engineering And Computer Science. John Wiley & Sons, 1995.

[119] D. Peter, C. Tape, L. Boschi, and J.H. Woodhouse. Surface wave tomography: global membrane waves and adjoint methods. Geophysical Journal International, 171:1098–1117, 2007.

[120] J. Peter and RP. Dwight. Numerical sensitivity analysis for aerodynamic optimization: A survey of approaches. Computers & Fluids, 39(3):373–391, 2010.

[121] O. Pironneau. Optimal shape design for elliptic systems. Springer-Verlag, New York, 1984.

[122] J.N. Reddy. Theory and analysis of elastic plates and Shells, 2nd edition. CRC Press, 2006.

[123] J. Reuther and A. Jameson. Aerodynamic shape optimization of wing and wing-body configurations using control theory. In AIAA paper 95-0213, 33rd Aerospace Sciences Meeting and Exhibit, Reno, Nevada, June 1995.

[124] J. Reuther, A. Jameson, J. Farmer, L. Martinelli, and D. Saunders. Aerodynamic shape optimization of complex aircraft configurations via an adjoint formulation. AIAA Paper, 96-0094, 1996.

[125] A. Roshko. On the development of turbulent wakes from vortex streets. National Advisory Committee for Aeronautics, 1954.

[126] T. Rung, D. Eschricht, J. Yan, and F. Thiele. Sound radiation of the vortex flow past a generic side mirror. In 8th AIAA/CEAS Aeroacoustics Conference, Breckenridge, Colorado, 17-19 June 2002.

[127] B. Sanders and N. Katopodes. Adjoint sensitivity analysis for shallow-water wave control. Journal of Engineering Mechanics, 126, 09 2000.

[128] A. Schell. Entwicklung einer Berechnungsmethode zur Vorhersage der Schallausbreitung im Nahfeld eines umstroemten Kraftfahrzeuges. PhD thesis, Fakultaet fuer Luft- und Raumfahrttechnik und Geodaesie der Universitaet Stuttgart, Stuttgart, Germany, 2014.

[129] M. Shur, P. Spalart, M. Strelets, and A. Travin. A hybrid RANS-LES approach with delayed-DES and wall-modelled LES capabilities. Journal of Heat and Fluid Flow, 29(6):1638–1649, 2008.

[130] P. Spalart and S. Allmaras. A one-equation turbulence model for aerodynamic flows. AIAA Paper 1992-0439.

[131] D. Thévenin and G. Janiga. Optimization and Computational Fluid Dynamics. Springer, 2008.

[132] A. Travin, M. Shur, M. Strelets, and P. Spalart. Physical and numerical upgrades in the detached-eddy simulation of complex turbulent flows. In 412th Euromech Colloquium on LES and Complex Transitional and Turbulent Flows, Munich, Germany, 2012.

[133] Turaj Ashuri Tristan Dhert and Joachim R.R.A. Martins. Aerodynamic shape optimization of wind turbine blades using a Reynolds-Averaged Navier-Stokes model and an adjoint method. Wind Energy, 20(5):909–926, 2017.

[134] Z. Tukovic and H. Jasak. Simulation of thin liquid film flow using openfoam finite area method. Presented at 4th OpenFOAM Workshop, Montreal, Canada, June 2009.

[135] J. Utke and U. Naumann. OpenAD/F: User Manual. Technical report, Argonne National Laboratory. latest version available online at http://www.mcs.anl.gov/OpenAD/openad.pdf.

[136] C. Vezyris, I.S. Kavvadias, E.M. Papoutsis-Kiachagias, and K.C. Giannakoglou. Unsteady continuous adjoint method using pod for jet-based flow control. In 11th World Congress on Computational Mechanics (WCCM XI), Barcelona, Spain, July 21-25, 2014, 2014.

[137] M. Wang, J. Freund, and S. Lele. Computational prediction of flow-generated sound. Annu. Rev. Fluid Mech., 38:483{512, 2006.

[138] Q. Wang and J. Gao. The drag-adjoint field of a circular cylinder wake at reynolds numbers 20, 100 and 500. Journal of Fluid Mechanics, 730:145–161, 2013.

[139] Q. Wang, P. Moin, and G. Iaccarino. Minimal repetition dynamic checkpointing algorithm for unsteady adjoint calculation. SIAM Journal on Scientific Computing, 31(4):2549–2567, 2009.

[140] Arthur B. Williams and Fred J. Taylor. Electronic Filter Design Handbook. McGraw-Hill, 1999.

[141] J. Ffowcs Williams and D. Hawkings. Sound generated by turbulence and surfaces in arbitrary motion. Philosophical Transactions of the Royal Society, A264(1151):321–342, 1969.

[142] P. Wolfe. Convergence conditions for ascent methods. SIAM Review, 11:226–235, 1969.

[143] P. Wolfe. Convergence conditions for ascent methods. ii: Some corrections. SIAM Review, 13:185–188, 1970.

[144] Z. Zhang, PC. Chen, S. Yang, Z. Wang, and Q. Wang. Unsteady aero-structure coupled adjoint method for flutter suppression. In AIAA Paper 2013-2849, 21st AIAA Computational Fluid Dynamics Conference, San Diego, California, 2013.

[145] B. Zhou, T. Albring, N. Gauger, C. Ilario da Silva, T. Economon, and J. Alonso. An efficient unsteady aerodynamic and aeroacoustic design framework using discrete adjoint. In 17th AIAA/ISSMO Multidisciplinary Analysis and Optimization Conference, Washington, D.C., 13-17 June 2016.

[146] AS. Zymaris, DI. Papadimitriou, KC. Giannakoglou, and C. Othmer. Continuous adjoint approach to the Spalart-Allmaras turbulence model for incompressible flows. Computers & Fluids, 38(8):1528–1538, 2009.

[147] JA Özkaya, E Hay, N Gauger, and F Thiele. Development of an adjoint caa solver for design optimization of acoustic liners. In 22nd AIAA/CEAS Aeroacoustics Conference, Lyon France, 30 May - 1 June 2016.